INVESTIGATION OF SOME TEMPERATURE-RELATED PHENOMENA IN ELASTOHYDRODYNAMIC CONTACTS INCLUDING SURFACE ROUGHNESS EFFECTS

A THESIS

Presented to

The Faculty of the Division of Graduate Studies

By

Holavanahally Seshachar Nagaraj

In Partial Fulfillment

of the Requirements for the Degree

Doctor of Philosophy in the

School of Mechanical Engineering

Georgia Institute of Technology

December, 1976

INVESTIGATION OF SOME TEMPERATURE-RELATED PHENOMENA IN ELASTOHYDRODYNAMIC CONTACTS INCLUDING SURFACE ROUGHNESS EFFECTS

Approved:

Ward O. Winer, Chairman

David M. Sanborn

Warren C. Strahle

Alan V. Larson

Donald C. O'Shea

Date approved by Chairman 17 Dec. 76

Dedication

This thesis is dedicated to my beloved mother

H. S. Subhadramma, who has inspired

me most, in my life.

ACKNOWLEDGMENTS

The advice, assistance, and constant encouragement of Professor Ward O. Winer, is greatly appreciated. The author is thankful to Professor David M. Sanborn for assistance and suggestions throughout this work. The author wishes to thank his thesis committee for their time, interest, and suggestions.

The assistance of Mr. William R. Jones of the NASA Lewis Research Center, Cleveland, Ohio, in carrying out the ferrographic analysis of oil samples and the assistance of Mr. Vernon K. Ausherman during the development of the infrared temperature measurement technique are greatly appreciated. The author's thanks are due to Mr. Scott S. Bair for building the combined rolling and sliding EHD simulator and the rotation attachment for the Bendix profilometer. The sliding EHD simulator used in the present study is a slightly modified version of the rig originally built by Dr. David M. Sanborn. The author would also like to thank Mr. Gene Clopton for help during instrumentation.

The research reported herein was supported by NASA (NGR-11-002-133), and by NSF (ENG 74-21002).

TABLE OF CONTENTS

TABLE OF CONTENTS (Continued)

LIST OF TABLES

LIST OF ILLUSTRATIONS

LIST OF ILLUSTRATIONS (Continued)

LIST OF ILLUSTRATIONS (Continued)

LIST OF ILLUSTRATIONS (Continued)

LIST OF ILLUSTRATIONS (Continued)

LIST OF ILLUSTRATIONS (Continued)

SUMMARY

Elastohydrodynamic Lubrication has been recognized as an important mode of lubrication, especially of nonconforming machine elements. This research is aimed towards answering the question how and when does an elastohydrodynamic film fail. It envisages a better understanding of several phenomena like thermal effects, asperity interactions characteristic of rough surfaces operating under severe conditions, and transition from elastohydrodynamic to boundary regimes of lubricated concentrated contacts.

The present research consists of the development of a reliable technique for measuring the ball surface and fluid film temperatures in an elastohydrodynamic contact. This technique is then used to determine temperatures at peak Hertz pressures from 0.52 GPa (75,500 psi) to 2.03 GPa (294,000 psi) for sliding speeds ranging from 0.02 m/s to 12.7 m/s including varying amounts of rolling. The measured temperatures are compared with values predicted using Blok-Jaeger-Archard surface flash temperature theory. Effects of surface roughness as they influence the surface temperatures are explored using rough balls. Finally, high frequency temperature fluctuations emanating from interacting asperities are measured and used to predict the onset of severe asperity interactions. A digital frequency analysis of surface profiles before and after running is also performed and correlations with temperature fluctuations are made. Results obtained indicate that only a band of wavelength of surface features is important for any given application, such as $\frac{1}{4} \leq \hat{\lambda} \leq 2$; $\hat{\lambda} = \frac{\lambda_s}{2a}$, where λ_s is the wavelength of surface feature of importance and 2a is the Hertzian contact diameter.

NOMENCLATURE

a	Hertzian contact radius, m
a_1, a_2	Constant in ΔT_b versus R_a correlations
b_1, b_2, b_3, b_4	Constants in ε_F and τ_F
c	specific heat, J/(kg·K)
C	Auto-correlation function
d	Hertzian contact diameter = 2a, m
E	Modulus of elasticity of the two contacting surfaces, N/m^2
E'	Effective modulus of elasticity, where $\frac{2}{E'} = [\frac{1-\nu_{st}^2}{E_{st}} + \frac{1-\nu_{sa}^2}{E_{sa}}]$
h_c	Film thickness at contact center, m
h_m	Minimum film thickness, m
H	Hardness, N/m^2
k	Thermal conductivity, W/(mK)
K_W	$= \Omega \cdot H/(W \cdot S)$, Wear Coefficient
L	Non-dimensional time parameter = $t_1/t_2 = \frac{Va}{2\alpha}$, $(2L = \frac{Va}{\alpha}$ Peclet number)
ℓ	Length, m
N	Radiation, $W/(sr \cdot m^2)$
ΔN	$= N_{max} - N_{min}$
n	Fringe order
$P(\omega)$	Power spectrum
P_H	Peak Hertz contact pressure, Pa
$\bar{q}$	Heat flux, W/m^2

r	Correlation coefficient
R_1, R_2	Radii of the two contacting surfaces, m
R	$\frac{1}{R_1} \pm \frac{1}{R_2}$, equivalent radius of conjunction, m (for external and internal contacts respectively)
S	Distance travelled by ball surface, mm
t	Time, s
t_1	Thermal diffusion time = $a^2/2\alpha$,s
t_2	Characteristic resident time = a/V,s
T	Temperature, C
T_{bath}	Bath Temperature, C
ΔT	Temperature rise, C
T^*	=T + 273.16, K
T_o	Upstream (bulk) temperature, C
T_f	Surface flash temperature, C
T_c	Critical temperature, C
TC	Traction coefficient
V'	Voltage output of IR detector preamplifier
V	Surface Velocity, m/s
$\overline{V}$	Rolling velocity = $(V_b + V_{sa})/2$, m/s
V_{BP}	Break-point velocity in correlation study, m/s
V_s	Sliding velocity = $V_b - V_{sa}$, m/s
W	Normal load, N
x	Distance along surface, m
α	= $k/\gamma c$
α'	Lubricant absorptivity, m^{-1}
β	Length shift in computing autocorrelation function, m
β^*	Correlation distance, m

γ	density, kg/m^3
K	A constant = $.968\ a^{1/2}\alpha^{1/2}/k$, $m^{3/2}s^{1/2}$ C/N
ϵ	Emissivity
ζ	Refractive index of Lubricant
η	Attenuation factor
Λ	h_c/σ
λ	Wavelength, m
λ_s	Wavelength on Surface, m
μ	Viscosity, Ns/m^2
ν	Poisson's ratio
ξ	Fringe radius, m
ρ	Reflectivity
ρ_1	Air/sapphire interface reflectivity
ρ_2	Lubricant/sapphire interface reflectivity
ρ^*	$= \rho_1 + \tau_s^2(1 - \rho_1)^2\rho_2$
Σ	Slide roll ratio = $V_s/\overline{V}$
σ	$=\sqrt{\sigma_b^2+\sigma_{sa}^2}$, composite, surface roughness, rms or R_a, m
σ_b	Ball surface roughness, rms or R_a, m
σ_{sa}	Sapphire surface roughness, rms or R_a, m
σ_θ	Rms slope of asperities
τ	Transmissivity
$\Delta\phi$	Phase change, rad
ω	Wave numbers = $1/\lambda$, m^{-1}
Ω	Wear volume, mm^3

ubscripts

	ball
	fluid
a }	sapphire
t	steel
	Ambient
	monochromatic
B	black body
ax	maximum
in	minimum
ff	Effective

CHAPTER I

INTRODUCTION

A. Need for Study of Tribology

Tribology has been defined as the science and technology of interacting surfaces in relative motion. The science of tribology plays a vital role in our advanced technological society. Friction consumes and wastes energy. The loss of energy due to friction is very high. A conservative estimate of the frictional energy loss [1], reveals a figure of one-third to one-half of the total production of energy in the world. Wear causes changes in dimensions, and eventual breakdown of the machine element and the entire machine and all that depends on it.

Several reasons for studying tribology are: reducing the waste of world's production of energy, conserving critical natural resources, maintaining production schedules in a plant, and increasing the effective service life of machines.

Tribology is concerned with the entire realm of interacting surfaces in relative motion and as such, is interdisciplinary, requiring attention from virtually all branches of science.

From the macroeconomic point of view, the Jost report [2] quoted a possible savings of $1.24 billion per annum for the United Kingdom in 1966 through a systematic study and implementation of tribological principles. In a recent article Jost [3], through a similar study, quotes a potential annual saving of $12 to $16 billion for the

United States.

Many societal benefits have been derived from the study of tribology. Highway safety has been and will be a great societal concern. After a systematic study of the chronic problem of hydroplaning, many suggestions have been made to reduce the threshold for hydroplaning. Tribology has also contributed towards the alleviation of human misery. A few examples are: lubrication of contact lenses, microcirculation related to cardiovascular problems, natural and prosthetic human joints (especially human synovial joints). Several fatal failures and disasters caused by failure of mechanical equipment have been traced to tribological problems. Mechanical equipment reliability [4] is also an important concern in part dependent on tribology.

Lubrication problems of today are complicated because of the severe operating conditions to which many systems are subjected. There are many machine elements whose contacting surfaces do not conform to each other and the full burden of the load must be carried by a very small area of contact. This is unlike hydrodynamic lubrication where the surfaces conform to each other so that the load is supported by a relatively larger area. Some examples of these non-conforming surfaces are: mating gear teeth, cam and followers, and rolling element bearings. The ball and race in a ball bearing conform to some degree in one direction, but to a very little extent in the other direction. There was very little belief until the 1950's that these nonconforming surfaces with extremely small areas of contact could be separated by an oil film. The lubrication of these nonconforming surfaces is referred to as elastohydrodynamic lubrication [5,6].

B. Elastohydrodynamic Lubrication

Elastohydrodynamic lubrication (EHD) is the study of lubrication situations in which elastic deformation of the surrounding solids plays a significant role in the hydrodynamic lubrication process. The mechanism of elastohydrodynamic lubrication is essentially an extension of that of ordinary hydrodynamic lubrication which was described by Osborne Reynolds in 1886 in his masterpiece work [7].

When two non-conforming bodies are pressed against each other, the surfaces contact each other over a small but finite region, which is called the Hertzian region. The interface pressure is referred to as the Hertzian pressure. This Hertzian condition of contact is a dominating feature of elastohydrodynamic lubrication, since it establishes the overall shape of the contacting surfaces. The enormous increase of viscosity of the lubricant with high pressures and the physical dimensions of the EHD film (length is 1000 times the thickness) together cause the buildup of the elastohydrodynamic film.

The terms point and line contacts commonly used in EHD lubrication, refer to the shape of the Hertzian region. These two terms correspond to the limiting cases of the general shape (an ellipse) of a Hertzian contact. Furthermore, the EHD problems are characterized by the slide-to-roll ratio of the bearing surfaces. Sliding is defined as the difference in speed between the bearing surfaces, while rolling is referred to the average speed of the bearing surfaces.

Temperature rise and its effects encountered in elastohydrodynamic films for the case of pure rolling are small, and hence, an isothermal approximation appears adequate. But, even with moderate sliding the heat

roduced due to viscous dissipation becomes very important. The average luid temperature in the vicinity of the inlet to the Hertzian zone has a lgnificant effect on the film thickness in the Hertzian plateau region. ıis is because the inlet viscosity which controls the lubricant film ıickness is influenced to a great extent by the inlet temperature. In ldition, surface tractions seem to be significantly affected by the temp- :ature rise.

The temperature rise within the Hertzian contact zone of both the ırfaces of the solid and the fluid are of great importance. The surfaces : the solid experience a temperature rise as they pass under the heat ɔurce produced by viscous dissipation. To conduct the energy into the ırfaces of the solid, a temperature variation across the film of the ıbricant is necessary. The temperature rise of the solid and the fluid :e important since they have a direct relevance to the widely held view ıat the failure of highly loaded lubricated contacts is governed by the ıermal properties of the lubricant and the solids.

Until very recently theoretical and experimental elastohydrodynamics :re concerned only with the existence of very thin, but operative, hydro- ɲamic films. The conditions under which these films can be estab- .shed are well understood. The difficult question of deciding when .astohydrodynamic conditions cannot prevail is now the interesting prob- :m area.

Mixed lubrication, that is when both elastohydrodynamic and bound- y lubrication are present, is also a common occurrence in machine ele- nts and therefore of great importance.

C. Current State of Knowledge

Excellent reviews of the subject of elastohydrodynamics through 1965 are available in literature [8,9,10,11]. Recent reviews by Winer [12] and Cheng [13] concerning experimental and theoretical EHD work, spell out briefly the achievements accomplished to date and also highlight the problem areas of present and future interest.

A quest for understanding the mechanism of gear lubrication formed the need for the study of elastohydrodynamic lubrication. Martin in 1916 [14] examined the existence of a hydrodynamic film between gear teeth in contact, but failed to show the existence of a moderately thick film because of his assumptions of rigid surfaces and an isoviscous fluid. However, Martin's work marked the beginning of studies on EHD. In a pioneering paper in 1941 [15] Beeck, Givens, and Smith reported the existence of a moderately thick film, determined through measurements. The other milestone, which was a theoretical breakthrough, occurred in 1949 [16] when Grubin and Vinogradova (Prof. Blok [17] suggests that Ertel's name also be included in Ref. [16]) reported a film thickness formula which included enough parameters to be of good practical utility.

Experimental work in EHD has received more attention because the general solution for the governing equations appears almost impossible and also because, in several particular problems of interest, formulation appears not to be possible. For example, when thermal effects are considered, the equations describing the formation of an elastohydrodynamic film require extensive computing facilities using subtle mathematical techniques.

EHD is best studied by considering the important physical variables of an EHD conjunctive region. The main independent variables are surface velocities, load, solid material properties, lubricant bulk temperature, initial surface roughness and topography, and lubricant rheological properties. The dependent variables are film thickness, traction, lubricant pressure, solid stress field, temperatures of solid and lubricant, changes in surface topography, and sometimes lubricant rheological properties and shear degradation.

EHD Film Thickness

Film thickness has perhaps received more attention than any other dependent variable because of its direct practical relevance. An empirical solution was developed by Dowson and Higginson [18] in 1961 for the isothermal elastohydrodynamic case (for nominal line contacts). An excellent agreement exists between measured film thickness and that predicted by the empirical equation of Dowson and Higginson [18] for rolling and moderate load cases. Even with moderate sliding, the thermal effects become important. Cheng [19,20,21] after extensive numerical work gave thermal reduction factors by which the isothermal film thicknesses are reduced. For nominal point contacts, Archard and Cowking [22] give side leakage factors by which the corresponding line contact film thicknesses are reduced. Cheng [21] gives a comprehensive account of the method for calculating film thickness including the thermal reduction factors and side leakage factors. Very recently, Hamrock and Dowson [23,24,25,26] have developed an isothermal EHD theory for point contacts. Some observations concerning film thickness for point contacts under high loads have been reported by Lee, Sanborn,

and Winer [27]. However, some discrepancies still exist for the high load cases. Also deviations between analytically predicted and experimentally measured film thickness exist with respect to fluid rheological properties as observed by Sanborn and Winer [28], and Hamilton and Robertson [29].

There are four basic techniques which have been used to measure the film thickness in EHD contacts. They are based on the electrical resistance of the film, the capacitance of the lubricant-bearing system, the attenuation of x-rays transmitted through the film, and the optical interference of the lubricant-bearing system. The optical interference technique has been most useful for point contact studies. The x-ray technique can determine only minimum film thickness in a point contact and not the film thickness at center because of the side and exit restrictions in the film. The two electrical techniques can measure only an average film thickness over the contact area. The most important advantage of the optical technique, used in the present investigation, is the fact that the film thickness at all points in the contact is determined at once.

Traction

Tractive force in elastohydrodynamic contacts can be determined, in principle, by integrating over the contact area the shear stress evaluated at one of the bearing surfaces. Although this concept is straightforward, acceptable analytical results covering various regimes of EHD lubrication do not exist to date. Many simplified approaches are available in references [30-36]. However, the measurement of

traction in EHD contacts is quite easily accomplished by measuring the reaction forces in the bearing system. In this investigation, traction is measured using the EHD simulators and these values are used in the calculation of fluid and surface temperatures in EHD contacts.

Contact Temperatures

Temperatures both of the surfaces and of the fluid have been receiving attention recently. The chemical stability of the lubricant and the surfaces govern the limits of EHD. The high temperatures of short duration, which occur close to the areas where the energy is being dissipated in a friction system, are called flash temperatures. Several attempts have been made to define a failure criterion in terms of these surface flash temperatures. One of the first of these scoring criteria was that of Blok [37]. This criterion suggests that scoring occurs when the bulk oil temperature plus the flash temperature $(T_{b0} + T_f)$ exceeds a certain critical temperature T_c.

Cheng and Sternlicht [19] and later Cheng [20] calculated EHD contact temperatures by simultaneously solving the Reynold's equation, the elasticity equation, and the energy equation while assuming certain rheological models for the fluid. These idealized conditions and assumptions introduce uncertainty into the result because of incomplete knowledge of the behavior of the lubricant under high pressure, temperature and shear stress, because the surfaces are not ideally smooth as assumed, and because of the uncertainty of appropriate thermal boundary conditions on the film.

Cheng and Orcutt [38] measured the surface temperature using a platinum film gage on a glass disk and later Hamilton and Moore [39]

used a vapor deposited nickel film gage on a glass disk. A similar method has been used by Bartz & Ehlert [40]. Although the probes were small they accounted for eight to ten percent of the film thickness under operating conditions. The operating conditions were limited in severity because of the glass surface and fragility of the gages. The non-contacting technique developed by Turchina, Sanborn, and Winer [41] and further developed as reported in this work has the advantage that it in no way interferes with the conjunctive region and can be utilized at conditions of contact severity comparable to those in real engineering applications.

Several theories including those of Blok [42,43] and Jaeger [44] have been advanced for a calculation of the flash temperatures. More recently, Archard [45] has given a useful summary of the formulation along with a graphical procedure for the determination of these flash temperatures. Several analogies including the one of an electrical contact have been developed by Holm [46] and others [47]. Attempts have also been made to measure the flash temperatures developed in the highly localized regions of contact using the sliding contact of two different metals as a thermocouple by Bowden and Ridler [48,49] and Bowden and Hughes [50]. These experiments were either confined to the dry sliding of two metals or in some cases, for boundary lubricated conditions, and were successfully applied to a study of the mechanism of polishing and formation of the Beilby layer. So, thus far, there has not been a dependable experimental verification of the calculated flash temperatures. The present AGMA gear scoring criterion [51] is based on surface flash temperature calculations of Blok [42], later

modified by Dudley [52], and Kelley [53,54], and thus awaits an experimental verification also.

Surface Roughness Characterization and Effects

The characterization of surface topography and detailed analysis of surface contact has reached a very high degree of sophistication. There are two basic models available in literature for surface characterization; Greenwood-Williamson-Tripp [55,56] and the Whitehouse-Archard [57] models. The Greenwood-Williamson-Tripp model is defined by three parameters:

σ^* = standard deviation of asperity height distribution

R = radius of curvature of the asperities (assumed constant for all asperities)

η = density of asperities per unit area

The Whitehouse-Archard random surface model is defined by two parameters:

σ = standard deviation of the asperity height distribution

β^* = the correlation distance which corresponds roughly to the spacing between asperities of equal heights

Archard [58] shows that the three parameters of the Greenwood-Williamson-Tripp theory are not all independent and in fact $\sigma^* R\eta$ = constant. Further, there is a more sophisticated version due to Nayak [59,60,61] which takes into account the fact that when asperity peaks are plastically deformed, the valleys rise up and approach the mean plane.

As yet the developments in surface characterization, referred to above have had a rather small impact upon the concepts of lubrication [62,63]. The influence of surface topography on the mechanisms of lubrication involved in concentrated contacts has recently been

studied by Christensen [64] using a random surface model for a rough engineering surface and a stochastic approach. The important conclusion has been that roughness oriented normal to relative motion increases the EHD film thickness while roughness oriented along the relative motion decreases the EHD film thickness. Cheng and co-workers [66, 67] have been recently studying the effect of preferentially oriented surface roughness pattern on EHD lubrication using a deterministic approach. Jackson and Cameron [65] have used an optical interferometric technique to study EHD lubrication of rough surfaces. This technique has limited application because the specular reflectance decreases very much with increasing roughness.

As a parallel development, some investigators, notably Fein and Kruez [68] and Fowles [69], have considered the possibility of EHD lubrication occurring at individual asperities. Explanation of several dependent variables of the contact using this microelastohydrodynamic theory has not been completely satisfactory.

A very useful parameter first introduced by Dawson [70] in 1962, and later deduced by Johnson, Greenwood and Poon [71] is Λ which is equal to the ratio of elastohydrodynamic film thickness (h) to the composite surface roughness (σ). More recently, Bamberger, et al. [72] suggest the use of the Λ-factor in bearing design and selection. It is suggested that $\Lambda > 2$ is satisfactory, $\Lambda < 1$ is unsatisfactory, $1 < \Lambda < 2$ being the transition region.

The asperity contacts which appear to occur through the elastohydrodynamic films have not been well understood. The interaction of several mechanisms of lubrication and solid asperity contacts poses a

very difficult problem.

D. Need for Present Research

It has been remarked above that the conditions under which elastohydrodynamic films can be built up, are well understood. The conditions which lead to a failure of these films however, need to be investigated. In other words, failure of elastohydrodynamic lubrication needs to be understood. This has been one of the main objectives of the present study. Toward understanding the elastohydrodynamic scuffing failure, some temperature-related phenomena have been studied. These studies are based on the assumption that the contact scuffing failure is temperature-dependent. As speeds and loads increase owing to a need for faster operation and compact design, more understanding of failure of EHD contacts is needed in order to extend the limits of operation.

A real engineering surface is a rough surface as opposed to an ideally smooth one assumed in most analyses. Several phenomena like surface asperity interactions and running-in are characteristic of rough surfaces. Also, during transition from pure elastohydrodynamic to boundary lubrication, surface asperity interactions are very important. If these asperity interactions are too severe, microcracks might develop at the surface and may lead to surface initiated fatigue failure. On the other hand, successful running-in of the surface may result if asperity interactions are not very severe. Another possible effect due to severe asperity interactions is thermal scuffing at the site of interacting asperities, because high local temperatures are

perhaps developed at these sites. A deeper study of all these important phenomena is required.

E. Summary of Research Performed

The present study is directed toward a deeper understanding of thermal effects and asperity interactions in elastohydrodynamic lubrication. This work includes the study of transition from the elastohydrodynamic regime through the boundary regime to failure by scoring of the surfaces. Through the approach of experimental investigation, some temperature related phenomena occurring in elastohydrodynamic point contacts have been investigated.

It was mentioned earlier that typical elastohydrodynamic contacts are small and so also, the conditions are severe in terms of pressure, temperature, shear stress, and shear rate. This demands a non-contact mode of temperature measurement (some type of radiation measurement). A technique for measuring the ball surface temperature and the average film temperature (fourth power average through the thickness of the fluid film) in an EHD conjunction has been developed. An infrared microdetector (Barnes' model RM-2A) has been used to collect the infrared radiation emitted by the EHD contact from a spot size of 0.0356 mm (0.0014") diameter. The technique employs two interference filters for separating the individual contributions from the total IR radiation received by the detector. If the filters have certain spectral characteristics, then through analysis and calibration, the equivalent black body radiation and the respective temperatures can be determined. Film thicknesses needed for film temperature calculations are measured

using an optical interference technique.

Temperatures have been measured at peak Hertz pressures ranging from 0.52 GPa (75,500 psi) to 2.03 GPa (294,000 psi) for sliding speeds ranging from 0.02 m/s to 12.7 m/s. Temperature contour maps have been prepared by scanning the EHD contact. From the measured values of ball surface temperature, the effect of speed and load on surface temperature is deduced. The average ball surface temperatures calculated by using the Blok-Jaeger-Archard theory are compared with the measured values. This also serves as a verification for the gear scoring criterion recommended by the American Gear Manufacturer's Association (AGMA) which was based on the flash temperature formula of Blok [37].

Surface temperature measurements for the case of combined rolling and sliding have also been made. The rolling velocity is kept constant in most of the experiments. Centerline temperature distributions have been measured as a function of slide-roll ratio, Σ. The slide-roll ratio was varied from a value of 0 which corresponds to pure rolling to a value of ± 2 which correspond to one of the surfaces moving and the other stationary. The flash temperature theory was extended to cover the case of two moving surfaces.

For the purposes of investigating the effect of surface roughness on ball surface temperatures, steel balls of three different roughnesses with .011 μm, .076 μm, and .38 μm R_a value were used. The ball surface temperature rise is then correlated with respect to R_a value of surface roughness in addition to including the effect of the speed and load parameters.

During transition from pure elastohydrodynamic to boundary lubrication, surface asperity interactions are very important. In this part of the work, the high frequency temperature fluctuations resulting from the interaction of individual asperities have been measured, using the infrared temperature measurement technique developed earlier. The surface wear has been measured by relocation profilometry of the surface and lubricant sample analysis (both ferrographic and spectrographic). During low lambda ratio experiments, the temperature fluctuations and the surface profile were recorded before and after the experiment and later subjected to spectral analysis. The purpose of this type of analysis was to determine the relative importance of surface features of different wavelengths. The effects of running-in were also studied by such an analysis.

F. Experimental Variables

The two main dependent variables in this study are the temperature and the change in surface topography. Both time-steady and fluctuating surface temperatures were measured. In addition, fluid temperature was also measured whenever possible. Surface topography was measured before and after an experiment to detect any changes. Wear measurements were also performed by measuring debris in the used oil samples. These wear measurements indicate surface wear and therefore, the change in surface topography. Two other dependent variables, the film thickness and traction coefficient have also been studied. Film thickness values are needed for computing fluid temperatures, whereas traction values are required for calculating energy dissipation in the contact.

The independent variables are the velocities of the surfaces, the normal load and the initial surface topography. The normal load on the contact was varied. The maximum load was limited by the rigidity of the experimental rig and the capacity of the drive system. The lowest value of the load was determined by the resolution of the load measuring system. The range of loads used represents Hertz pressures encountered in practice. The minimum values for surface velocities were determined by minimum film thickness when no change in surface topography was desired. When a change in surface topography was either required or could be tolerated, the resolution of the speed measuring system was the controlling factor. The maximum speed was determined both by lubricant starvation and drive system capacity. The initial surface topography was mainly characterized by the R_a value, even though other parameters were considered. The surface finish of the commercially available steel balls determined the lowest R_a value. The maximum R_a value was chosen rather arbitrarily. The rougher balls were finished by the standard grinding process and did not have any preferred orientation.

The environmental temperature or the lubricant bath temperature controls the viscosity of the lubricant in the EHD inlet region. No effort was made to vary this temperature. On the other hand, in many experiments, the lubricant bath was controlled to remain constant ($\approx$ 40 C).

The material parameters were not varied in this investigation. However, the influence of some of the material parameters can be easily

estimated. The following materials were chosen for the present investigation. The two solid surfaces were hardened steel (AISI-52100) and synthetic sapphire (Al_2O_3). The synthetic sapphire was chosen because of its optical and infrared transmission properties, and extremely good mechanical properties. The sapphire also has thermal properties close to those of AISI-52100 steel. The lubricating oil chosen was a pure mineral oil of naphthenic base (designated N1 - see Appendix A for properties). This fluid is known to have very good pressure-viscosity characteristics and has been used in earlier EHD experiments. Some implications of holding the material parameters constant are discussed in later chapters.

CHAPTER II

EHD SIMULATORS - MEASUREMENT OF FILM THICKNESS AND TRACTION

A description of the two EHD Simulators used in the present study is given in this chapter. In addition, the techniques and the equipment used to measure traction and film thickness are briefly described.

A. Sliding EHD Simulator

Nonconformal bearing surfaces are required for obtaining an elastohydrodynamic lubricating film. For the study of point contacts, sphere-on-flat configuration is by far the most convenient. The load is applied normal to the plane of contact. By rotating one of the surfaces and keeping the other stationary, sliding can be introduced. Rotating the sphere about an axis parallel to the plane of the contact is easier than rotating the flat, and therefore, this kinematic configuration is used in the sliding EHD simulator. However, in the sliding/rolling EHD simulator (to be described in the next section), the flat surface can be rotated and the sphere held stationary, to yield the sliding motion. This arrangement was necessary for studying the stationary surface temperatures. The normal load, the sliding velocity, the lubricant properties, and the surface texture of the bearing surfaces, then control the formation of a full elastohydrodynamic film.

A synthetic sapphire disc is used as the flat bearing surface. A metallic adaptor permits the use of different size sapphire discs (1/4" dia.

x 1/16" thick, 1" dia. x 1/8" thick, 2" dia. x 1/8" thick). The synthetic sapphire was selected because it has the following properties: mechanical properties necessary in a highly loaded bearing, optical properties necessary for optical film thickness measurement, infrared properties necessary for infrared temperature measurement, and thermal properties comparable to those of steel. The synthetic sapphire used in this study is very smooth with .006 μm R_a (.25 μ-in. AA) and optically flat to within an eighth of a wave. The position of the sapphire disc in the EHD simulator is shown in the schematic diagram of the test apparatus shown in Figure 1.

The sphere is a commercially available steel ball 31.8 mm (1.25") in diameter, made of bearing steel - AISI 52100, chrome steel. The properties of the steel and sapphire appear in Appendix B. For all optical film thickness measurements, the steel ball of .011 μm R_a is used. This ball is referred to as the smooth ball in the present study. Balls of .076 and .38 μm R_a were also used for studying the effect of surface roughness, and are referred to as medium rough and rough balls respectively.

The sliding EHD simulator (Figure 1) is a slightly modified version of the rig originally built by Dr. David M. Sanborn [79].

The ball is driven by a variable speed motor and a drive shaft through a flexible coupling. This coupling provided a high torsional rigidity and a low bending rigidity for the drive shaft - qualities which are necessary for accurate traction measurement. The drive shaft is connected to the ball through a collar that is cemented onto the ball surface.

The test ball is supported on three sapphire pads. These sapphire pads are at an angle to the normal load and are offset so that the tracks

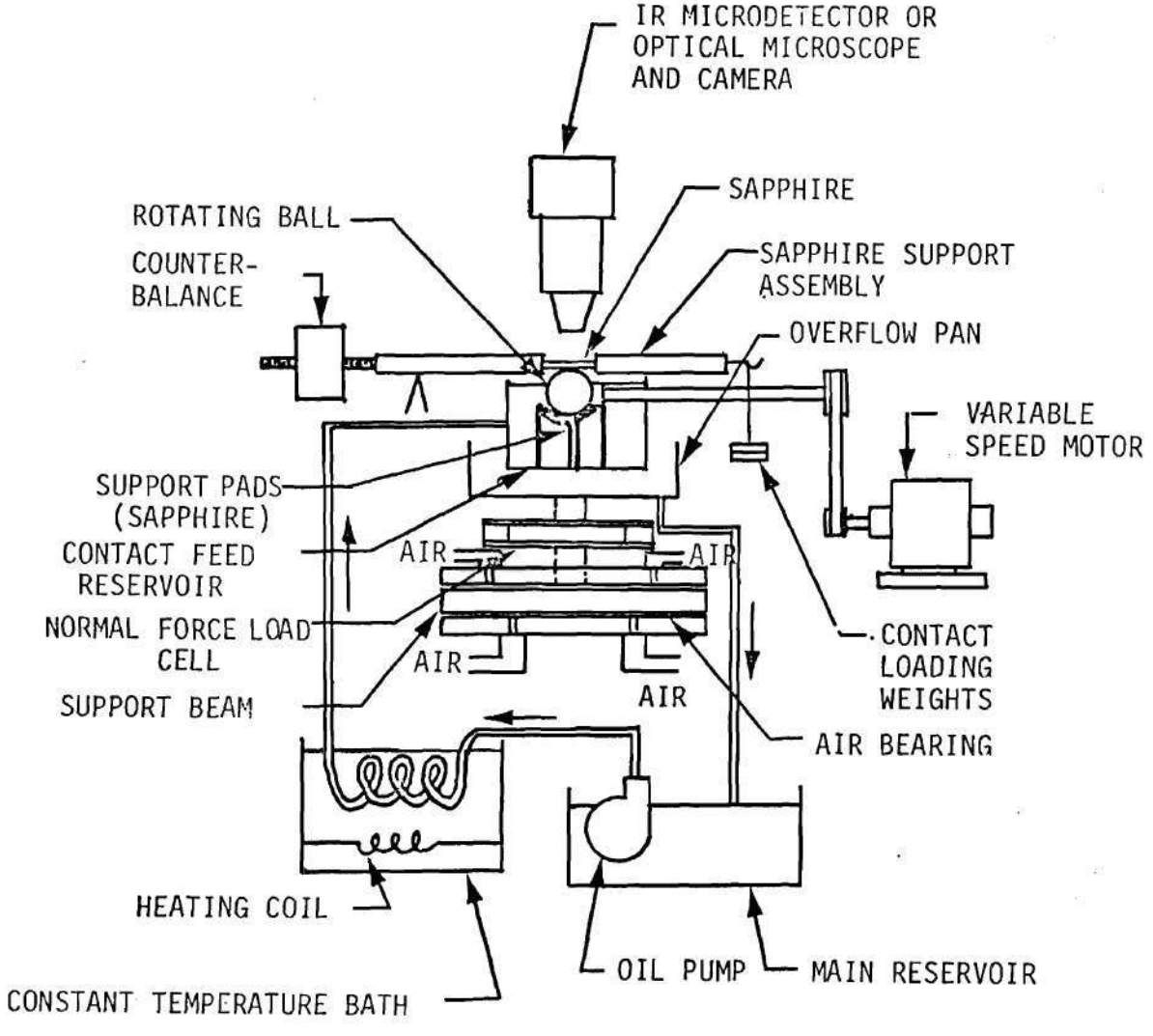

Figure 1. Schematic of the Sliding EHD Contact Simulator.

on the test ball are noncoincident. This arrangement was found to be more convenient than the standard four ball configuration because in this arrangement the top contact is the most severe of the four contacts. This feature of higher severity at the top contact is of particular significance at high normal loads. The four ball configuration becomes inoperable under these conditions because of severe scoring at the bottom contacts.

A dead weight loading system is used to apply normal load on the contact. Since only steady load data was of interest, this system was found adequate. Excellent repeatability and high load range were obtained. Figure 2 shows the loading system also, where the sapphire mount is shown housed in the loading lever.

A lubricant supply system was needed in order to maintain an adequate supply of lubricant to the bearing reservoir at a constant temperature. Without such a system, each test run resulting in a different amount of energy dissipation would have a different equilibrium reservoir temperature. The lubricant supply system consists of a sump pump, an oil filter, a constant temperature bath, a control valve, bearing reservoir overflow pan and the main reservoir. This system is shown in Figure 1. Lubricant temperature in the bearing reservoir is periodically measured by a thermocouple.

The rotational speed of the ball is measured by counting the revolutions digitally during a known interval of time. This system consists of a light tube (focussed on the surface of the drive shaft), fiber optics, a sensor and a digital counter. A portion of the drive shaft circumference is painted black in order to provide the contrast.

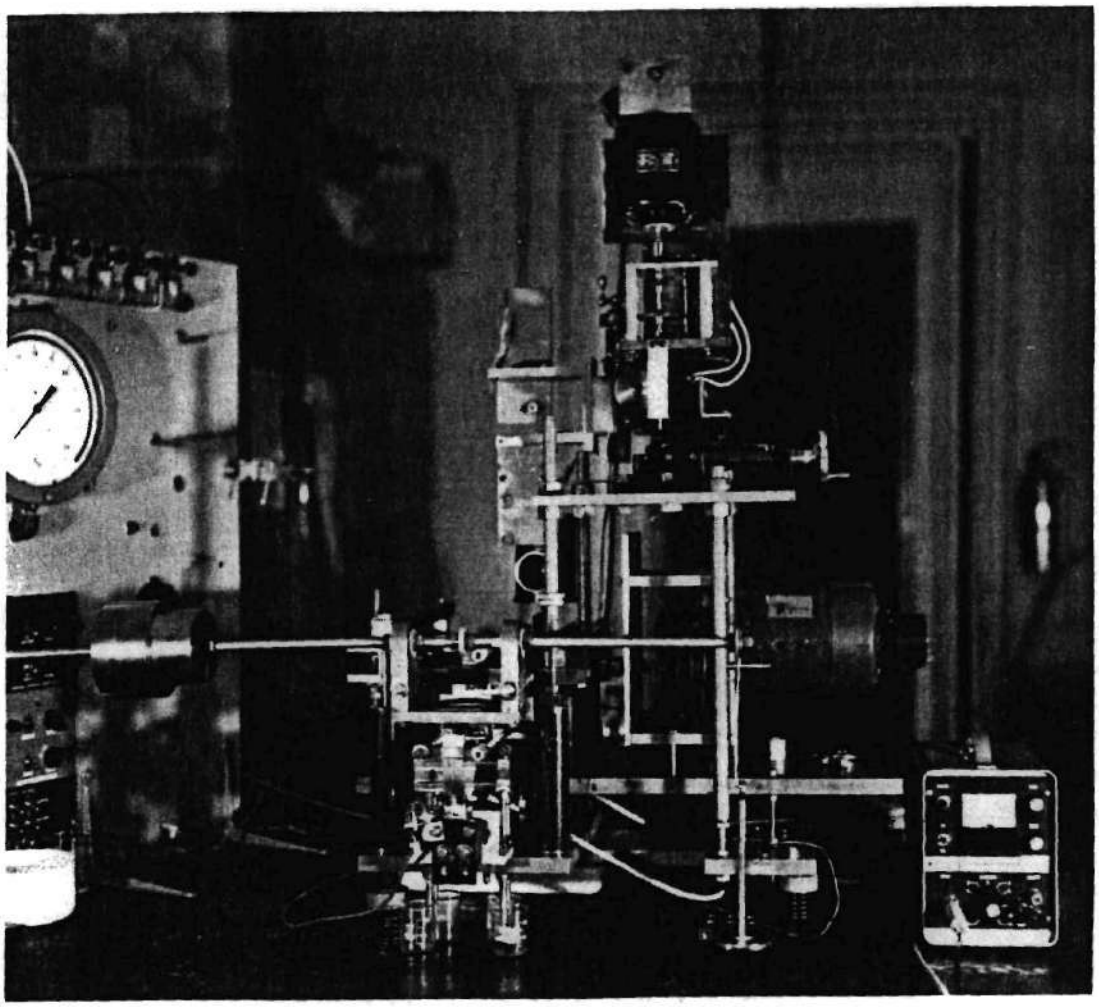

Figure 2. Sliding EHD Simulator.

B. Combined Rolling and Sliding EHD Simulator

This equipment differs from the sliding EHD simulator primarily in that the sapphire disc may be rotated by a separate drive system to achieve various amounts of slip. A schematic diagram of this equipment is shown in Figure 3. The sapphire disc (3 1/2" dia. x 1/8" thick) is mounted inside a ball thrust bearing (4.331" dia. outside). A bevel gear train driven by a motor, rotates the sapphire disc about an axis perpendicular to that of ball rotation. All these elements are directly mounted on the contact loading lever. Both the ball and the sapphire disc are driven by independently controlled variable speed D.C. motors with very stable transistorized closed-loop control systems. Speed regulation was better than 1 percent. Under conditions of high load and low sapphire speed, a controlled braking torque had to be applied to the sapphire drive system in order to maintain good speed control. This was necessary because the faster rotating ball had a tendency to drag the sapphire disc. By a combination of braking and speed control, the desired slide-roll ratio could be obtained. The speed of rotation of the ball and the sapphire disc were separately measured using a system similar to the one used in the sliding EHD simulator. A small lamp and a photo-diode were used instead of the light tube. Speed was again displayed on a digital counter. The loading system, the lubricant supply system and other features are very similar to those used in the sliding EHD simulator. Figure 4 shows the assembled apparatus. The author is indebted to Mr. Scott S. Bair for building this rig.

C. Traction Measurement

In all the experiments reported in this work, only the time-steady

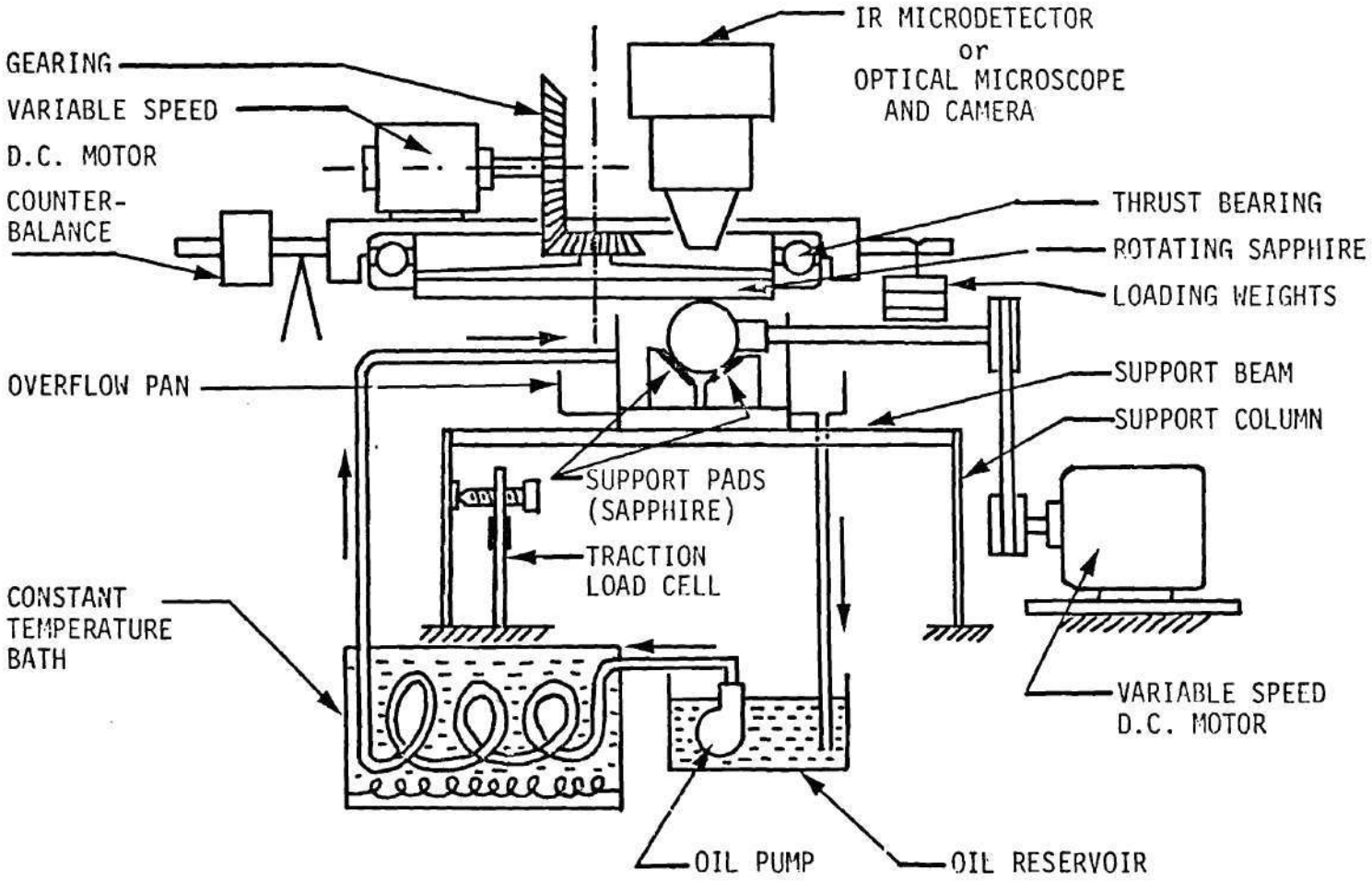

Figure 3. Schematic of the Combined Rolling and Sliding EHD Contact Simulator.

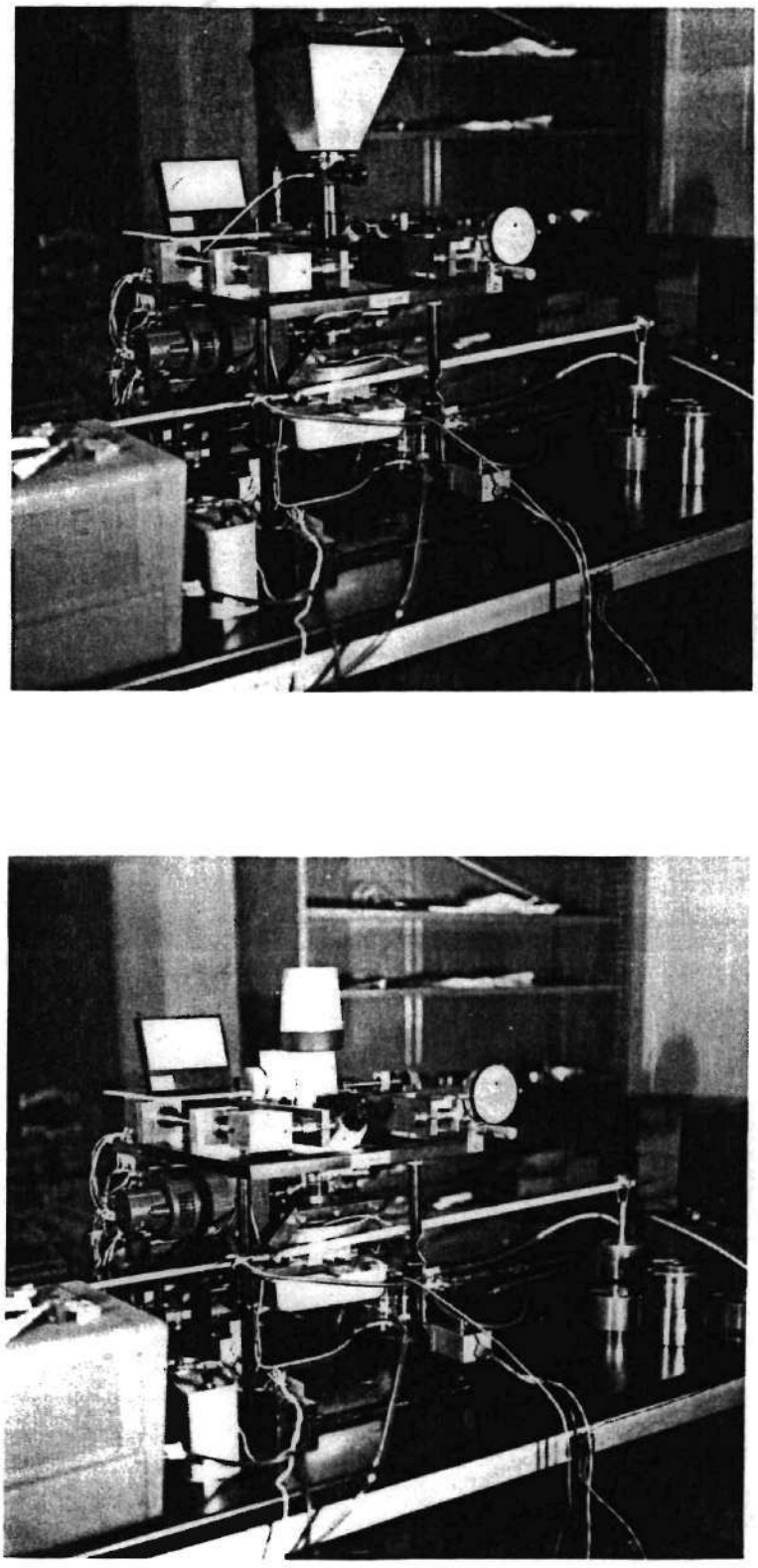

Figure 4. Combined Rolling and Sliding EHD Simulator.

value of the traction force was measured. The magnitude of these traction forces is quite small (0 to 2N). The load cells selected for the experiments consist of semi-conductor strain gages (BLH make) mounted on cantilever beams. Since two types of EHD simulators were used, two different arrangements were adopted for the traction load. The common feature for the two arrangements is the mode of traction measurement. Reaction force of the rotating ball and the support system against the sapphire, directly yields the traction force.

The traction load cell arrangement used in the sliding EHD simulator is shown in Figure 5. The rotating ball and the support system are mounted on a load beam. This load beam is supported on four air bearings. When the ball is rotated, the load beam moves laterally, offering negligible resistance to motion in this direction. The lateral motion of the load beam is measured by a cantilever and four strain gages.

Two bearing pads each having an area of 6 in^2 are used at each end of the air bearing. The combined upper and lower clearance is between .0015" and .0020". The opposing bearing pads offer high rigidity. Air is supplied at about 70 psi to the bearing through a 3/32 inch diameter hole in each bearing pad. The inlet pressure compensation needed for fluctuating bearing loads is accomplished both inherently by the orifice restriction of the sharp-edged 3/32 inch diameter inlet hole and externally by means of needle valves in each air supply line.

The cantilever beam used for the traction load cell is made of stainless steel .019" thick x 2.00" wide on which four semiconductor

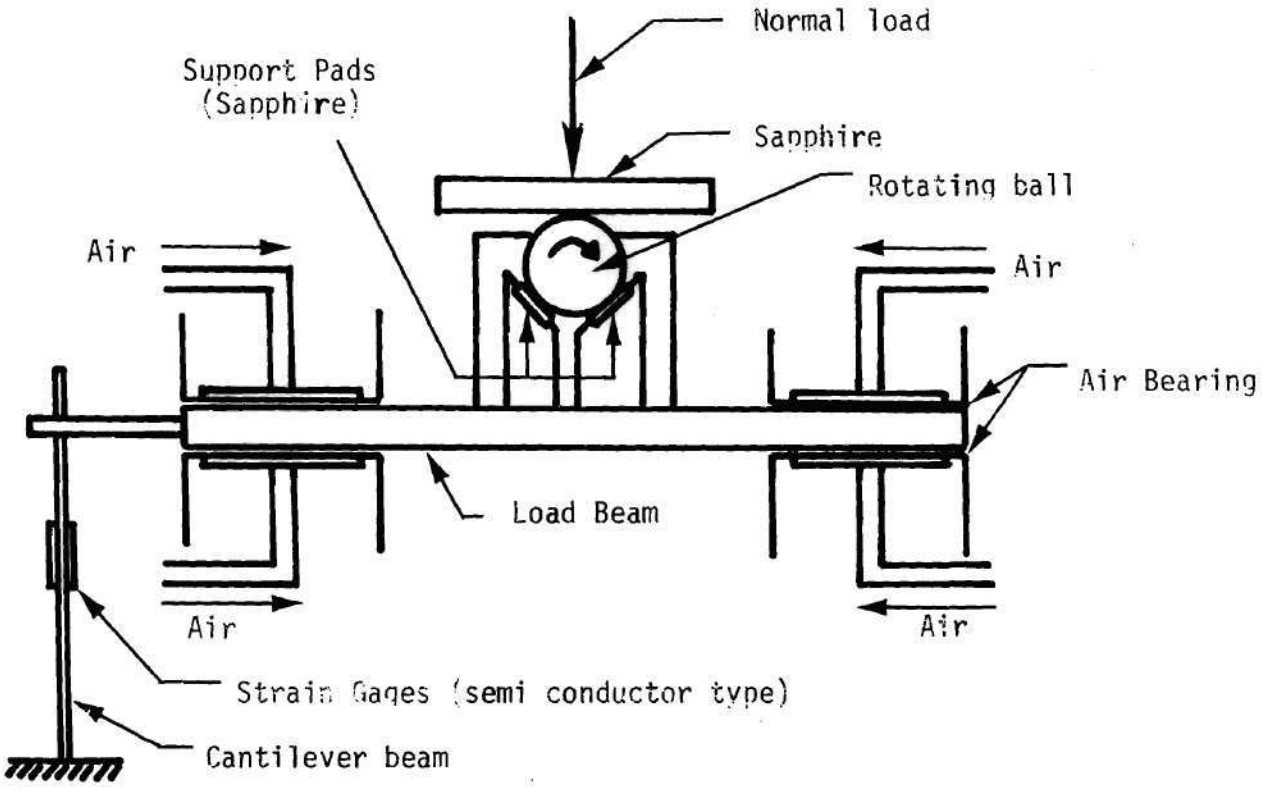

Figure 5. Traction Load Cell Arrangement Used in the Sliding EHD Contact Simulator.

strain gages have been mounted. The strain gage circuit used is of the standard wheatstone bridge type with a separate potentiometer for gain control and balancing. The bridge output is displayed on an oscilloscope. The sensitivity of the load cell was determined under steady-state conditions. A known force was applied by means of a weight, a pulley supported in a hydrostatic air bearing, and a piece of nylon cord attached to the ball support such that it passes close to the point where the EHD contact would normally occur. Care is taken not to apply any other resisting force (except through the traction load cell). The resulting calibration curve was essentially linear with .03 lbf/mV of output.

The traction load cell arrangement used in the combined rolling and sliding EHD simulator is shown in Figure 6. The load beam, in this case, is supported on two sheet metal columns which are flexible in the lateral direction. With such an arrangement, the normal load has an effect on the lateral motion of the load beam, in the deflected position of the beam. The normal load effect can however be estimated by measuring the output while rotating the ball first in one direction and then in the other direction.

The load cell arrangement for the combined rolling and sliding EHD simulator is as shown in Figure 6. The strain gages and the bridge circuit used here are very similar to the ones used in the sliding EHD simulator. The calibration procedure was similar to the one described earlier, and yielded .4675 lbf/mV sensitivity. Noise in the output signal was eliminated by using a capacitor across the output terminals.

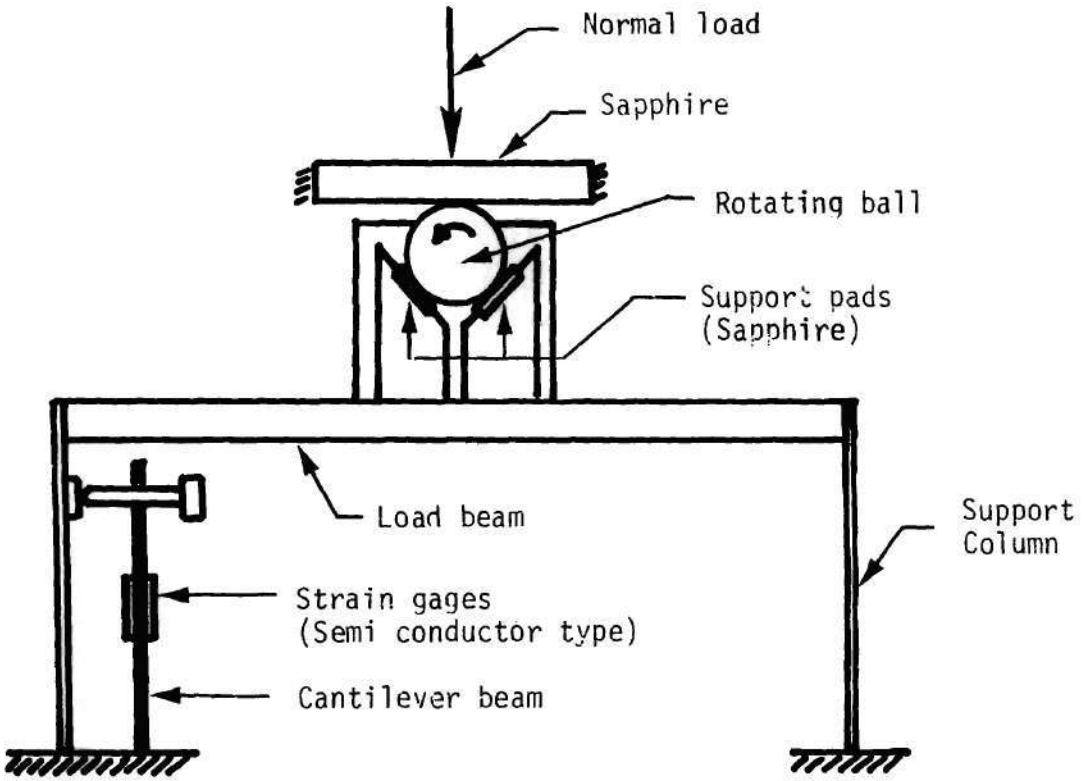

Figure 6. Traction Load Cell Arrangement Used in the Combined Rolling and Sliding EHD Contact Simulator.

D. Film Thickness Measurement

An optical interference technique was used for the measurement of fluid film thickness. The main advantage of this method is that it offers the capability of mapping the film thickness over the entire conjunction region. This method has proven successful because, the EHD film thicknesses are of the same order of magnitude as the wavelength of visible light. The method is very similar to the Newton's rings method often used to measure the geometric accuracy of optical elements like, lenses and optical flats.

The method consists of using the solid bearing surfaces as an optical interferometer. This requires one of the surfaces to be optically transparent. The knowledge of the order of an interference fringe at any desired location yields the film thickness, because, the order of an interference fringe is related to the optical path length and wavelength of the incident radiation. The desired film thickness at any location in the conjunction region is therefore directly related to refractive index of the lubricant, order of the interference fringe and the angle of incidence of the incoming radiation. For the case of point contact geometry, the interference fringes are close-looped. For a parallel beam of incident light, an interference fringe is merely a locus of a constant value of film thickness times the refractive index of the lubricant.

The use of optical interferometry in measuring EHD film thicknesses was introduced by Archard & Kirk [73-76] in 1962. Cameron, Wedeven and co-workers [77-82] have considerably refined the above method since 1966. Many investigators including Sanborn and Winer

[79,28] have adopted the above technique and introduced many improvements. The optical interference technique used in the present work, is an adaptation of their technique.

The interference mechanism is easily explained with reference to Figure 7 which shows the undeformed surfaces (of sapphire and steel ball) in proximity and surrounded by transparent medium of lubricating oil. A partially reflecting layer of Inconel is shown on the bottom surface of sapphire. The principles of optical interference are thoroughly explained by Tolansky [83]. A ray of light is shown incident upon the sapphire at an angle θ. In the actual case, only normal incidence is used ($\theta \approx 0$), but the incident ray is shown at an angle in the figure. The optical path followed by the two rays with intensities I_a and I_b are clearly shown (Figure 7). It is the recombination of these time-coherent reflected rays I_a and I_b which gives rise to the interference fringe pattern. Since part of each ray is reflected at each interface, an infinite number of rays with rapidly diminishing intensities contribute to the interference mechanism. It is the purpose of multiple-beam interferometry to use this infinite sequence of time-coherent rays to yield very sharp, well defined interference fringes. Because of the limited choice available for the selection of the optical properties of bearing surfaces, the resulting interference pattern is more typical of that found in two-beam interferometry rather than multiple-beam interferometry. Two-beam interference patterns are characterized by bright and dark interference bands of nearly equal width. An excellent comparison between multiple-beam interferometry and two-beam interferometry is available in the work of Foord, Wedeven, et al. [77].

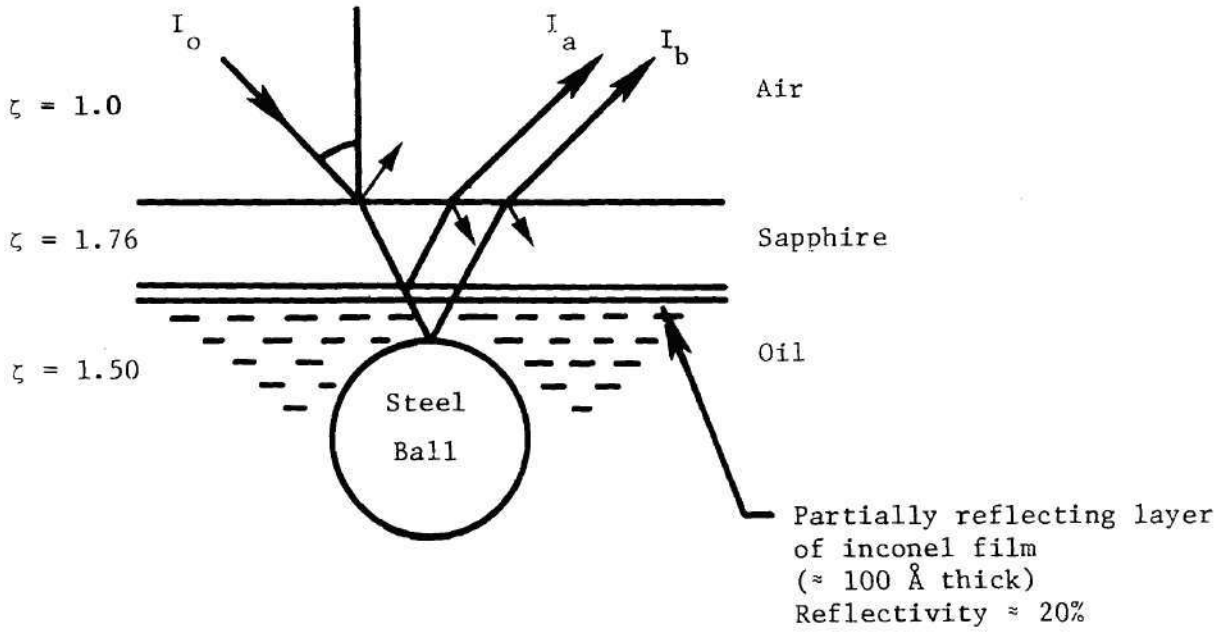

Figure 7. Optical Arrangement for Film Thickness Measurement (Monochromatic Light Source).

Two different interference systems namely the monochromatic system and the dichromatic system were used in this study. An improved optical design was used for the dichromatic system to provide better fringe visibility. These two systems are discussed separately here.

Monochromatic System

The light used in this system is predominantly, but not strictly, monochromatic.

The bright and dark interference fringes are attributed respectively to the constructive and destructive interference of time-coherent rays I_a and I_b. By following the optical paths for rays I_a and I_b with their amplitude and phase representations, one can arrive at (see reference [79]) the following results. Bright fringes appear when

$$h = \frac{\lambda}{2\zeta}\left(n + \frac{\Delta\phi}{2\pi}\right);\ n = 0,1,2,.... \qquad (1)$$

and dark fringes occur when

$$h = \frac{\lambda}{2\zeta}\left(n + \frac{\Delta\phi}{2\pi} - \frac{1}{2}\right);\ n = 0,1,2,..., \qquad (2)$$

where $\Delta\phi$ is the net phase change.

There are several effects contributing to the value of $\Delta\phi$. A phase shift of π radians is encountered on reflection from the ball surface (when it is perfectly flat). No phase change will occur when the light passes from the sapphire to lubricant while a phase shift of π radians will occur for light passing in the opposite direction. This is because the refractive index of sapphire is higher than that of

the lubricant. With surface finish in the neighborhood of .025 μm R_a and with average asperity slope of .03 - .05 rad, the incident wave does not reflect from a single flat surface. Considerable effect due to this factor is therefore to be expected in the value of $\Delta\phi$. Further complications exist because of the presence of a finite thickness of inconel film (≈ 100 Å), whose effect is very difficult to predict. However, as a combined effect of all the above factors, values for $\Delta\phi$ can be obtained by calibration of the optical system with zero film thickness. Sanborn [79] quotes values of $\Delta\phi$ to lie in the range given by

$$\frac{5\pi}{4} \leq \Delta\phi \leq \frac{3\pi}{2} \tag{3}$$

The limit $\frac{5\pi}{4}$ corresponds to very lightly loaded contacts whereas the value $\frac{3\pi}{2}$ corresponds to heavily load contacts with peak Hertz pressures greater than .65 GPa. Variation of $\Delta\phi$ with load is perhaps due to local deformation of asperities. Since the loads used in almost all of the experiments reported in the present work yielded Hertz pressures greater than about .65 GPa, $\Delta\phi = \frac{3\pi}{2}$ was used in the film thickness formula. The roughness of steel ball, in addition to affecting $\Delta\phi$, has a significant effect on the quality of the interference fringes. Adequate reflectivity was obtained for smooth ball (.011 μm R_a) and a marginal reflectivity was obtained for medium rough ball (.076 μm R_a). However, it was not possible to get any reflectivity with the rough ball (.38 μm R_a). Increasing roughness with deeper surface valleys produces multiple reflections and consequent multiple absorptions and

therefore limits the reflectance of the surface [84-86].

It was mentioned earlier in this section that, the interference fringes are loci of constant values for the product $h \cdot \zeta$. The actual value of film thickness therefore requires the value of refractive index to be known. Since local pressures and temperatures vary greatly within the EHD conjunction zone and so also the density, variations in ζ are to be expected. Estimates of the changes in ζ can however, be made. Effect of pressure has been considered by Sanborn [79]. Density changes can be estimated by assuming Hertzian pressure profiles and the generalized bulk modulus relationships. Lorenz-Lorentz relation

$$\frac{\zeta^2 - 1}{\zeta^2 + 1} \cdot \frac{1}{\gamma} = \text{constant} \qquad (4)$$

can then, be used to estimate changes in ζ. Variation in ζ over the contact area was found to be less than 10%. The assumption of Hertzian pressure profile does not introduce significant errors since, at a pressure level of .65 GPa, and for a 50 percent error in pressure estimate, the density change is less than 4% and refractive index and so also film thickness changes are less than 2%.

The effect of temperature on refractive index is also through density changes. Referring to Appendix A, the density of fluid N1 at .138 GPa decreases by less than 3% over an increase of temperature from 38°C to 100°C, and thus refractive index changes by less than 1.5% and is therefore negligible.

The anisotropic crystal structure in sapphire results in the undesirable birefringence effect. Although this birefringence effect was observed, film thicknesses could be determined with sufficient accuracy. In the combined rolling and sliding EHD simulator, however, a

sapphire disc with the optic axis normal to its plane was used, which eliminated the birefringence effect.

The value of fringe order n must be known in order to determine film thickness using equations (1) and (2). The initial or the reference value of n for any one fringe is determined by observing a single point in the contact as the speed goes to zero. Once the correct integer has been selected for one fringe, values of n for all other fringes are easily determined.

Recalling equation (2), dark fringes occur when

$$h = \frac{\lambda}{2\zeta}\left(h + \frac{\Delta\phi}{2\pi} - \frac{1}{2}\right);\ n = 0,1,2,....$$

For $\Delta\phi = \frac{3\pi}{2}$, and $\lambda = 5340$ Å $= .534$ μm and $\zeta = 1.51$, (therefore, $n = -\frac{1}{4}$ at $h = 0$)

$$h = \frac{\lambda}{2\zeta}\left(n + \frac{1}{4}\right) = .177\left(n + \frac{1}{4}\right) \qquad (5)$$

with dark fringes @ n = 0,1,2,.... Values of h versus n are given in Table 1.

Dichromatic System

The light used in this system consists of two predominant wavelengths namely Green (5460 Å) and Red (6300 Å).

The optical arrangement used in this system is shown in Figure 8 and is very similar to the system used by Foord, et al. [77] but, with minor modifications. The advantage of the dichromatic system over the monochromatic system is that, once the calibration procedure has been carried out, the color fringe sequence in a dichromatic system

Table 1. Film Thickness versus Fringe Order for Fluid N1 and Schott Filter (G = Grey, DG = Dark Grey, D = Dark, LG = Light Grey, and B = Bright.)

Fringe Identification	Fringe order	$h(\frac{2\zeta}{\lambda})$	h μ-in	h μm
G	- 1/4	0	0	0
DG		1/8	.87	.0221
D	0	1/4	1.74	.0442
DG		3/8	2.61	.0663
G		1/2	3.48	.0884
LG		5/8	4.35	.1105
B	1/2	3/4	5.22	.1326
LG		7/8	6.09	.1547
G		1	6.96	.1768
DG		1 1/8	7.83	.1989
D	1	1 1/4	8.7	.2210
DG		1 3/8	9.57	.2431
G		1 1/2	10.44	.2652
LG		1 5/8	11.31	.2873
B	3/2	1 3/4	12.18	.3094
LG		1 7/8	13.05	.3315
G		2	13.92	.3536
DG		2 1/8	14.79	.3757
D	2	2 1/4	15.66	.3978
DG		2 3/8	16.53	.4199
G		2 1/2	17.4	.4420
LG		2 5/8	18.27	.4641
B	2 1/2	2 3/4	19.14	.4862
LG		2 7/8	20.01	.5083
G		3	20.88	.5304
DG		3 1/8	21.75	.5525
D	3	3 1/4	22.62	.5746

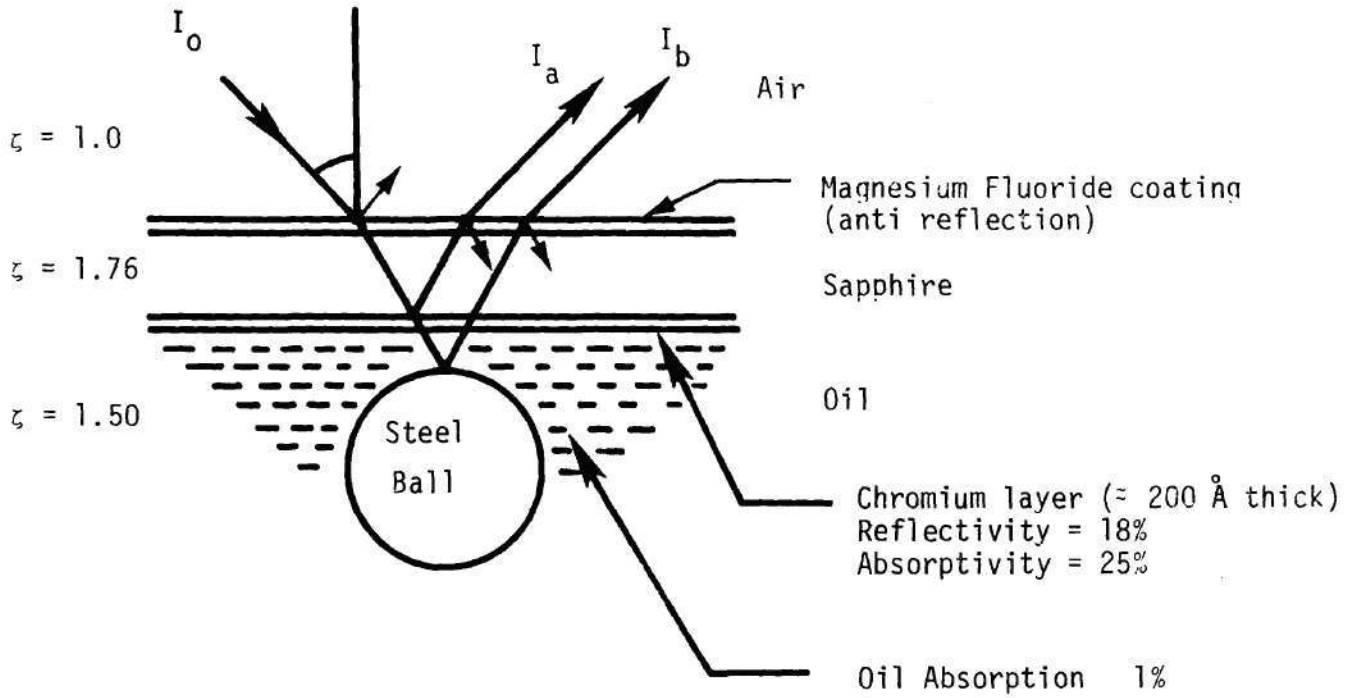

Figure 8. Optical Arrangement for Film Thickness Measurement (Dichromatic Light Source).

has an absolute reference from zero film thickness.

As in the previous system, considering $\Delta\phi$ to be the net phase change for each of the two predominant wavelengths,

$$h = \frac{\lambda}{2\zeta}\left(n - \frac{\Delta\phi}{2\pi}\right);\ n = 0,1,2,.... \qquad (6)$$

for dark fringes to occur. The absolute thickness h corresponding to each fringe is determined [87] as before by observing a system of known geometry, which most conveniently is a steel ball loaded against sapphire. For ideal conditions of zero load, thickness h can be calculated by measured fringe radius ξ using the relation

$$h = \frac{\xi^2}{2R} \qquad (7)$$

where, R is the radius of the steel ball. This relation can be used for h up to 3 μm with negligible error. Fringe radii ξ for zero load conditions can be obtained by extrapolated values of ξ for loaded conditions. Such a calibration procedure was carried out by Foord, et al. [77] and $\Delta\phi$ was found to be $-2\pi/5$. Using this value of $\Delta\phi$ in equation (6),

$$h = \frac{\lambda}{2\zeta}\left(n + \frac{1}{5}\right);\ n = 0,1,2,.... \qquad (8)$$

for dark fringes to occur. Using such a relation for green and red colors separately, the chart shown in Figure 9 was prepared by Foord, et al. [77]. The color fringe system for the dichromatic case of green and red is then obtained by combining the two separate monochromatic systems. Figure 9 shows the fringe system corresponding to air as

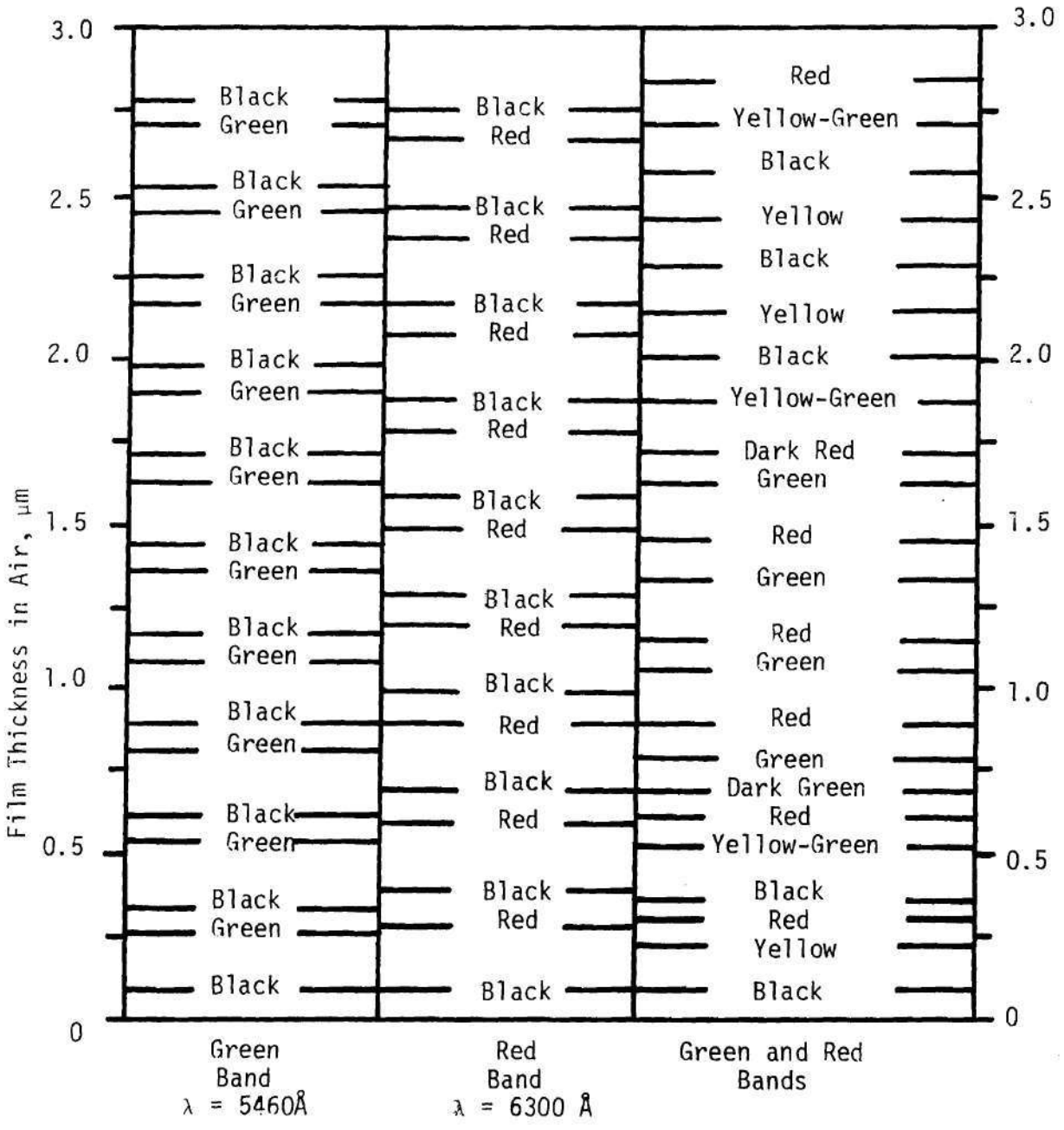

Figure 9. Color Fringe Sequence versus Film Thickness in Air for the Dichromatic System (From Reference 77).

the medium, and thus, film thickness can simply be obtained in the dichromatic system by using Figure 9 and knowing the refractive index of the lubricant.

Reflective Coatings

The interfacial reflection between most lubricants and sapphire is only .64%, because the refractive indices of the two media are close to each other (1.5 and 1.76, respectively). A good fringe contrast can be obtained only when the intensities of the interfering beams are approximately equal. In order to accomplish this, a reflective coating is deposited on the bottom surface of sapphire. Based on the amounts of reflection, transmission, and absorption present at each of the interfaces, the amount of reflection needed is about 18% for chromium coating (≈ 200 Å thick) and 20% for inconel coating (≈ 100 Å thick). Chromium coating was found adequate for combined rolling and sliding experiments, where as inconel coating was required for sliding experiments. The coatings were vapor deposited in high vacuum, and can withstand the high shear stresses produced in an EHD contact.

Light Sources

Light Source for Monochromatic System. This consists of a 300 Watt tungsten projection lamp, an air-cooled housing with a condensing lens and a diaphragm stop, a 5340 Å Schott filter (bandwidth at half intensity is 220 Å), and the vertical illuminator of a Leitz metallurgical microscope. The intensity of the incident light can be controlled by adjusting either the voltage applied to the projection bulb or the aperture at the entrance to the vertical illuminator.

Light Source for Dichromatic System. In combined rolling and sliding experiments, the EHD contact appears more dynamic in the field of view of the microscope. Therefore, it was decided to use an electronic flash for a light source, since very low exposure times (30 to 40 microseconds) can be obtained. A commercially available (Vivitar 283) flash unit was used. A concentrator was placed in front of the flash unit to increase the light intensity. A condensing lens system then focussed the light from the flash unit onto the vertical illuminator of the Leitz metallurgical microscope. The dichromatic light was obtained by passing the light through a 77 A filter (5460 Å green band and 6300 Å red band). An aperture in the light path controls the amount of light to the microscope. In addition to this light system, a continuous light source was required to observe the EHD contact. For this purpose, a 30 watt variable intensity lamp was used. All the above optical elements were mounted on an optical bench behind the EHD simulator. This facilitated shifting light sources without losing alignment. Figure 10 shows a photograph of this light system.

By using the vertical illuminator of the metallurgical microscope to direct the light onto the contact area, it is not possible to have a perfectly collimated incident beam. The effect of non-perfect beam collimation is to make the system more nearly a two beam interferometer rather than a multiple beam interferometer, resulting in less distinct broader fringes. This however, did not pose a serious problem in the present work.

Photography. The remainder of the film thickness measuring system

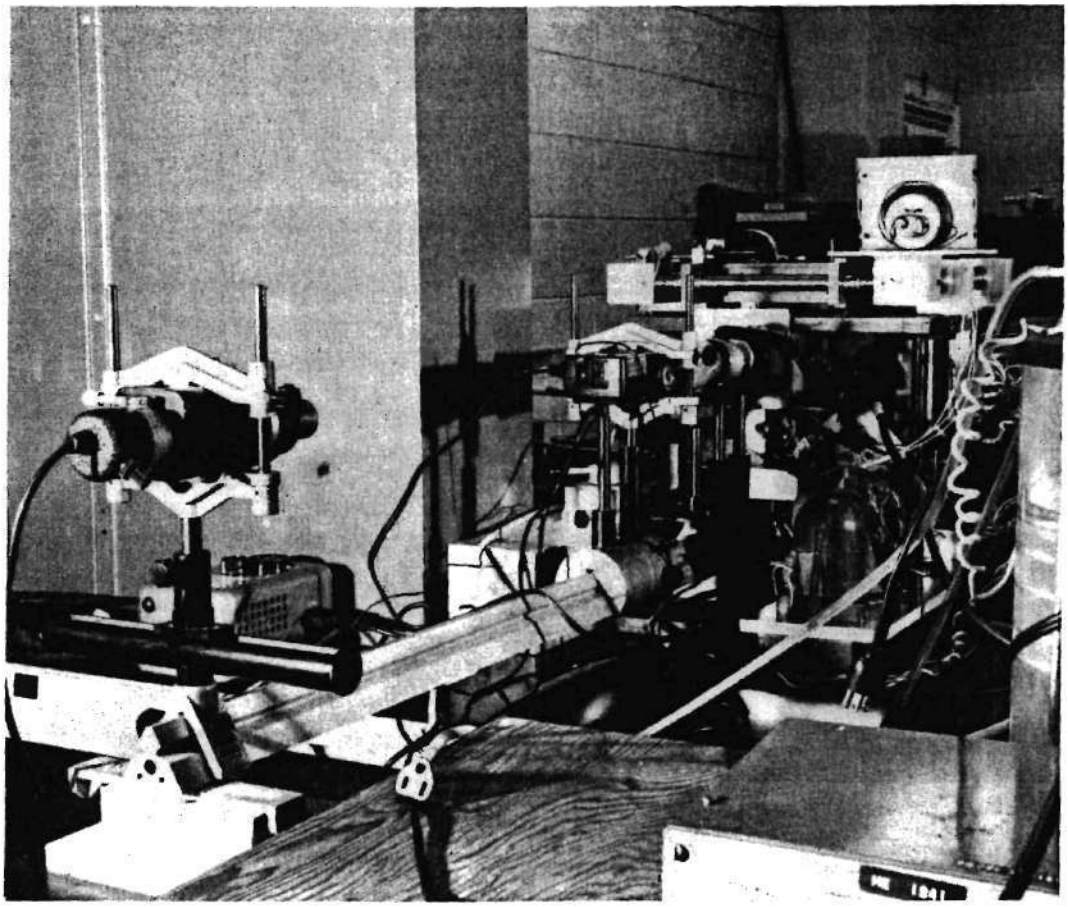

Figure 10. Light source, filters and aperture mounted on an optical bench.

consists of equipment needed to observe and photograph interference patterns. The Leitz metallurgical microscope mentioned above was used together with a Polaroid camera.. Visual observation is made at either X100 or X200 using a X10 or X20 objective and a pair of X10 binocular eyepieces. A X10 photographic eyepiece is used in conjunction with the camera. For the monochromatic system Polaroid type 107 black and white film was used, yielding 3 1/4 in. x 4 1/4 in. prints. An exposure time of 1/125 sec was found adequate for this 3000 ASA film while using the 300 watt tungsten lamp. For the dichromatic or the color systems, after much experimentation, it was found that Polaroid type 58 color film, 4 x 5 in., was satisfactory. This 75 ASA film gave proper exposures at 30 to 40 microseconds while using the vivitar 283 flash unit. The exposure time is controlled by settings on the flash unit which trigger a thyristor control circuitry. Polaroid type 545 land film holder was used in conjunction with the camera. The good quality of the interference fringes produced in the dichromatic system can be seen in Chapter IV.

CHAPTER III

TEMPERATURE AND SURFACE ROUGHNESS MEASUREMENT

In this chapter, the infrared technique developed and used for the measurement of temperatures in an EHD contact is described. The method used for surface roughness measurement and subsequent analysis is also described.

A. Temperature Measurement

An infrared technique for measuring the ball surface temperature and the fluid film temperature (averaged through the thickness) in an EHD conjunction was developed and used in the temperature measurements reported.

The infrared technique for measuring contact temperatures has proven successful because, the optically transparent sapphire (used as one of the bearing surfaces) is also transparent to infrared radiation in the emission band of many lubricating oils. The technique employs two interference filters for separating the individual contributions of the total infrared radiation received by the detector. If the filters have certain spectral characteristics, then through analysis and calibration, the equivalent black body radiation and the respective temperatures can be determined.

Radiation Contribution

Figure 11 shows the various sources contributing to the total radiation received by the infrared detector from an arbitrary spot in the EHD contact.

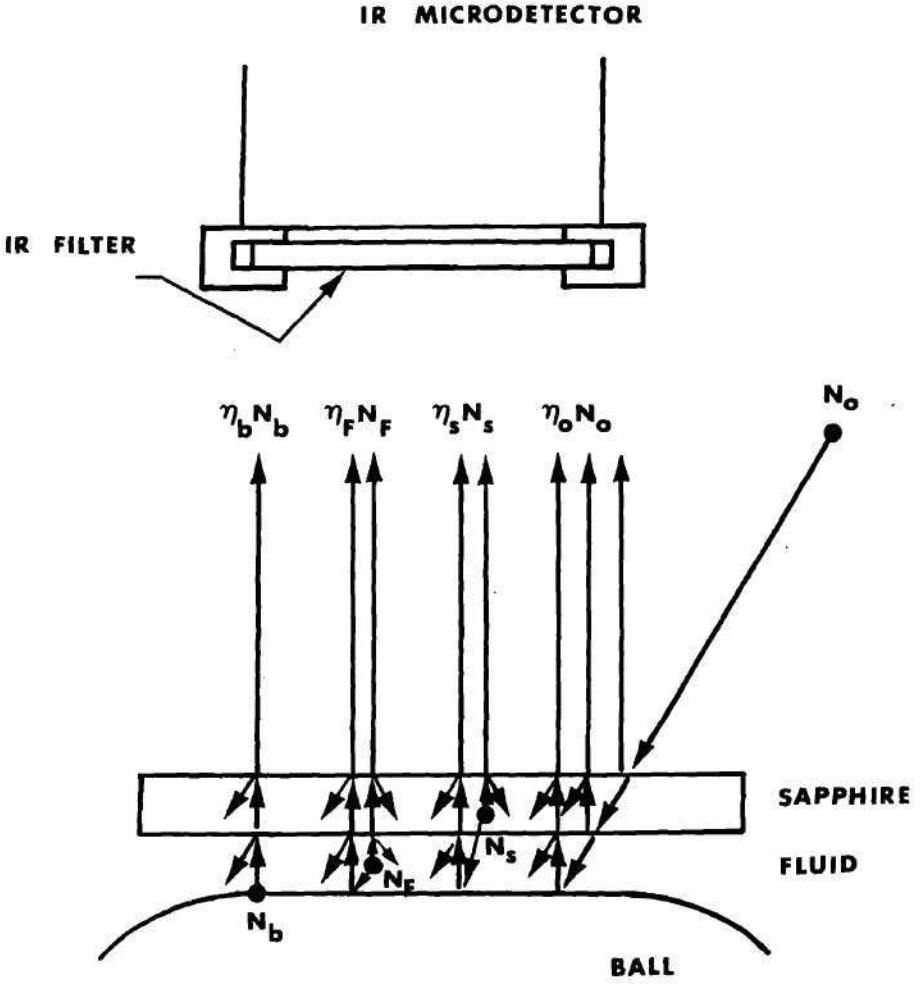

Figure 11. Sources of IR Radiation Emitted from any Location in the EHD Contact.

The four contributions N_b, N_F, N_s, and N_0 are the nonattenuated values of radiations emitted by the ball, fluid, sapphire, and the ambient respectively. Each of the above contributions is associated with an attenuation factor which includes absorption losses in various media and Fresnel reflection losses at interfaces between any two media. The ball surface, being opaque, either only emits or absorbs. The fluid and sapphire are partially transparent and partially absorbing media. The ambient radiation refers to the background radiation from the room reflected from the spot. The radiation collected by the detector is the sum of all the above contributions and is given by

$$N = \eta_b N_b + \eta_F N_F + \eta_s N_s + \eta_0 N_0 \qquad (9)$$

Individual values of N_b, N_F, and N_s are required in addition to knowledge of the corresponding emissive properties in order to determine the respective temperatures. The individual values of N_b and N_F could be determined by considering the difference in spectral emission characteristics of the various sources. The contribution from the sapphire surface could not be separated and therefore the sapphire surface temperature has not been determined. In most of the cases this contribution however, was found negligible. The reasons for this are discussed later in this section. Although the sapphire surface temperature was not measured, stationary surface temperature was successfully determined using a different configuration, which will be described in Chapter IV.

Two infrared filters were used to separate the contributions from the ball and the fluid, and were chosen based on the spectral emission

characteristics of the lubricant used in the present study (Fluid N1). The spectral characteristics of the lubricant and the IR filters are shown in Figure 12. The curve labelled lubricant emission is in fact, complementary to the lubricant transmission curve obtained by using an infrared grating spectrophotometer. The emission curve for the lubricant corresponds to a film of thickness 25 μm sandwiched between two 1.6 mm thick sapphire discs. This result shows that the lubricant emission is highly spectral in the range 3.1 to 3.7 μm, with peak emission at 3.4 μm. The spectral emission of fluid N1 in the wavelength band 3.1 to 3.7 μm, is due to stretching vibrations of the C-H bond. In order to enhance the contribution from the fluid to the total radiation, a narrow band filter which transmits radiation between 3.1 and 3.7 μm is chosen.

The spectral emission data of the lubricant shown in Figure 11 also indicates that there is no emission either below 3.1 μm or, beyond 3.7 μm up to 40 microns by an oil film of 25 μm thickness. The dotted lines in Figure 12 show the monochromatic black body radiation as a function of wavelength at two different temperatures plotted in arbitrary units. These curves show that the spectral region of interest in this study is to the left of the peak in black body radiation even at temperatures of 177 C. The ball radiation which can be considered grey body radiation (emissivity is constant over all wavelengths) is therefore, more predominant in the region of 3.7 to 5.5 μm compared with the 1.8 to 3.1 μm region. Accordingly, a wide band filter was selected which transmits radiation in the spectral range 3.7 to 5.1 μm. The spectral response of this filter is also shown in Figure 12.

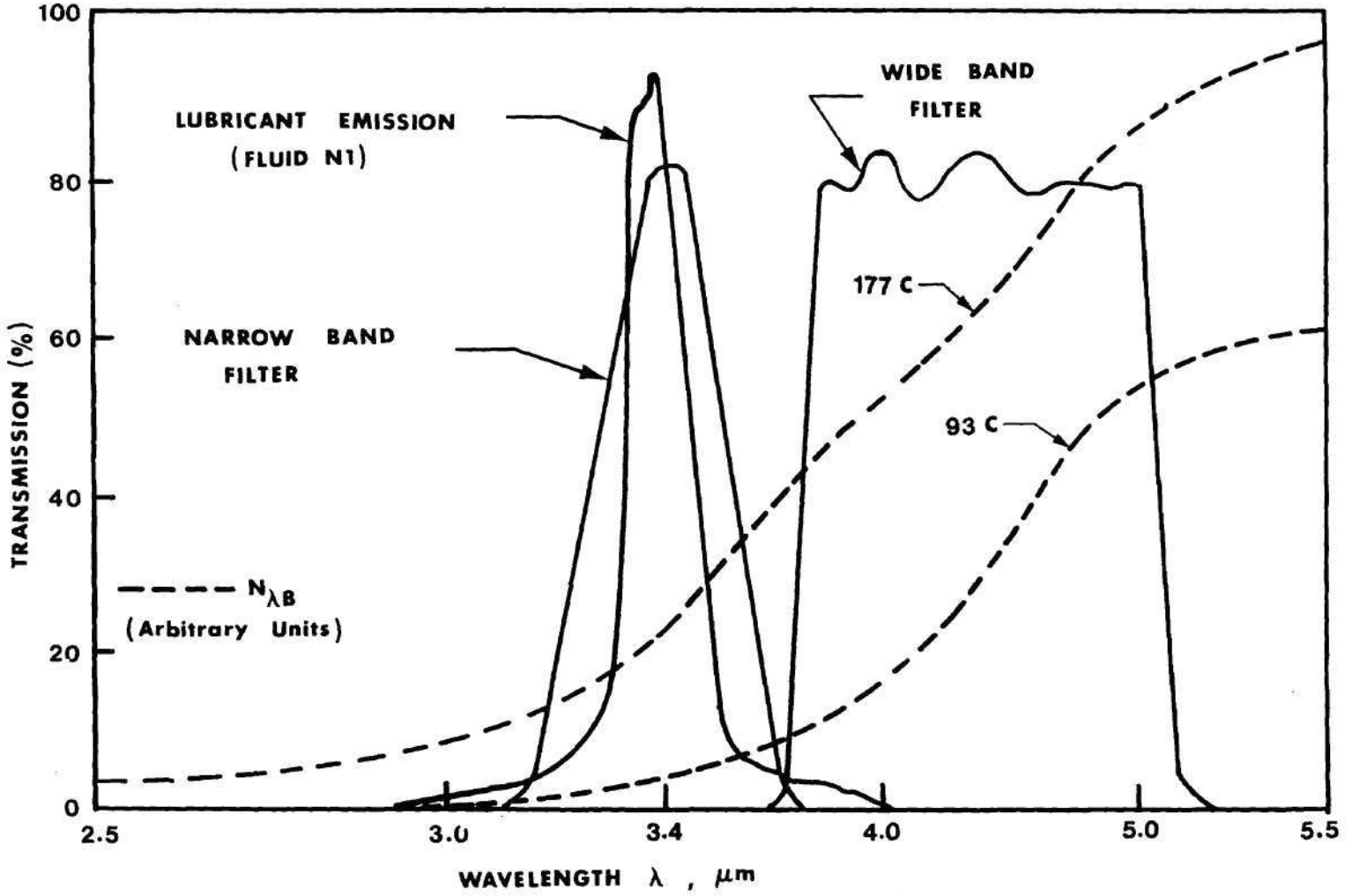

Figure 12. Spectral Characteristics of the Fluid Film, Filters, and Ball.

To facilitate computations, when using one filter or the other, the influence of the filter was assigned to the detector rather than the radiation source. When using the filters, the calibration curves of black body radiation versus temperature supplied by the manufacturer for the detector are no longer applicable, and the detector must be recalibrated for each filter.

Radiation Analysis

The analysis reported in this section is applicable for any filter. Later on, these expressions will be specialized for the wide band filter and the narrow band filter separately.

The ball radiation N_b, is given by the expression

$$N_b = \varepsilon_b N_{BB}(T_b) \tag{10}$$

The quantity ε_b is the emissivity of the ball surface and T_b is the ball surface temperature. The emissivity was measured in a separate experiment using the microdetector. The method consisted of painting a black spot of known emissivity of .95 on the previously heated ball surface in the immediate neighborhood. In this way, emissivity was measured as a function of temperature. However, in the range of ball surface temperatures expected in an EHD contact, the emissivity was essentially a constant and equal to .21. This value has been used throughout. It was determined that the IR filters used in the experiments had no effect on the measured value of the ball surface emissivity.

The variable $N_{BB}(T)$ is the radiation that would be observed through the filter from a black body at temperature T. By measuring the

radiation through the two filters from a black body calibration source (Barnes' RM-121) at known temperature, plots of $N_{BB}(T)$ versus T were obtained. Figures 13 and 14 are the calibration curves of $N_{BB}(T)$ versus T for the wideband filter and the narrow band filter respectively.

The ball radiation attenuation η_b is dependent on the optical properties of the sapphire and oil. The attenuation factor is determined by reflection losses at the sapphire-air and sapphire-oil interfaces and absorption in the sapphire and lubricant films. Therefore,

$$\eta_b = \tau_s(1-\rho_1)(1-\rho_2)\tau_F(h,T_F) = \eta_s\tau_F(h,T_F) \qquad (11)$$

The variable τ_s represents the sapphire transmissivity and ρ_1 and ρ_2 represent the Fresnel reflection losses at the sapphire-air and sapphire-oil interfaces. η_s is the total transmittance which includes the reflection losses at the two interfaces and the absorption losses in the sapphire. Secondary reflections have been neglected throughout the analysis because of small values of interfacial reflections.

The variable $\tau_F(h,T_F)$ is the transmissivity of the fluid film of thickness h at a temperature T_F. This fluid film transmissivity is a strong function of wavelength because of the spectral characteristics of the lubricant shown in Figure 12. The value of transmissivity is determined through calibration. The exact calibration procedure will be discussed later in this section.

The value of ambient radiation N_0, is equal to the intensity of radiation emitted from a blackbody at room temperature and is obtained through calibration. A portion of the ambient radiation is reflected

from the sapphire surfaces before reaching the fluid. This reflectance, ρ_s^*, is given by

$$\rho_s^* = \rho_1 + \tau_s^2(1 - \rho_1)^2\rho_2 \tag{12}$$

Another portion of the ambient radiation is transmitted through the sapphire, reflected off the ball surface, and then reaches the detector. The total attenuation of ambient radiation including the portion just discussed, is given by

$$\eta_0 = \rho_s^* + \rho_b\eta_s^2\tau_F(2h,T_F) \tag{13}$$

$\tau_F(2h,T_F)$ is the fluid transmissivity for a film 2h in thickness at a temperature T_F. Film thickness of 2h has been used in fluid transmissivity because, the radiation travels twice through the thickness of the lubricant film.

The contribution from the sapphire disc is harder to analyze because of two reasons: (1) the sapphire temperature varies through its thickness from EHD contact temperature at the fluid interface to very near ambient temperature at the air interface; and (2) the sapphire radiation is not spectral in the active bandwidth of the detector - 1.8 to 5.5 μm to facilitate separating it using a filter. For these reasons, it has not been possible to measure sapphire surface temperature. However, as will be reported in a later chapter (Chapter IV), the stationary surface temperature has been successfully measured using a different configuration (sapphire moving and ball surface stationary). Nevertheless, it was found that the sapphire contribution to total radiation could be neglected for

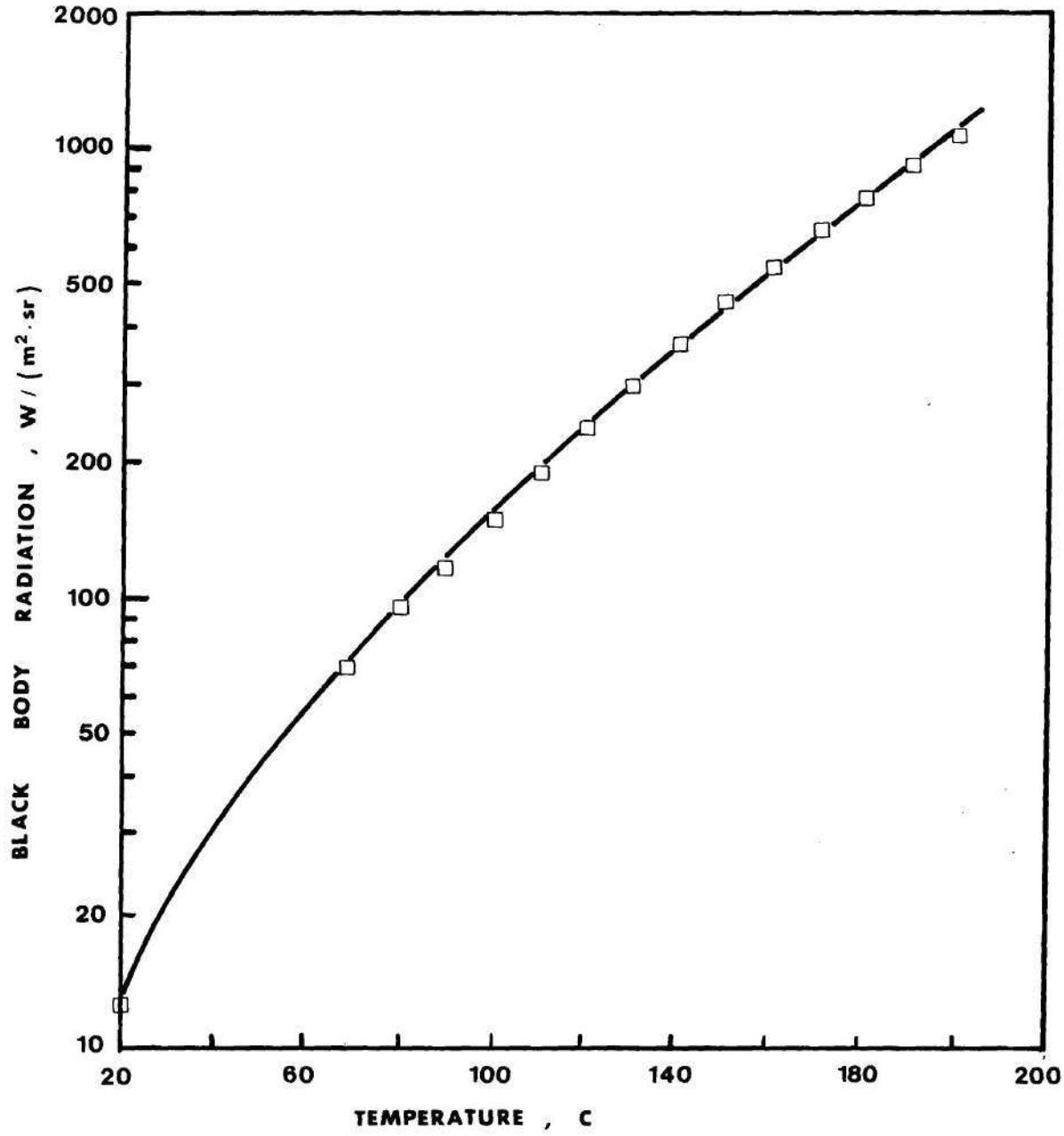

Figure 13. Wide Band Filter Calibration for Black Body Radiation.

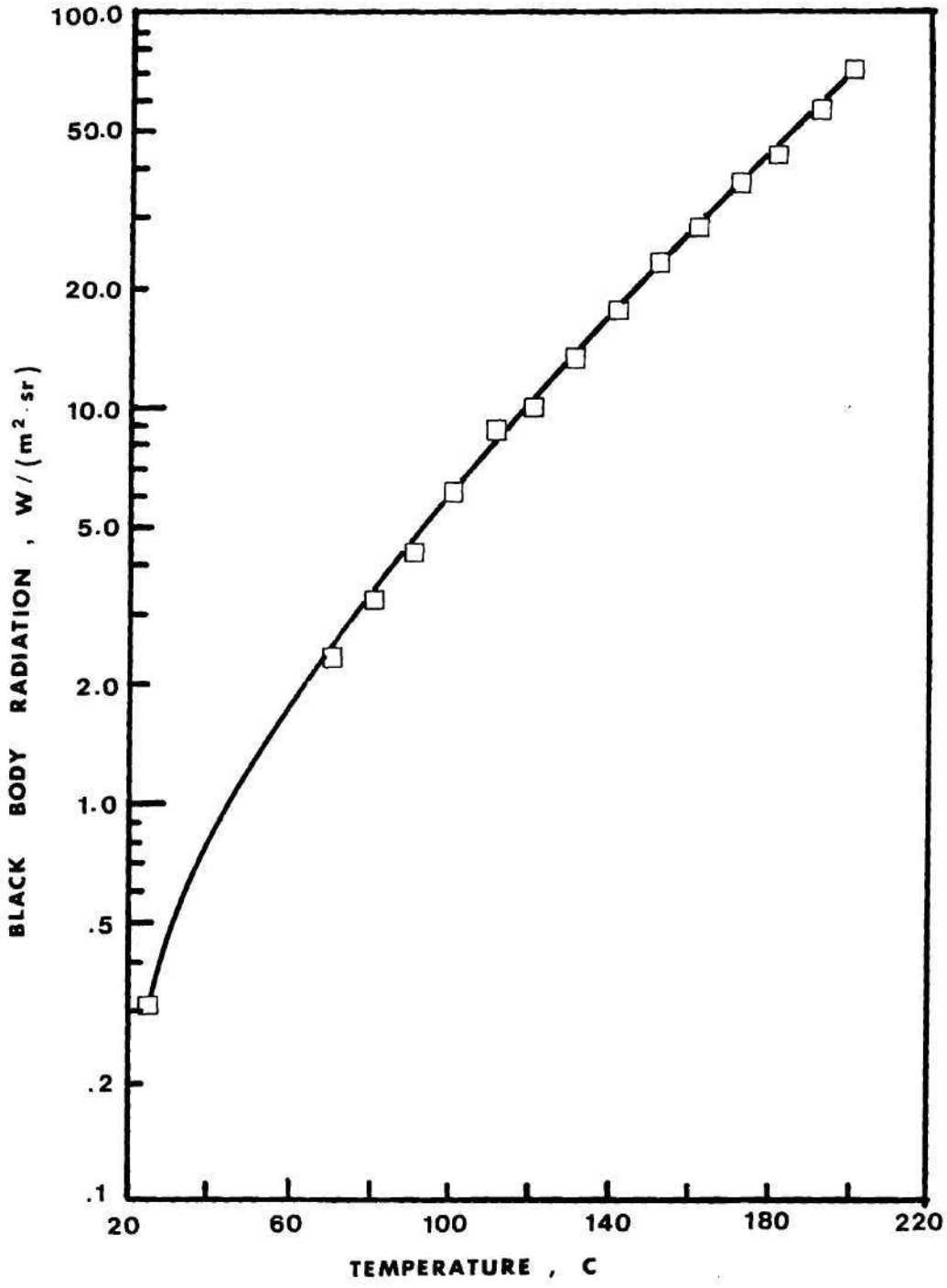

Figure 14. Narrow Band Filter Calibration for Black Body Radiation.

two reasons: (1) the sapphire emissivity in the bandwidth of wide band filter is approximately 1/10th the ball surface emissivity and negligible in the narrow band filter bandwidth, based on absorption data [88]; and (2) the average temperature of the sapphire is significantly lower than the ball surface temperature. Considering the stationary surface temperature to be the sapphire temperature (which is reasonable because the thermal conductivity of ball is only 1.4 times that of sapphire) which is typically about 30 to 40 C higher than the ball surface temperature, the sapphire temperature varies from (T_b + 30) to about 25 C through its thickness of 1.6 mm. Assuming an average sapphire temperature based on the above limits, the sapphire contribution is less than 2% of the ball surface radiation. Neglecting the sapphire contribution results in an error of less than 2 to 3 C on the ball surface temperature. For these reasons, the sapphire contribution is neglected in the entire analysis.

The total fluid radiation is given by the expression

$$N_F = \varepsilon_F(h, T_F, \rho_b) N_{BB}(T_F) \tag{14}$$

The emissivity of the oil film ε_F is a function of film thickness, fluid temperature, and the ball reflectivity. A portion of the fluid radiation travelling downward is reflected from the ball surface and then reaches the detector. The ball reflectivity ρ_b is included in the emissivity function in order to account for this portion of the fluid radiation. The black body radiation $N_{BB}(T)$ is given by the calibration curve of black body radiation versus temperature for the narrow band filter shown in Figure 14. Only the narrow band filter need be considered for fluid radiation calculations because of the spectral response of the wide band

filter.

The exact expression for the emissivity function $\varepsilon_F(h_1 T_F, \rho_b)$ is not possible to derive since the exact spectral response of various optical elements including the IR filter and the detector response are not known. However, an approximate expression can be derived using the monochromatic approach. Radiation from the fluid film passes in both the directions, upward and downward. Accounting for both the portions of this radiation, the net monochromatic fluid radiation is

$$N_{\lambda F} = \varepsilon_{\lambda F} N_{\lambda BB}(T_F) + \rho_b \tau_{\lambda F} \varepsilon_{\lambda F} N_{\lambda BB}(T_F) \tag{15}$$

The terms $\varepsilon_{\lambda F}$ and $\tau_{\lambda F}$ have the form [86,87]

$$\varepsilon_{\lambda F} = \varepsilon_{\lambda F}(h, T_F) = 1 - e^{-\alpha'(\lambda, T_F) \cdot h} \tag{16}$$

and

$$\tau_{\lambda F} = \tau_{\lambda F}(h, T_F) = 1 - \varepsilon_{\lambda F} = e^{-\alpha'(\lambda, T_F) \cdot h} \tag{17}$$

The variables $\varepsilon_{\lambda F}$ and $\tau_{\lambda F}$ are the monochromatic emissivity and transmissivity respectively and are shown as functions of local film thickness h and local average film temperature T_F. The quantity α' is an absorption coefficient dependent on both wavelength and film temperature. $N_{\lambda F}$ is the total monochromatic fluid radiation reaching the detector. $N_{\lambda BB}(T)$ is the monochromatic blackbody radiation measured through the filter. In the equations (16) and (17), the temperature is assumed to remain constant through the film at an average value. Because of the fourth power relationship between emitted radiation and temperature, the

calculated average temperature will be weighted toward the maximum temperature in the oil film. By writing transmissivity equal to one minus emissivity, an assumption of local thermodynamic equilibrium is made. This assumption may be a good one in elastohydrodynamic lubrication situations.

Substituting (16) and (17) in (15) and integrating over the entire wavelength region,

$$N_F = \int_o^\infty N_{\lambda F} d\lambda = \int_o^\infty [(1 - e^{-\alpha'(\lambda,T_F)\cdot h}) + \rho_b\{(1 - e^{-\alpha'(\lambda,T_F)\cdot 2h}) - (1 - e^{-\alpha'(\lambda,T_F)\cdot h})\}]N_{\lambda BB}(T_F)d\lambda$$

or,

$$N_F = \int_o^\infty [\varepsilon_{\lambda F}(h,T_F) + \rho_b\{\varepsilon_{\lambda F}(2h,T_F) - \varepsilon_{\lambda F}(h,T_F)\}]N_{\lambda BB}(T_F)d\lambda \qquad (18)$$

An approximate integrated expression can be written as,

$$N_F = [\varepsilon_F(h,T_F) + \rho_b\{\varepsilon_F(2h,T_F) - \varepsilon_F(h,T_F)\}]N_{BB}(T_F) \qquad (19)$$

ε_F is the integrated film emissivity and $N_{BB}(T_F)$ is the integrated value of black body radiation at temperature T_F, given by Figure 14. Equation (19) can also be written as

$$N_F = [\varepsilon_b\varepsilon_F(h,T_F) + \rho_b\varepsilon_F(2h,T_F)]N_{BB}(T_F) \qquad (20)$$

since $\varepsilon_b = (1 - \rho_b)$.

Now that expressions for attenuated radiation from the fluid, ball, and ambient have been derived, an equation can be formulated to give the total radiation received through a filter, in terms of the ball and fluid

temperatures. The total radiation N is given by

$$N = \eta_s \tau_F(h,T_F) N_{BB}(T_b) + [\varepsilon_b \varepsilon_F(h,T_F) + \rho_b \varepsilon_F(2h,T_F)] N_{BB}(T_F)$$

$$+ [\rho_s^* + \rho_b \eta_s^2 \tau_F(2h,T_F)] N_o \qquad (21)$$

with, $\eta_s = \tau_s(1-\rho_1)1-\rho_2)$; $\varepsilon_b = (1-\rho_b)$; and $\rho_s^* = \rho_1 + \tau_s^2(1-\rho_1)^2\rho_2$

It should be remembered that the numerical values of various quantities in the above equation depend on which filter is used in the experiment.

Black body Calibration. It was mentioned earlier that the manufacturer's calibration curve of black body temperature versus radiation is not applicable when a filter is used. Therefore, in order to use the IR microscope while using a filter, new calibration curves were obtained experimentally and these were shown in Figures 13 and 14. The technique used for obtaining this data is described below.

Measurements of the radiation from a black body calibration source (Barnes' RM-121) were made as a function of temperature using each filter. The experimental arrangement is shown in Figure 15. Because of the internal chopper in the IR microdetector when using the D.C. mode of operation, the measured radiation (N_m) is related to the target radiation (N) by

$$N_m = N - N_0$$

where N_0 is the reference ambient radiation corresponding to the filter used.

The value of N_0 should be added to the measured radiation N_m to obtain the total radiation N. In fact, in all the measurements reported

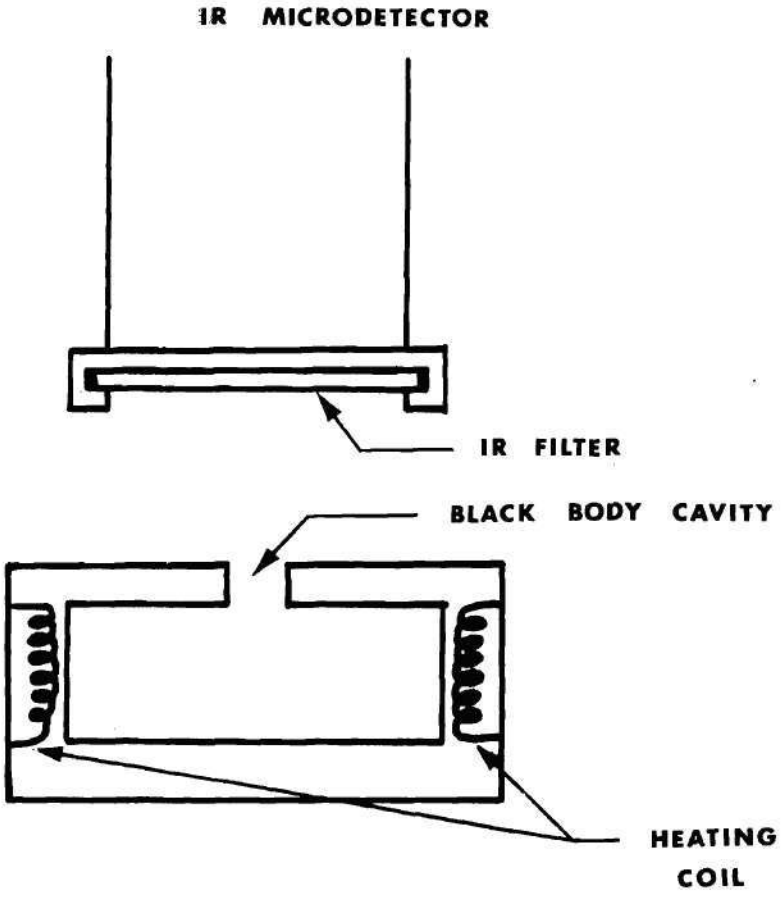

Figure 15. Black Body Calibration Experiment.

in this work this procedure is followed. Therefore, the value of N_0 must be known for each filter used. The magnitude of N_0 is equal to the intensity of radiation from a black body at room temperature. Radiation measurement from a cryogenic black body source was taken in order to measure N_o. The experimental arrangement was the same as shown in Figure 15. But a black body cavity immersed in a bath of liquid nitrogen (T = 77 K) was used instead of the black body calibration source shown in Figure 15. Since the emission from a black body at 77 K is much lower than the emission at room temperature (a ratio of approximately 10^{-10}), the black body emission at 77 K can be neglected. The radiation measured by the IR microscope is then the negative of the ambient radiation.

Calibration for Determining Emissivity and Transmissivity Functions

Suitable models for the emissivity and transmissivity functions are,

$$\varepsilon_F(h,T_F) = 1 - e^{-b_1 h e^{b_2 T_F^*}} \tag{22}$$

$$\tau_F(h,T_F) = e^{-b_3 h e^{b_4 T_F^*}} \tag{23}$$

Emissivity and transmissivity are linear with respect to film thickness for small values of h. However, it is known that [89,90] emissivity increases greatly with temperature and transmissivity decreases greatly with temperature. These are also satisfied by the models shown in equations (22) and (23). The assumption of emissivity being equal to one minus transmissivity can be relaxed at this time since the extra constants can easily be determined during calibration. The calibration results, however, show that emissivity is close to one minus transmissivity for small values

of film thickness at small values of film temperature.

To determine the constants b_1, b_2, b_3 and b_4, radiation measurements were taken using a stationary contact where both the ball and fluid temperatures were known. In the calibration experiment (Figure 16), the same basic test apparatus is used as is used in the EHD experiment but the ball is not rotated and there is no load on the contact. The film thickness at the contact center is zero and can be calculated at other locations by geometry. The circulating oil bath keeps the ball, oil, and sapphire all at the calibration temperature. Under these conditions, a curve giving radiation as a function of film thickness is obtained as the detector transverses the contact. The same experiment is repeated at different calibration temperatures ranging from 50 to 140 C. Experiments are also conducted with two different balls, one polished and the other oxidized to yield different surface emissivities. From all these radiation experiments, the values of b_1, b_2, b_3 and b_4 are calculated in sets. Average values of these constants are used in calculating the fluid film temperatures from radiation measurements. Figure 17 shows emissivity and transmissivity as functions of film thickness for fluid N1 at a calibration temperature of 100 C. The linearity of these functions at small values of film thickness can be seen in the above figure. Figure 18 shows emissivity and transmissivity as functions of temperature for a film thickness of .175 μm for fluid N1. The strong dependence of emissivity and transmissivity on temperature is clearly seen in the above figure.

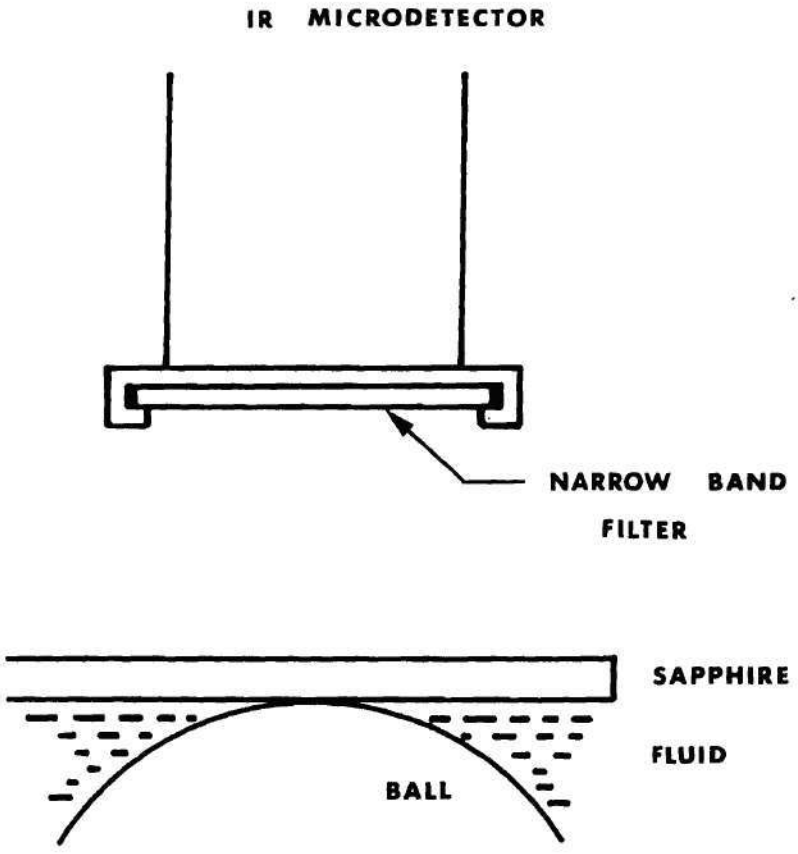

Figure 16. Emissivity and Transmissivity Calibration Experiment.

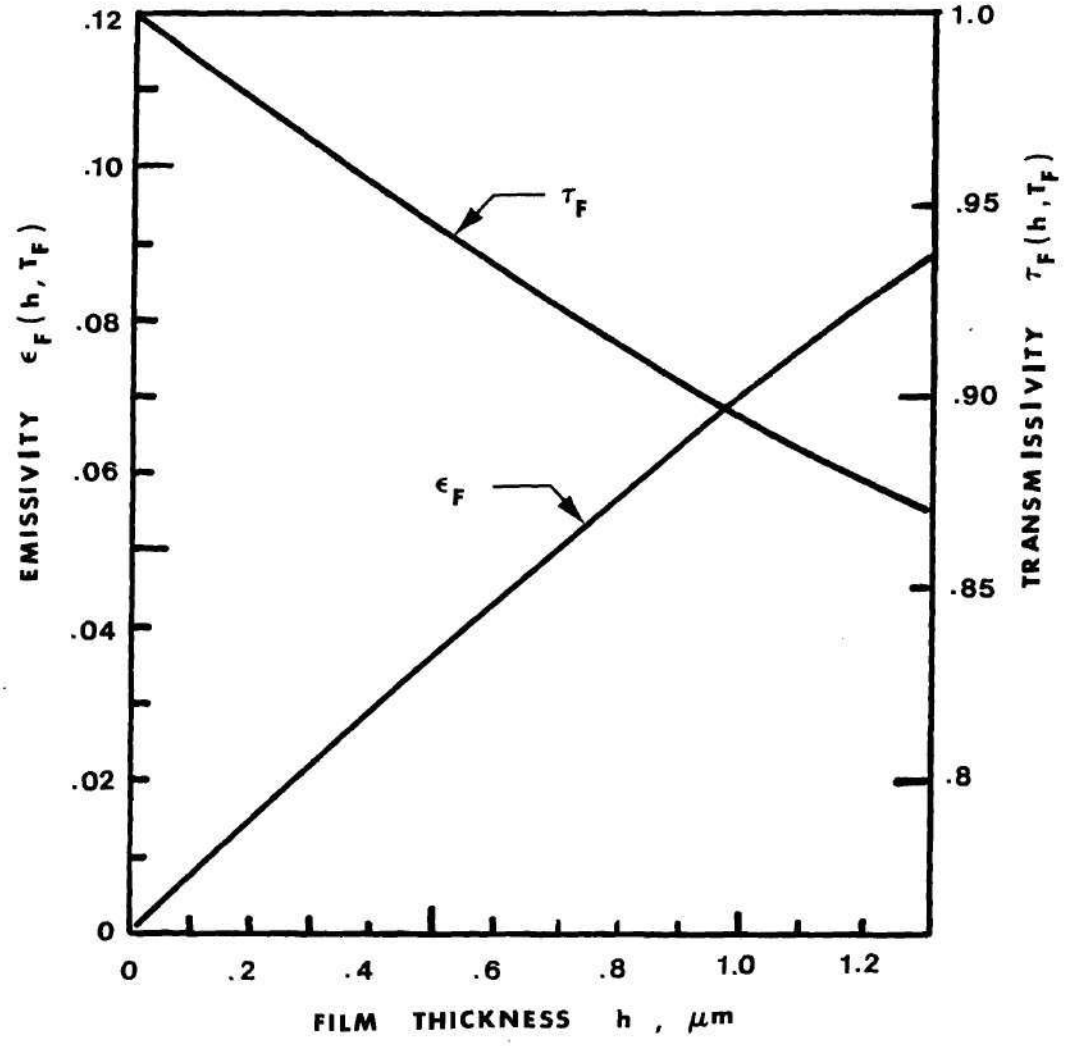

Figure 17. Emissivity and Transmissivity versus Film Thickness (Calibration Temperature T_F = 100 C, Fluid N1).

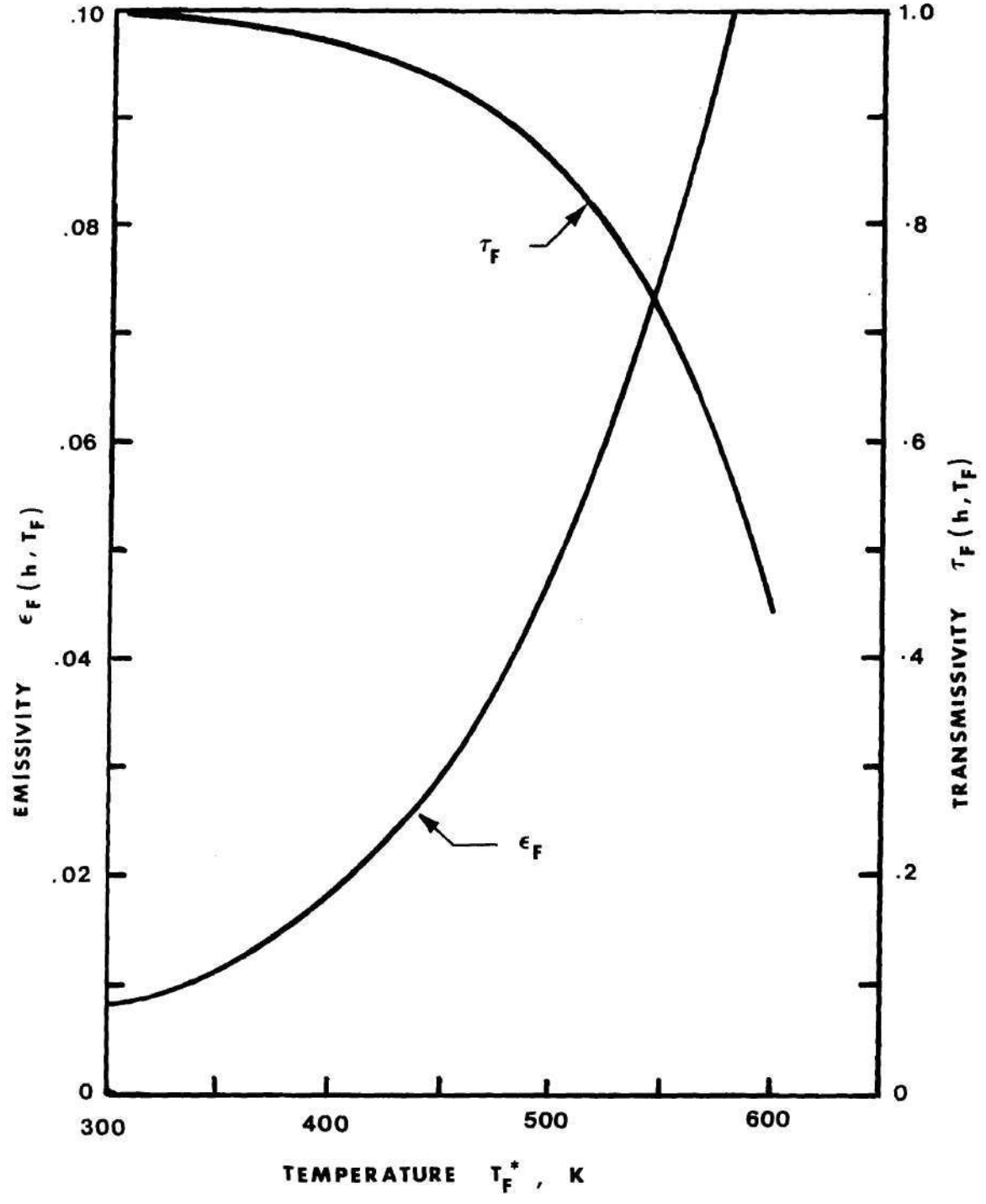

Figure 18. Emissivity and Transmissivity versus Temperature (Film Thickness h = .175 μm, Fluid N1).

Ball Surface Temperature Determination

With the wide band filter, no fluid radiation enters the detector and therefore, $\varepsilon_F = 0$ and $\tau_F = 1$.

The equation for total radiation through the wide band filter simplifies to

$$N = N_m + N_O = \eta_s \varepsilon_b N_{BB}(T_b) + (\rho_s^* + \eta_s^2 \rho_b) N_O \tag{24}$$

solving this equation for $N_{BB}(T_b)$,

$$N_{BB}(T_b) = \frac{(N_m + N_O) - (\rho_s^* + \eta_s^2 \rho_b) N_O}{\eta_s \varepsilon_b} \tag{25}$$

The values of various constants appearing in equations 24 and 25 are given in Appendix C. The ball surface temperature T_b can now be obtained by calculating $N_{BB}(T)$ using equation (25) and by referring to the black body calibration curve for the wide band filter given in Figure 13. T_b can also be obtained by using Figure 19, which shows a plot of the detector output in millivolts versus the ball surface temperature. Figure 19 was obtained by substituting calibration data into equation (25). Equation (26) is a least squares fit to Figure 19 which allows calculation of ball surface temperatures directly from test data.

$$T_b = .1174X^3 + 4.621X^2 + 4.653X + 38.94 \tag{26}$$

where, $X = \ln(N - N_O) = \ln N_m$; N_m = detector output in millivolts while using wide band filter.

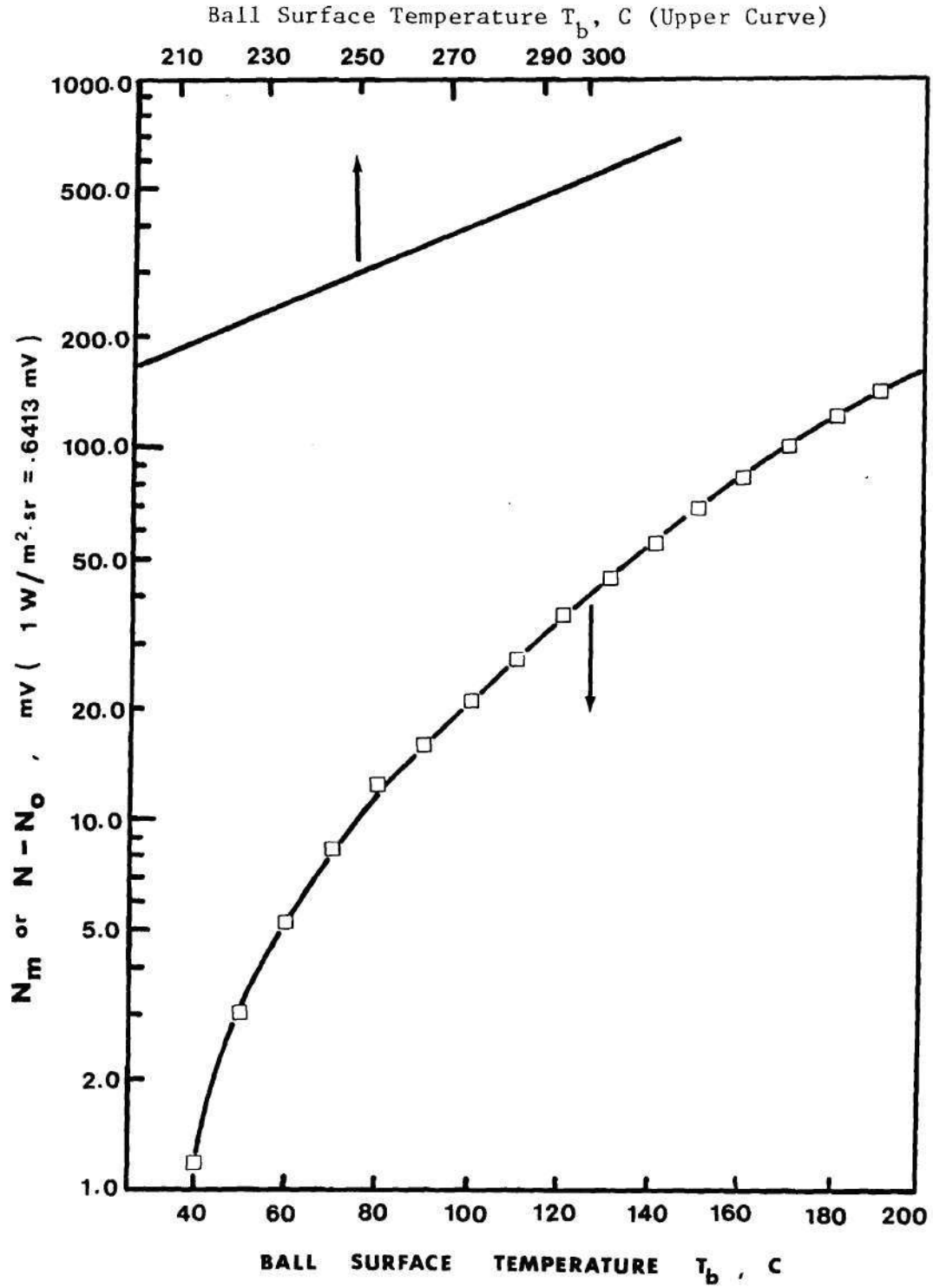

Figure 19. Wide Band Filter Calibration for Ball Surface Temperature Determination.

In order to verify the radiation analysis through the wide band filter, ball surface temperature was measured under known conditions. In these experiments, the ball was held stationary in a circulating oil bath at a known temperature. The ball and the fluid were therefore at the same temperature. It was found that the fluid film did not have any effect on the radiation measured through the wide band filter and that the calculated ball temperatures were consistently within 2C of the bath temperature as measured by a thermocouple. These test results tend to substantiate the radiation analysis.

Fluid Film Temperature Determination

The equation for the total radiation through the narrow band filter is identical to equation (21). Emissivity and transmissivity functions for the fluid are given by equations (22) and (23). The values for the relevant constants appear in Appendix C. Equation (21) can now be solved for fluid temperature by using Figure 14 of black body radiation through narrow band filter versus temperature or equation (27). The calibration curve of Figure 14 is analytically expressed as equation (27) by means of a least squares data fit;

$$N_{BB}(T) = \text{Exp}[((2.45E\text{-}7*T - 1.5702E\text{-}4)*T + .05463)*T - 2.808] \quad (27)$$

Ball surface temperature and local film thickness must be known in order to calculate the fluid temperature. Since many of the terms

comprising the total radiation received contain parameters dependent on the unknown T_F, an iterative solution procedure is necessary. For example, a certain T_F is assumed and using all the equations developed above and the associated calibration curves, the total radiation that should be received is calculated. This is compared with the measured value. If the agreement is not satisfactory, the procedure is repeated with a new T_F (assumed) until an acceptable T_F is obtained. A computer program (Appendix D) was developed to perform all this using a Newton-Raphson iteration scheme. The iteration was continued until the calculated radiation was within .01 percent of the measured radiation.

In order to prepare a map of temperature over the contact area, it was necessary to scan the contact at regular intervals. The sampled values of radiation were then used to calculate temperatures throughout the EHD contact region. Because of the large number of grid points (ex.: 200 grid points per map), the computer program shown in Appendix D was employed to calculate temperatures. Furthermore, by using least squares method (in the computer program) to determine the contact centerline, it was possible to minimize the IR microdetector positioning and alignment errors.

Results of a sample calculation of radiation through narrow band filter are shown in Appendix E. The contributions from different sources and their relative importance is evident from the calculations in this appendix.

Sources of Error in Temperature Measurement

Errors were introduced in temperature measurements mainly because

of possible errors in the calibration procedure. Effort was made to minimize these errors. Errors were also introduced due to misalignment of the optical elements.

Interference between infrared radiation emitted by ball surface and sapphire flat was found negligible in the present study, since the film thickness under EHD conditions is a very small fraction (1/25 to 1/100) of the wavelength of infrared radiation. Also, the different sources of IR radiation do not produce coherent radiation. Furthermore, the presence of oil in between the ball surface and the uncoated sapphire considerably reduces the interfacial reflectivity. This poor reflectivity almost eliminates interference effects, unlike the IR interference fringes observed by Wedeven [91] in a dry contact between ball and sapphire.

Error in film thickness measurement results mainly from improper reading of the fringe brightness or color. This has been estimated to be within $\pm .006$ μm ($\pm .25$ microinch). This error in film thickness affects only film temperature (±5 to 10 C) and not the surface temperature. Possible error due to neglecting the sapphire contribution has been discussed earlier. In the bandwidth of narrowband filter the sapphire emissivity is close to zero and this therefore, does not directly introduce any error in film temperature except through error in ball temperature. Ball surface emissivity was assumed .21 at all operating temperatures. However, ball surface emissivity decreased slightly at high values of T_b (> 200 C). Fluid emissivity and transmissivity calibration was carried out only up to a temperature of 140 C,

but assumed to hold for higher temperatures. Possible error in the calibrated value of the ambient radiation through the narrow band filter is not critical except at very low values of radiation (≈ .2 mv) as encountered in pure rolling conditions. Errors due to improper matching of the radiation scans were eliminated by employing a cam operated microswitch to start each traverse. However, when a filter is introduced in front of the microscope, a lateral shifting of IR focal point may result. This shift was estimated to be less than 7.5 μm per degree of slant of the IR filter with respect to the focal plane. With a possible error in IR filter alignment of 1 to 2 degrees, a shift of less than 15 μm may occur in IR focal point. This position shift is about one-half the distance between scans and nearly one-third the detector spot size. An error in measured temperature can be associated with this source.

Considering all the above sources of error, the ball surface temperatures are within 2 to 3C of the measured values and fluid film temperatures are within 10 to 12 C of the measured value.

The Infrared Microdetector

The Barnes RM-2A infrared microdetector used for measurement of time averaged temperature as discussed above, is used for the measurement of temperature fluctuations also. For this purpose, the microdetector is operated in the A-C mode. The response time of the detector-preamplifier combination used in the microdetector is 8 μ-sec. For most applications reported in this work, this response was found adequate.

Figure 20 shows a simplified block diagram which shows the operation of the Barnes' RM-2A infrared microdetector [92] in both D.C. and A.C. modes. The IR radiation received by the reflective type objective is sensed by the detector and a difference voltage signal proportional to the input radiation appears at the output. This signal is amplified with a gain of approximately 100 by a high stability, high impedance preamplifier with D.C. feedback. The preamplifier has a low output impedance of 100 Ω. The preamplifier signal, is available directly at an output jack (in the A.C. mode of operation) or processed by the control unit circuits (D.C. mode of operation).

The detector used in the Barnes RM-2A IR microdetector is a single crystal of indium-antimonide in the photovoltaic mode. In the photovoltaic mode, a voltage is produced in the conductor when it is irradiated. In order to give high sensitivity, it is necessary to cool the detector to very low temperatures. This is accomplished here by contacting the detector with liquid nitrogen (boiling point 77 K). This results in some loss of wavelength range, the cutoff falling from 7.5 μm at room temperature to about 5.5 μm at 77 K. Response time is 8 microseconds at 77 K and about 10 ns at room temperature. But, the minimum detectable power drops from 10^{-9} watts at room temperature to about 10^{-11} watts at 77 K. This limiting sensitivity is mainly due to random noise generated in the detector itself. Both the thermal noise and current noise generated in the detector are proportional to the bandwidth of the measuring system [93]. In order to avoid this noise in the temperature measurements, an electrical bandpass filter with variable bandwidth is used. Since noise components are present in

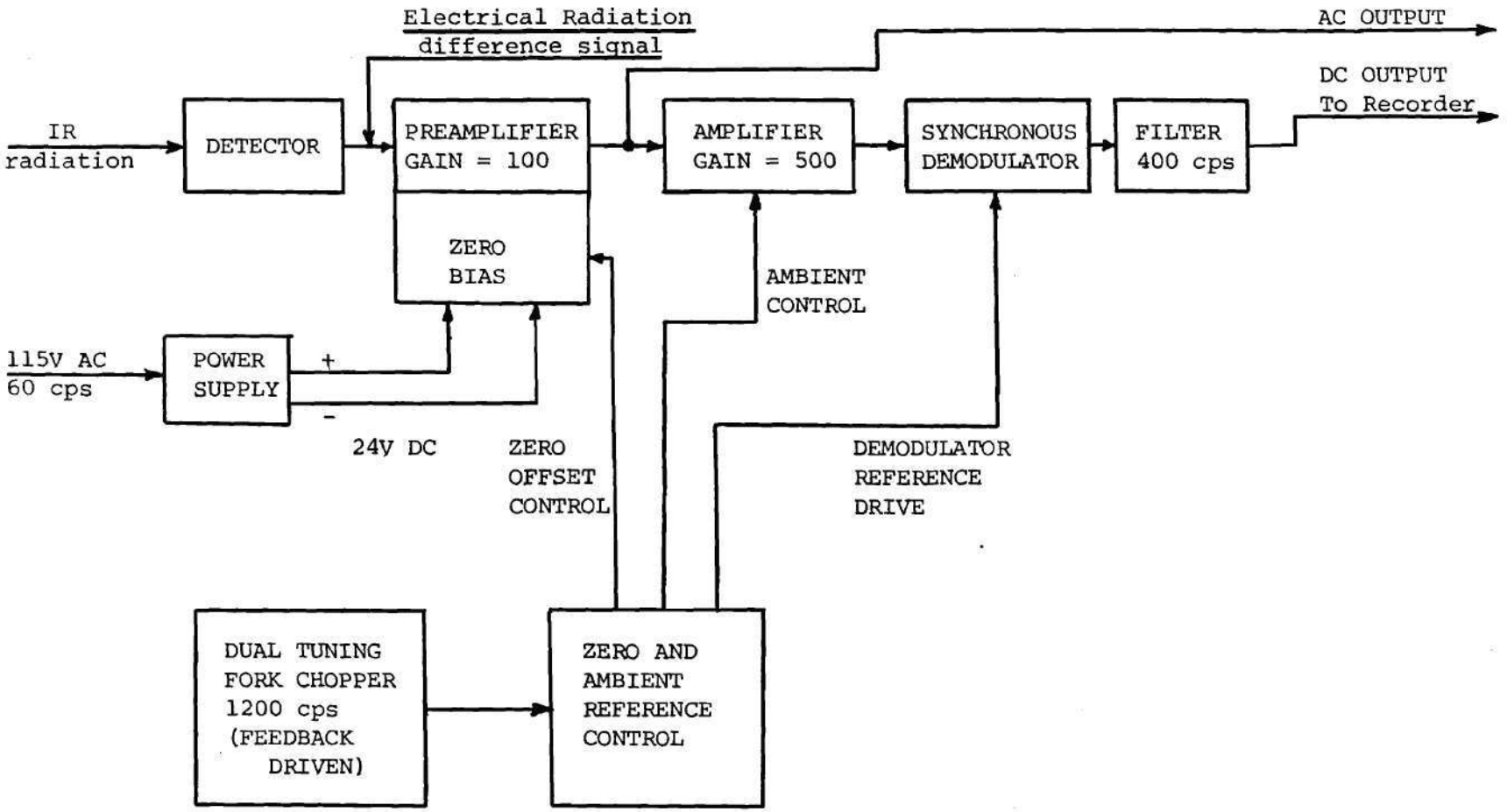

Figure 20. Block Diagram Showing Operation of Barnes RM-2A IR Microscope in Both DC and AC Modes.

the neighborhood of signal frequencies also, noise cannot be completely eliminated from the signal. However, by having the upper cutoff frequency at 20 KHz (at 3 db point) and a roll-off of 28 db/octave outside the pass band, the magnitude of noise was within tolerable limits as will be shown later in Chapter V. The above pass band was adequate for all signal frequency components produced under moderate sliding speeds.

In the A.C. mode, the preamplifier output voltage will fluctuate between two levels V'_{max} and V'_{min} given by,

$$V'_{max} = D[\varepsilon_b N_{BB\,max} + (1 - \varepsilon_b)N_O] \tag{34}$$

and,

$$V'_{min} = D[\varepsilon_b N_{BB\,min} + (1 - \varepsilon_b)N_O] \tag{35}$$

where D = Detector constant = 6.417 $mV/(mW \cdot sr^{-1}cm^{-2})$

Subtracting (35) from (34),

$$V'_{max} - V'_{min} = D\varepsilon_b[N_{BB\,max} - N_{BB\,min}]$$

$$\text{or} \quad \Delta V = D\varepsilon_b \Delta N_{BB\,eff} \tag{36}$$

Through independent calibration experiments it was determined that these radiation fluctuations $\Delta N_{BB\,eff}$ were centered around the effective black body radiation N_{eff} determined from the D.C. mode operation of the IR microdetector. The calibration experiments consisted of operating the microdetector in the A.C. mode with an external chopper, the target being the black body calibration source. Then,

$$N_{BB\,max} = N_{BB\,eff} + \frac{N_{BB\,eff}}{2} \tag{37}$$

$$N_{BB\,min} = N_{BB\,eff} - \frac{N_{BB\,eff}}{2} \tag{38}$$

The maximum and minimum surface temperatures can then be determined using the black body calibration data. Since only ball surface temperature fluctuations are measured, the wide band filter is used. All the effective radiances and voltage outputs, then, refer to wide band filter data discussed earlier and also available in references [94, 95].

B. Surface Roughness Measurement and Analysis

A stylus instrument - Bendix group XV measuring system - was used to measure the profile and other important surface geometry parameters.

A photograph of the system is shown in Figure 21. The instrument has four principal operating parts; a tracer, a pilotor, amplimeter and recorder, an averaging meter. The tracer is moved mechanically along the workpiece. It has a diamond-pointed stylus that touches the work and moves up and down to follow the surface contour. The stylus used is a conical diamond with 60° cone angle and a rounded tip with a tip radius of 12.5 μm (.0005 in). This stylus did not cause any mechanical damage [96,97] and was found adequate for all the work reported here. The output voltage produced by the tracer is proportional to the height or depth of the surface irregularities. The pilotor supports and moves the tracer along the desired path of trace.

Figure 21. Bendix group XV measuring system.

The tracer is mounted beneath an optical flat which serves as a reference datum for straight line tracing. The speed of traverse is constant at 1.25 mm/s (.005 in/sec). A modification to this traversing attachment was incorporated in order to allow tracing along a spherical surface. This was necessary because spherical balls were used in the EHD simulators. Details of this modification will be described later in this section. The amplimeter housed an amplifier that amplified sufficiently (250X to 100,000X) the voltage produced by the tracer. The recorder consists of a galvanometer type pen meter and a chart drive mechanism. In order to give the desired horizontal magnification to the profile, the chart is driven at six different speeds. The averaging meter is designed to provide both the arithmetical average and root-mean-square value reading of surface roughness.

Rotary Attachment with Relocation Stage

Figure 22 shows a photograph of the specimen rotation attachment with a relocation stage fitted to the Bendix group XV system. The rotation attachment was necessary to allow measurements over an adequate arc length at high vertical magnification. For this purpose, the ball is rotated about its arcs under a fixed tracer; effectively increasing the ball radius to obtain increased arc length. Figure 23 shows the arrangement used.

A relocation mechanism is incorporated in the rotation attachment. This mechanism helps in recording the profile at precisely the same point on the ball surface before and after being run in the EHD simulator, to detect any change in the surface profile. Referring to Figure 23, four of the possible six degrees of freedom (along z, c,

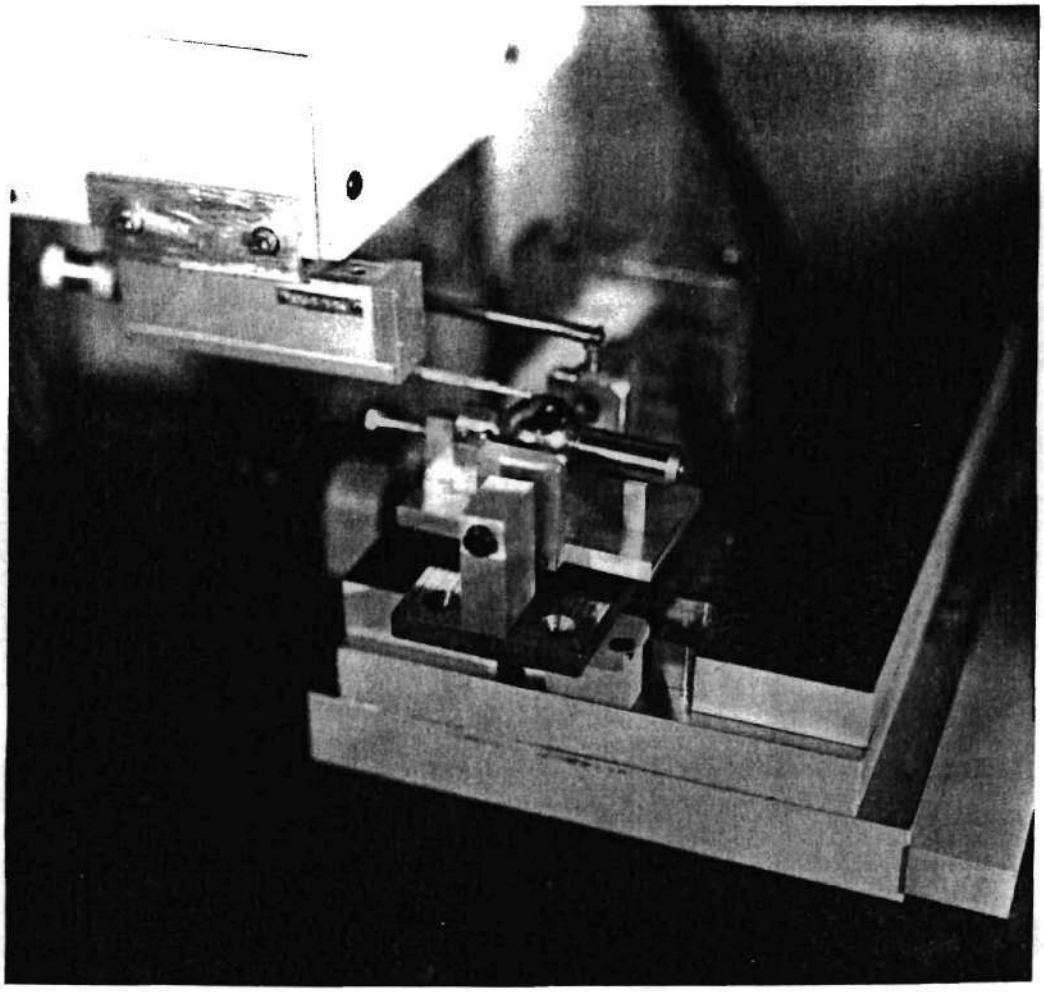

Figure 22. Rotary attachment with relocation stage.

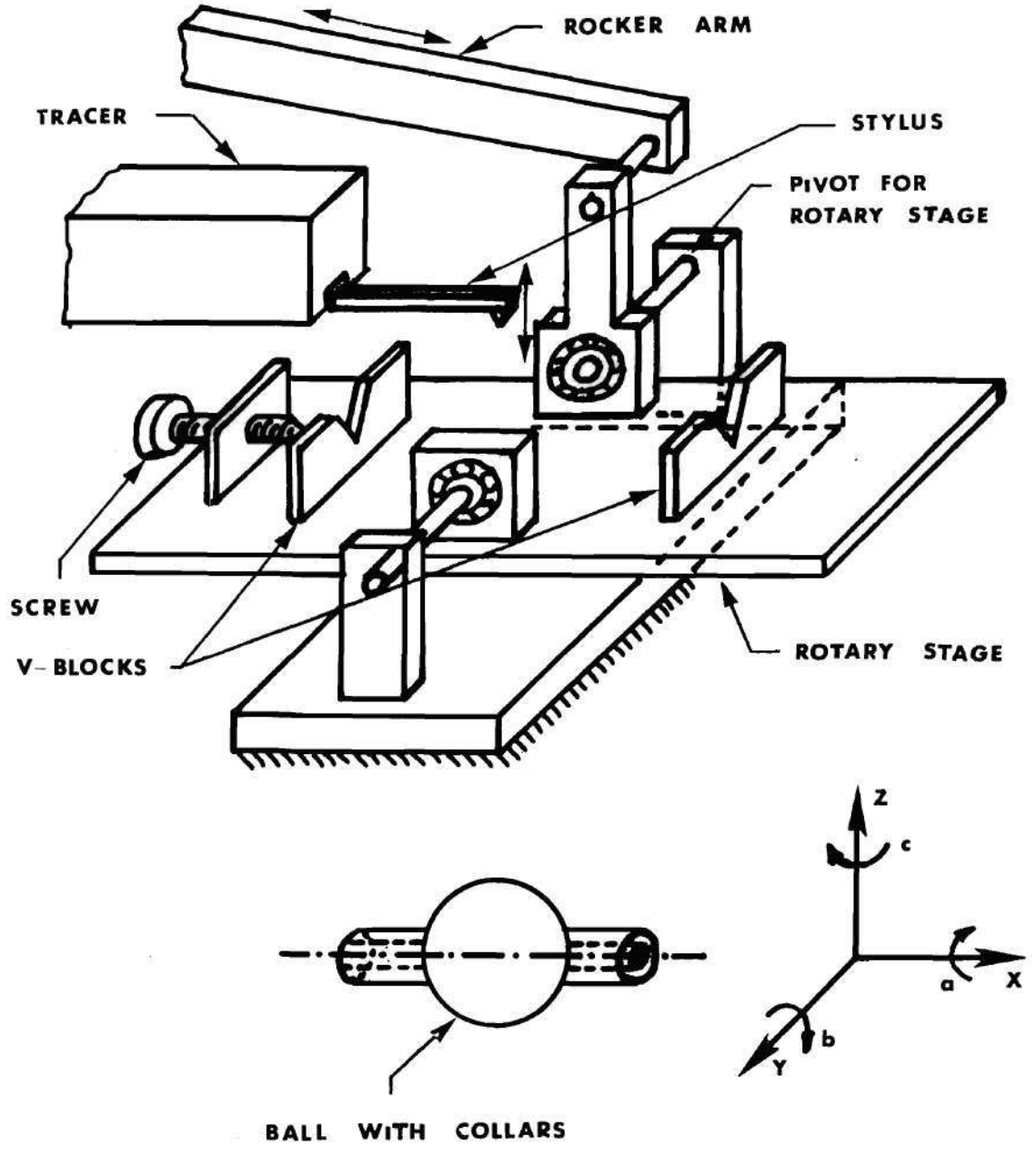

Figure 23. Schematic of the Rotary Attachment with Relocation Stage (mounted on the Bendix Group. XV Profilometer).

b, and y) are removed by using a pair of v-blocks. The other two degrees of freedom are removed by providing stops. Extreme care had to be exercised in not disturbing any of the settings on the profilometer while a relocation profile was being taken.

Surface Texture Assessment

The electrical signal out of the instrument often includes various wavelengths irrelevant to the texture of interest. Establishing a reference line within the profile permits roughness to be separated from the profile. In the Bendix system, this is done by a filter (2CR type) in the electronic unit, which effectively looks at a length of the surface equal to the sampling length. One of the following sampling lengths [93,94]; 0.08 mm (.003 in), 0.25 mm (.010 in), 0.8 mm (.030 in) can be selected on the Bendix machine. A sampling length of .030 inch was chosen for all the parameters reported in this work. Reasons for this selection will become apparent in Chapter V. In addition to filtering the surface profile in the longer wavelength region, the stylus tip itself provided filtering of short wavelength features by virtue of its finite tip dimensions and sometimes by the slope of its flanks. Figure 24 shows the total profile of a typical surface [98]. When this profile is filtered by choosing suitable sampling lengths, the important components of the surface texture namely, roughness (primary texture), waviness (secondary texture), and error of form, are revealed. Details of filtering and different types of filters are available in references [98-106].

The R_a value [British CLA (μ-in), American AA (μ-in), or R_a (μm)]

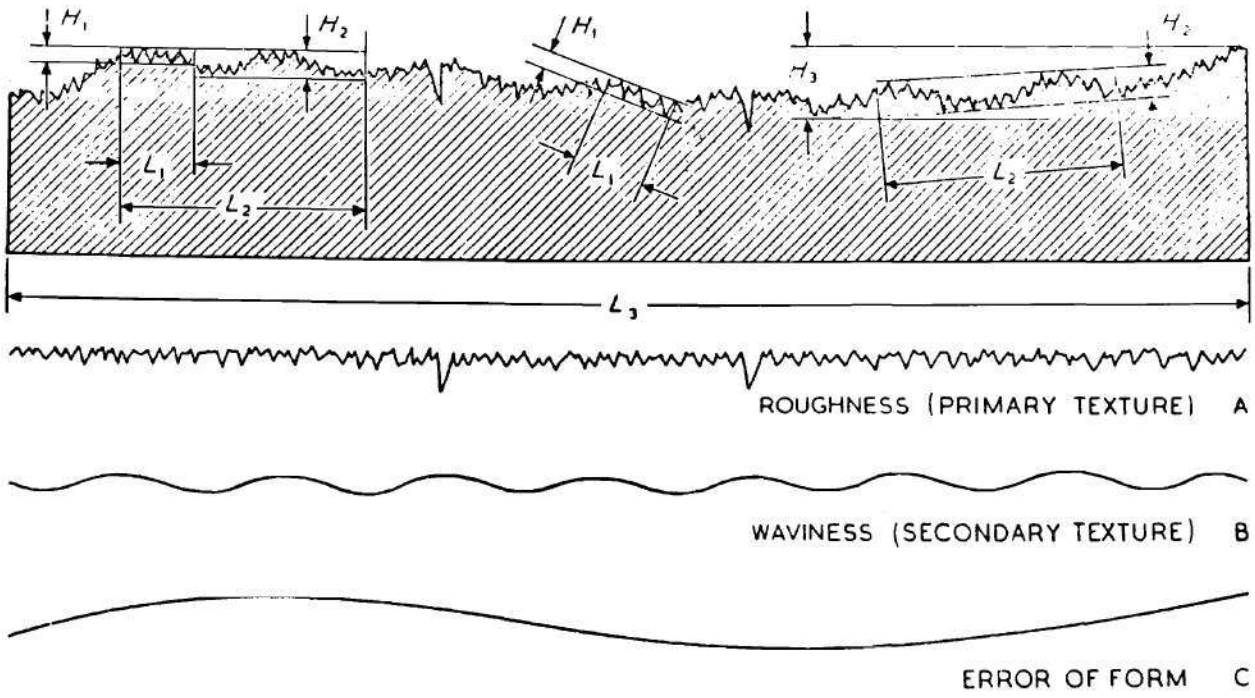

Figure 24. A Surface Texture Representing the Combined Effects of Several Causes. (From Reference [98])

which is simply the average value of the modulus of the deviations of the profile from the mean line, is used as the single most important parameter in this work. Being of an integrated nature, it tends to be reliable.

Fundamentally, in order to specify the information in a single-dimensional random waveform (such as a surface profile graph), two quantities are needed; the amplitude density function and the auto-correlation function. The former, commonly called the height distribution, is a measure of the frequency with which the profile equals a given level; the autocorrelation function is a measure of the dependence of one part of a profile on another. The autocorrelation function (or alternatively, its Fourier transform, the power spectral density) is therefore, a measure of the spacings on the surface. Further discussion on these functions are given in Chapter V. Also excellent discussions of these and other parameters are available in literature [56,57,107-119].

Profile Recording

The output data from the profilometer is available in the form of analog voltage fluctuations corresponding to the height readings on the surface. These voltage fluctuations were subjected to the commonly used time-series analysis techniques to reveal the important features of the surface. It was found convenient to record the output from the profilometer since an online analyses was not available. However, this method was useful because the frequency of the profilometer data could be stepped up to a convenient value for the analysis. The

profilometer scanning speed being .125 mm/s (.005 in/sec), the output frequencies were very low ranging from .1 Hz to 100 Hz. By recording this data at a low speed of 1 7/8 in/sec and playing it back at a higher speed of 15 in/sec, the data frequency could be stepped up by a factor of 8.

An Ampex SP-300 instrumentation recorder was used. This recorder offers pushbutton selection of either direct or FM recording, and by an internal jumper connection, audio recording. The FM recording technique was used for surface profile recording because of the low frequencies involved. Frequency response in the FM mode, with a clean tape and head, is 0 to 312 Hz at 1 7/8 in/sec speed, and was adequate for the purpose of this work. Maximum output voltage level (output impedance = 100 Ω) was 1 volt rms but could be monitored for any lower value.

Frequency Analysis

Frequency analysis of the surface profile data was conveniently performed on an available Fourier analyser system (Hewlett-Packard 5451 A). The Fourier analyser system uses digital signal processing techniques. This was found convenient because: (1) digital equipment is more accurate and insensitive to environmental factors, (2) digital equipment is more flexible and easily adaptable, in addition to having a greater dynamic range (DC to 25 KHz for HP 5451 A system).

The basic system consists of an analog to digital converter (HP 5465A), a control unit (HP 5475 A), a dedicated 8K mini computer (HP 2100 A), a display unit (HP 5460 A), an oscilloscope (HP 180 AR/DR).

Data input and output are controlled from the keyboard. Data can be entered in analog form through the 10-bit 2 channel A/D converter.

Results of all operation are displayed on the oscilloscope. In addition, results can be printed out in decimel numbers on the teleprinter, punched on paper tape or plotted on an external X-Y plotter. The Fourier analyser system is a completely calibrated system; all displays and data outputs are accompanied by a scale factor. The constructional and operational details of the Fourier analyser and the associated theoretical background are available in references [120-126].

CHAPTER IV

RESULTS AND DISCUSSION - I, TIME STEADY TEMPERATURE

In this chapter, time steady temperatures of the ball surface and the fluid are reported. The operating conditions include different Hertz pressure levels, a range of sliding and rolling velocities and slide-roll ratio varying from -2 to +2. Values of film thickness and traction are also reported under certain operating conditions. Comparison of the measured temperatures with the average temperatures predicted by using the flash temperature theory of Blok is also reported.

A. Results for Simple Sliding

Results given in this section are concerned with the case of simple sliding where the sapphire is stationary and the ball surface is moving. The operating conditions consist of different Hertz pressure levels and a range of sliding velocities.

The film thickness distribution was determined by laying a transparent grid on top of the fringe pattern photograph and observing through a low power microscope. Fringe order and therefore film thickness was determined at each grid location corresponding to the corners of a .025 x .025 mm square. These film thickness values have been tabulated in Appendix F. Because of symmetry, only one half of the contact region is shown. Tables F1-F6 are for P_H = 1.02 GPa,

T_{bath} = 40 C, and six different speeds. Difficulty was experienced in acquiring film thickness data at the highest speed of 12.7 m/s due to the dynamic nature of the EHD contact. Therefore, film thickness values were extrapolated from the known values at lower sliding speeds. Tables F7-F9 correspond to P_H = 1.51 GPa, T_{bath} = 40 C at three different sliding speeds. Figure 25 shows the film thickness distribution along the centerline of the EHD contact from inlet to exit, for the case of P_H = 1.02 GPa and T_{bath} = 40 C at six different sliding speeds. The film thickness in the high pressure plateau region for the three lower sliding speeds are essentially constant. But with increase in speed the exit restriction becomes noticeable. The position of the local maximum film thickness which occurs slightly before the exit restriction is believed to correspond to the position of the secondary pressure spike in the EHD contact. The manner in which these results influence the temperature distribution will be described later in this section.

Temperatures of the ball surface and the fluid film are measured using the infrared technique described earlier. Tables G1 - G18 in Appendix G show the results obtained at 9 different operating conditions. Because of symmetry, only one half of the EHD contact is considered. The direction of sliding is from top to bottom in the results shown. The numbers 1 through 9 indicate the distance of the grid point from the center of the contact in thousandth's of an inch.

Using the results shown in Tables G5, G6, G15 and G16, temperature contour maps were prepared. Contours were drawn by linearly interpolating between the grid points for the required values of

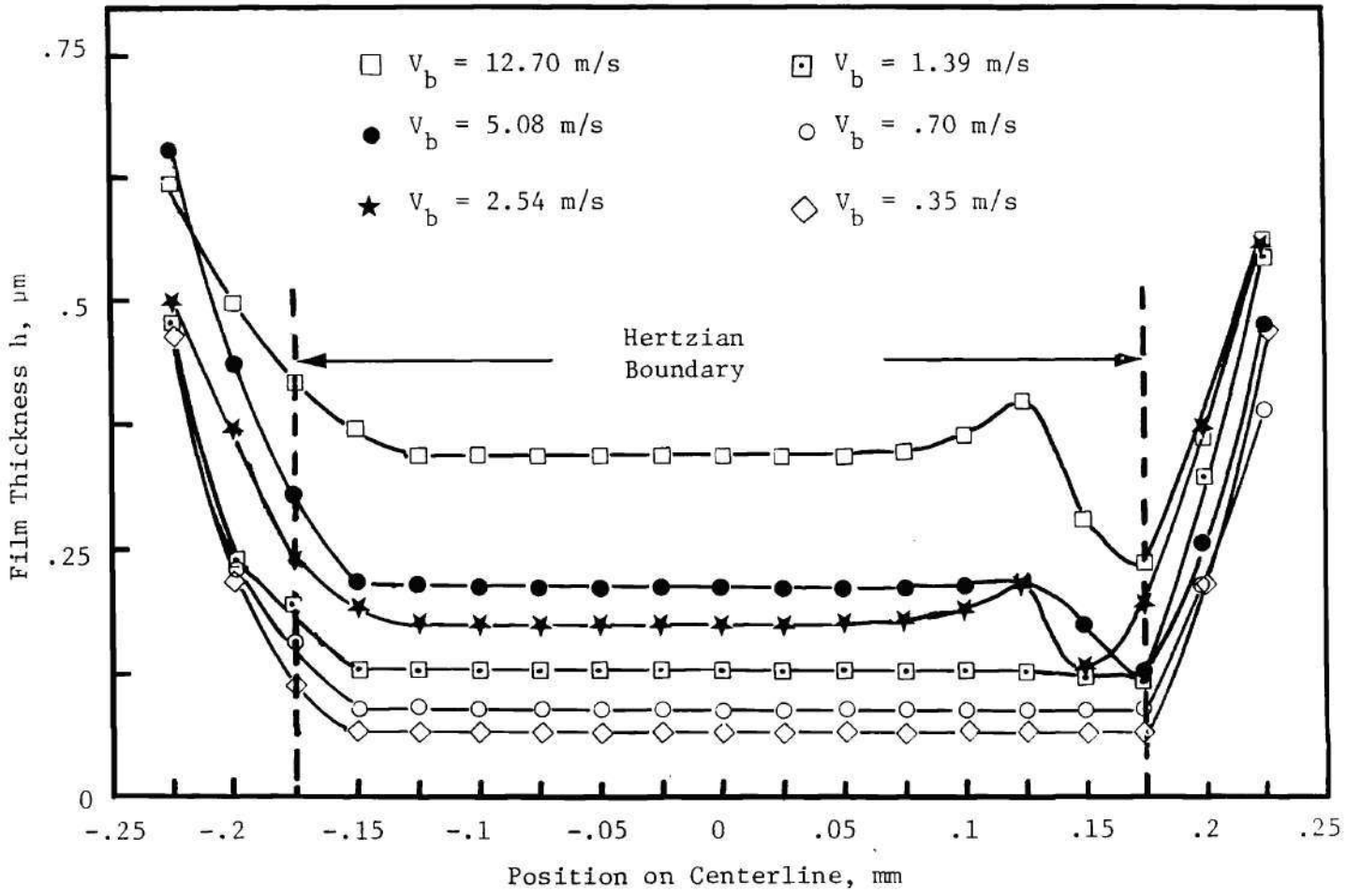

Figure 25. Film Thickness Profiles along Centerline versus Speed (Smooth ball: .011 μm R_a, Fluid N1, P_H = 1.02 GPa T_{bath} = 40 C, V_{sa} = 0)

temperature. Figure 26 is a temperature contour map showing the ball surface temperature as a function of location in the EHD contact for a sliding speed of 1.39 m/s and a load of 67 N (peak Hertz pressure is 1.02 GPa). Along with the boundary of the Hertzian contact zone, isotherms are shown for increments of 10 C. For a bath temperature of 40 C, the ball surface temperature increases to a maximum of 117 C at a point on the centerline downstream of the contact center. Figure 27 shows a similar plot for the lubricant temperature for the same conditions. Unlike the well behaved distribution of ball surface temperatures (Figure 26), the fluid temperature (Figure 27) varies dramatically, indicating the possible presence of local hot spots. It should however be remembered that the margin of error on fluid temperature is 10 to 12 C. This may in part explain the dramatic variation of fluid temperature over the contact region. Although one of the locations of maximum fluid temperature is near the point of maximum ball surface temperature, extreme temperatures are also found at the sides of the contact at the film constriction. The film thickness at this point is approximately 0.05 micron. Figure 28 presents some of the temperature data given in Figures 26 and 27 along with the film thickness variation, as a function of distance along the centerline in the direction of flow. It can be seen that film thickness values as low as 0.05 μm are present. However, no significant asperity interactions are present because the composite surface roughness of the ball and sapphire is .013 μm. The fluid temperature is typically 40 to 50 C higher than the ball surface temperature in the same location. Figure 29 shows the effect of sliding

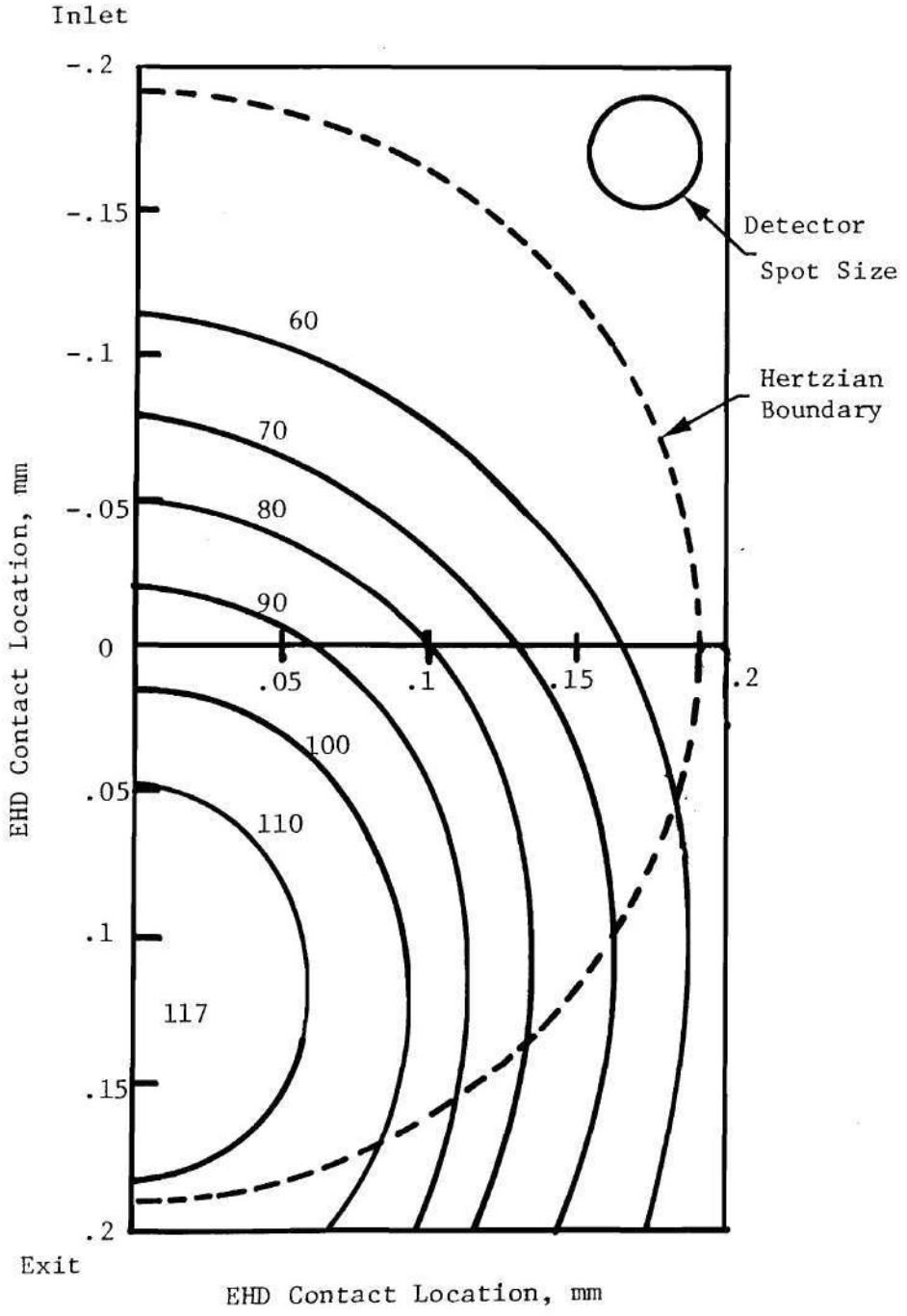

Figure 26. Ball Surface Temperature T_b (C) versus EHD Contact Location (Smooth Ball: .011 μm R_a, P_H = 1.02 GPa, Fluid N1, T_{bath} = 40C, V_b = 1.39 m/s, V_{sa}^H = 0)

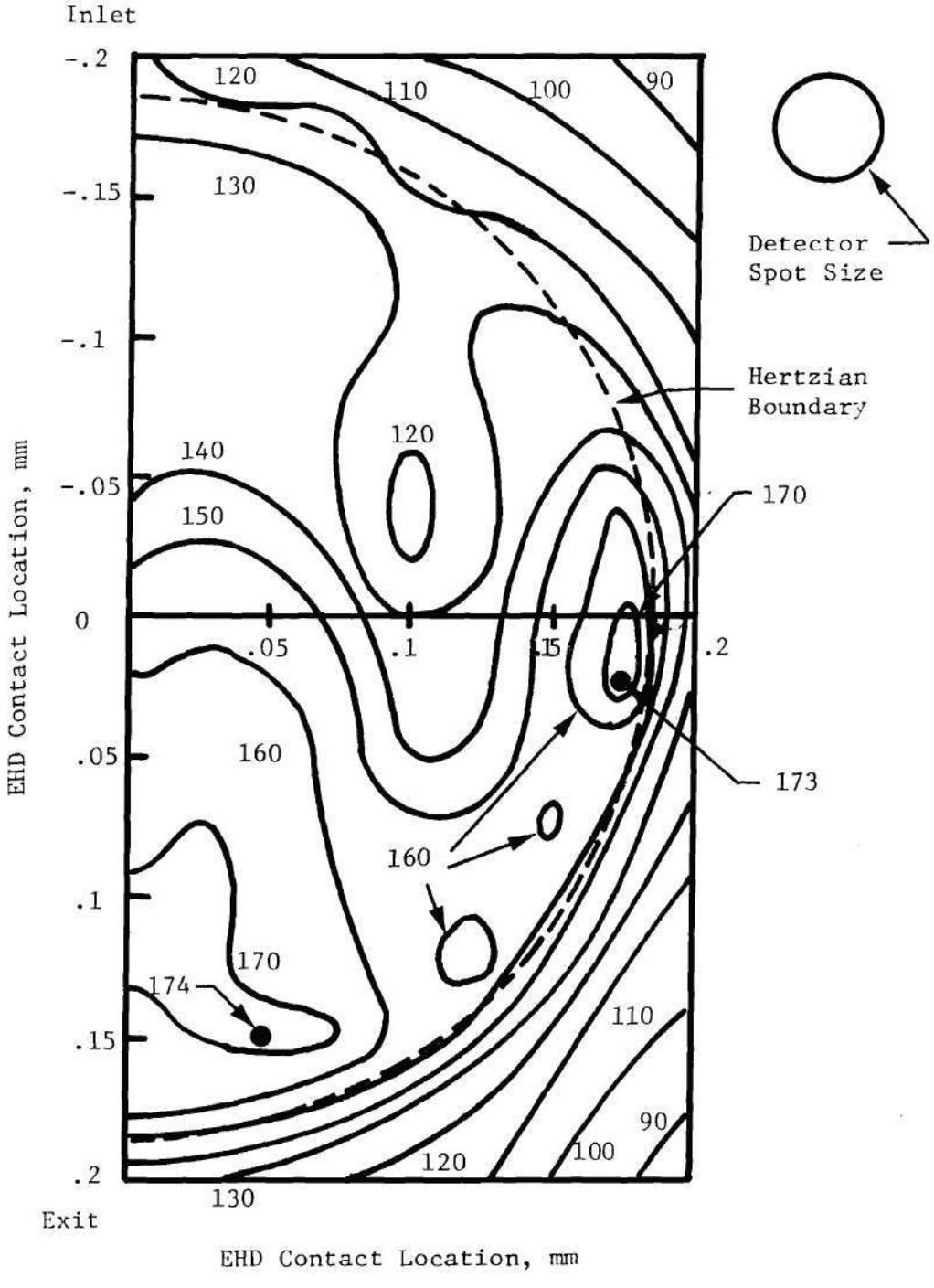

Figure 27. Fluid Temperature T_F (C) versus EHD Contact Location (Smooth ball: .011 m R_a, P_H = 1.02 GPa, Fluid N1, T_{bath} = 40 C, V_b = 1.39 m/s, V_{sa} = 0).

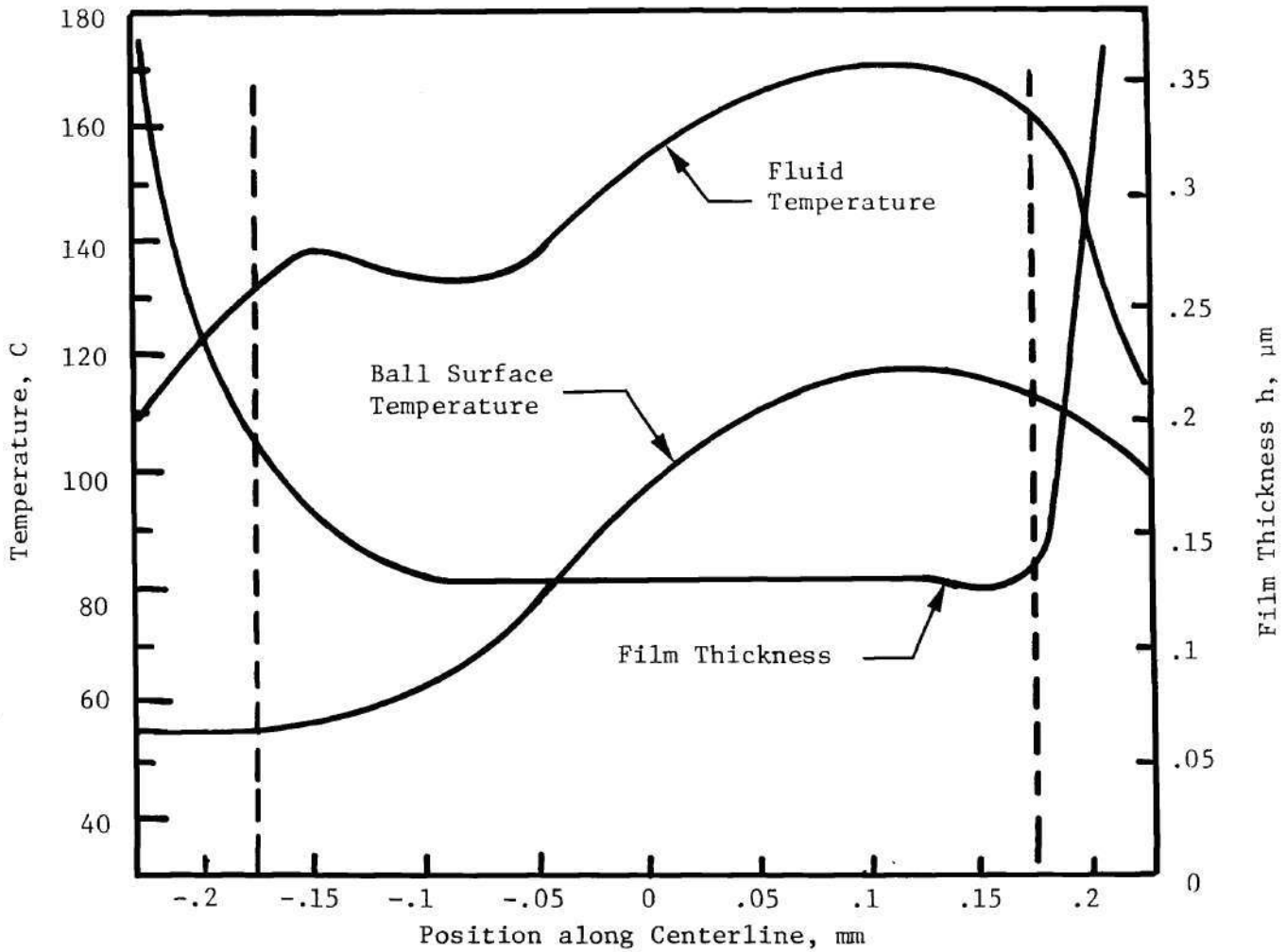

Figure 28. Fluid and Ball Surface Temperature along Contact Centerline (Smooth ball: .011 µm R_a, Fluid N1, P_H = 1.02 GPa, T_{bath} = 40 C, $V_b = V_s$ = 1.4 m/s, V_{sa} = 0)

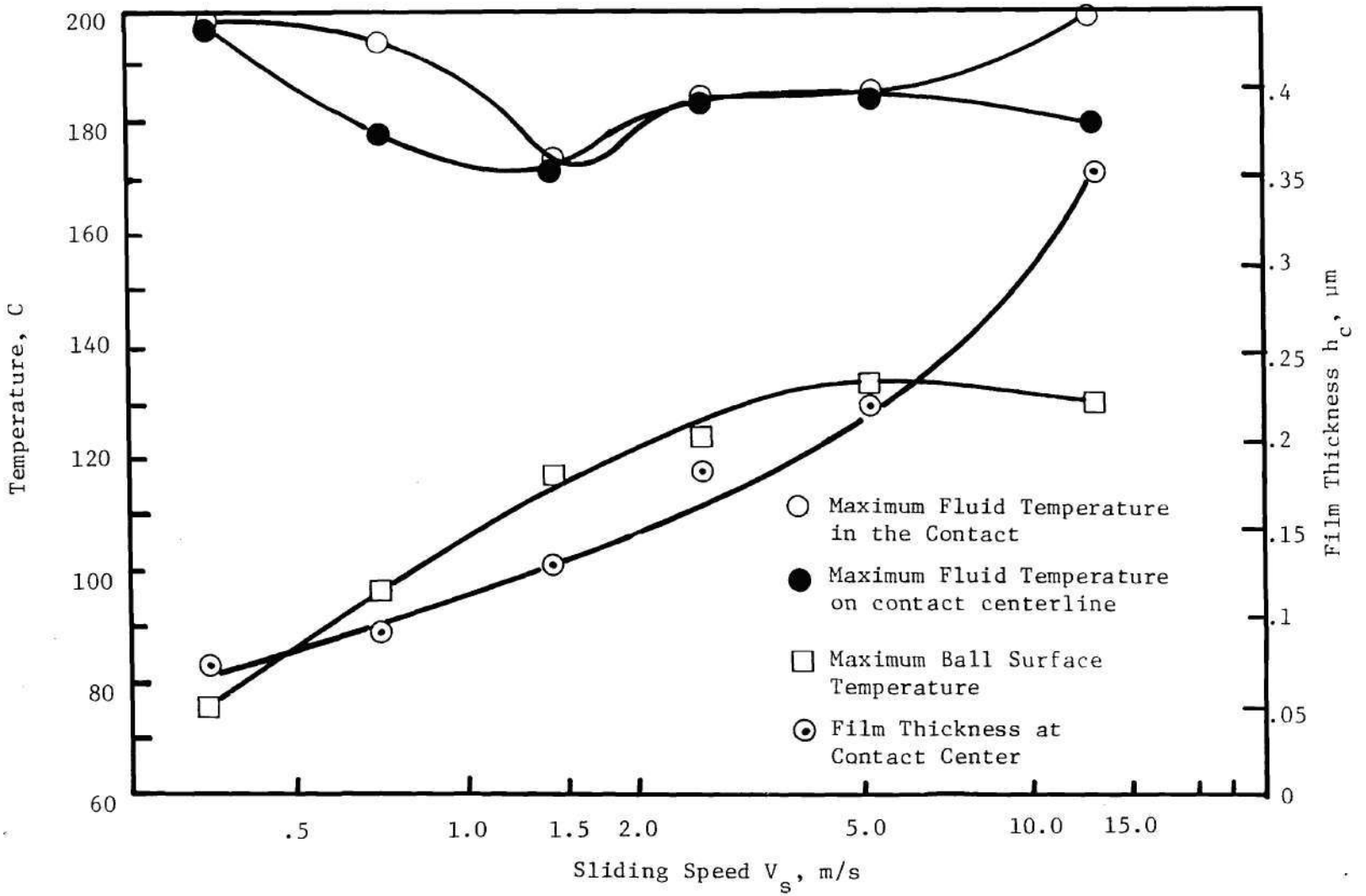

Figure 29. Ball Surface and Fluid Temperature versus Sliding Speed (Smooth ball: .011 µm R_a, Fluid N1, P_H = 1.02 GPa, T_{bath} = 40 C, V_{sa} = 0)

speed on the maximum ball surface temperature, the maximum fluid temperature in the contact, the maximum fluid temperature on the contact centerline, and the film thickness at contact center. The maximum fluid temperature in the contact remains substantially constant (with in ±12 C) while the ball surface temperature increases with speed from 75 C at .35 m/s to 133 C at 5 m/s and then is constant at 135 C to 12.7 m/s.

The maximum fluid temperature in the contact and the maximum fluid temperature on the centerline are not necessarily equal to each other even though they are very close in value. In other words, depending on the operating conditions of speed and load the maximum fluid temperature may occur on the centerline or at the side lobe constriction. The effect of speed and load is considered at a greater length later in this section. A summary of the most significant portions of the results obtained are shown in Table 2. This data includes the pertinent film thickness values along with the ball and fluid temperatures at four points in the contact: the Hertzian boundary in the inlet zone, the contact center, the maximum temperature along a contact centerline parallel to the direction of sliding, and the maximum temperature in the contact side lobe constrictions.

Similar measurements for the case of a normal load of 215 N (1.51 GPa peak Hertz pressure) were made and the most important results are given in Table 3. It can be seen from Table 3 that the film thickness at the center of the EHD conjunction, at the side lobes and at the contact exit are all essentially the same. This constant film

Table 2. Summary of Experimental Results for 67 N Normal Load

(smooth ball: .011 μm R_a, Fluid N1, P_H = 1.02 GPa, T_{bath} = 40 C, V_{sa} = 0)

Sliding Speed m/s	h_c μm	h_o Side Lobe Min. μm	h_o Center Line Min. μm	Temp. at Inlet* C		Temp. at Center C		Temp. Center Line Max C		Temp. Side Lobe Max C	
				Ball	Fluid	Ball	Fluid	Ball	Fluid	Ball	Fluid
12.7	0.35	0.16	0.25	67	124	102	154	130	180	116	200
5.08	0.22	0.11	0.13	56	102	120	179	133	185	78	155
2.54	0.18	0.09	0.13	56	115	113	132	123	185	88	177
1.4	0.13	0.09	0.09	54	125	98	156	117	171	60	173
0.7	0.09	0.08	0.08	46	120	83	166	96	178	58	194
0.35	0.07	0.05	0.05	45	155	67	188	76	198	46	162

*Hertzian boundary in the inlet region.

Table 3. Summary of Experimental Results for 215N Normal Load

(Smooth ball: .011 μm R_a, Fluid N1, P_H = 1.51 GPa, T_{bath} = 40 C, V_{sa} = 0)

Sliding Speed m/s	h_c m	h_o Sidelobe min m	h_o Center Line min m	Temp. at Inlet* C		Temp. at Center C		Temp. Centerline Max C		Temp. Sidelobe Max C	
				Ball	Fluid	Ball	Fluid	Ball	Fluid	Ball	Fluid
0.70	0.065	0.065	0.065	67	155	136	212	149	217	76	168
1.39	0.088	0.088	0.088	85	163	156	224	175	226	110	186
2.54	0.088	0.088	0.088	91	177	187	243	197	246	No Sidelobe max.	

*Hertzian boundary in the inlet region.

thickness tends to give more symmetric temperature distributions than previously observed.

In addition, at the higher load (215 N), the maximum ball surface and fluid temperatures always occurred on or near the contact centerline at a point downstream of the contact center. The reason for this is that the pressure, and the viscosity, is greatest at the contact center, and consequently, for a uniform film thickness, viscous dissipation is a maximum at the center. However, since the fluid residence period increases as the fluid moves toward the exit, the position of the maximum temperature could be between the contact center and exit depending on the effectiveness of heat transfer at the bearing surfaces. At lower loads (67 N), the maximum fluid temperature may occur off the contact center line, for example, at the side lobe constriction.

Figures 30 and 31 show temperature contours for a sliding speed of 1.39 m/s and peak Hertz pressure of 1.51 GPa. The general shape of the ball surface temperature contours (Figure 30) is similar to that found at lower loads (Figure 26). In this case, the ball surface enters the Hertzian contact at 85 C and reaches a maximum of 180 C downstream of the contact center and exits at 163 C. The fluid temperature contours shown in Figure 31 show that the difference between the primary maximum (226 C) on the centerline and the secondary maximum (186 C) in the side lobes has significantly increased compared to the lower load of 67 N (Figure 27). In the lower load case, the temperatures were 171 C and 173 C respectively. At 215 N, the secondary maximum disappears as the speed is increased.

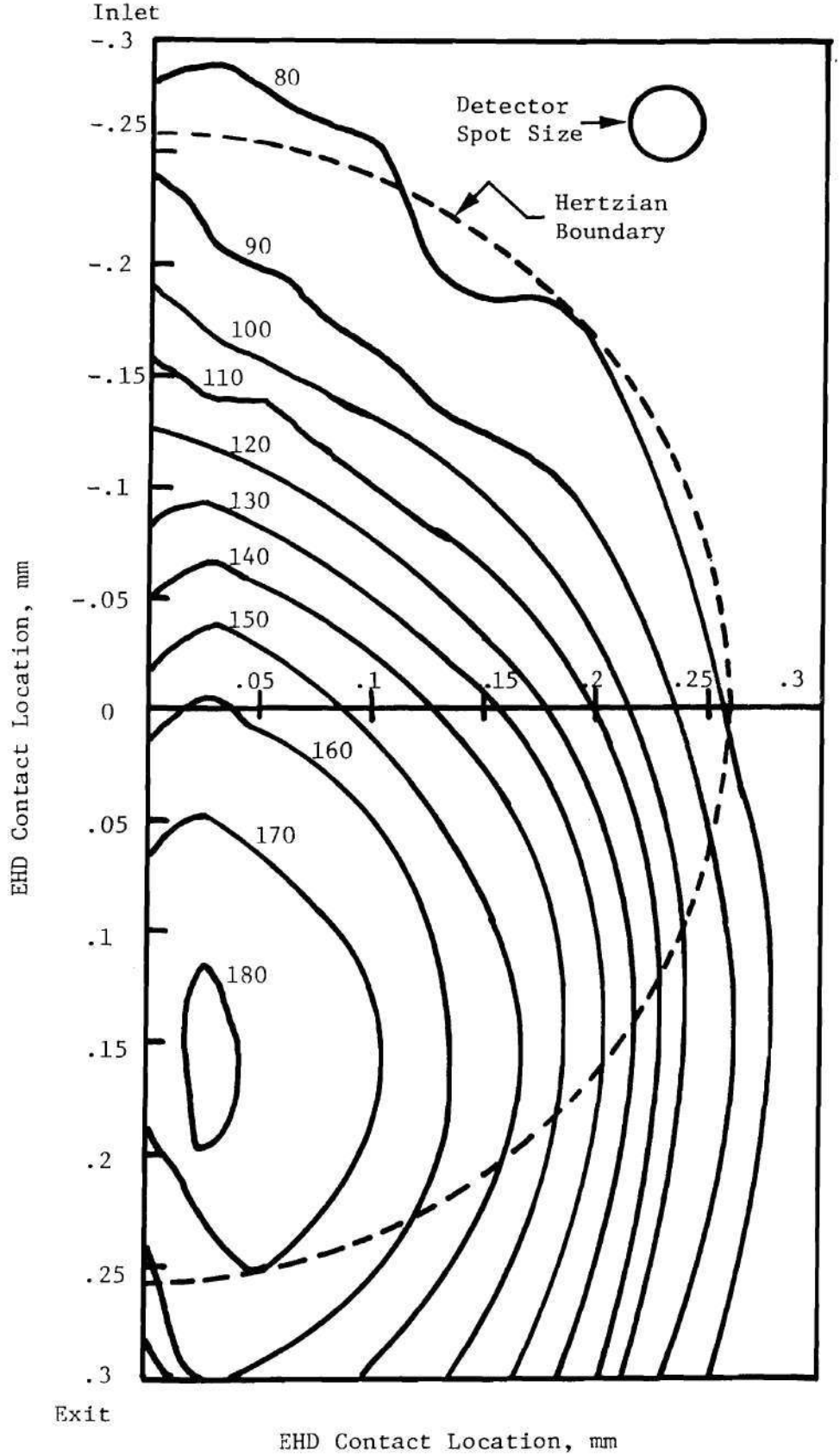

Figure 30. Ball Surface Temperature T_b (C) versus EHD Contact Location (Smooth ball: .011 µm R_a, P_H = 1.51 GPa, Fluid N1, T_{bath} = 40 C, V_b = 1.39 m/s, V_{sa} = 0).

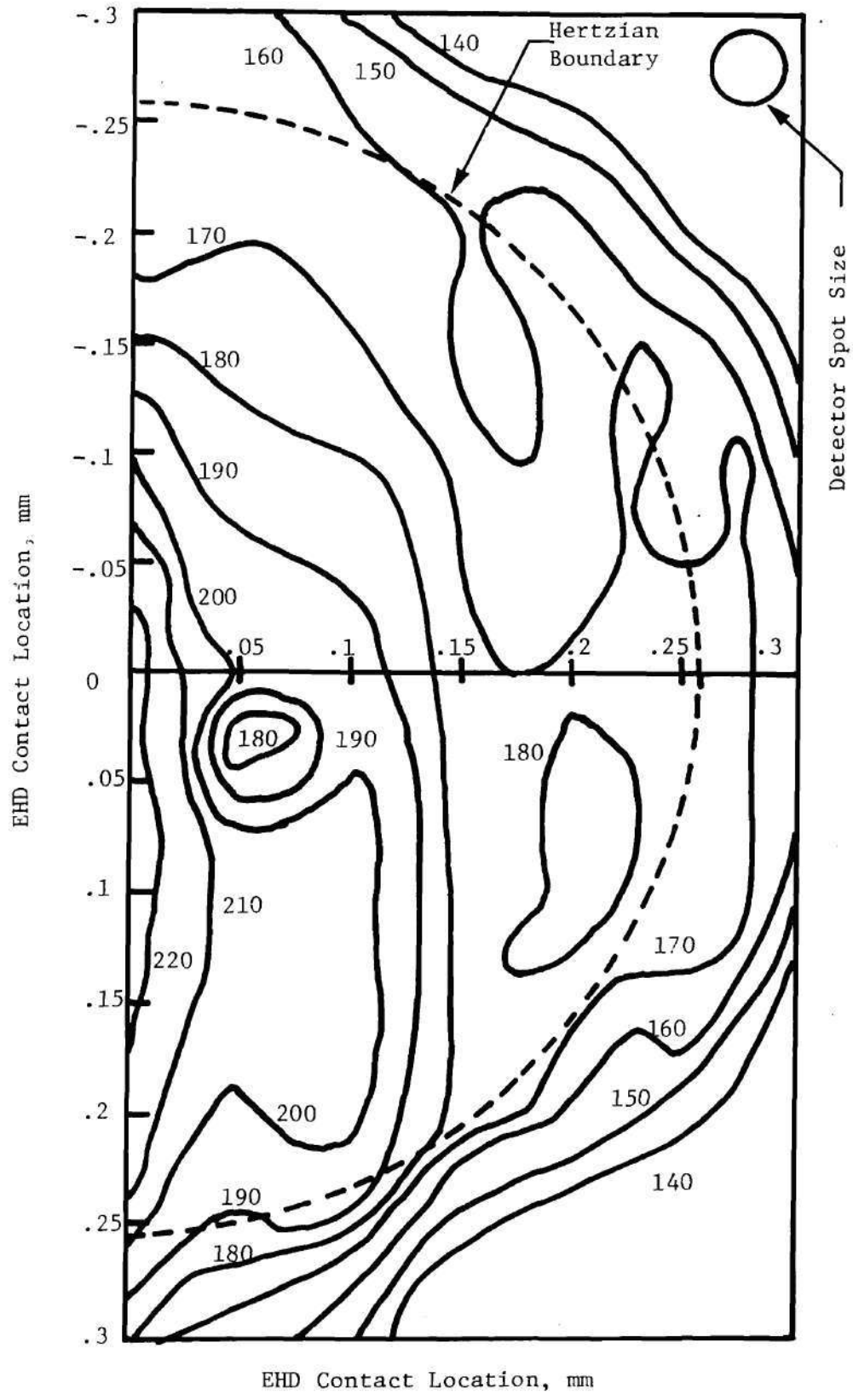

Figure 31. Fluid Temperature T_F (C) versus EHD Contact Location (Smooth ball: .011 μm R_a, P_H = 1.51 GPa, Fluid N1, T_{bath} = 40 C, V_b = 1.39 m/s, V_{sa} = 0)

Also, the position of the maximum fluid temperature is upstream of the position of the maximum ball surface temperature. Keeping in mind that the fluid film temperatures are essentially fourth power averages through the film. The observed shift in peak temperatures does not imply a violation of physical principles, since the fluid temperature gradients at the ball surface may change considerably with position along the centerline allowing a matching of ball and fluid temperature levels at the interface.

Figures 32 and 33 show respectively the ball surface and fluid temperatures along the centerline for a range of speeds. Results for both 67 N and 215 N are shown. The difference between the nature of the temperature distribution along the centerline for the two loads is attributable to different shapes of the film thickness profiles. The nearly constant film thickness at the 215 N load yields fluid temperatures, which like the ball surface temperatures in both cases, change smoothly along the centerline. The position of the maximum temperatures and the manner in which they vary can be clearly seen in these two figures. Since the fluid reservoir was maintained at 40 C, it is apparent that a significant amount of viscous heating in the contact inlet is occurring and the amount of dissipation increases with load.

The amount of inlet heating is clearly shown in Figures 34 and 35. Figure 34 shows ball surface temperature rise at the inlet boundary of the Hertzian contact zone as a function of sliding speed at two different Hertz pressures of 1.51 and 1.02 GPa. It is apparent that inlet heating is very important at all but very low speeds and small loads. An inlet

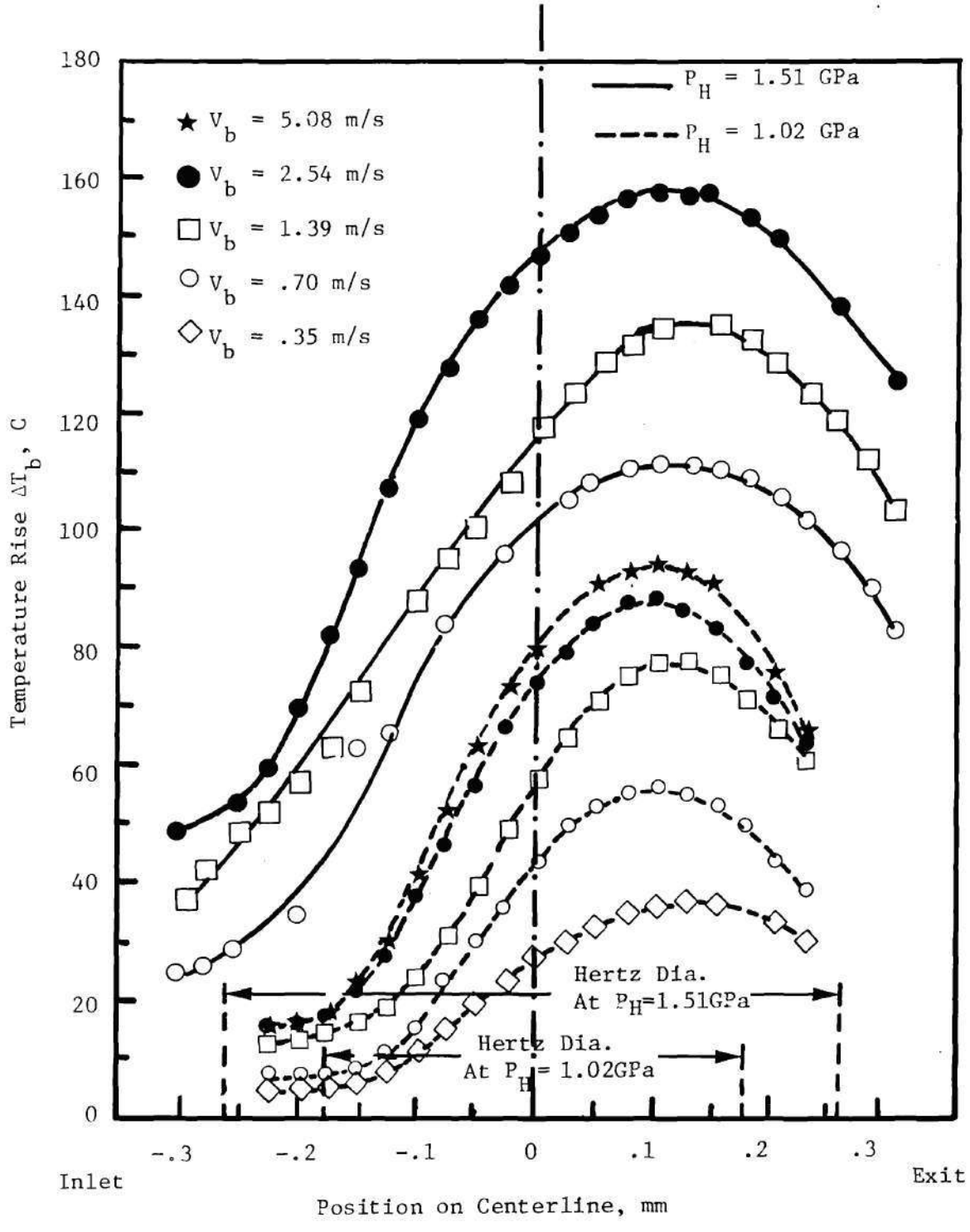

Figure 32. Ball Surface Temperature Rise Along Centerline versus Speed (Smooth ball: .011 μm R_a, Fluid N1, T_{bath} = 40 C, V_{sa} = 0).

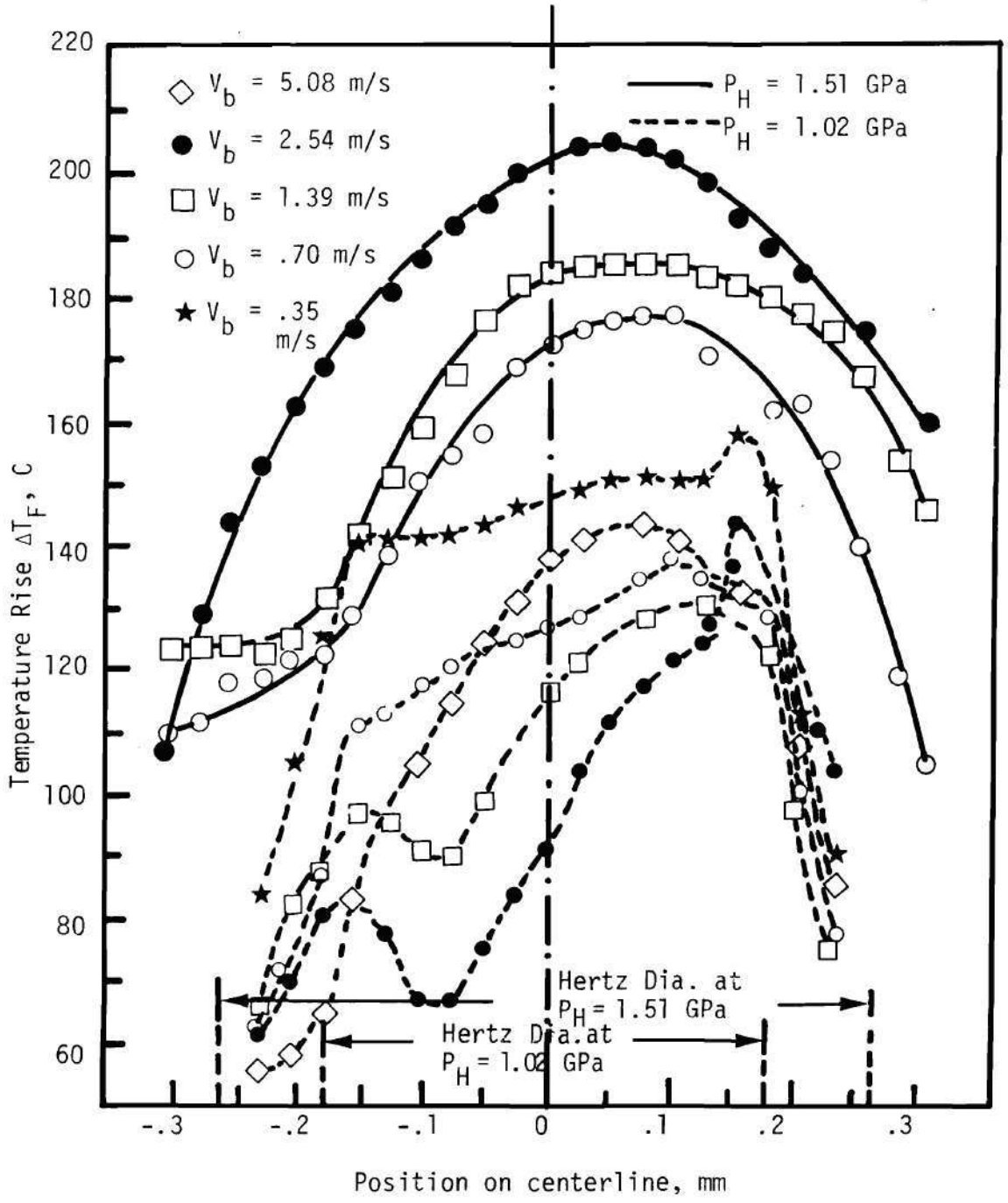

Figure 33. Fluid Temperature Rise along Centerline versus Speed (Smooth ball: .011 μm R_a, Fluid N1, T_{bath} = 40 C, V_{sa} = 0)

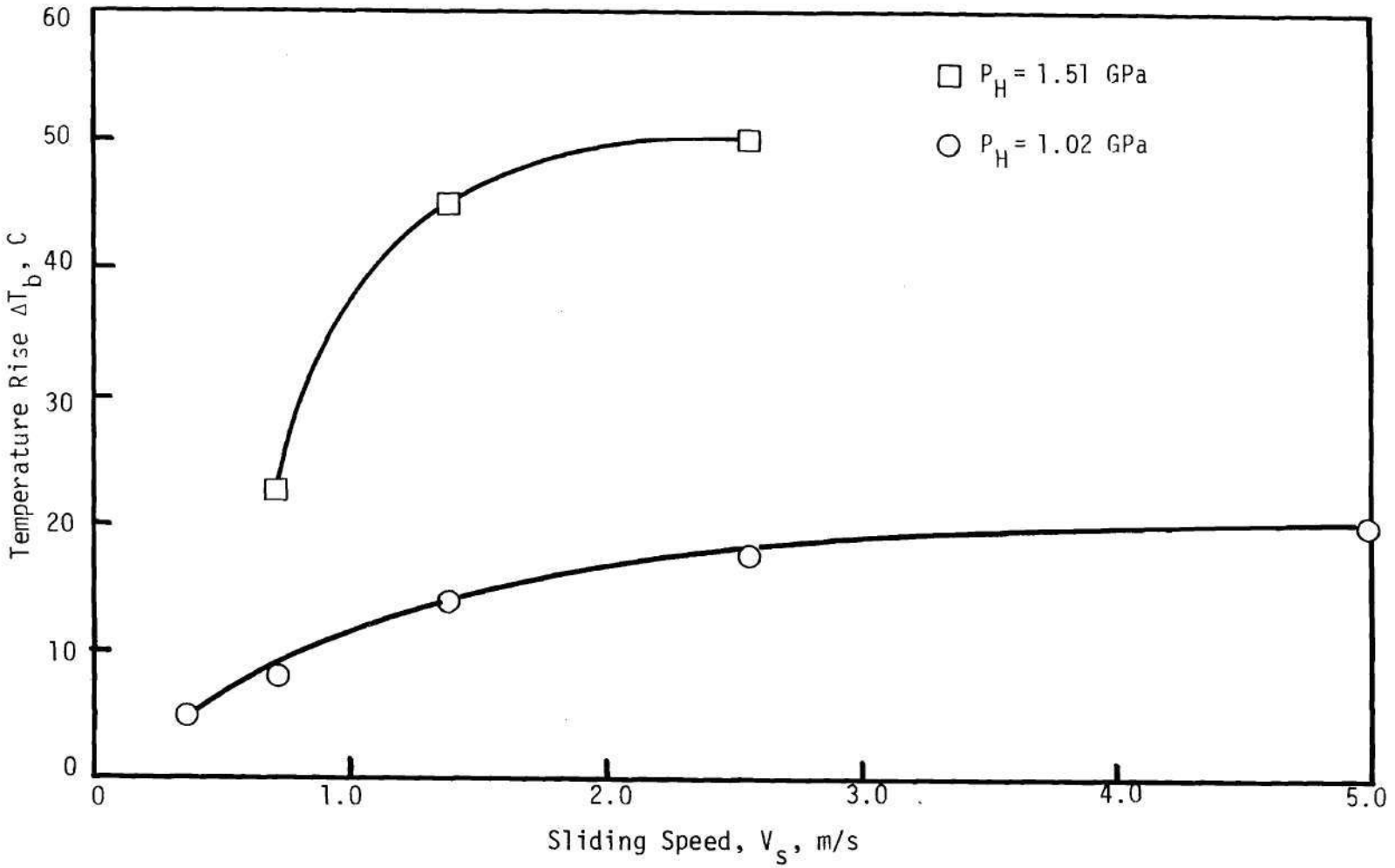

Figure 34. Ball Surface Temperature rise at Inlet Boundary of the Hertzian Region versus Sliding Speed (Smooth ball: .011 μm R_a, Fluid N1, T_{bath} = 40 C, V_{sa} = 0)

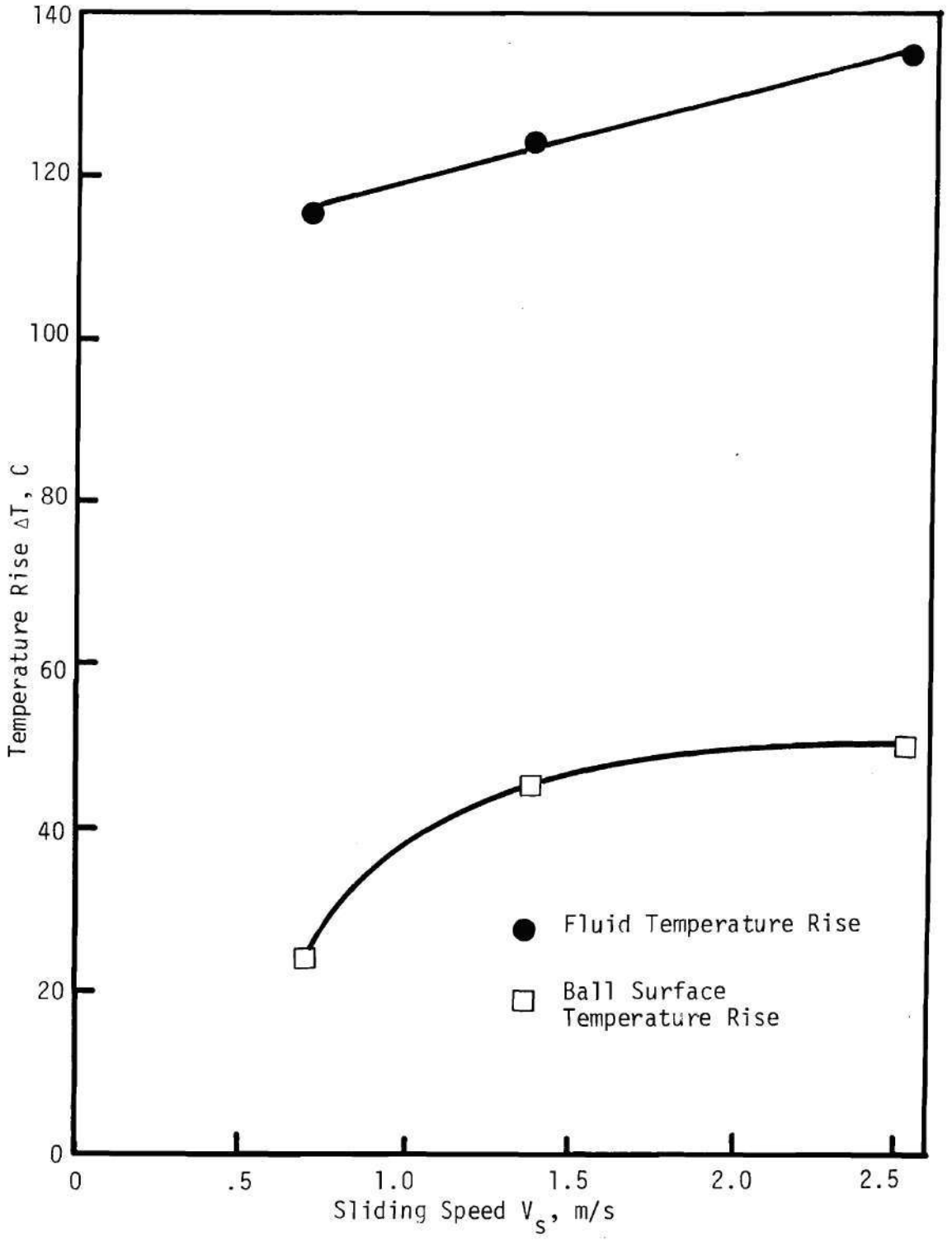

Figure 35. Temperature Rise (above Bath Temperature) at the Inlet Boundary of the Hertzian Contact, versus Sliding Speed (Smooth ball: .011 μm R_a, Fluid N1, P_H = 1.51 GPa, T_{bath} = 40 C, V_{sa} = 0).

surface temperature rise of 50 C at P_H equal to 1.51 GPa and V_s equal to 2.54 m/s, can considerably reduce the viscosity of the fluid in the inlet zone and so also the film thickness. The increase of temperature rise with increasing speed and load is due to increased shearing in the inlet zone. Figure 35 shows ball surface and fluid temperature rise at the inlet boundary of the Hertzian contact zone as a function of sliding speed at P_H = 1.51 GPa. The fluid temperature rise is about 70 to 80 C higher than the surface temperature rise. Since this temperature difference is maintained in an oil film .075 μm thick, very large temperature gradients through the film exist. These large temperature gradients in the film are required because the large amount of energy dissipated in the film has to be conducted away by the sapphire and ball surfaces.

Greenwood and Kauzlarich [127] have developed a model for inlet shear heating in elastohydrodynamic lubrication with which the excess of fluid temperature rise over the ball surface temperature rise at contact inlet boundary can be calculated. Even though this model is applicable for pure rolling only, they have suggested an expression for the case which includes sliding. When this expression is used for conditions referred to in Figure 35, the calculated temperature-excess is much lower than the experimental values. This apparent discrepancy can be explained as follows. The model assumes that the two surface temperatures are equal. This assumption is not valid for the case of simple sliding, where the stationary surface temperatures can be significantly higher than the moving surface temperature. Stationary surface temperatures are reported in the next section. Figure 54 in the next section indicates that the temperature rise for the stationary ball surface at the Hertzian inlet

boundary is 47 C for P_H = 1.02 GPa. Since the thermal properties of sapphire and ball are similar, a sapphire surface temperature rise at the Hertzian inlet boundary of 140 C can be expected for P_H = 1.51 GPa and V_s = 2.0 m/s. Referring now to Figure 35, fluid temperature rise (fourth power average through the thickness) of 130 C appears very reasonable. Therefore, the large fluid temperature rise in the inlet zone is due to high temperature of the stationary surface in the inlet region.

Figure 36 shows the ball surface and fluid temperature at the center of the contact as a function of sliding speed at P_H = 1.51 GPa. The uniform increase of temperatures is due to increasing dissipation in the oil film at increasing sliding speeds. The fluid temperature is typically 50 C higher than that of the ball surface.

The excess (averaged over the contact area) of fluid temperature over the ball surface temperature can be calculated by using the simple approach due to Archard [45]. It is assumed that conduction to the surfaces is the main mechanism of heat transfer. This assumption can be justified by calculating the heat convected away by the fluid.

For purposes of calculating the heat convected by the fluid, a linear velocity profile can be assumed. With $T_{F\,max}$ being the maximum temperature of the fluid (through the thickness), the rate at which heat is convected away by the fluid is

$$= 0 \left| \rho_F \cdot c_F \cdot \left(\frac{V_b}{2} \cdot 1 \cdot h\right) \cdot (T_{F\,max} - T_b) \right|$$

Heat conducted to the surfaces

$$= 0 \left| k_F \cdot 1 \cdot 2a \cdot \frac{(T_{F\,max} - T_b)}{h} \right|$$

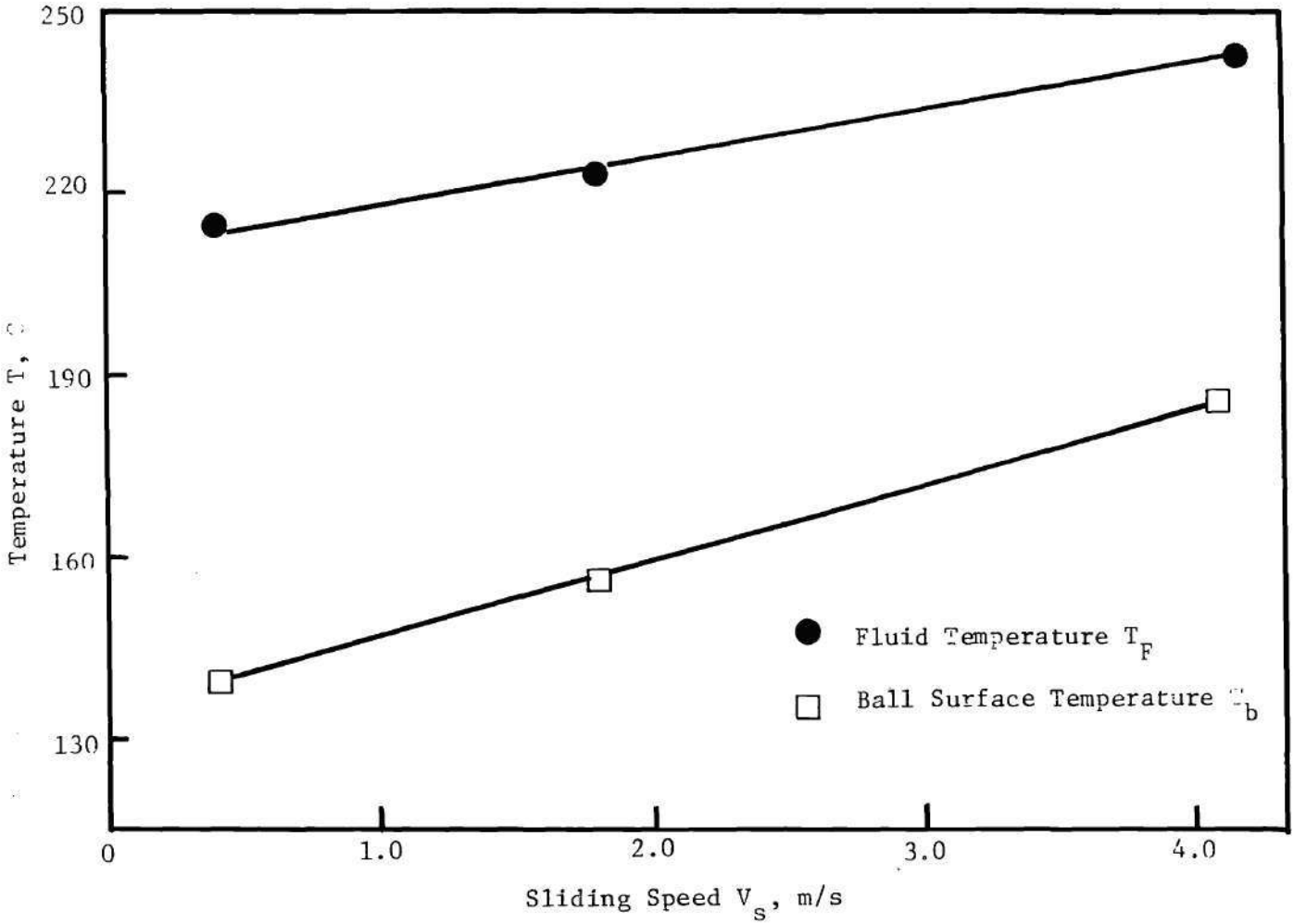

Figure 36. Temperature at Contact Center versus Sliding Speed (Smooth ball: .011 m R_a, Fluid N1, P_H = 1.51 GPa, T_{bath} = 40 C, V_{sa} = 0).

$$\frac{\text{Heat Conducted to Solids}}{\text{Heat Convected away by the lubricant}} = 0\left|\frac{k_F}{\rho_F c_F}\cdot\frac{2a}{\frac{V_b}{2}h^2}\right|$$

For a mineral oil, the above ratio comes out to be [9] approximately 120. Clearly, then, a reasonable assumption in elastohydrodynamic analysis is to assume that the heat produced by viscous dissipation is conducted directly to the solids. This assumption is further justified by the fact that the solid surfaces are nearly 200 times more conductive than the fluid.

With the assumption of conduction as the main mechanism of heat transfer in the film, it can be shown that (Jakobsen and Winer [33]), the shear stress across the fluid film is a constant, and therefore the rate of shear strain and also the rate of heat generation which determines the temperature distribution is inversely proportional to the viscosity. Since viscosity decreases dramatically with temperature, the rate of heat generation is a maximum in the plane (parallel to the flow direction) of highest temperature. The plane of maximum temperature is obviously the adiabatic plane. The adiabatic plane is assumed to be located at the fluid midplane. This has been found reasonable by many investigators [9,33,45,128,129] for small values of slip velocity. Further discussion on this assumption appears in the next section when both the solid surfaces are allowed to move. However, the value of the midplane temperature obtained from this assumption, will be higher than that for any other location of the adiabatic plane, since the value of the maximum temperature is not greatly influenced by the location of the adiabatic plane (Refer Jakobsen [33,130]).

Following Archard [45] and using the above assumptions, the steady state temperature-excess in the fluid midplane is given by

$$T_{F\,max} - T_b = \frac{\bar{q}\,h}{4k_F} \tag{39}$$

where,

$$\bar{q} = \frac{TC \cdot W \cdot V_s}{\pi a^2} \tag{40}$$

for a nominal sliding point contact problem. For the case of 215 N normal load (P_H = 1.51 GPa) at a sliding speed of 2.54 m/s with measured traction coefficient equal to .07, the calculated value of ($T_{F\,max} - T_b$) is 30 C. But, the measured value is 60 C. Similar discrepancies exist at other operating conditions.

An inherent assumption in the above calculation has been that the two surface temperatures are equal. The stationary surface temperature reported in the next section clearly shows that this assumption is not valid for simple sliding. Referring to Figure 54 (Chapter V), the stationary ball surface temperature can be significantly higher than that of the moving ball surface. Approximate calculation based on data of Figure 54 shows that the stationary sapphire temperature is 60 C higher than the moving ball surface temperature at a load of 215 N and a sliding velocity of 2.54 m/s. Under these conditions a measured excess fluid temperature of 60 C (fourth power average through the thickness) over the moving ball surface temperature appears very reasonable.

Archard [45] mentions that the pressure-viscosity effect (which makes the heat flux to peak at contact center) is a possible reason for

the discrepancy between the calculated and the measured values. This however is not true because discrepancies exist all over the contact region, where the pressures are not necessarily high.

Therefore, it can be concluded that any calculation used to predict the excess fluid temperature over the ball surface temperature must take into account the significant difference between the stationary and the moving surface temperatures.

Ball Surface Temperature Measurements and Correlations with Flash Temperature Theories

In order to understand the failure of elastohydrodynamic films and the behavior of the contact temperatures, it is necessary to examine the EHD contact under conditions which result in relatively thin films, i.e., films of the same thickness as the composite roughness of the bounding surfaces. Under such circumstances, the fluid may be locally discontinuous, resulting in ambiguous fluid temperature readings. Therefore, during this study, only the ball surface temperature was measured. In addition, for convenience, measurements were taken only at the center of the Hertzian contact. The temperature at the contact center is near the maximum and is, therefore, representative of the most severe conditions in the EHD contact.

In the following discussion, only temperature rise i.e. the ball surface temperature minus the bath temperature, is considered because of the reasons cited below. The local frictional energy dissipation gives rise to high temperature level in the vicinity of the contacting surfaces. The surface temperature attained consists of two parts. First, the overall

heat transfer characteristics of the system primarily influence the bulk temperatures. These bulk temperatures are representative of the fairly uniform level of those parts of the temperature fields in the rubbing bodies that do not lie too close to the conjunction zone. Second, during the passage of the surface under the heat source due to local frictional energy dissipation, the surface temperatures increase rapidly and these are referred to as flash temperatures. Several theories exist for predicting the flash temperatures of rubbing solids. In order to compare the experimentally measured ball surface temperatures with those predicted by flash temperature theory, the bulk temperature has to be subtracted from the experimental values. The oil bath temperature as measured by a thermocouple in the reservoir can be considered as the bulk temperature in the present case. The amount of time the ball surface is in contact with the oil bath is typically more than 500 times the thermal diffusion time of the material of the steel ball (defined as the time required for heat to penetrate one Hertzian radius below the surface) and therefore, the bulk temperature for the ball surface should be fairly close to the oil bath temperature. In fact, through his approach of thermal network theory, Blok [42] has calculated the bulk temperature for an example case of a gear transmission system and has found that the calculated bulk temperature is close to the oil bath temperature within 2 C. However, in some contact systems where the surface heat transfer is not as effective as in the present system, the appropriate bulk temperature can be significantly higher than the oil bath temperature. This complicates the system flash temperature calculation considerably, since bulk temperature is hard to estimate.

Figure 37 shows a plot of the ball surface temperature rise at the contact center above the bath temperature, as a function of sliding velocity for peak Hertz pressures ranging from 0.52 to 2.03 GPa. For a given Hertz pressure, the data plotted on log-log coordinates falls on one straight line for velocities up to a break-point value and then on another line, of lower slope, for higher velocities. The data of Figure 37 has been replotted at selected velocities as a function of Hertz pressure in Figure 38. The temperature rise is the difference between the ball surface temperature at the contact center and the lubricant bath temperature as measured with a thermocouple. Figure 38 shows that except for the combined conditions of relatively high velocity and Hertz pressure, the data for a given speed follows a power law model with an exponent on Hertz pressure of approximately 2.

The trends shown in Figures 37 and 38 can be predicted using the techniques of Blok [42], Jaeger [44], and Archard [45]. The energy dissipation rate in the contact is equal to the product $(W \cdot TC \cdot V_s)$. The heat flux to each surface is then proportional to the dissipation rate divided by the area of the contact, or

$$\bar{q} \propto \frac{W \cdot TC \cdot V_s}{\pi a^2} \propto TC \cdot P_H \cdot V_s \qquad (41)$$

where the constant of proportionality includes the portion of the total heat flux transferred to the ball.

According to Jaeger [44] and Archard [45] the temperature rise on the surface of a solid moving at velocity V_b and subjected to heat flux $\bar{q}$ can also be described in terms of a non-dimensional parameter

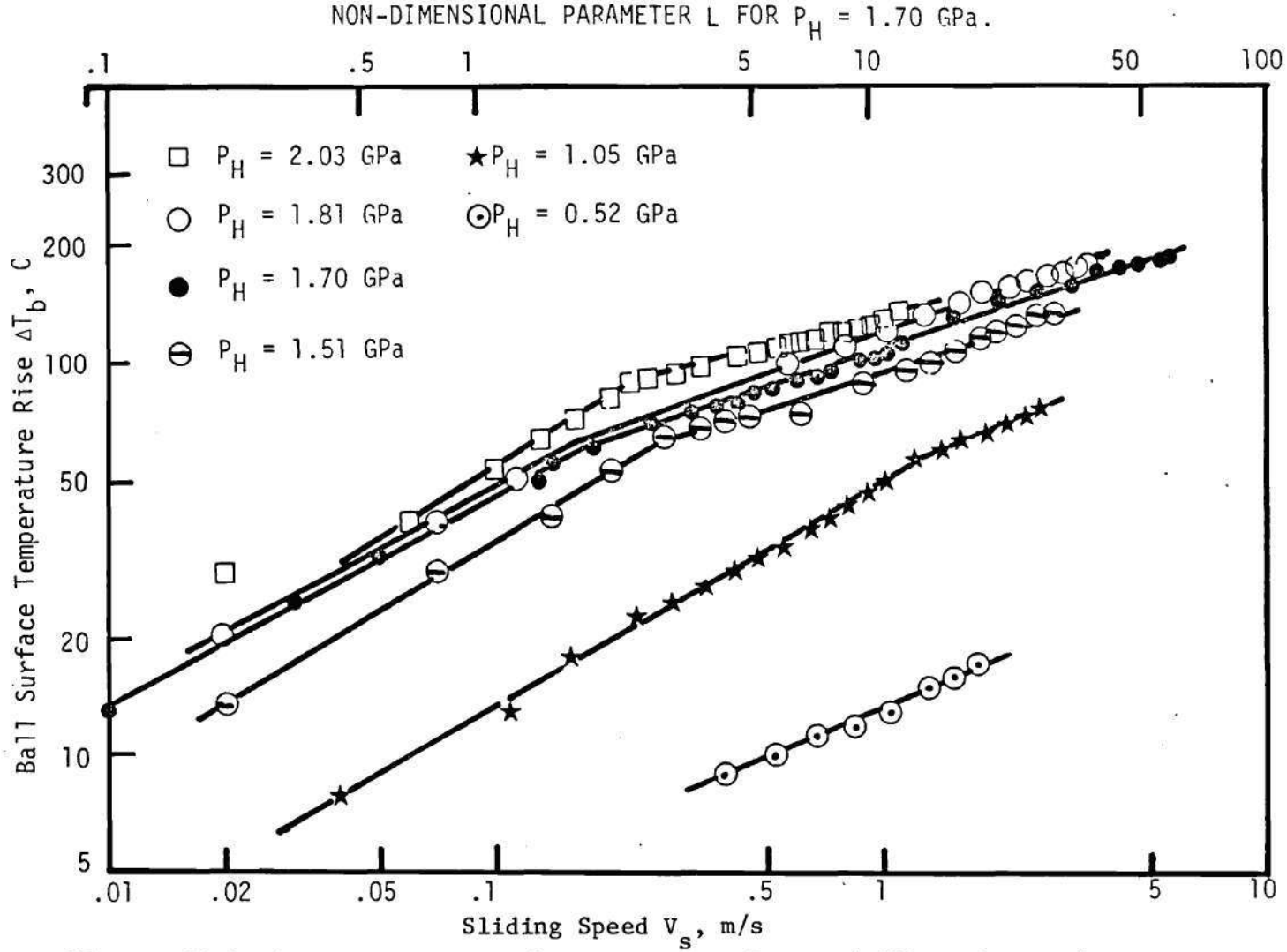

Figure 37. Ball Surface Temperature Rise at Contact Center (.011 μm Ra roughness, $1 < \Lambda < 2$ for P_H = 2.03 GPa, otherwise $\Lambda > 2$).

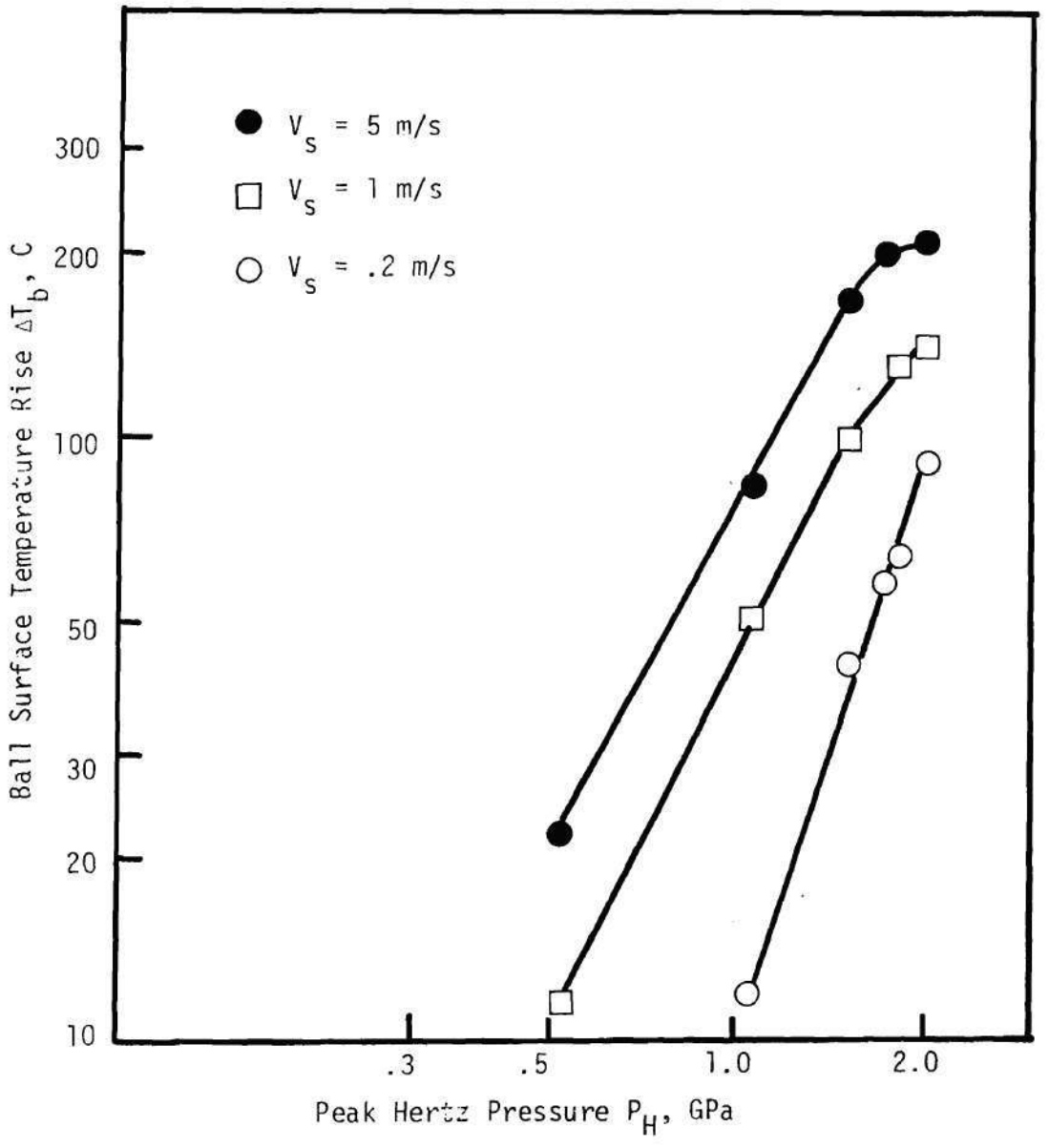

Figure 38. Ball Surface Temperature Rise at Contact Center versus Peak Hertz Pressure (Smooth ball: .011 μm R_a, Fluid N1, T_{bath} = 40 C, V_{sa} = 0) ($1 < \Lambda < 2$ for P_H = 2.03 GPa only, otherwise $\Lambda > 2$).

$L = t_1/t_2$ (2L is called Peclet number by many authors). The term $t_1 = a^2/2\alpha_b$ represents the time required for the effect of $\bar{q}$ to penetrate a distance a below the surface, whereas $t_2 = a/V_b$ represents the time required for a point in the contact to move a distance a. Therefore, for a given fluid and ball, L is proportional to $(P_H \cdot V_b)$. The variation in ΔT_b (ball surface temperature at the center - bulk oil temperature) is given as (for simple sliding $V_b = V_s$)

$$\Delta T_b \propto TC \cdot P_H \cdot L \quad \text{for} \quad L < 0.1 \tag{42}$$

and

$$\Delta T_b \propto TC \cdot P_H \cdot L^{1/2} \quad \text{for } L > 5 \tag{43}$$

or that

$$\Delta T_b \propto TC \cdot P_H^2 \cdot V_b \quad \text{for } L < 0.1 \tag{44}$$

and

$$\Delta T_b \propto TC \cdot P_H^{3/2} \cdot V_b^{1/2} \quad \text{for } L > 5 \tag{45}$$

The parameter L has been plotted in Figure 37 for the case of $P_H = 1.70$ GPa. The values 0.1 and 5 represent points for which the full solution is in good agreement with the limiting cases of equation (44) (stationary heat source solution) and equation (45) (fast moving heat source solution) respectively.

In order to determine how well the data fits the Jaeger-Archard predictions of equations (44) and (45), a multiple regression analysis

of the data shown in Figure 37 was performed. For each Hertz pressure level, the data were divided into two regions separated by a break-point velocity. This break-point velocity is a function of Hertz pressure and can be described by

$$V_{BP} = .53\ P_H^{-1} \tag{46}$$

with a correlation coefficient r = .95. This corresponds to a value of L equal to 3.4 at the break point, which compares reasonably well with the theoretical break point value of 1·0 [45]. The apparent discrepancy between the theoretical and experimental values of L at the break point is perhaps due to the unavailability of data for very small values of L. For sliding velocities below V_{BP},

$$\Delta T_b = 46.99\ P_H^{2.02} V_b^{0.53} \tag{47}$$

with $r^2 = .978$. For velocities above V_{BP},

$$\Delta T_b = 53.52\ P_H^{1.34} V_b^{0.34} \tag{48}$$

with $r^2 = .985$. In terms of normal load, equations (47) and (48) may be approximated by

$$\Delta T_b = 3W^{2/3} V_b^{1/2} \quad \text{for} \quad V_b \leq V_{BP} \tag{49}$$

and

$$\Delta T_b = 8.5W^{4/9} V_b^{1/3} \quad \text{for} \quad V_b \geq V_{BP} \tag{50}$$

These relations were obtained assuming a constant traction coefficient. However, from equations (41), (44) and (45) it is apparent that the influence of change in traction coefficient must be included. Based on data available elsewhere [79,131], the traction coefficient has only a slight positive dependence on P_H in the pressure ranges studied. Furthermore, the traction coefficient was found to be dependent on sliding velocity to the power -0.29 with r = .994. The traction data used were for $3 \leq L \leq 22$. Including this dependence in equations (47) and (48) results in

$$\Delta T_b \propto P_H^{2.02} V_b^{.82} V_b^{-.29} \propto P_H^{2.02} V_b^{.82} \cdot TC \qquad (51)$$

and

$$\Delta T_b \propto P_H^{1.34} V_b^{.63} V_b^{-.29} \propto P_H^{1.34} V_b^{.63} \cdot TC \qquad (52)$$

Recalling that equations (44) and (45) represent limiting cases, the experimental results appear to be in good agreement with the predicted trends (equations (44) and (45)).

In addition to a comparison of trends with P_H and V_b, a comparison of ball surface temperatures, calculated using the method outlined by Archard [45], and the experimental results has been made and the results are summarized in Table 4 and Figure 39. The measured values are either the temperature at the contact center, when only those temperatures were recorded, or the average of the temperatures in the Hertzian contact area. Table 4 shows these temperatures as functions of peak Hertz pressure and sliding velocity.

Table 4. Summary of Comparison of Measured Temperatures and Those Predicted by the Blok-Jaeger-Archard Theory for the Smooth Ball (0.011 μm R_a)

P_H (GPa)	V_s (m/s)	Traction Coefficient	Avg. Calculated Temperature (°C)	Measured Center Temperature (°C)	Avg. Measured Temperature (°C)
2.03	1.0	0.07*	158	172	-
1.81	1.0	0.07*	137	167	-
1.70	0.05	0.07*	40	60	-
	1.0	0.07*	129	154	-
	2.54	0.07*	198	202	-
1.51	0.70	0.07	98	124	109
	1.0	0.07*	111	136	-
	1.39	0.07	128	147	131
	2.54	0.06	156	175	156
1.05	0.35	0.16	77	65	58
	0.70	0.13	98	81	68
	1.39	0.07	92	100	81
	2.54	0.06	101	118	90
	5.08	0.04	104	120	93

*Assumed value based on similar conditions

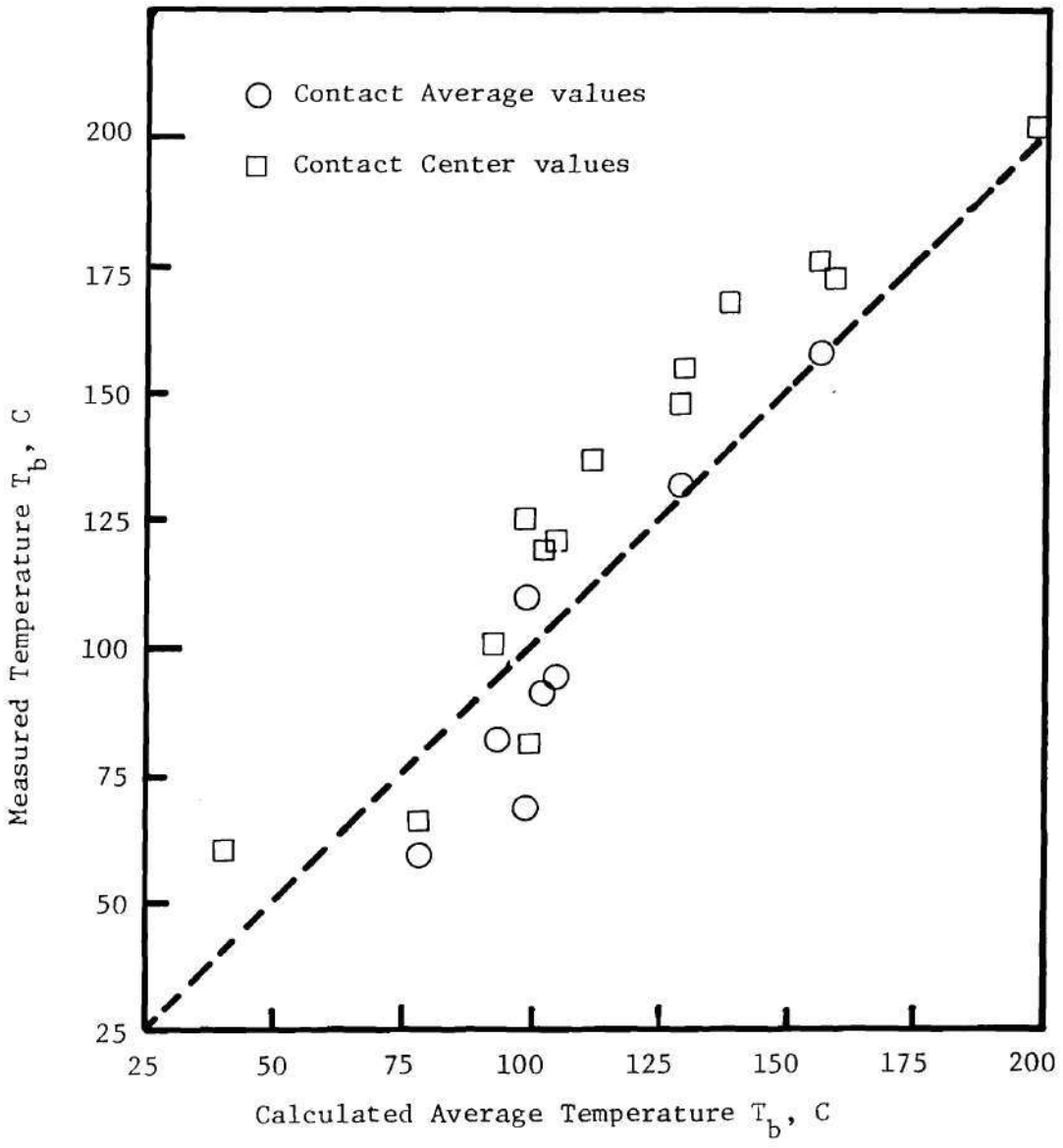

Figure 39. Comparison of the Average Contact Temperatures Calculated using the Blok-Jaeger-Archard Theory and the Measured Temperatures (Smooth ball: .011 μm R_a, Fluid N1, V_{sa} = 0).

It should be noted that the calculated temperatures were obtained by adding the bath temperature, as measured with a thermocouple, to the calculated temperature rise. The measured values, however, whether the centerline or contact average temperatures, are the values which result directly from the experimental data reduction for the cases where traction measurements were made. The measured values should be somewhat higher than the calculated values since both the lubricant and surface temperatures just outside the EHD contact are significantly higher than the bath oil temperature due to conduction and inlet heating.

Because it considers conduction as the only heat transfer mechanism, the flash temperature theory should best agree with experimental results at high pressures [132,133]. In these cases, the ratio of contact length to film thickness is the greatest thereby making conduction more significant. This trend is supported by the data for $P_H = 1.51$ GPa and 1.05 GPa, in which contact average measured temperatures have been determined. The average deviation between calculated and measured temperatures was 4.8% for the 1.51 GPa data and 17% for the 1.05 GPa data.

B. Results for Combined Rolling and Sliding

A number of devices in which Hertzian contact conditions occur, have relatively small amounts of slip or none at all. Experimental results reported in the previous section have large amounts of sliding. The results presented in this section are primarily concerned with the influence of slip on lubricant film thickness, traction and ball surface temperature.

Very often a combination of rolling and sliding in kinematically described by a parameter referred to as the slide-roll ratio and denoted by Σ. Σ is the ratio of the slip speed (difference between the surface velocities) to the rolling speed (average or one-half the sum of the two surface velocities). Thus, Σ is given by $(V_b - V_{sa})/\frac{1}{2}(V_b + V_{sa})$. Σ can vary between $-\infty$ and $+\infty$. The value of Σ equal to 0 corresponds to conditions of pure rolling, when the two surfaces are moving at the same speed in the same direction. Values of Σ equal to ± 2 correspond to the cases when one of the surfaces is moving and the other stationary. Σ equals $\pm\infty$ refer to conditions where the rolling component is zero, when the two surfaces move at the same speed but in opposite directions. The range of practical interest is however, Σ equal to -2 to +2, and only this range is investigated in the present work. Even though incorrect, many investigators refer to Σ equal to ± 2 as pure sliding, and the reader is to be cautioned about this misuse. Instead, Σ equal to ± 2 is referred to as simple sliding in this work.

All the results reported in this section were obtained using the combined rolling and sliding EHD simulator described in Chapter II. The dichromatic optical interference technique was used for the determination of film thickness. Traction and ball surface temperature were measured using the techniques described in Chapters II and III. By independently measuring the ball surface and sapphire speeds, and knowing the track radius on the sapphire disk, the slide-roll ratio is easily computed for each experiment.

Table 5 is a summary of the film thickness and traction experiments. Rolling velocity, slide-roll ratio and peak Hertz pressure were all varied. In all cases, the smooth ball (.011 μm R_a) was used.

Table 5. Summary of Rolling Experiments: Film Thickness and Traction

(Smooth ball: .011 μm R_a, Fluid N1)

$\bar{V}$	Σ	V_s	P_H	T_{BATH}	h_c	h_m	TC
m/s	-	m/s	GPa	°C	μm	μm	--
0.5	2.00	1.00	0.81	34	.18	.076	.061
"	0.60	0.30	"	37	"	"	.056
"	0.40	0.20	"	38	"	"	.055
"	0.20	0.10	"	38	"	"	.050
"	0.00	0.00	"	39	"	"	.017
"	-.20	-.10	"	38	"	"	--
"	-.40	-.44	"	40	"	"	--
"	-.88	-.44	"	41	"	"	--
0.75	2.00	1.50	"	39	.19	.089	.058
"	1.20	0.90	"	"	.20	"	.058
"	0.67	0.50	"	"	.20	"	.055
"	0.13	0.10	"	"	.22	"	.049
"	0.00	0.00	"	38	.22	"	.024
"	2.00	1.50	0.66	33	.22	.15	.051
"	1.20	0.90	"	34	.24	.18	.051
"	0.67	0.50	"	34	"	"	.051
"	0.19	0.14	"	35	"	"	.051
"	0.00	0.00	"	"	"	"	.014
"	-.10	-.08	"	"	"	"	.041
"	2.00	1.50	1.02	40	.15	.064	.061
"	.27	-.20	"	38	.18	.076	.059
"	0.00	0.00	"	37	.22	"	.020
"	-.27	-.20	"	"	.17	"	.057
0.51	0.00	0.00	"	"	.18	"	.020
0.72	0.00	0.00	"	"	.22	"	.023
1.00	0.00	0.00	"	"	.24	.127	.023
1.25	0.00	0.00	"	"	.28	.178	.027

Photomicrographs of the optical interference fringes for one set of operating conditions are shown in Figure 40. Figure 40 contains data for slide-roll ratio ranging from -.10 to 2.00. It can be seen from Figure 40 that the film thickness at contact center is essentially constant over the entire range of slide-roll ratio. Photomicrographs similar to the ones shown in Figure 40 were taken for other operating conditions also. A map of film thickness over the entire contact region can be prepared using these pictures. However, only minimum film thickness and center film thickness values were recorded. By noting the color of the fringe appearing at the desired location and referring to the calibration chart for the dichromatic fringe system (Figure 9), the film thickness values were directly determined.

Film thickness and traction have been plotted as a function of Σ in Figures 41 and 42 respectively. The effect of the slide/roll ratio on film thickness is small. In fact, both the minimum and center film thickness depend on sliding velocity to a power in the range 0 to -0.09 depending on the Hertz pressure and rolling velocity. It is apparent from Figure 42 that the peak normally obtained in TC vs. Σ experiments in line contacts is not present here. Wedeven's traction data for point contacts [78] also lacks such a peak.

The influence of rolling velocity on film thickness and traction under conditions of zero slip is shown in Figure 43. A regression analysis of the data for P_H = 1.02 GPa and Σ = 0 results in

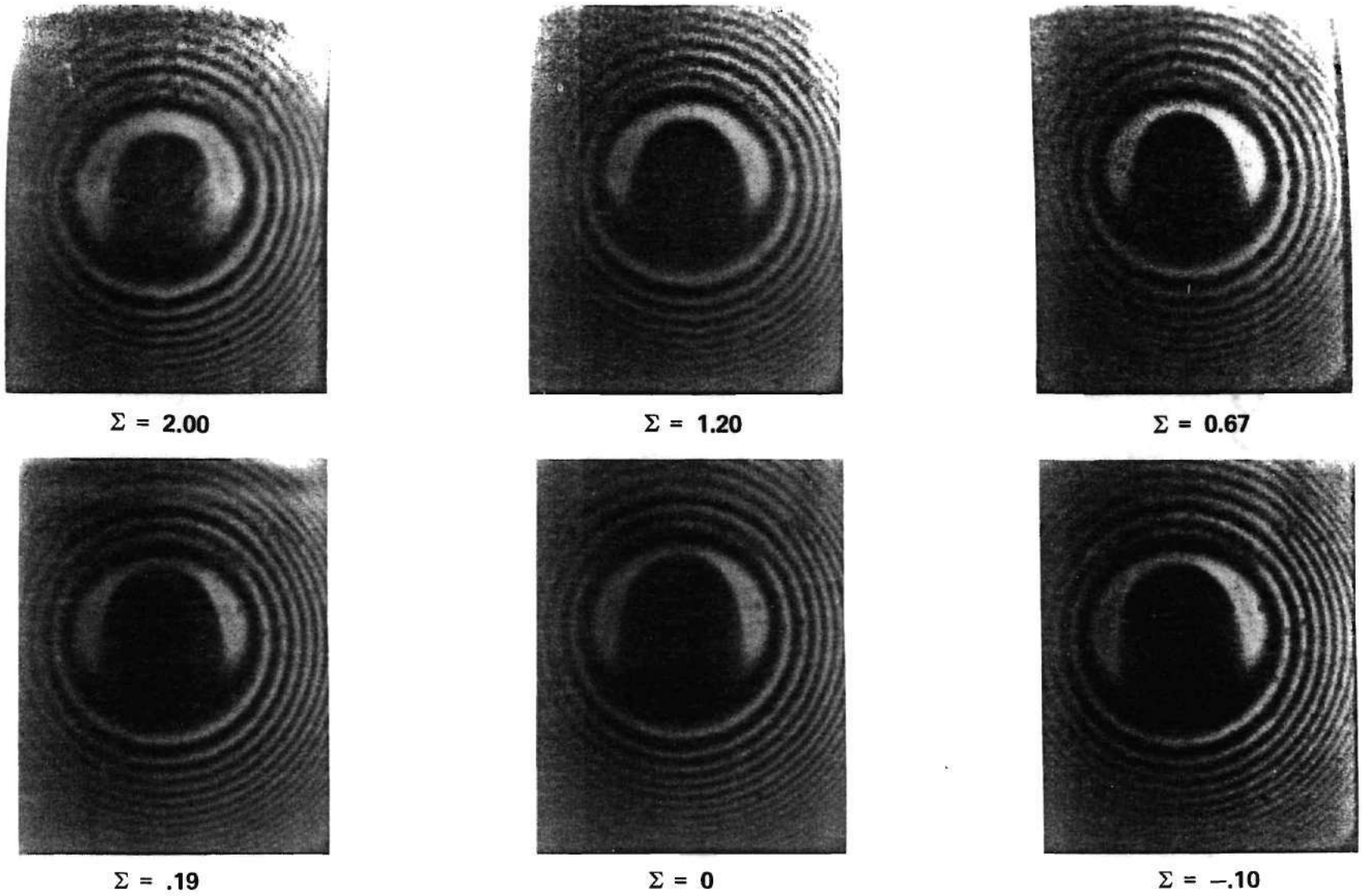

Figure 40. Photomicrographs of optical interference fringes representing film thickness (Smooth ball ⇒ .011 μm R_a, Fluid N1, P_H= .66 GPa, $\bar{V}$ = .75 m/s).

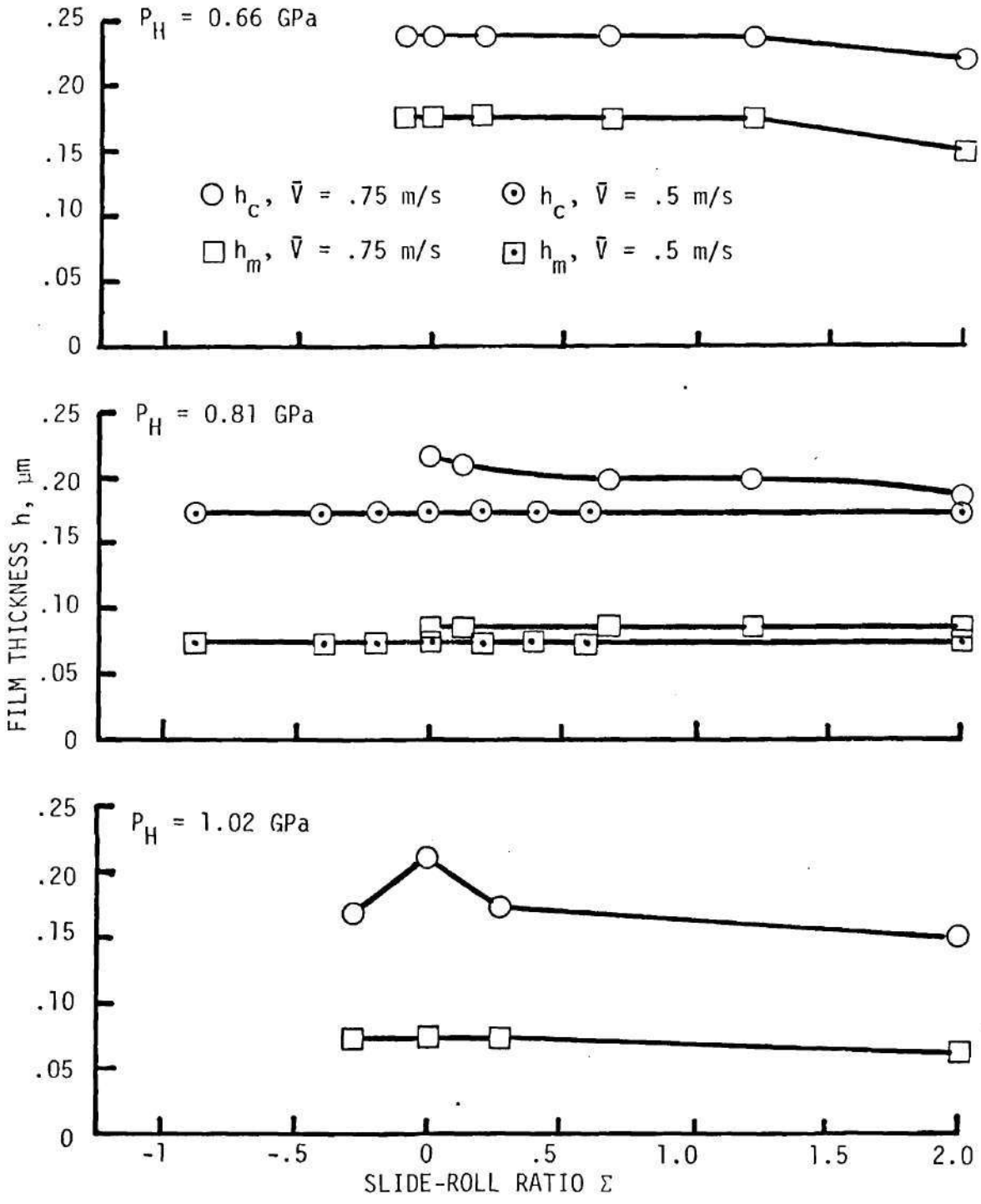

Figure 41. Film Thickness as a Function of Slide-Roll Ratio (.011 μm R_a roughness).

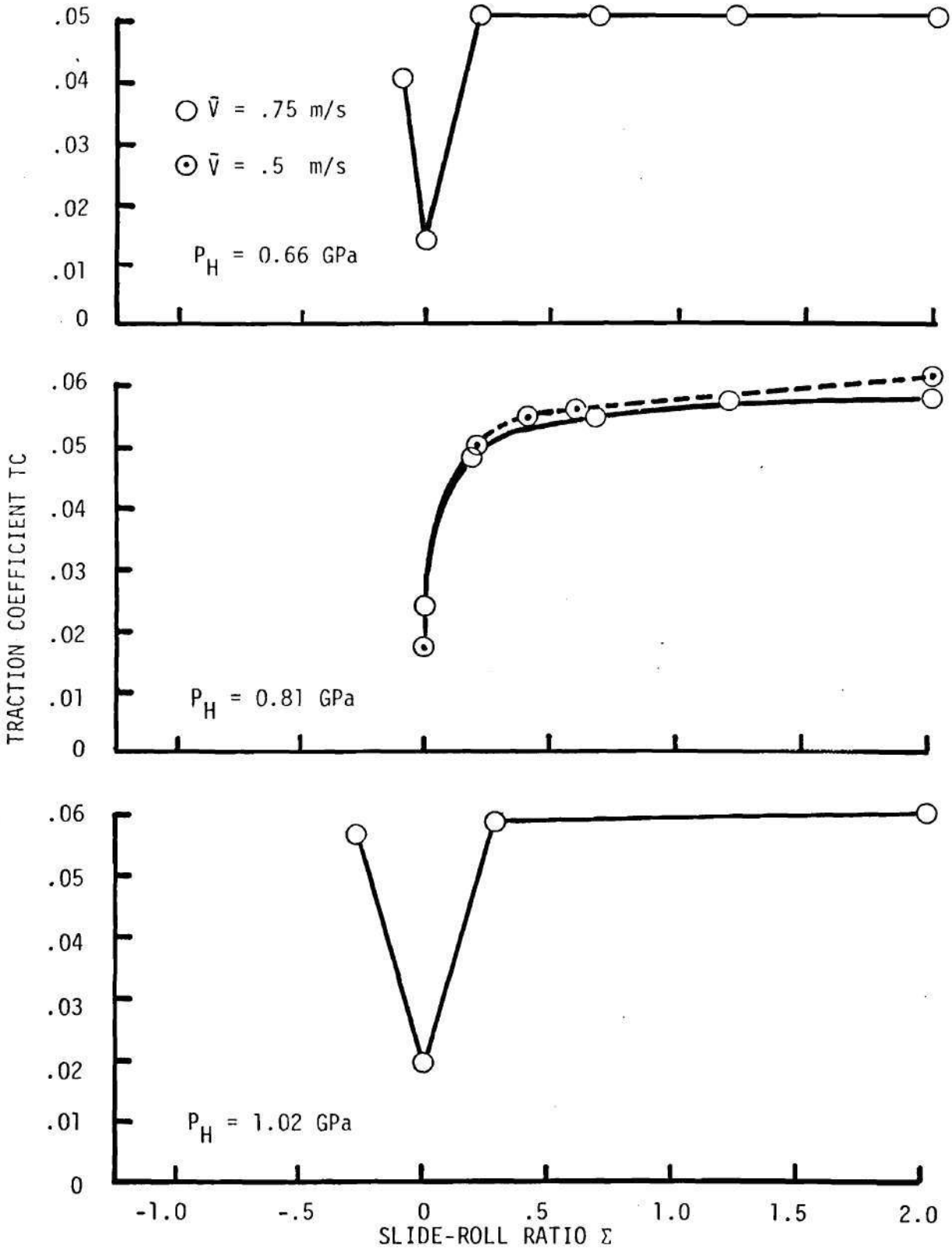

Figure 42. Traction Coefficient as a Function of Slide-Roll Ratio (.011 μm R_a roughness).

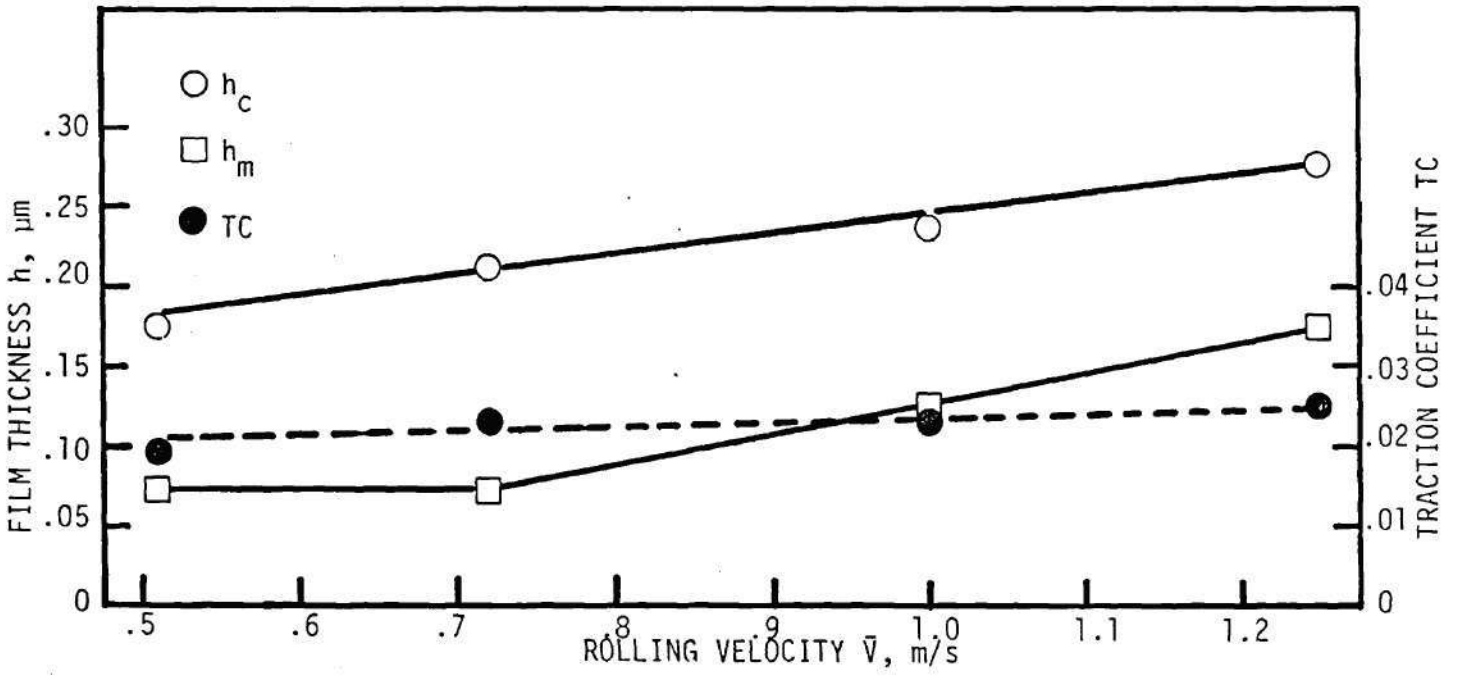

Figure 43. Film Thickness and Traction Coefficient as a Function of Rolling Velocity (Σ = 0, .011 μm R_a Roughness, P_H = 1.02 GPa).

$$h_c = 0.25\ \bar{V}^{.48}\ ,\quad r = .99 \tag{53}$$

$$h_m = .13\ \bar{V}^{.99}\ ,\quad r = .93 \tag{54}$$

$$TC = .024\ \bar{V}^{.29}\ ,\quad r = .93 \tag{55}$$

Table 6 shows the results of the ball surface temperature measurements. Because of small changes in the lubricant bath temperature during the course of the experiments, the temperature rise $\Delta T(\Delta T = T_b - T_{bath})$ has been tabulated instead of the absolute temperature of the surface. Also, due to the relatively low infrared detector signal level under conditions of small amounts of sliding, only the more severe conditions of those listed in Table 5 were used in the temperature measurement experiments. However, these conditions are closer to those found in normal practice.

The data from Table 6 has also been plotted and is shown in Figures 44 - 46. Figures 44 and 45 show the dependence of temperature rise on slide-roll ratio Σ for rolling velocities of 0.75 and 1.00 m/s respectively. A linear regression analysis of the maximum temperature rise data for both the rolling velocities resulted in

$$\Delta T_b = 30.3\Sigma + 1.2,\quad °C \tag{56}$$

with a correlation coefficient of 0.99.

Figure 46 shows the temperature rise as a function of rolling velocity for the case of pure rolling ($\Sigma = 0$). The data fit the straight line

Table 6. Summary of Rolling Experiments: Ball Surface Temperature Rises

(Smooth ball: .011 μm R_a, P_H = 1.02 GPa, Fluid N1)

$\bar{V}$	Σ	V_s	V_b	V_{sa}	T_{BATH}	CENTER ΔT_b	MAX. ΔT_b
m/s		m/s	m/s	m/s	°C	°C	°C
0.75	2.00	1.50	1.50	0.00	42	54	64
0.75	1.20	0.90	1.20	0.30	42	35	36
0.75	0.99	0.74	1.12	0.38	43	26	26
0.75	0.56	0.42	0.95	0.54	42	14.5	15
0.75	0.27	0.20	0.85	0.65	40	6	6
0.75	0.13	0.10	0.80	0.70	41	4.5	4.5
0.75	0.00	0.00	0.75	0.75	41	4	4
1.00	2.00	2.00	2.00	0.00	44	53	62.5
1.00	1.50	1.50	1.75	0.25	45	42	46.5
1.00	1.30	1.30	1.65	0.35	45	37.5	39
1.00	1.04	1.04	1.52	0.48	44	36	37.5
1.00	0.60	0.60	1.30	0.70	43	21	21.5
1.00	0.40	0.40	1.20	0.80	43	10.5	10.5
1.00	0.12	0.12	1.06	0.94	42	6	6
1.00	0.00	0.00	1.00	1.00	41	5	5
0.50	0.00	0.00	0.50	0.50	41	2	2
1.25	0.00	0.00	1.25	1.25	41	7	7
0.75	-2.00	-1.50	0.00	1.50	28	76	76
0.75	-1.28	-0.96	0.27	1.23	39.5	32	36.5
0.75	-0.80	-0.60	0.45	1.05	38.5	22.5	25
0.75	-0.45	-0.34	0.58	0.92	38	14.5	15
0.75	-0.27	-0.20	0.65	0.85	39	14	14
1.00	-2.00	-2.00	0.00	2.00	26	89	89
1.00	-1.52	-1.52	0.24	1.76	39.5	45	49.5
1.00	-0.90	-0.90	0.55	1.45	34	27.5	31
1.00	-0.40	-0.40	0.80	1.20	38.5	18	19.5
1.00	-0.12	-0.12	0.94	1.06	37.5	10.5	11

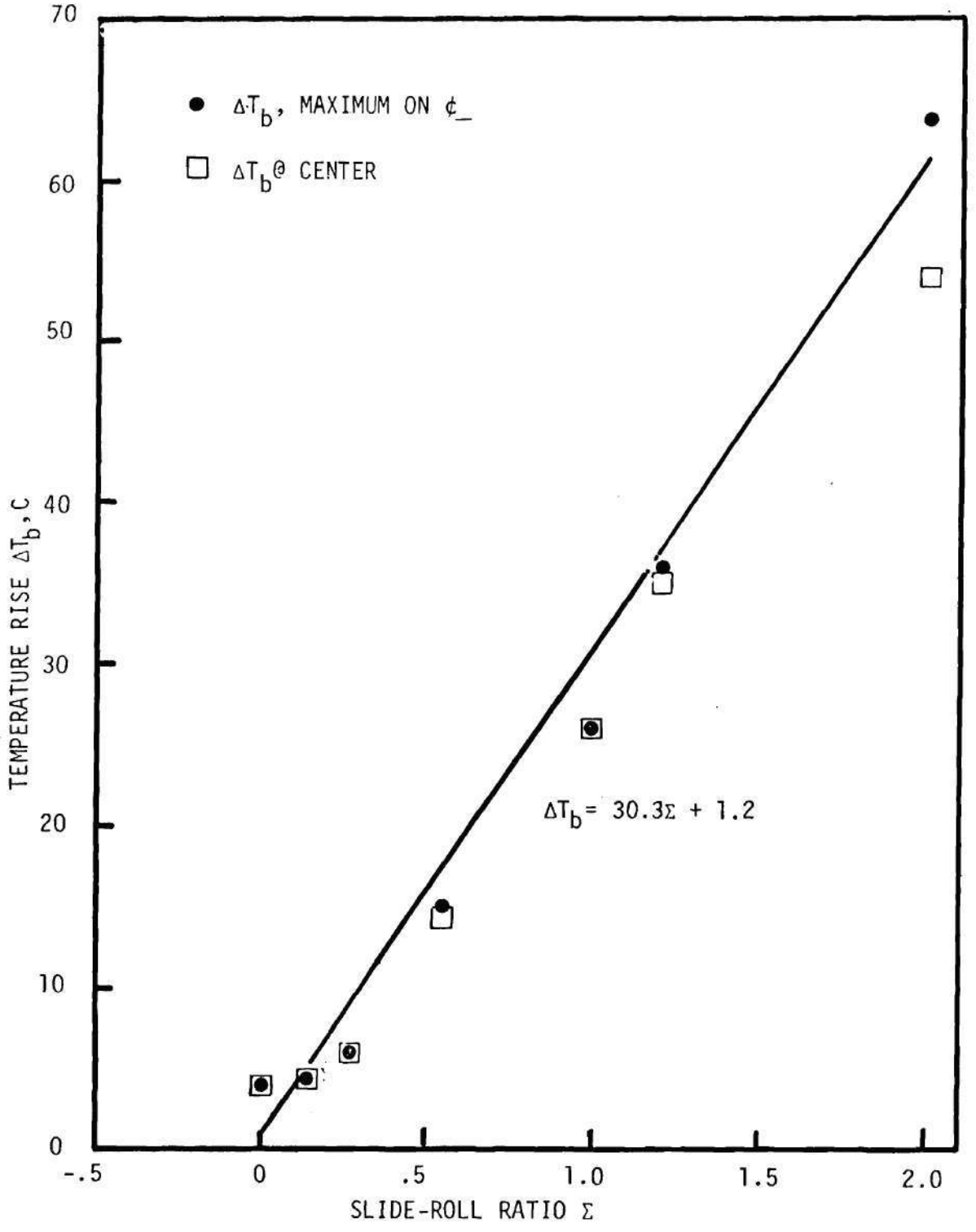

Figure 44. Ball Surface Temperature Rise as a Function of Slide-Roll Ratio (.011 μm R_a Roughness, P_H = 1.02 GPa, $\bar{V}$ = 0.75 m/s).

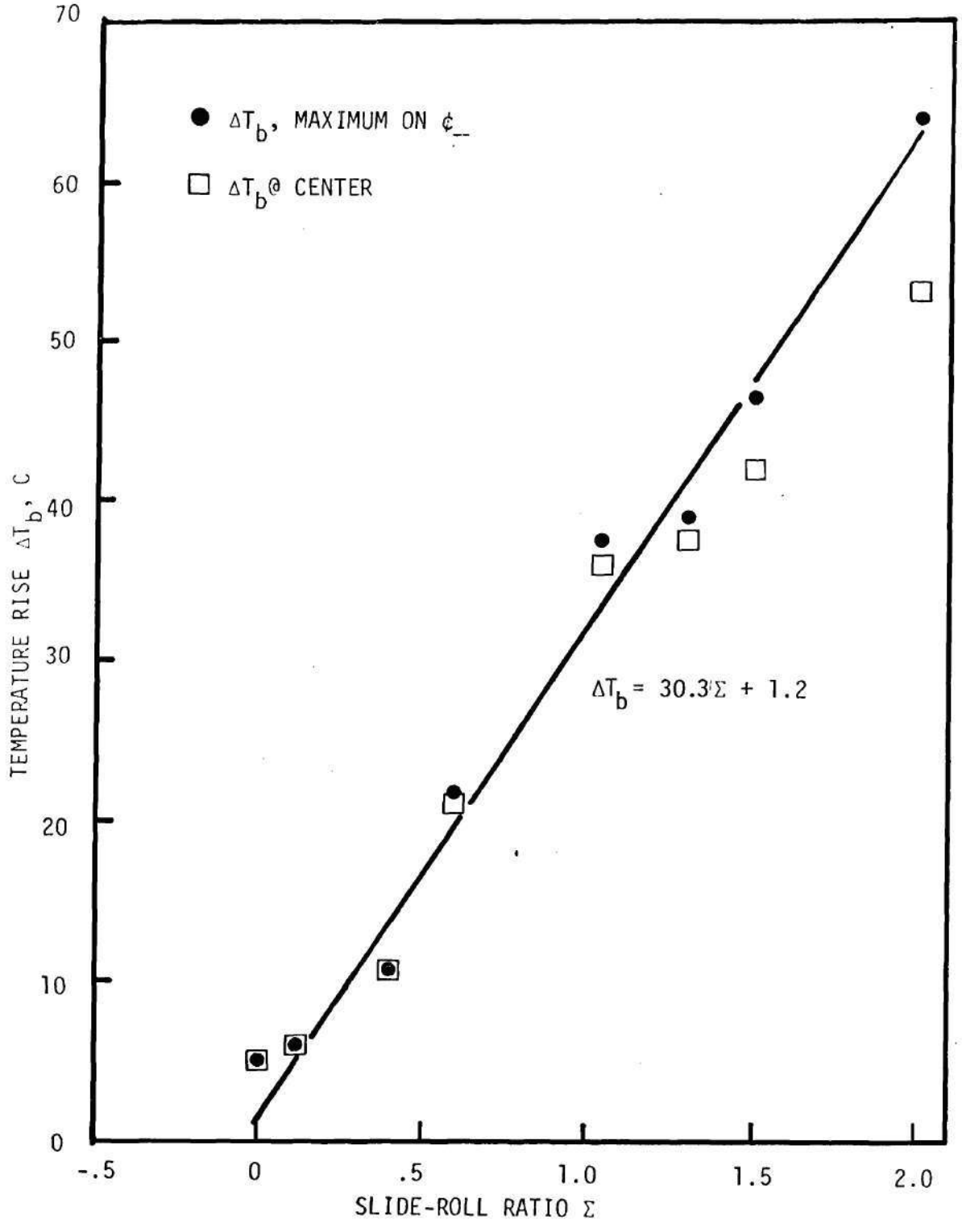

Figure 45. Ball Surface Temperature Rise as a Function of Slide-Roll Ratio (.011 μm R_a Roughness, P_H = 1.02 GPa, $\bar{V}$ = 1.0 m/s).

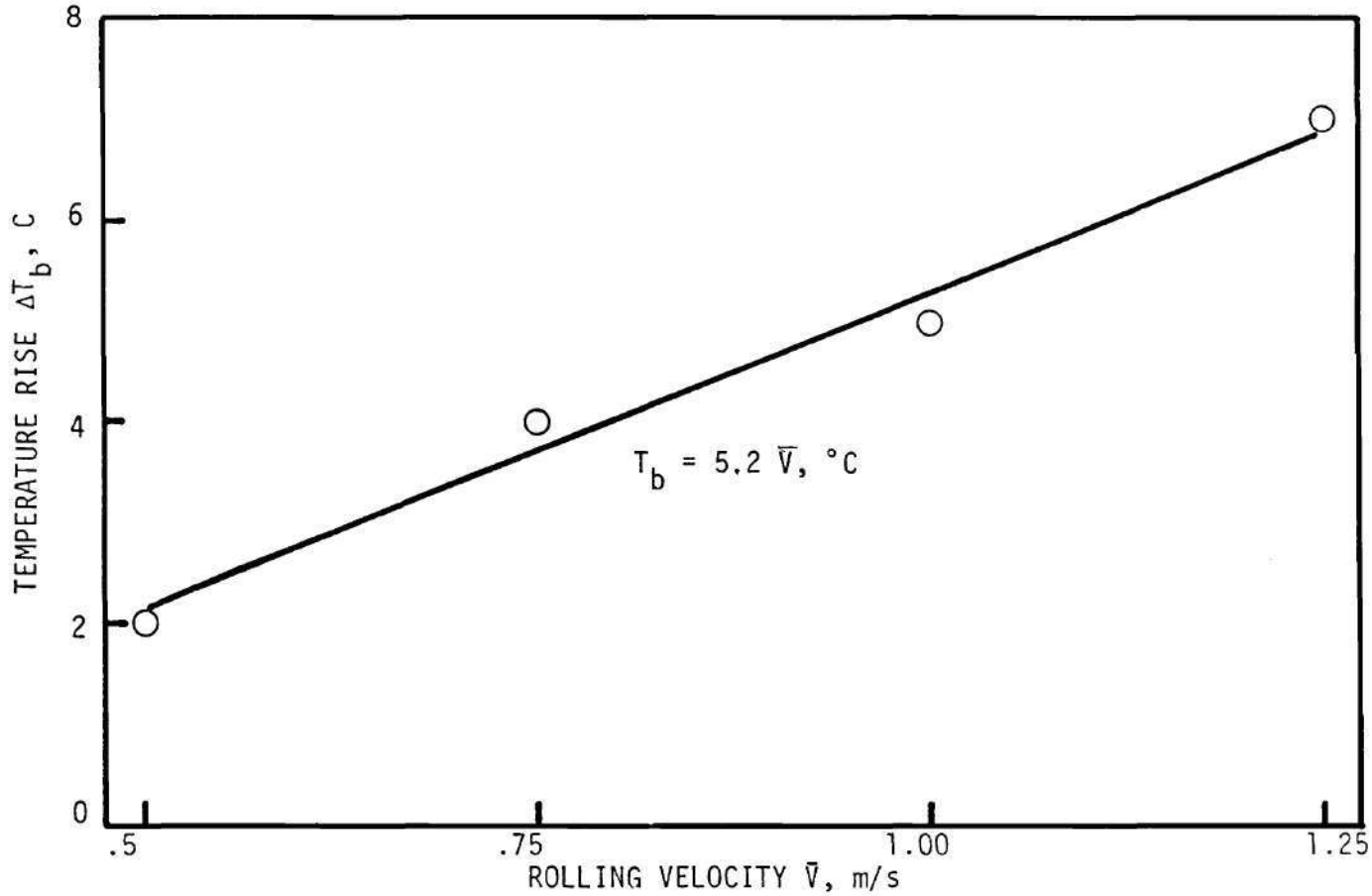

Figure 46. Ball Surface Temperature Rise as a Function of Rolling Velocity (.011 μm R_a Roughness, P_H = 1.02 GPa, Σ = 0, Maximum ΔT Occurs at Contact Center).

$$\Delta T_b = 5.2\overline{V}, \ ^\circ C \qquad (57)$$

with a correlation coefficient of 0.99.

The variation of surface temperature rise with position in the EHD contact is shown in Figures 47-49 for slide roll ratios in the range 0 to 2.0. The data for $\overline{V}$ = .75 m/s (Figure 47) and $\overline{V}$ = 1.00 m/s (Figure 48) are quite similar and the sliding results (Σ = 2.0) are in good agreement with the data reported in the previous section. It is interesting to note the small amount of inlet heating present under these conditions. For example, at 1.5 Hertz radii upstream of the contact center, the surface temperature is less than 5 °C above the bath temperature. This relatively low value is consistent with the film temperature rise in the inlet predicted by Greenwood and Kauzlarich [127].

A second observation from Figures 47 and 48 is the movement of the peak in the temperature profile toward the exit as Σ is increased. Also, Figure 49, which contains only zero slip data, shows that the peak occurs near the contact center and the temperature at the inlet and exit contact boundaries are nearly equal. The trend toward a symmetric temperature distribution as Σ approaches zero is a result of the primary mechanism of heat generation going from viscous shear when appreciable slip is present, to compression heating at $\Sigma \simeq 0$. Viscous shear results in a heat flux present throughout the contact region. If this flux were uniform, the ball surface temperature would continue to rise as it passed through the contact. The fact that the heat flux is

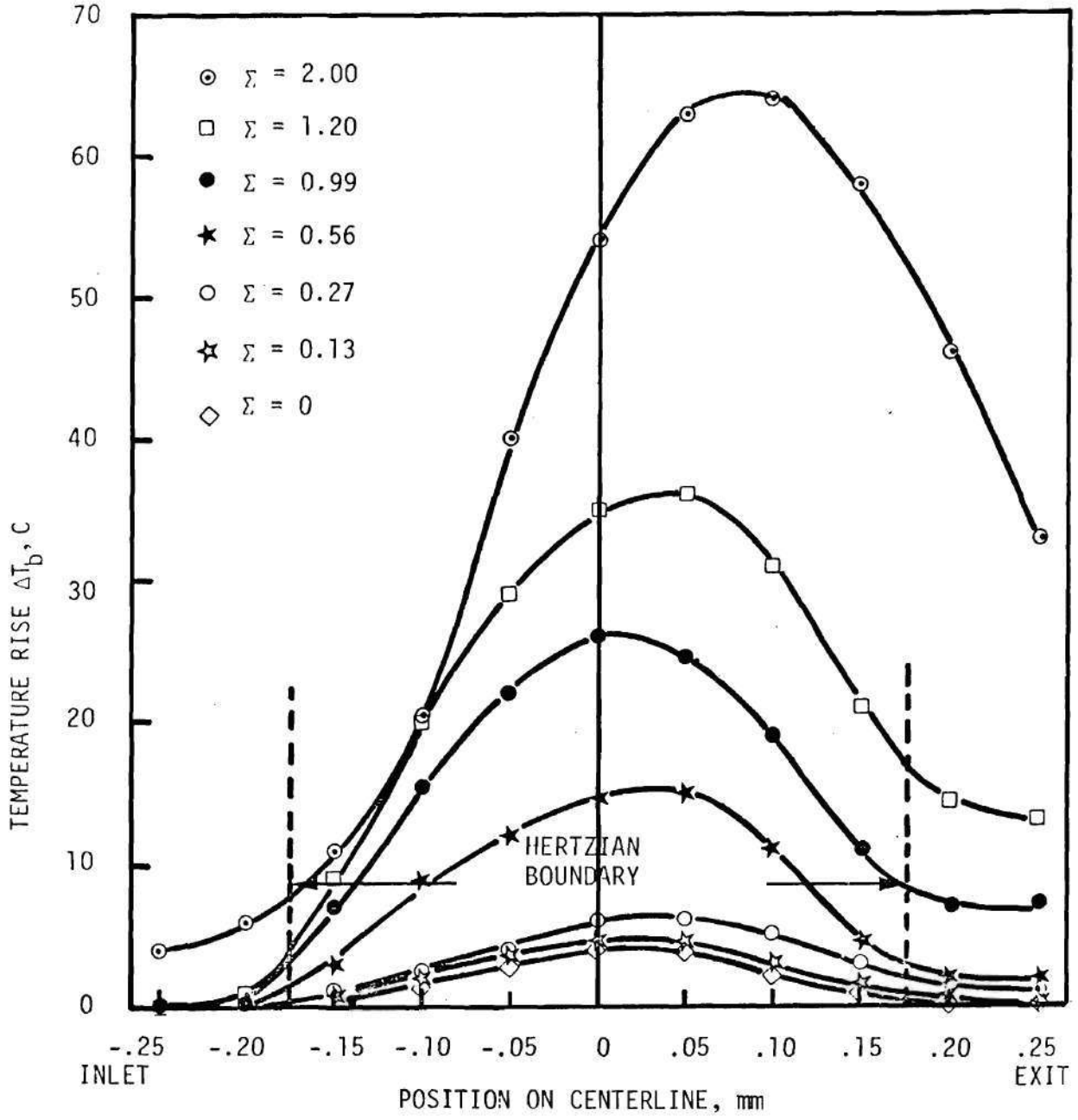

Figure 47. Ball Surface Temperature Rise Along the Contact Centerline (.011 μm R_a Roughness, P_H = 1.02 GPa, $\bar{V}$ = .75 m/s).

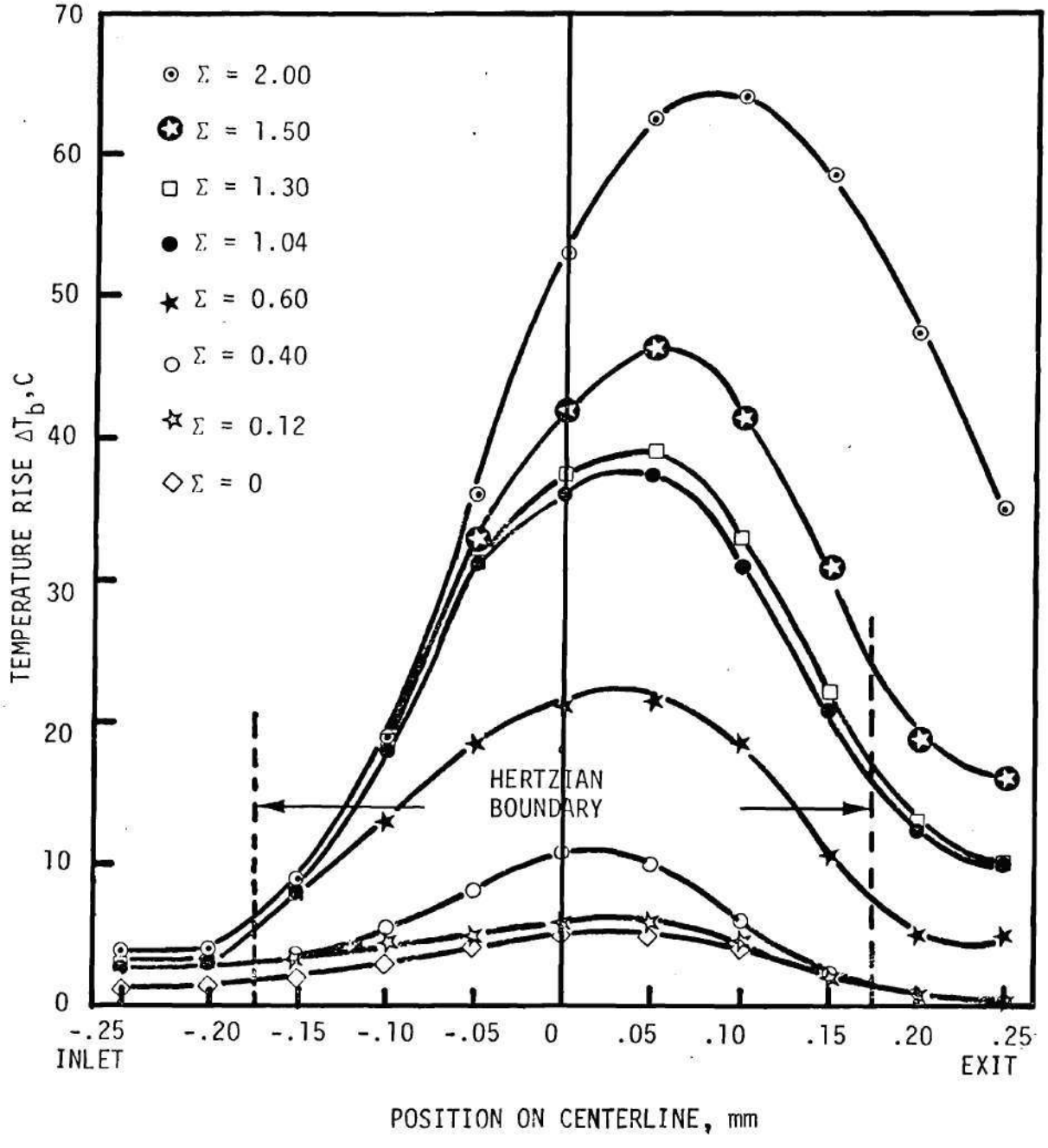

Figure 48. Ball Surface Temperature Rise Along the Contact Centerline (.011 μm R_a Roughness, P_H = 1.02 GPa, $\bar{V}$ = 1.00 m/s).

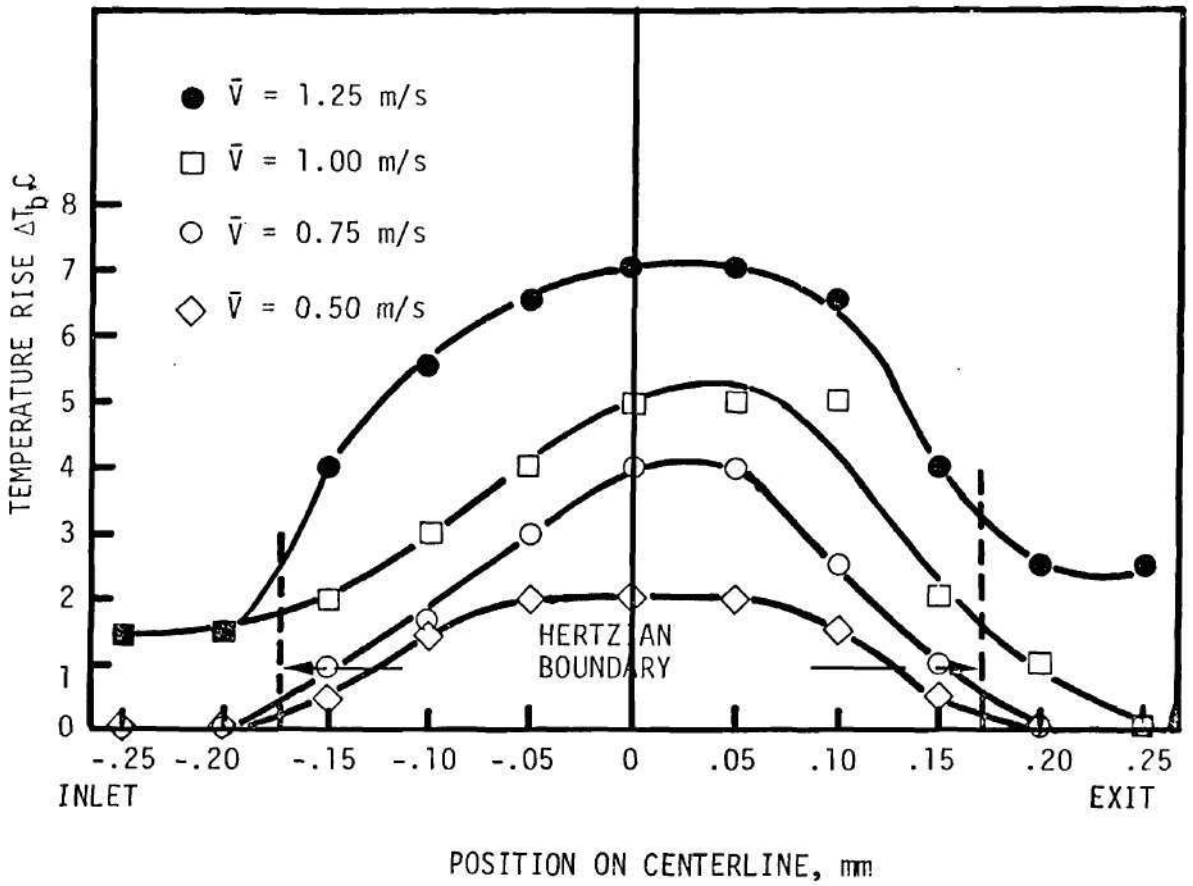

Figure 49. Ball Surface Temperature Rise Along Contact Centerline (.011 μm R_a Roughness, P_H = 1.02 GPa, Σ = 0).

very much greater at the contact center results in a temperature reduction as the exit boundary is approached. The faster the heat flux falls off, the lower the exit temperature should be. In the case of pure rolling, the viscous shear component is absent and the temperature rise is due to shear in the inlet and compressional heating. The latter term is a function of the pressure profile, which is nearly symmetric in the contact. The film and surface temperature should therefore rise and fall with pressure. Therefore, the trends shown in Figures 47-49 appear to be reasonable.

The flash temperature analysis done in a previous section has been extended by Sanborn [142] to consider the influence of rolling by assuming that the viscous dissipation takes place in the fluid midplane, and that the remaining fluid merely conducts the heat to the adjoining surfaces. Sanborn has derived the following expression for the ball surface temperature rise

$$\Delta T_b = \frac{\left(\frac{TC \cdot W \cdot V_s}{\pi a^2}\right)\left(\frac{h}{2k_f} + \frac{K_{sa}}{V_{sa}^{1/2}}\right) + (T_{osa} - T_{ob})}{1 + \frac{V_b^{1/2}}{K_b}\left(\frac{K_{sa}}{V_{sa}^{1/2}} + \frac{h}{2k_f}\right)} \qquad (58)$$

Equation (58) has been evaluated for the materials used, and by using an average film thickness of 0.16 μm (Figure 41) at a load of 67 N. Considering the temperature rise during pure rolling (equation (57)), the ball surface temperature rise is given by

$$\Delta T_b = 5.2\ \bar{V} + \frac{66.7\ TC \cdot V_s}{\frac{V_{sa}^{1/2}}{5.8\ V_{sa}^{1/2} + 14.9} + \frac{V_b^{1/2}}{11.8}} \qquad (59)$$

Equation (59) has been evaluated using the conditions shown in Table 6 except for the conditions of simple sliding ($\Sigma = 2$, $V_{sa} = 0$). The simple sliding data was excluded because $L_{sa} = 0$, thus not meeting one of the imposed restrictions. Also, with a stationary sapphire surface, T_b and T_{sa} are likely to be considerably different. resulting in the assumption of the adiabatic plane being at the center of the film being in error. The results are shown in Figure 50.

It should be remembered that the predicted temperature rise is the average over the contact area whereas the measured temperature rise is the maximum. From Figure 50, it is therefore clear that the predicted values of temperature rise are higher than the measured values.

There are a number of differences in the development of flash temperature theory and the conditions found in the experiments. First of all, the theory is based on a uniform heat flux over the contact area. The heat flux distribution in the EHD contact is probably non-uniform with the maximum occurring near the center. Also because of differences in thermal diffusivities of the materials of the contact, the adiabatic plane of the fluid film may not occur at the film center. Finally, the theory assumes a semifinite solid with the free surface being adiabatic except under the concentrated heat flux. This is not consistent with the conditions of the experiment. The ball and sapphire surfaces outside the contact area are constantly flooded with lubricant. The agreement shown in Figure 50 should therefore be viewed cautiously.

Because of the apparent agreement shown in Figure 50, equation (59) can be considered as a predictive equation for the maximum ball surface temperature.

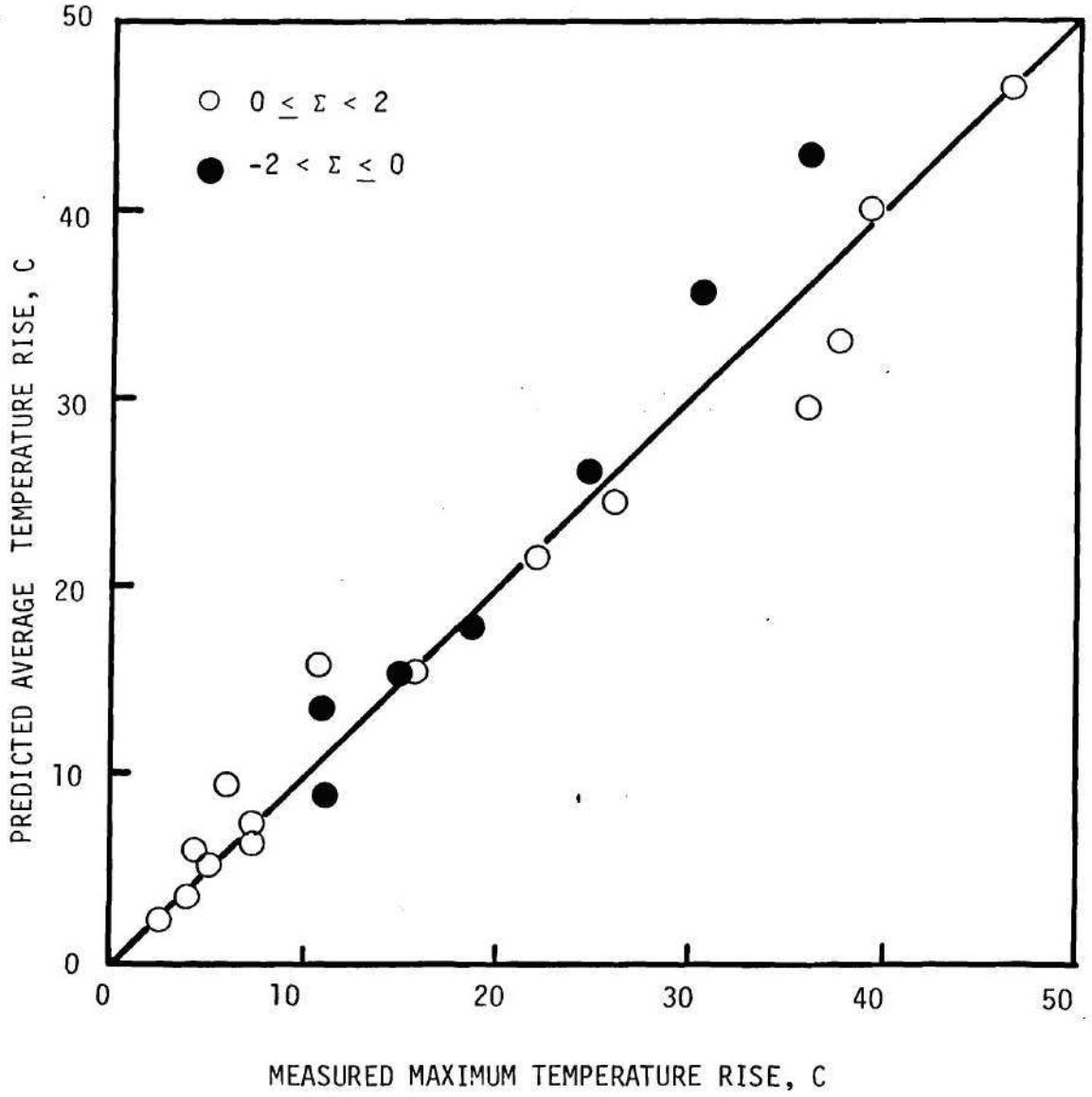

Figure 50. Comparison of Predicted Average and Actual Maximum Ball Surface Temperature Rises for $L > 5$.

Temperature Measurements for Negative Slide-roll Ratio

Ball surface temperatures for negative slide-roll ratio (ball surface speed - sapphire speed) will be discussed in this section. The combined rolling and sliding EHD simulator was used in these experiments. When the slide-roll ratio is -2, only the sapphire is moving and the ball surface is stationary. In order to run the EHD simulator under these conditions, it was found necessary to supply a jet of lubricant directly onto the sapphire disc slightly ahead of the contact zone, since the lubricant in the cup could not reach the contact zone because the ball was stationary. The measured ball surface temperature then corresponds to the stationary surface temperature. This technique therefore offers a way to measure stationary surface temperature. In the work reported in the previous section, the stationary surface temperature (i.e. sapphire surface temperature) was not measured because of low emissivity of sapphire. However, since the thermal conductivity of ball material is only 1.4 times that of sapphire the stationary ball surface temperature should approximately correspond to the stationary sapphire surface temperature.

Figure 51 shows the ball surface temperature at the contact center and its maximum value along the center line as a function of slide-roll ratio for a Hertz pressure level of 1.02 GPa and a constant rolling velocity of .75 m/s. The results for positive slide-roll ratio have been included in this figure for comparison. Slight asymmetry in ball surface temperature about $\Sigma = 0$ can be observed. Similar data for a higher rolling speed of 1.0 m/s is shown in Figure 52. It can be noticed in

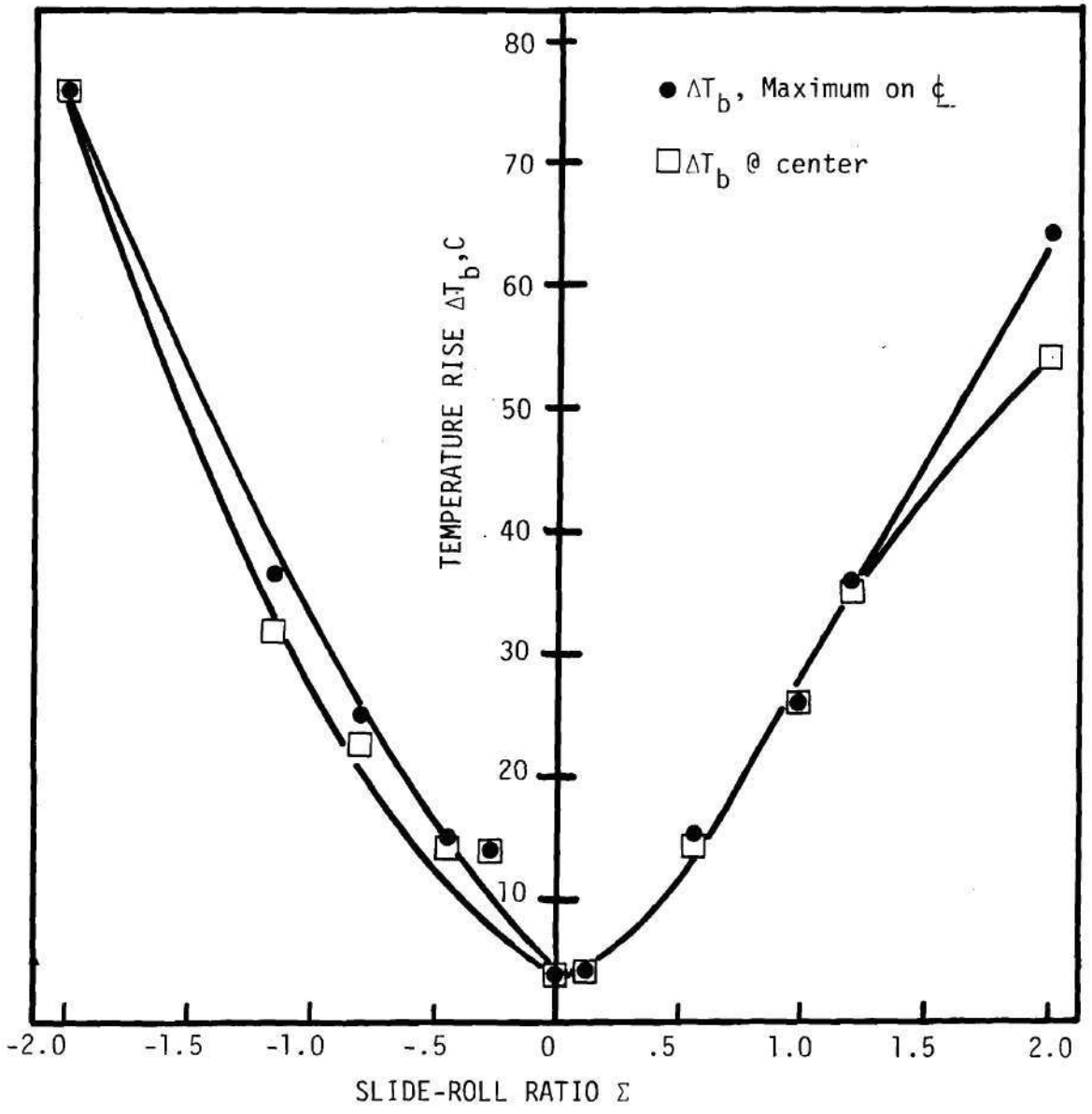

Figure 51. Ball Surface Temperature Rise as a Function of SLIDE-ROLL RATIO (-2 to +2) (Smooth ball ⇒ .011 μm Ra, P_H = 1.02 GPa, $\bar{V}$ = .75 m/s).

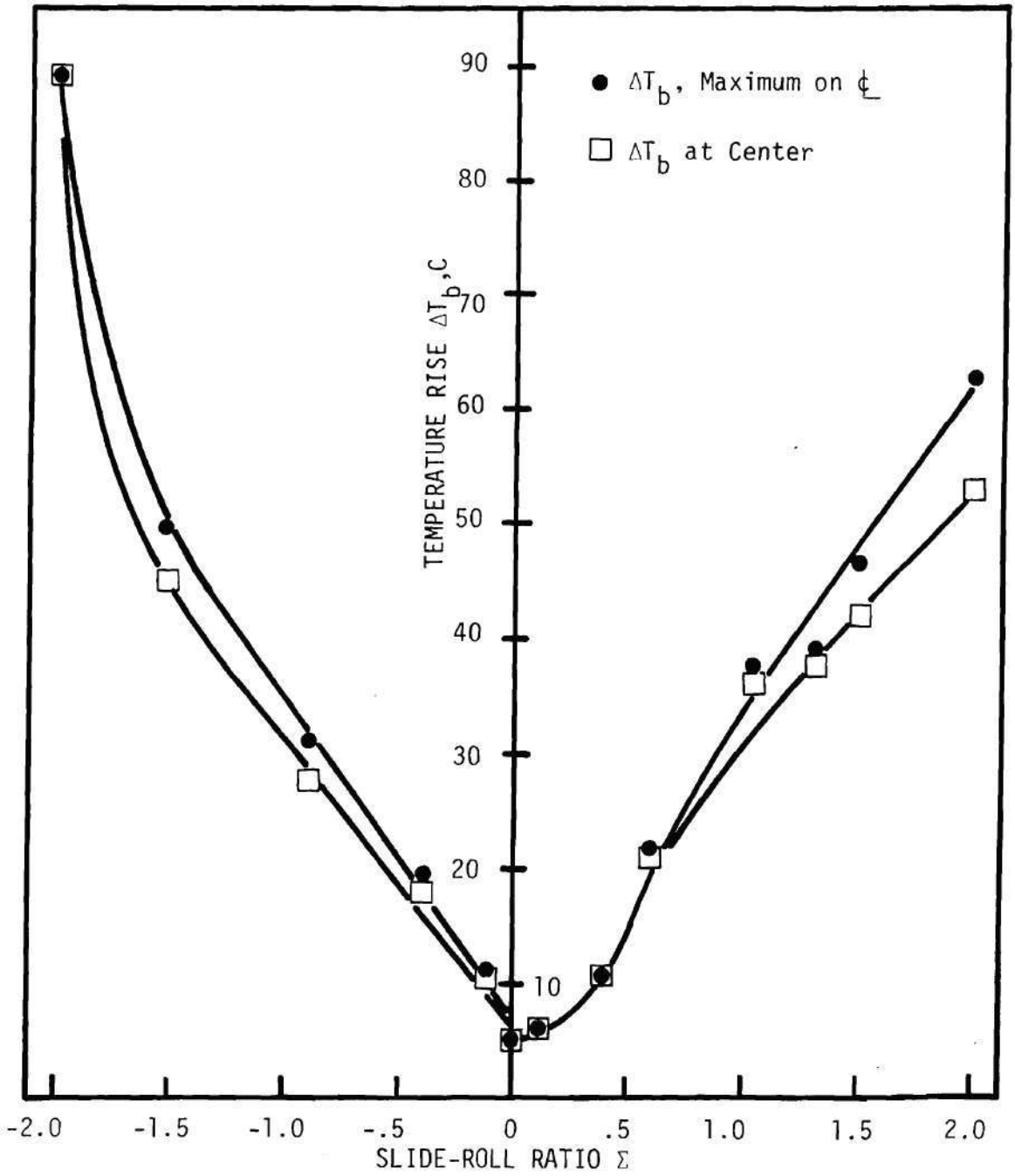

Figure 52. Ball Surface Temperature Rise as a Function of Slide-Roll Ratio (Smooth ball ⇒ .011 μm Ra, P_H = 1.02 GPa, $\bar{V}$ = 1.0 m/s).

both the figures that the stationary ball surface temperature ($\Sigma = -2$) is higher than the moving ball surface temperature ($\Sigma = 2$).

Figure 53 shows the ball surface temperature distribution as a function of position on centerline at various negative slide-roll ratios, including the one for pure rolling. A constant load yielding a peak Hertz pressure of 1.02 GPa is used and the rolling velocity is held constant at .75 m/s. Figure 54 shows similar data but for a higher rolling speed of 1.0 m/s. Figures 47 and 48 can be compared with Figures 53 and 54. Even though the temperature distributions are similar, the values are slightly higher for negative slide-roll ratios. It is rather interesting to note the movement of the position of peak temperature as the slide-roll ratio is varied. The peak is at the center for pure rolling. For slide-roll ratios increasing negatively, the peak occurs slightly beyond the center towards the exit. This behavior is because of a change in mechanism from compressional heating at pure rolling to significant viscous heating at higher values of slip. This is similar to the trend observed for positive slide-roll ratios. However, the position of peak temperature for $\Sigma = -2$, is at the center of the contact. Ball surface being stationary in this case, has a maximum temperature rise at contact center where the heat flux has a maximum intensity.

In addition to the results shown above, stationary ball surface temperature was measured at a peak Hertz pressure level of 1.02 GPa, for speeds ranging from 0.82 to 2.58 m/s. The results are summarized in Table 7. A linear regression analysis of the temperature rise with speed yielded

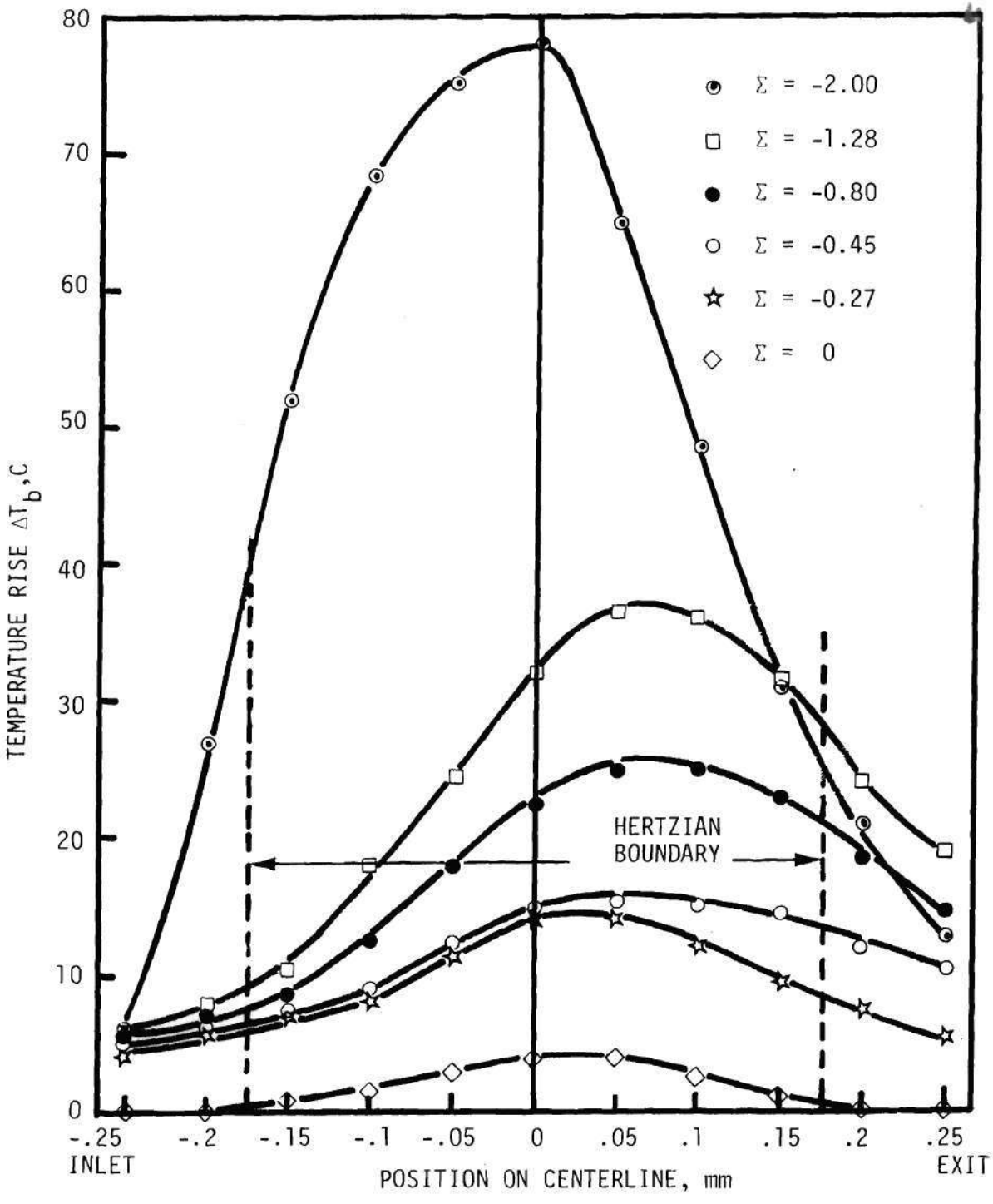

Figure 53. Ball Surface Temperature Rise along the Contact Centerline (Smooth ball => .011 μm Ra, P_H = 1.02 GPa, $\bar{V}$ = .75 m/s.)

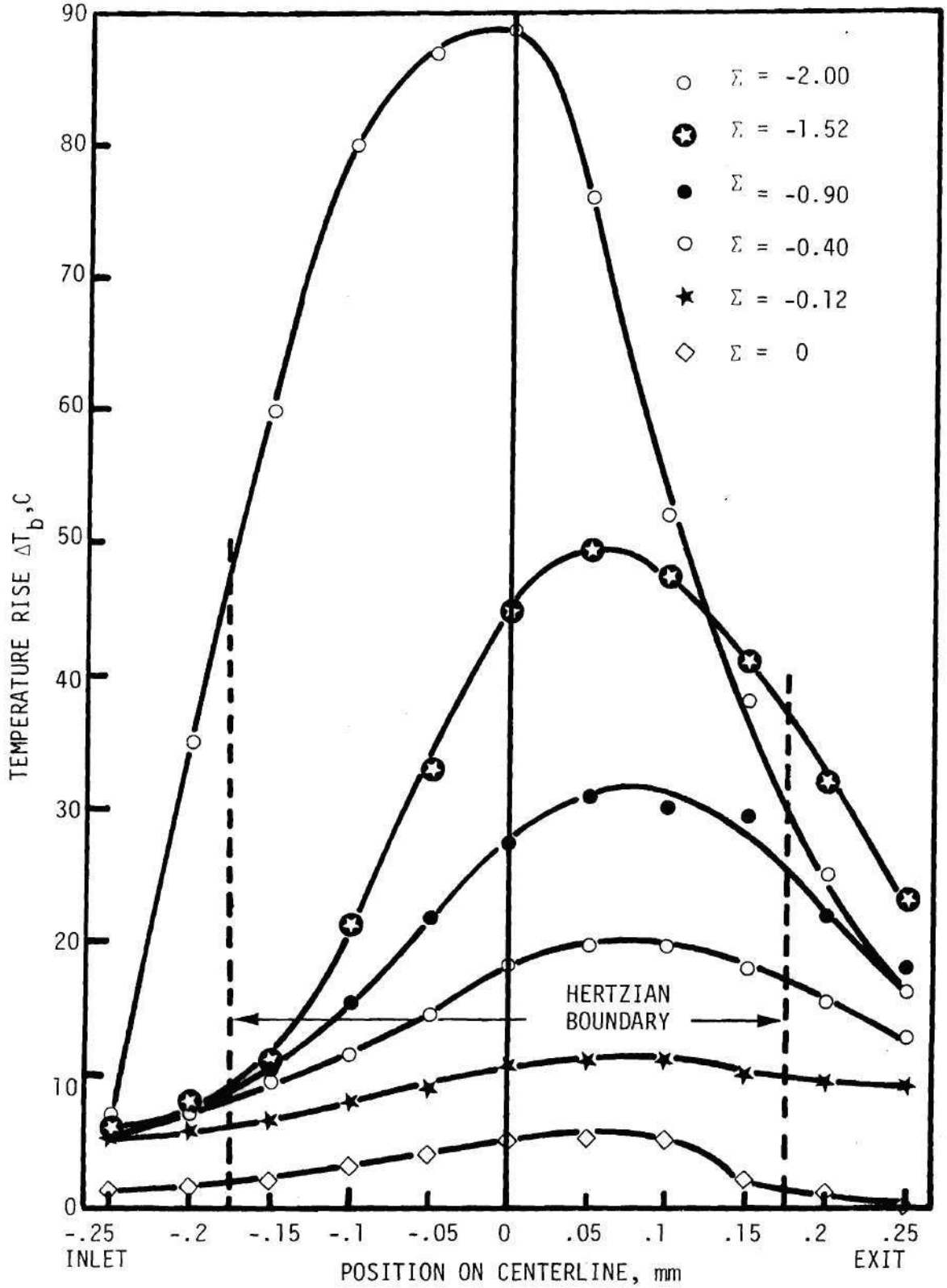

Figure 54. Ball Surface Temperature Rise along the Contact Centerline (Smooth ball ⇒ .011 μm Ra, P_H = 1.02 GN/m^2, $\bar{V}$ = 1.0 m/s).

Table 7. Summary of Stationary Ball Surface Temperature Measurement

(Smooth ball: .011 μm R_a, Fluid N1, P_H = 1.02 GPa)

V_b m/s	V_{sa} (= V_s) m/s	T_{bath} C	T_b @ Center (= $T_{b,max}$) C	ΔT_b ($T_b - T_{bulk}$)* C
0	.82	28	92.5	50.5
0	1.20	28	108	66
0	1.24	28	109.5	67.5
0	1.50	28	118	76
0	1.70	28	125	83
0	1.85	26	128	86
0	1.98	26	131	89
0	2.58	28	146	104

*T_{bulk} ≈ 42 C for all the experiments (T_{bulk} = T_b two to three Hertzian diameters before the contact).

$$\Delta T_b = 58.6\ V_{sa}^{0.62} \qquad (60)$$

with $r^2 = 1.00$. It is interesting to note that the exponent 0.62 on V_{sa} in equation (60) compares well with the exponent on speed in the low speed case given in equation (47) in the previous section. This means that the stationary heat source theory applicable for $L < .1$, can also predict the trend in stationary surface temperatures. The bath temperature does not represent the bulk temperature in the present case, since the ball is not rotating. However, the bulk temperature for this case was determined by measuring the ball surface temperature two to three Hertzian diameters before the contact.

The flash temperature analysis referred to earlier in this section can also be applied to negative slide-roll ratios, because individual surface velocities were used. This analysis however, cannot be applied to stationary surface temperature calculation since the assumption of mid-plane film temperature being the maximum is not valid in this case. This situation is similar to the case when $\Sigma = 2$, where again a similar assumption was not valid. The ball surface temperature rise calculated using equation (59) for negative slide-roll ratios is shown plotted (as triangles) versus measured temperature rise in Figure 50. The predicted values are again higher than the measured values. Probable reasons for this discrepancy have already been cited.

CHAPTER V

RESULTS AND DISCUSSION - II, TEMPERATURE FLUCTUATIONS

It has been remarked in Chapter I, that under certain operating conditions when the surface asperities are interacting with each other, the surface temperatures are not time-steady. In this chapter, the time averaged values and the fluctuations of ball surface temperature are reported for a range of sliding speeds at different Hertz pressure levels and various R_a values of surface roughness. The wear debris generated during asperity interactions is studied by analyzing the used oil samples. A frequency analysis of surface profiles and the temperature fluctuations before and after an experiment is performed to study the wavelength or frequency aspects of surface texture important in an EHD type application.

A. Surface Roughness Effects on Ball Surface Temperature

To study the effect of ball surface roughness on surface temperature, AISI 52100 steel balls of various roughness values were used in the EHD contact simulator. In the results described in Chapter IV, the arithmetic average roughness (R_a) of the balls was 0.011 μm. The surface finish of the sapphire in all cases was approximately 0.006 μm R_a. Surface profiles of both the ball and sapphire were measured on the profilometer and are shown in Figure 55. All these profiles are unfiltered, i.e. they include both roughness and waviness. The slope in sapphire surface profile is due to imperfect tilt adjustment. The

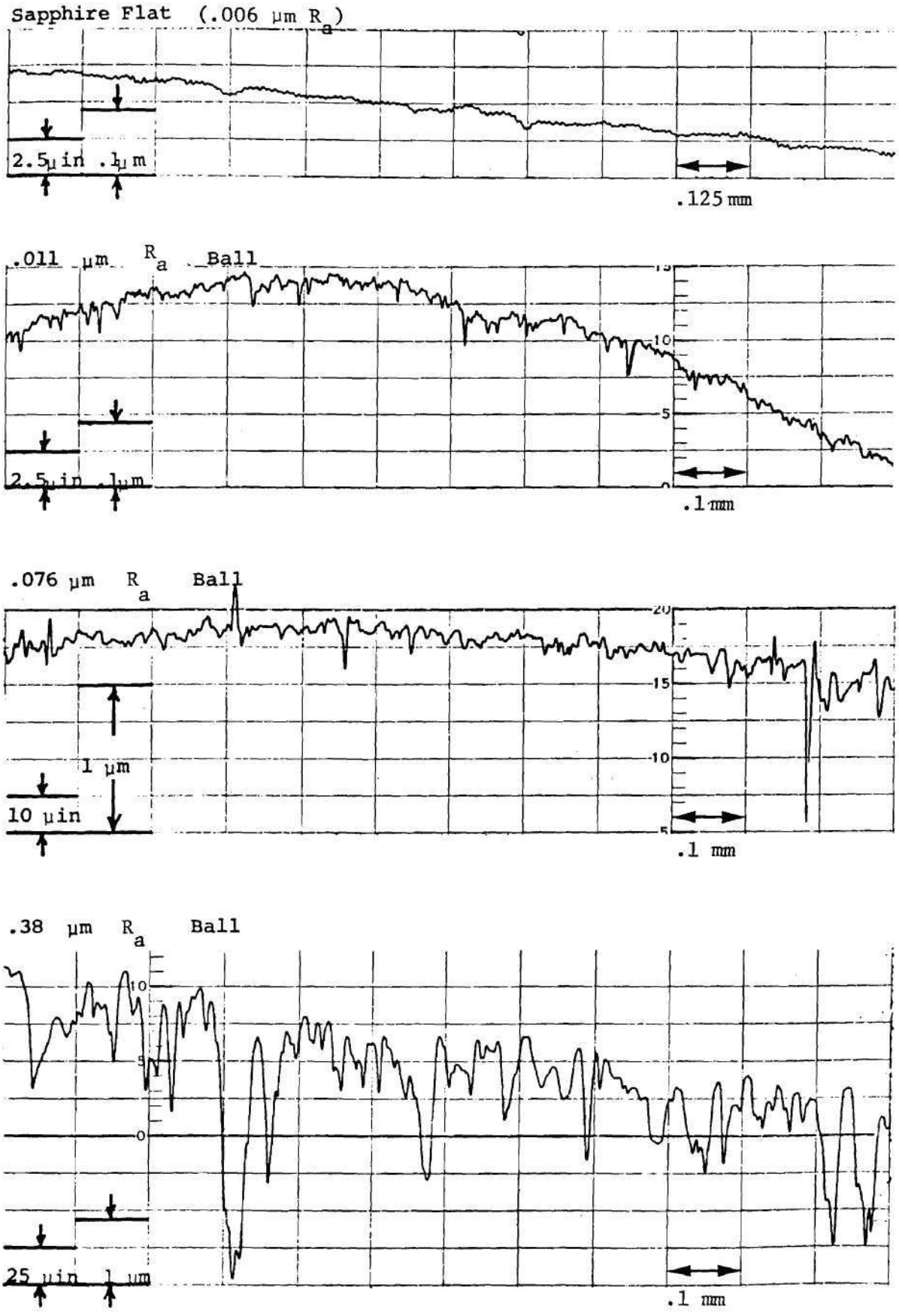

Figure 55. Surface Roughness Profiles.

large curvatures in the ball surface profiles are because of the effective curvatures of the steel balls. A substantial portion of the real curvature of steel balls (38 mm diameter) was eliminated by using the rotary attachment while recording the ball surface profiles (see Chapter III). Because of the difficulty in aligning the rotary attachment pivot axis to coincide with the ball center, it was not possible to obtain a flat unfiltered profile for the ball surface. This however, did not present any problem because a cutoff length of 0.030 inch is used while computing the R_a values.

Tables 8, 9, and 10 show ball surface temperature rise (difference between ball surface and bulk oil temperature) at contact center at various peak Hertz pressures for a range of sliding speeds. Table 8 contains data for the case of smooth ball which has already been described in Chapter IV. Only sliding velocities above the break point (V_{BP}) are reported in this table. Tables 9 and 10 contain data for the case of medium rough and rough balls respectively. Even though only maximum ball surface temperature values were determined from experiments (since the contact center could not be located while using the rough ball), the contact center values could be approximately calculated from similar temperature maps prepared for the smooth ball. In fact, the temperature rises reported in Table 10 have been calculated this way. The ball surface temperature rises increase with load, sliding speed and surface roughness. The correlations are described later in this section.

Figures 37, 56 and 57 show ball surface temperature rise at the center of the EHD contact as a function of speed and load for the smooth, medium rough and rough balls respectively. In addition, Figure 58 shows

Table 8. Ball Surface Temperature Rise at Contact Center versus Speed and Load for Smooth Ball (.011 μm R_a, Fluid N1)

P_H = .52 GPa		P_H = 1.02 GPa		P_H = 1.51 GPa	
V_s, m/s	ΔT_b, C	V_s, m/s	ΔT_b, C	V_s, m/s	ΔT_b, C
.39	9	.48	33	.45	74
.52	10	.56	35	.61	75
.67	11.5	.64	38.5	.90	89
.84	12	.73	41	1.14	96
1.05	13	.82	44	1.34	100.5
1.30	15	.92	48	1.55	108
1.53	16	1.02	50	1.81	117
1.76	17.5	1.21	58	1.99	122
		1.41	62	2.25	126
		1.61	66	2.53	131.5
		1.88	67	2.82	133
		2.08	72		
		2.36	74		
		2.52	77		

P_H = 1.7 GPa		P_H = 1.81 GPa		P_H = 2.03 GPa	
V_s, m/s	ΔT_b, C	V_s, m/s	ΔT_b, C	V_s, m/s	ΔT_b, C
.46	83	.56	102	.42	105
.52	87	.80	111.5	.48	108
.60	91	1.02	120	.53	111
.67	93	1.28	136	.58	113
.74	97	1.60	147	.62	115
.86	102	1.81	154	.68	118
.96	104	2.11	159.5	.73	120
1.02	108	2.38	165.5	.79	122
1.11	112	2.66	168	.86	125
1.54	131	2.94	171	.93	127
2.05	144	3.21	178	.99	128
2.54	153	3.48	179	1.04	131
3.13	162			1.12	136
3.65	172				
4.18	176				
4.70	182				
5.21	189				

Table 9. Ball Surface Temperature Rise at Contact Center versus Speed and Load for Medium Rough Ball (.076 μm R_a, Fluid N1)

P_H = 1.02 GPa		P_H = 1.24 GPa		P_H = 1.51 GPa	
V_s, m/s	ΔT_b, C	V_s, m/s	ΔT_b, C	V_s, m/s	ΔT_b, C
.55	38	.95	87	1.11	110
.83	50	1.71	92	1.67	120
.97	54	2.23	100	2.15	130
1.28	61.5	2.71	104	2.62	135
1.59	66.5	3.17	109	3.09	142
1.88	71.5	3.65	112	3.67	156
2.18	74	4.13	114	4.16	158
2.61	77.5	4.63	114	4.67	160
2.91	79	5.13	115	5.20	162
3.22	80.5				
3.55	81.5				
3.86	83.5				
4.18	85				
4.48	85				
4.78	85.5				
5.09	86				

P_H = 1.70 GPa		P_H = 1.89 GPa		P_H = 2.03 GPa	
.83	117	.87	140	.78	139
1.15	138.5	1.21	170	.95	142.5
1.44	152	1.53	178	1.13	146
1.80	162	1.88	185	1.37	168.5
2.11	170	2.24	193	1.75	180
2.47	176	2.59	195	2.09	190
2.77	181			2.37	195
3.12	185.5				
3.44	189				
3.77	193				
4.11	195				

Table 10. Ball Surface Temperature Rise at Contact Center* versus Speed and Load for Rough Ball (.38 μm R_a, Fluid N1)

P_H = .52 GPa		P_H = 1.02 GPa	
V_s, m/s	ΔT_b, C	V_s, m/s	ΔT_b, C
.41	6.5	.50	45.5
.69	10.5	.82	61
.99	13.5	1.08	73
1.27	15.5	1.37	79
1.57	16.5	1.66	91
1.83	17.5	1.94	101
2.13	20.5	2.23	108
2.42	21.5	2.52	115
2.72	23.5	2.79	131
3.01	26	3.11	133
3.29	27	3.44	135
3.60	28	3.75	138
3.93	35.5	4.07	140
4.22	35.5	4.41	142
4.58	36.5	4.70	144
4.86	38	4.95	148
5.16	39.5	5.31	148

P_H = 1.51 GPa		P_H = 1.89 GPa	
V_s, m/s	ΔT_b, C	V_s, m/s	ΔT_b, C
1.10	137	.94	159
1.41	140	1.23	170
1.70	157	1.45	171
1.94	165	1.75	187
2.23	172	2.08	192
2.57	185	2.54	196
3.00	191	3.00	196

*Temperatures at contact center were approximately determined from the measured values of maximum ball surface temperature rise.

the temperature data replotted as temperature rise as a function of peak Hertz pressure and sliding speed. In the experiments with the rough ball, the temperature plotted is the maximum in the contact, whether or not it occurs at the contact center.

The temperatures reported in Figures 56 - 58 are time averaged values, since the infrared detector was operated in the DC mode during these experiments. Under certain operating conditions when asperity interactions are taking place, the instantaneous temperatures developed at the individual asperities may be significantly different from the average values. This subject will be treated in detail in the next section. Even the time averaged temperatures would overshoot the new steady state temperature and then return to the new value whenever a velocity step was introduced. This is shown in Figure 59. The dotted line and the solid line correspond to two different velocity steps. While the velocity response of the system was as shown, the temperature overshoot was 10 to 15 C. The temperatures reported in Figures 56, 57 and 58 correspond to the steady state values at those operating conditions and not the overshoot values. The temperature overshoot and subsequent return to a new steady state value is attributable to the phenomenon of short time running in. With a sudden increase in velocity, the rate of asperity interactions increases. Not able to withstand this increased rate, the system undergoes some local surface smoothing. Accordingly, the time averaged temperature decreases from the overshoot value and settles down to a new steady state value. A similar phenomenon can be expected with a load step, this time the asperity interactions becoming more severe since they have to carry the suddenly imposed additional normal load. In fact,

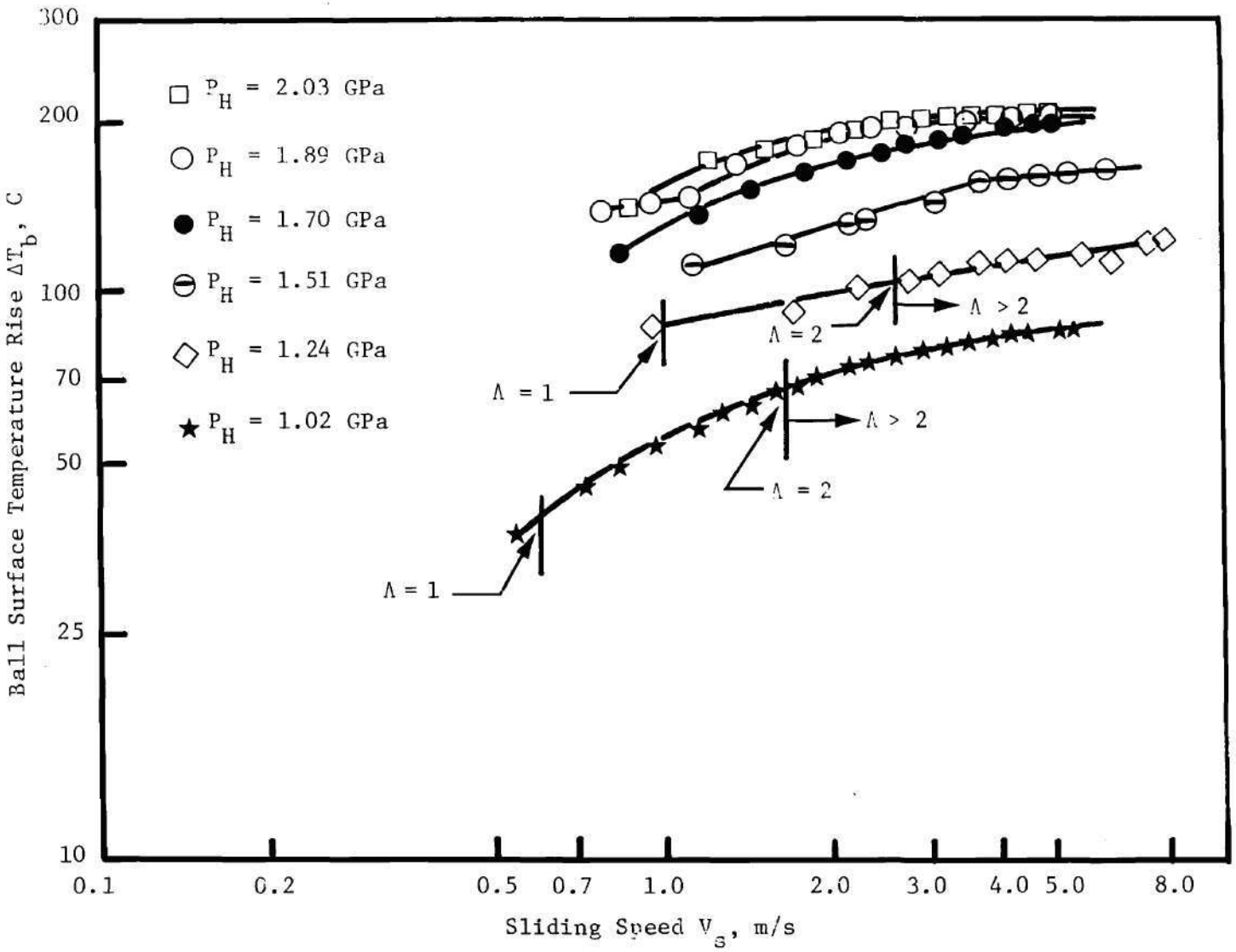

Figure 56. Ball Surface Temperature Rise at Contact Center versus Sliding Speed (Medium Rough ball: .076 μm R_a, Fluid N1, V_{sa} = 0, Λ < 1 except as noted).

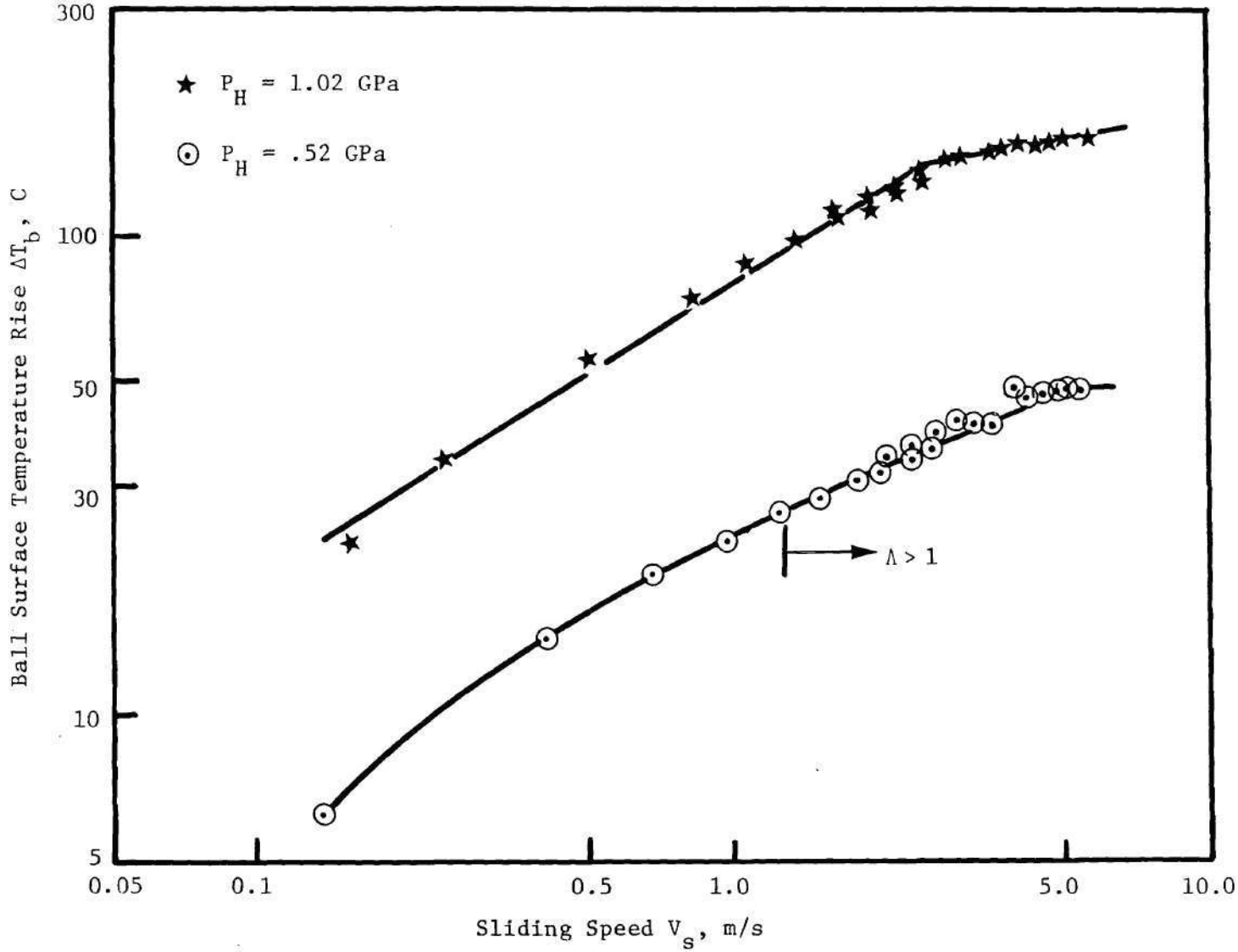

Figure 57. Maximum Ball Surface Temperature Rise versus Sliding Speed (Rough Ball: .38 μm R_a, Fluid M1, V_{sa} = 0, Λ < 1 except as noted).

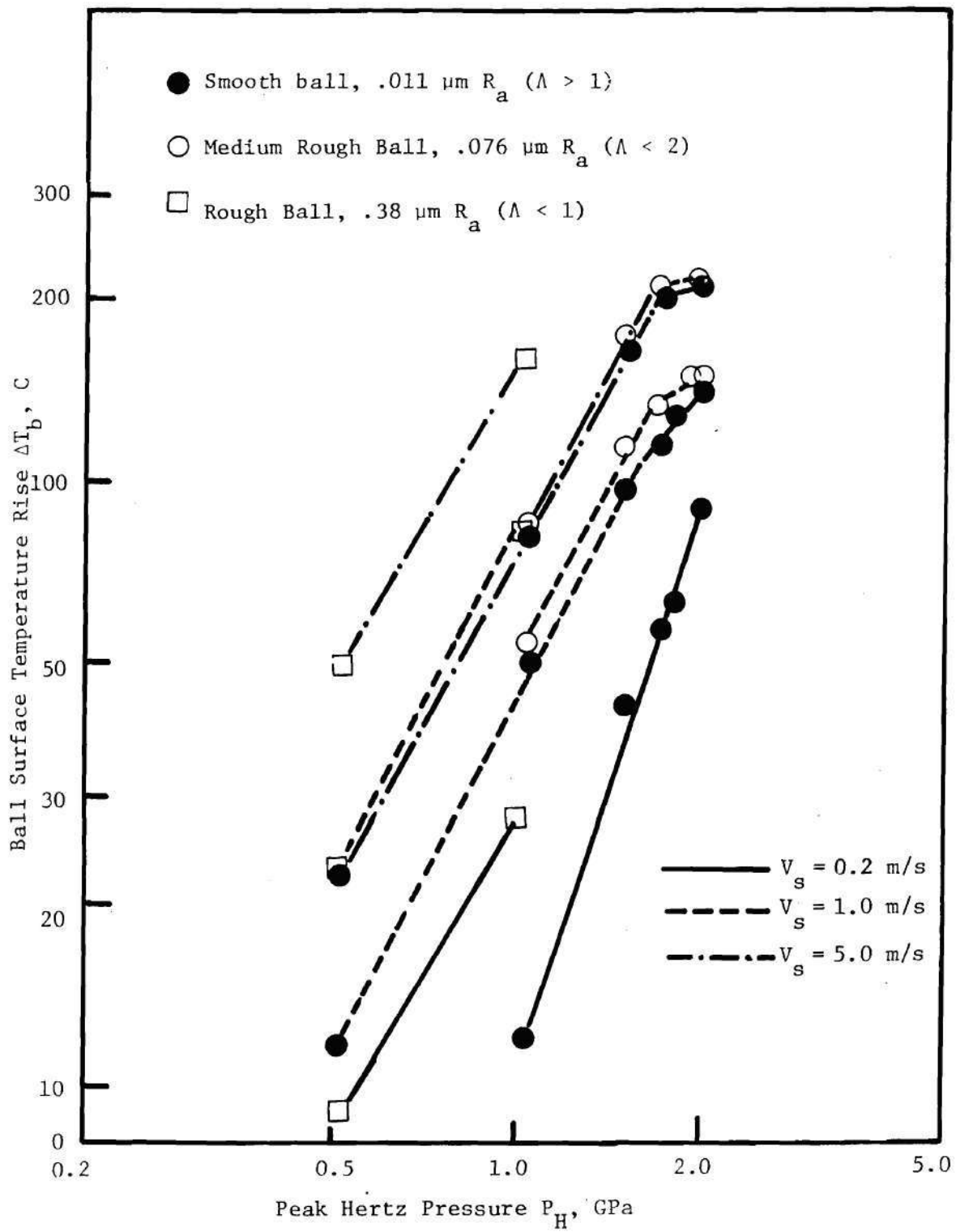

Figure 58. Ball Surface Temperature Rise versus Peak Hertz Pressure (Fluid N1, V_{sa} = 0).

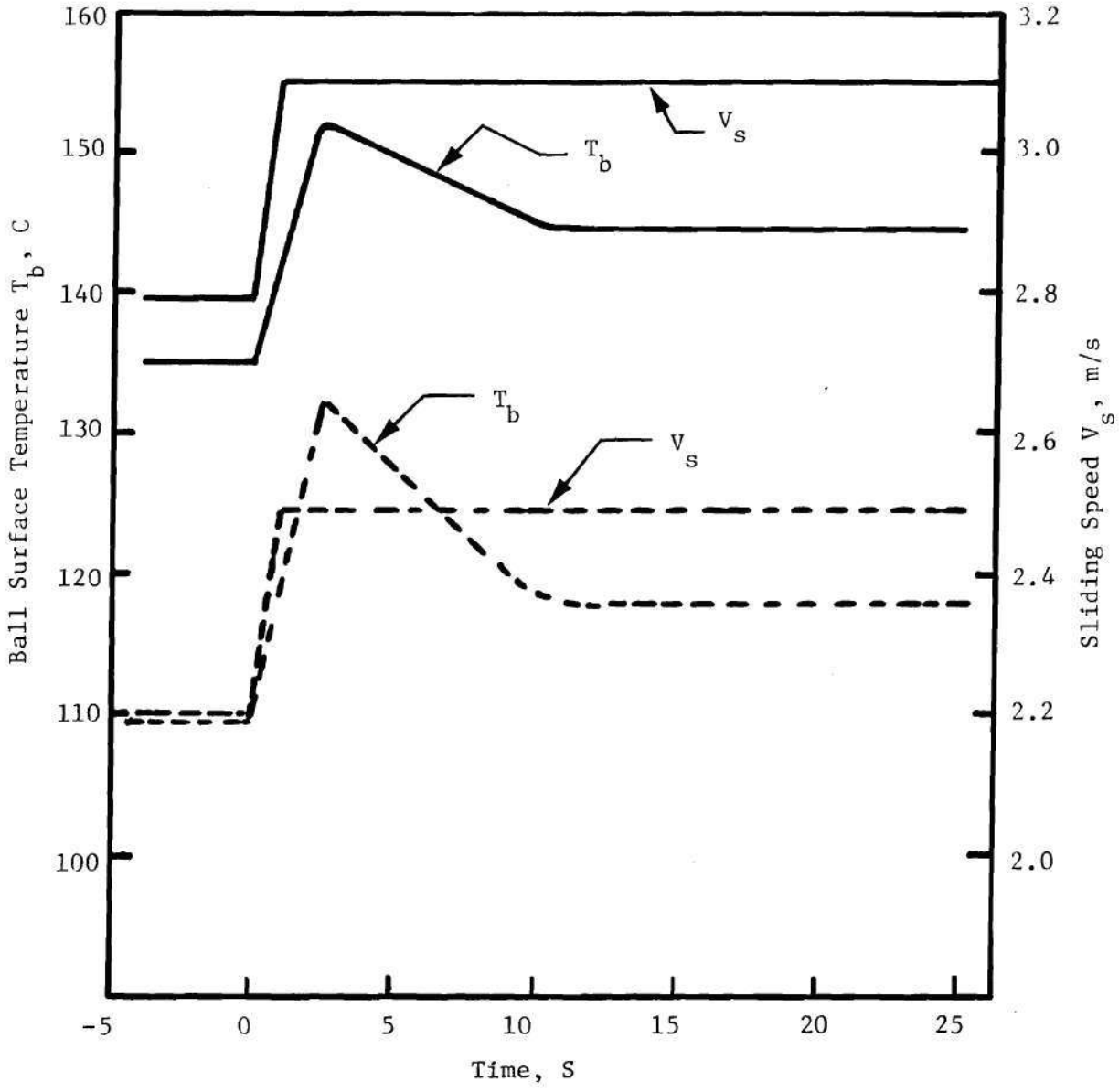

Figure 59. Maximum Ball Surface Temperature versus Time (Time 0^+ Corresponds to a Velocity Step) (Rough Ball: .38 μm R_a, P_H = 1.02 GPa, Fluid N1, V_{sa} = 0).

such an effect was observed whenever load was suddenly increased.

The temperatures for the smooth and medium rough balls are only slightly different throughout the range of operating conditions. The surface temperatures for the rough ball appear to be significantly higher than those of the smoother balls. To put all temperatures on an equivalent basis, the rough ball data in Figures 57 and 58 should be reduced by approximately 10 C. This is the difference between the maximum and center surface temperatures for the smooth ball (Figure 32). The higher temperatures for the rough ball are perhaps due to increased traction under these conditions. The increase in traction coefficient with roughness (decreasing Λ values) is discussed in the next section.

Surface roughness effects have been considered in the flash temperature formulas recommended by the American Gear Manufacturer's Association (AGMA) in their gear scoring criterion [51]. A multiplicative factor of $1/(1 - .8R_a)$ has been used for this purpose with the range of R_a being from .25 μm to .75 μm. In the literature [52-54], factors similar to the one mentioned above have been used with the coefficient accompanying R_a varying from .62 to .89. The percent increase in flash temperature predicted by these factors versus R_a is shown plotted in Figure 60. The applicable range for the AGMA factor is indicated in this figure. Three values of R_a corresponding to the three different types of balls used, are marked in the same figure. It can be seen that up to 40 percent increase is predicted for the rough ball whereas about 7% is predicted for the medium rough ball. 0.7 to 1% increase is predicted for the smooth ball (.011 μm R_a) as compared to an ideally smooth one. An approximate

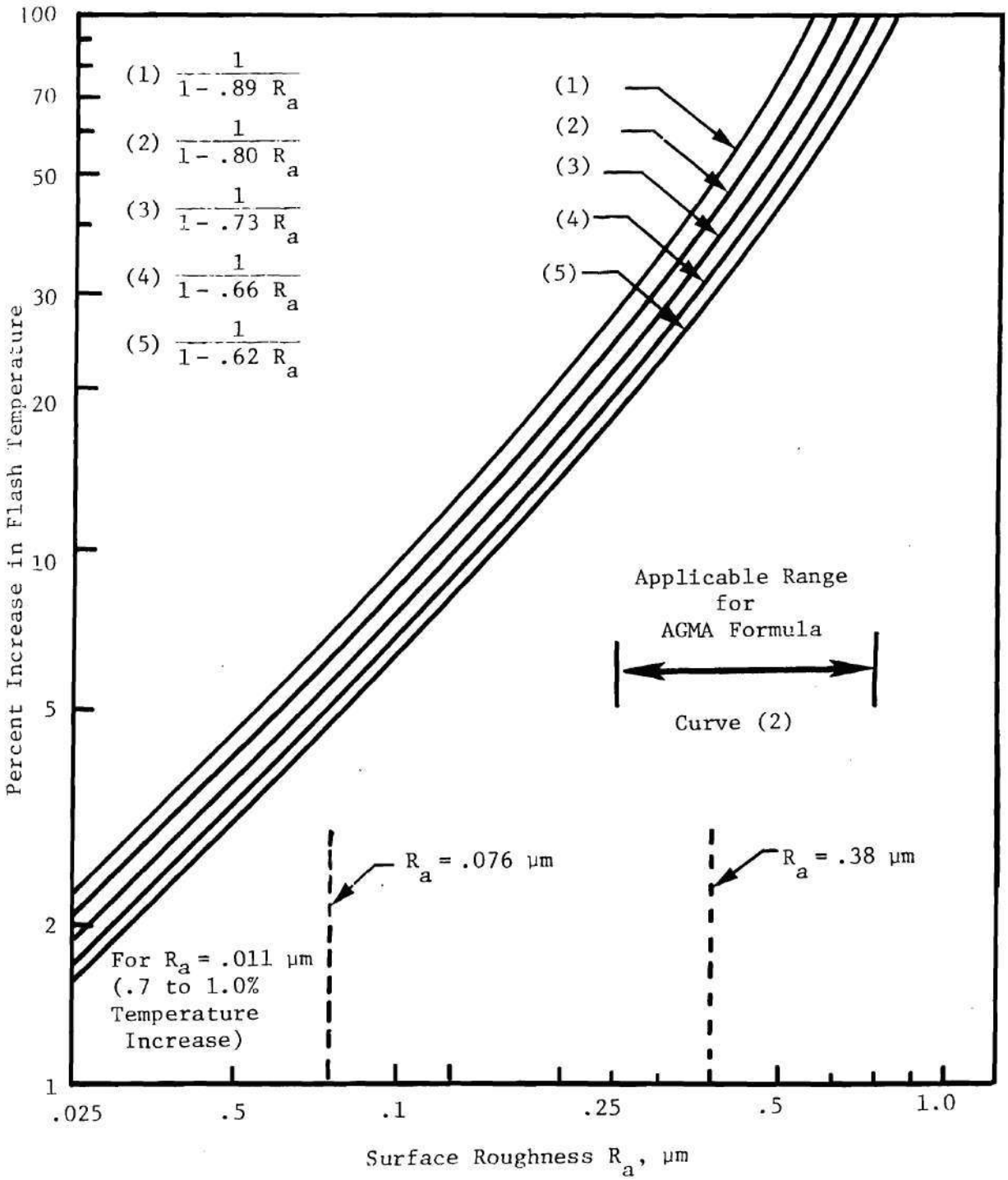

Figure 60. Percent Increase in Flash Temperature Due to Surface Roughness. Curve (2) Corresponds to the Factor Recommended by AGMA [51].

comparison of the measured values with the predicted percent increases reveals a satisfactory agreement.

In order to determine an expression for the measured ball surface temperature at contact center, a surface roughness factor of the form $1/(1 - a_1 R_a)$ discussed above, is used. A multiple regression analysis of the data in Tables 8, 9, and 10 (181 data points in all) yielded the following expression for the ball surface temperature at contact center

$$\Delta T_b = 41.6\ P_H^{1.73}\ V_s^{.42}\ \left(\frac{1}{1 - .7R_a}\right) \qquad (61)$$

It is very interesting to note that the surface roughness factor $1/(1 - .7R_a)$ obtained from the experimental data (equation (61)) is in very good agreement with the factor recommended by AGMA (Curve (2) of Figure 60). In fact, the surface roughness factor of equation (61) lies in between curves (3) and (4) in Figure 60. For the case of the smooth ball (R_a = .011 μm), the surface roughness factor is close to unity and the expression for ΔT_b from equation (61) can be compared with the similar expression for ΔT_b derived earlier [equation (48), Chapter IV]. Even though a satisfactory agreement between the two expressions is observed, an exponent of 1.73 on P_H is obtained in equation (61) whereas an exponent of 1.34 was obtained earlier. The apparent discrepancy between the two values is due to a considerable scatter in the data when P_H, V_s, and R_a are all considered as variables. However, when the exponents on P_H and V_s from equation (61) are compared with the theoretical predictions (equation (45)) of 1.5 and .5 as exponents on P_H and V_s and keeping in mind the variation of traction coefficient with the sliding

velocity (discussed in Section A, Chapter IV), a reasonable agreement is observed.

A surface roughness factor of the form $(40R_a + 1)^{a_2}$ is more convenient for correlating the experimental data. Even though, there appears to be no special advantage of using the above form for the surface roughness factor, it is possible to use such a form simply for convenience. A multiple regression analysis of the data in Tables 8, 9, and 10, with the surface roughness factor of the above form, yielded the following expression for ΔT_b at contact center:

$$\Delta T_b = 37.8\ P_H^{1.84}\ V_s^{.31}\ (40R_a + 1)^{.18} \qquad (62)$$

The parameter Λ, which is the ratio of EHD film thickness h to the composite surface roughness σ, is a recognized parameter for predicting EHD contact performance [72]. For values greater than 2, no asperity interactions are expected. At Λ less than 1, severe asperity interaction is anticipated. The range $1 < \Lambda < 2$ is a transition region. The values of Λ obtained using R_a rather than r.m.s. roughness are not sufficiently different that the transition values noted above are significantly altered [72]. Also, in computing the parameter Λ, the film thickness value used is that measured for the smooth ball. This is necessitated for two reasons. First of all the interference fringe pattern used to determine film thickness disappears as the roughness is increased. Secondly, the meaning of film thickness is ambiguous at significantly high roughness levels, since the local thickness changes greatly from point to point. The appropriate Λ values are shown in

Figures 37, 56-58.

In the case of the smooth ball, Λ is greater than 2 for Hertz pressures up to 1.81 GPa, suggesting no asperity interaction. At P_H = 2.03 GPa, Λ is in the range 1 to 2. However, a subsequent measurement of the surface profile did not reveal any surface alteration. Experiments using the medium rough ball resulted in $\Lambda < 1$ for $P_H > 1.5$ GPa and $1 < \Lambda < 2$ at lower pressures. Moderate to severe asperity interaction is therefore expected at all speeds and loads investigated. A relocation surface profile measurement was obtained and is shown in Figure 61. At a Hertz pressure of 1.70 GPa it can be seen that peaks have been removed in the wear track. For the rough ball, Λ is less than one for all operating conditions. A profile measurement for P_H = 1.24 GPa and V_s = 5 m/s is shown in Figure 62. The removal of asperities is clearly visible on the trace. In addition, the alteration of the surface in the wear track could be visually detected.

The above observations reinforce the importance of the parameter Λ in describing the extent of asperity interaction. In addition, it is now apparent that significant asperity interaction will result in increased surface temperatures. As can be seen from Figure 61, the method has been successful in relocating the same area on the ball surface for re-examination. However, since it is not practical to obtain profiles of the entire wear track region before and after running in the EHD contact, an indication of no asperity interaction is inconclusive. Asperity interaction may have taken place at locations other than those measured.

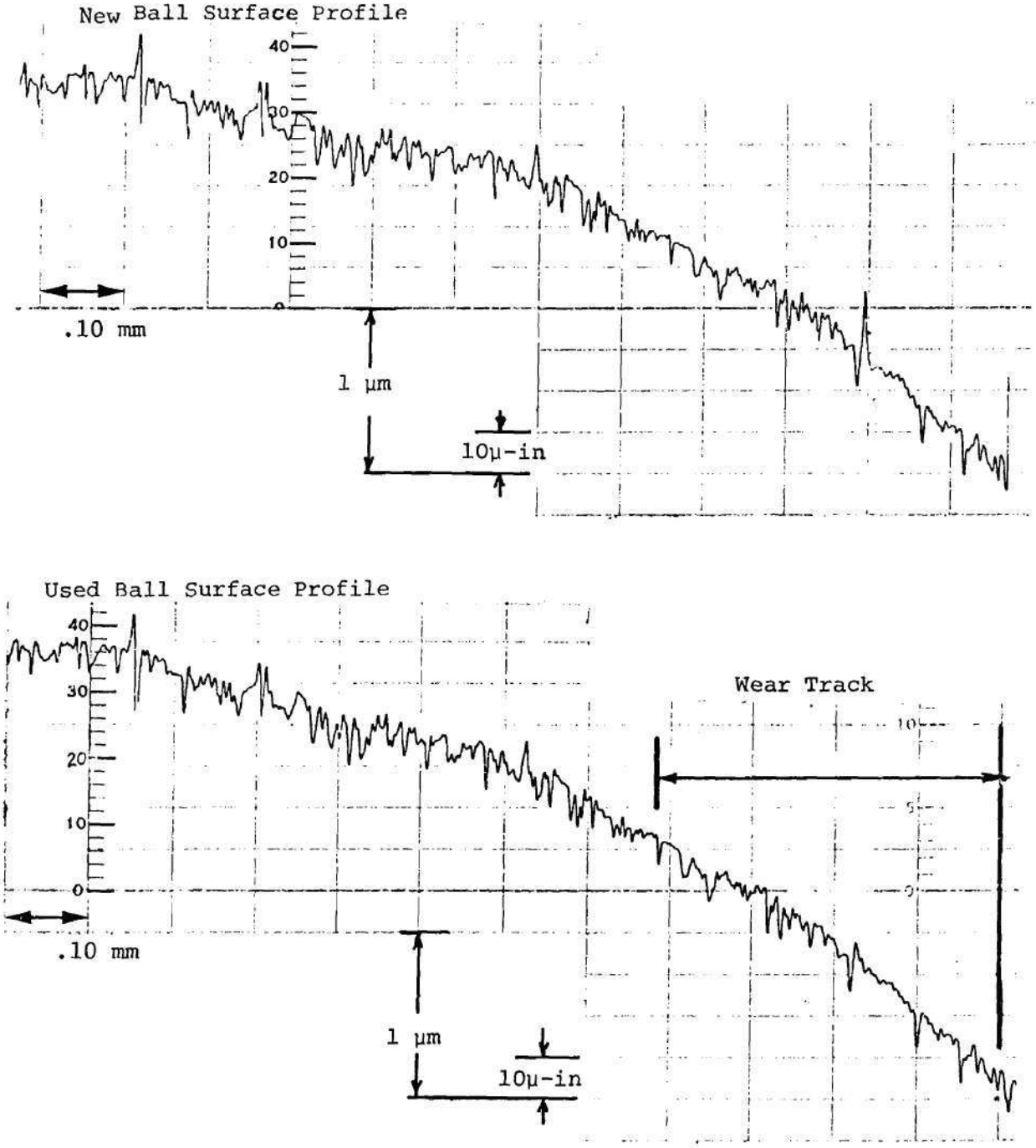

Figure 61. Relocation Profile for the Medium Rough Ball (.076 µm R_a), (P_H = 1.70 GPa, 0.83 $\leq V_s \leq$ 5.0 m/s).

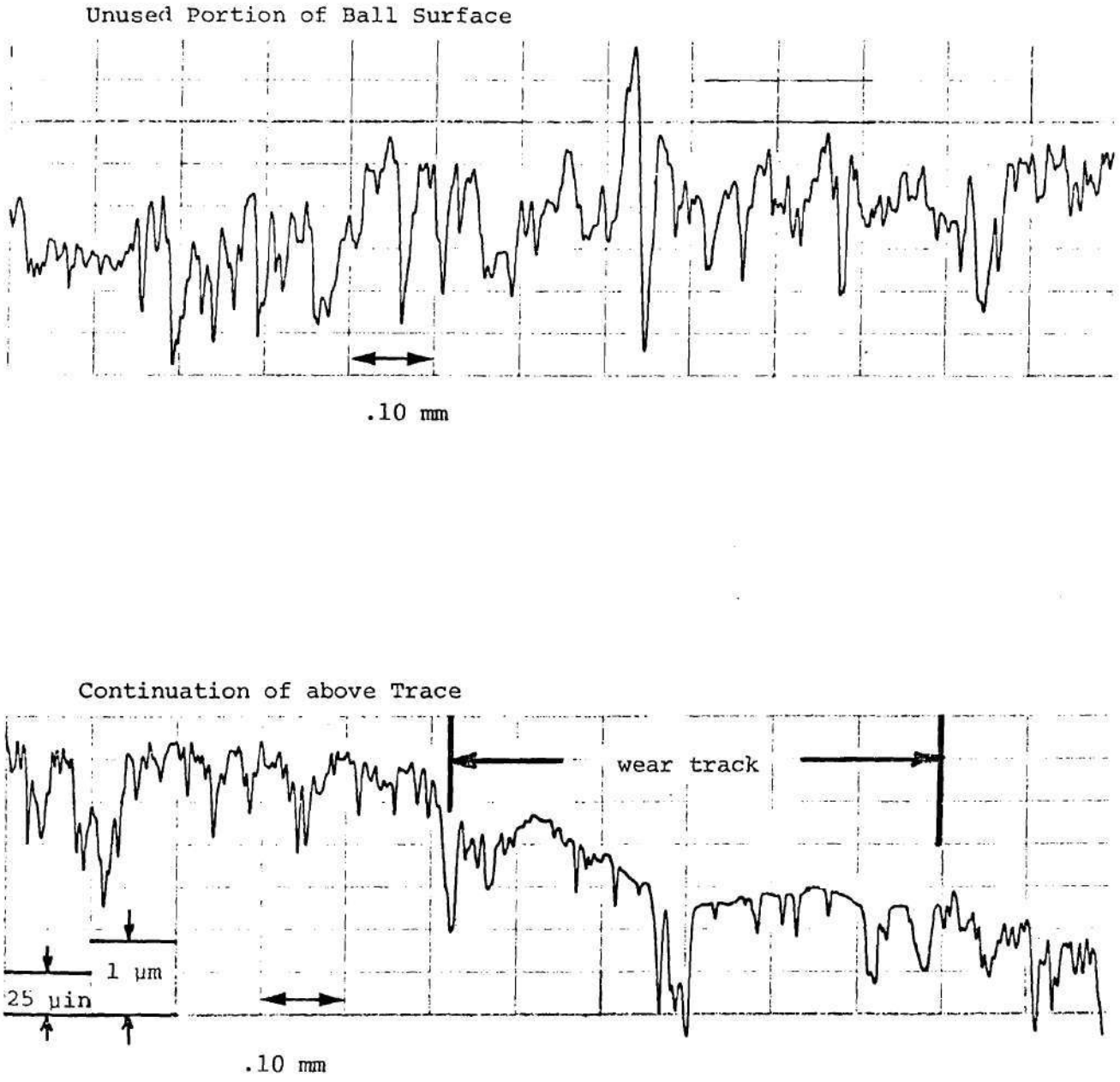

Figure 62. Surface Profile Showing Severe Wear, Rough Ball (.38 µm R_a) (P_H = 1.24 GPa, V_s = .5 to 5.0 m/s).

B. Ball Surface Temperature Fluctuations and Wear Study

High Frequency Temperature Fluctuations

It has been shown in the previous section that asperity interaction can significantly alter the ball surface temperature level. The results given thus far, however, are time-averaged temperatures obtained with the infrared detector in the DC mode. In this mode of operation, the highest frequency response is 400 Hertz. From the surface profile measurements (Figure 50) it has been determined that only a single asperity can occupy the detector's field of view (36 μm diameter) at any one time. However, at 1.0 m/s sliding velocity the asperity resident time in the field of view is only about 40 μs. The DC mode, therefore, cannot respond to a temperature rise caused by a single asperity interaction. The available AC mode of operation, however, can detect such temperature transients. The liquid nitrogen cooled detector has a response time of 8 μs. An important consequence of operating in the AC mode, however, is that the reference signal is absent. Instead, the instrument will produce a voltage difference proportional to the variation in target radiation emitted. Through an independent experiment, using an external chopper, it has been determined that the variation indicated in the AC mode is centered on the signal received in the DC mode. From this information a plot of time-averaged surface temperature along with the maximum and minimum values can be obtained.

Because electrical noise problems were encountered when using the AC mode, a variable frequency electrical band pass filter was also used. Although the noise and signal could not be entirely separated due to the closeness of their frequencies, a pass band of 1.0 to 20 KHz proved

effective, since the high peaks in the signal are within 20 KHz for most of the sliding speeds.

Figure 63 shows a plot of the ball surface temperature at the contact center as a function of Hertz pressure. The .076 μm R_a surface roughness ball was used at a sliding speed of 1.0 m/s. The plot shown was constructed using the DC mode data at five different Hertz pressures. In addition, the AC mode was used at all the Hertz pressure levels. As is shown in Figure 63, the AC data shows no fluctuation about the DC level up to P_H = 1.05 GPa, but shows an increasing amount of fluctuation as the pressure is increased. The upper and lower curves represent the range of temperatures detected. It is believed that the peak values represent individual asperity interactions. Figure 63 also shows the significance of the parameter Λ in predicting the onset of asperity interaction.

Upon examination of the AC radiation signal over a time interval of about one ball revolution it was found that the highest radiation emitted from the contact surface was immediately followed by a very low radiation value. This suggests that the high pressure and local energy dissipation at the asperity is causing the high temperature, while the region immediately behind the asperity is a relatively low pressure thick oil film in which the energy dissipation is low, resulting in a lower surface temperature. This reasoning depends on the assumption that the surface emissivity is constant over the region of interest, since radiation fluctuations have been interpreted as temperature fluctuations. Recent observations by Wedeven [154] of the passage of a debris dent

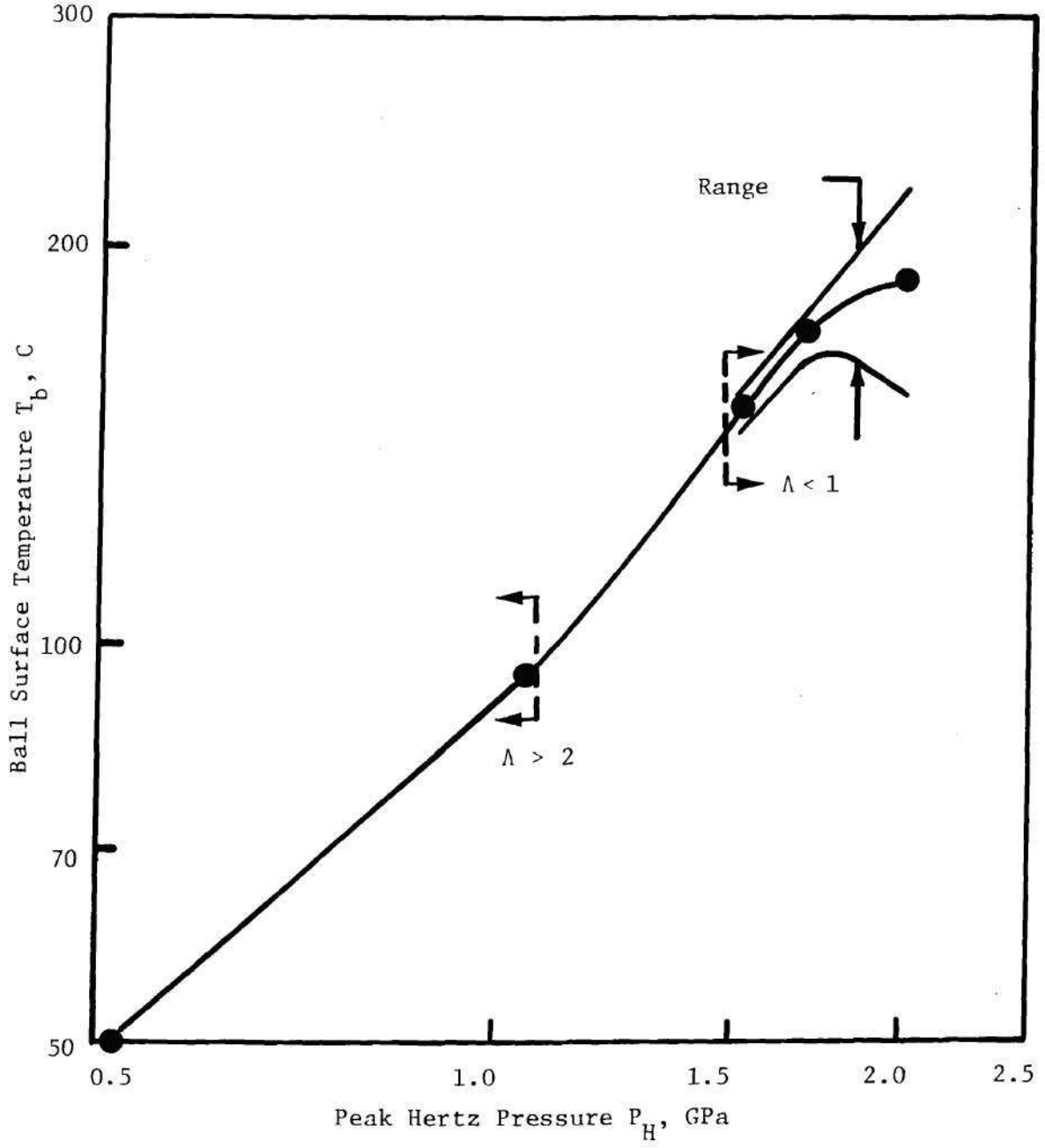

Figure 63. Average Value and Range of Ball Surface Temperature Fluctuation versus Peak Hertz Pressure (Medium Rough Ball: .076 μm R_a, Fluid N1, V_s = 1.0 m/s, V_{sa} = 0).

through an EHD contact, where he observed a decrease in film thickness at the leading edge of the dent compared to the value at the trailing edge, appear to support the above observation on asperity temperature.

It seems reasonable to consider that even though fresh metal surface may be formed at the asperity tip due to wear, the surface film formation on a fresh surface in an oil environment, which has absorbed oxygen present, occurs in the order of nanoseconds. Therefore, the surface emissivity would not be observably changed on the time scale of the measurements. The radiation fluctuations observed are therefore not affected by fluctuations in emissivity and are in fact due to temperature fluctuations. The generation of wear particles under such operating conditions has been confirmed through a ferrographic analysis of the used oil samples reported later in this section.

Figure 64 is a graph of the same data, along with data from higher sliding speeds. In all cases, the center value represents the DC (time averaged value). From this data it appears that the range of temperatures detected in the AC mode of operation increases significantly as more of the normal load is supported by individual asperities. This corresponds to a condition of decreasing Λ values. Similar results have been obtained for the case of the rough ball (.38 μm R_a), where the Λ values are much smaller and the magnitude of radiation fluctuations is much greater. For the case of the smooth ball, where Λ is never less than one, no high frequency temperature fluctuations have been observed.

Figure 65 shows the ball surface temperature data as a function of sliding velocity at various Hertz pressures. The time averaged values

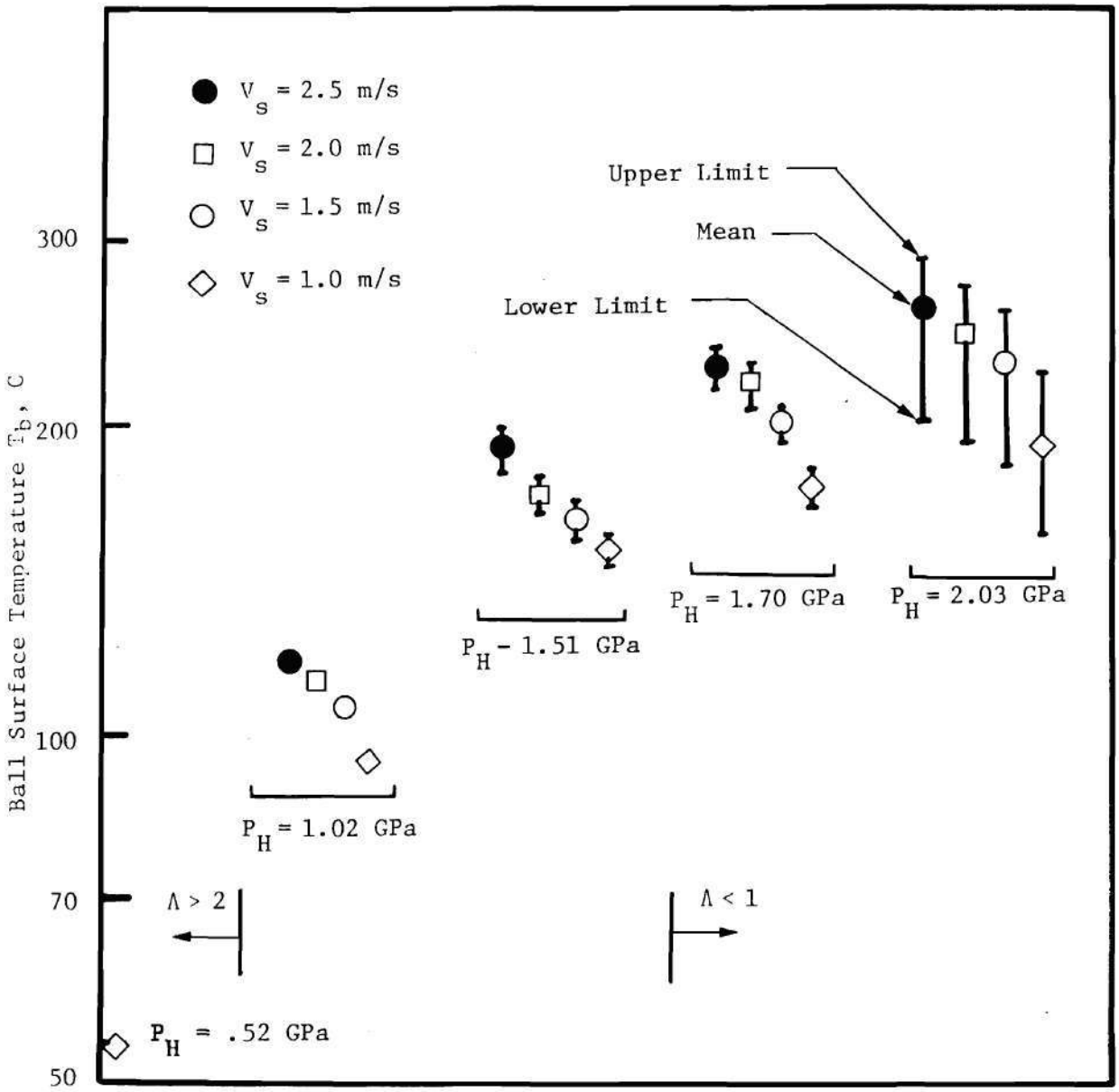

Figure 64. Average Value and Range of Ball Surface Temperature Fluctuations (Medium Rough Ball: .076 μm R_a, Fluid N1, V_{sa} = 0).

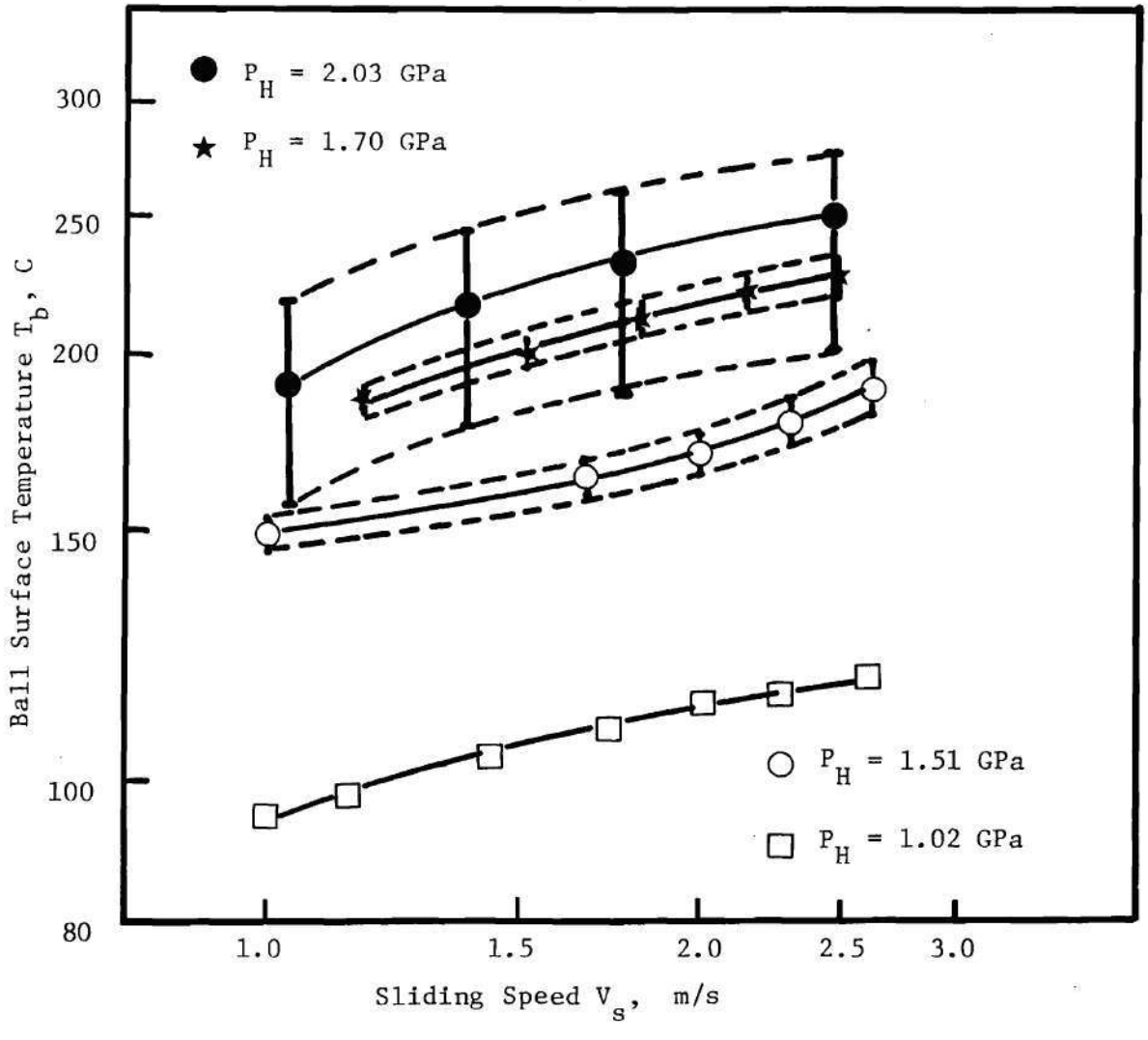

Figure 65. Average Value and Range of Ball Surface Temperature Fluctuation versus Sliding Speed (Medium Rough Ball: .076 μm R_a, Fluid N1, V_{sa} = 0).

of temperature along with the maximum and minimum values are shown over a range of 1.0 to 2.5 m/s of sliding speed, the range of temperature fluctuations increases but not drastically. However, the drastic increase in the range of temperature fluctuations with Hertz pressure is apparent from this figure.

Normal Load Sharing

The lubrication situation described in this section is characterized by the coexistence of elastohydrodynamic fluid film and interacting asperities. Such a situation is usually designated as partial elastohydrodynamic lubrication. In addition to many important parameters describing the contact, normal load sharing between asperities and EHD film is directly influenced by the degree of asperity interaction characterized by the lambda ratio (Λ).

It was mentioned earlier in this section that the upper curve in Figure 63 corresponds to the temperature developed at the site of an interacting asperity. Also, the lower curve in the same figure corresponds to the temperature of the fluid pocket (relatively low pressure region) in the neighborhood following an asperity. It can be seen from Figure 63 that the temperature of the fluid pocket (lower curve) increases up to a certain value of peak Hertz pressure (P_H), reaches a maximum, and then decreases with further increase in P_H. This can be explained as follows; even though the total load on the contact is increased, beyond a certain load, the average fluid pressure begins to decrease because the asperities share an increasing portion of the total load. In order to determine the exact proportion of the total load shared by the asperities, normal load sharing calculations were performed using Tallian's

approach [135,136]. Tallian's method was found more easily applicable for this purpose than the methods proposed by others [137,138]. These calculations were made for the operating conditions corresponding to Figure 63. An approximate statistical description of the surface is used for the medium rough ball. Some details of the calculation appear in Appendix H.

Table 11 shows the calculated value of the portion of load carried by the EHD film (W_{EHD}) and the corresponding average fluid pressure (P_{EHD}) at various normal loads for two different asperity slopes (σ_θ). The area of fluid pockets is assumed to be equal to the Hertzian area. This assumption is valid since the area of the contacting asperities is indeed small [55]. The assumed RMS slopes of asperities (σ_θ), represent their typical values. It can be seen (Table 11) that the average fluid pressure increases with the normal load up to a certain value, reaches a maximum (depending on σ_θ), and then decreases with further increase in normal load. Although the calculations shown in Table 11 correspond to a sliding velocity of 1.0 m/s, similar results were obtained for other sliding speeds referred to in Figure 64.

Figure 66 shows a plot of average fluid pressure versus peak Hertz pressure for the medium rough ball at a sliding velocity of 1.0 m/s, corresponding to the results shown in Table 11. The dotted line corresponds to conditions when the entire load is supported by the EHD film. At low values of Hertz pressure, the Λ ratio is greater than one and therefore, the entire load is supported by the EHD film. As the Hertz pressure is increased, Λ decreases below one and the curve falls below the dotted line. The influence of the asperity slopes is apparent at this

Table 11. Normal Load Sharing Between Asperities and the EHD Film (Calculated using Tallian's (Ref. (135)) approach)
(Medium rough ball: .076 μm R_a, Fluid N1, V_s = 1.0 m/s, V_{sa} = 0)

				σ_θ = .0349		σ_θ = .122	
W N	P_H GPa	P_{avg} GPa	Λ	W_{EHD} N	P_{EHD} GPa	W_{EHD} N	P_{EHD} GPa
8.9	.52	.3483	4.33	8.8857	.3479	8.8590	.3469
17.8	.65	.4354	3	17.7590	.4346	17.6700	.4326
25.4	.74	.4925	2.5	25.1537	.4886	24.6639	.4790
40	.86	.5731	2	39.0459	.5590	36.7755	.5266
66.7	1.02	.6777	1.5	62.3589	.6362	54.3259	.5517
214.7	1.51	1.0044	1	192.4309	.9002	152.7890	.7147
222.4	1.52	1.0184	.8	191.2383	.8757	141.6173	.6485
253.5	1.59	1.0625	.6	208.0815	.8720	143.6693	.6021
293.6	1.67	1.1145	.4	228.1304	.8660	146.4828	.5561
307.4	1.7	1.1270	.33	233.7596	.8571	146.2137	.5361

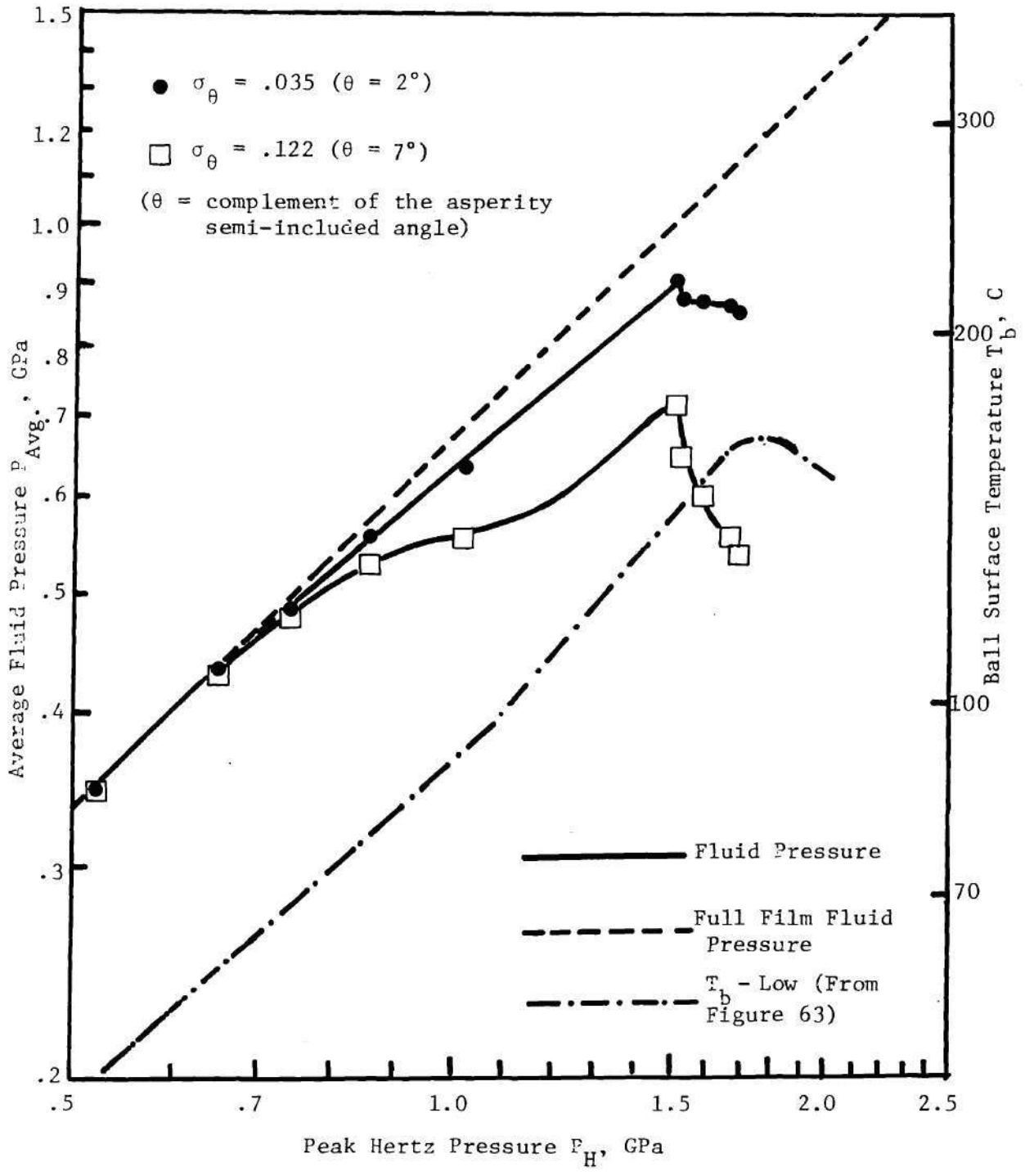

Figure 66. Average Fluid Pressure versus Peak Hertz Pressure under Partial EHD Conditions (Medium Rough Ball: .076 μm R_a, Fluid N1, V_s = 1.0 m/s, V_{sa} = 0).

stage. With further increase in P_H, the average fluid pressure reaches a peak and then starts decreasing. The trend shown in Figure 61 is in excellent agreement with temperature fluctuation results shown in Figure 63. The position of peak fluid pressure (Figure 66) and that of maximum fluid pocket temperature (Figure 63) also are in very good agreement. Even though the exact value of σ_θ for the medium rough ball was not measured, the two values of .035 ($\theta = 2°$) and .122 ($\theta = 7°$) appear to be in a reasonable range and therefore direct comparisons can be made.

It therefore appears that the temperature of the fluid pocket increases with normal load up to a certain value, reaches a maximum, and then decreases with further increase in normal load. This phenomenon is due to an increasing portion of the load shared by the asperities when the normal load on the contact is increased.

Wear Study

The objective of this investigation was to use the ferrographic and spectrographic oil analysis techniques described in Appendix I to determine the presence of wear particles in the experiments reported earlier in this section. The presence of wear particles in the used oil sample confirms the occurrence of asperity interactions. It was also found useful to determine the total amount of wear debris and the wear particle types generated in a sliding EHD contact as the film thickness was gradually decreased and asperity interactions began to occur. In other words, the effect of Λ ratio on the amount and type of wear debris was investigated in this part of work. This is also closely linked with the transition from one to another among the following regimes: EHD,

partial EHD, boundary, and eventually catastrophic failure.

The EHD apparatus used in this study has been explained in Chapter II. Film thicknesses were determined optically at the contact center for the smooth ball. These values were also used for the medium rough and rough ball series. The temperature of the oil reservoir was monitored with a thermocouple as a function of test time. The oil was not recirculated in these experiments in order to eliminate particle contamination from the recirculation system. A total lubricant charge of 50 cm^3 was used. Three series of test balls (AISI 52100, chromium steel) were used having roughnesses .011, .076, and .38 μm R_a respectively. These balls will be referred to as smooth (S), Medium Rough (MR), and Rough (R), respectively, and have been referred to earlier in this chapter. Tests will be referred to as S-1, MR-1, R-1, etc. corresponding to the ball roughness and load. Experimental conditions included a sliding speed of 1.08 m/s, a range of loads from 8.9 to 522 newtons (peak Hertz stress range, .52 to 2.03 GPa), and a test duration of 25 minutes. Experimental conditions for each test are summarized in Table 12. Tests were conducted at room temperature. The fluid used in this study is the napthenic mineral oil N1 that has been used earlier.

Ferrogram Results. Optical density measurements were made on each Ferrogram (corresponding to each test listed in Table 12) at several different locations: entry, 54, 50, 40, 30, 20, and 10 mm. In addition, a composite or representative density was determined by averaging the several different readings. A density reading of less than 1 percent was treated as a

Table 12. Experimental Test Conditions for Oil Samples Tests for Wear Study

Test	Load, N		Hertz Pressure GPa		Sliding Speed, m/s	Initial Λ Ratio
	Top Contact	Bottom Contact	Top Contact	Bottom Contact		
S1	8.9	3.6	.52	.39	1.08	42
S2	67	27	1.0	.76	1.08	15
S3	215	88	1.5	1.1	1.08	10
S4	307	125	1.7	1.3	1.08	3.6
S5	522	213	2.0	1.5	1.08	2.7
MR1	8.9	3.6	.52	.39	1.08	8.4
MR2	67	27	1.0	.76	1.08	3.1
MR3	215	88	1.5	1.1	1.08	2.0
MR4	307	125	1.7	1.3	1.08	0.6
R1	8.9	3.6	.52	.39	1.08	1.7
R2	67	27	1.0	.76	1.08	0.6
R3	215	88	1.5	1.1	1.08	0.4
R4	307	125	1.7	1.3	1.08	0.1

zero. Optical density measurements for all tests appear in Table 13.

The author is indebted to Mr. William R. Jones, Jr. of the NASA Lewis Research Center, Cleveland, Ohio for the ferrographic analysis of oil samples and the interpretation of Ferrogram results.

Photomicrographs of the Ferrogram entry region were taken for each of the tests with smooth, medium rough, and rough series. The general trend of increasing wear particle density with increasing load (or decreasing film thickness) was evident in most cases. Occasionally, nonmetallic debris or large oxide flakes, unrelated to the wear process, were observed which caused some high optical density readings. In fact, many of the density readings in the smooth series were caused, in part, by this type of debris.

Often pile-ups of both metallic and nonmetallic debris occur at the entry position. Since this makes it difficult to assess the wear level, an alternate procedure is to examine the debris at a location some distance from the entry. Typically this is the 54-mm position. Micrographs taken at this location for all tests appear in Figures 67, 68, and 69. Again, the trend of increasing amounts of wear debris with increasing load in both the medium rough and rough ball series is obvious. However, most of the particles present at the 54-mm position in the smooth series are not wear related. These particles are transparent and nonmetallic.

A convenient parameter for predicting the degree of surface interactions is the ratio of the central film thickness to the composite surface roughness. This parameter (Λ) has been referred to earlier in

Table 13. Optical Density of Ferrograms at Various Ferrogram Positions

Position	Optical Density at Various Positions on Ferrogram, Percent							Composite Density Percent
	Entry	54	50	40	30	20	10	
S1	<1	<1	1.2	<1	<1	<1	<1	0.2
S2	15.3	4.4	1.0	1.9	1.3	1.8	<1	3.7
S3	4.2	4.3	<1	<1	<1	1.5	<1	1.4
S4	3.1	<1	<1	<1	<1	<1	<1	0.4
S5	7.1	<1	<1	1.2	<1	<1	<1	1.2
MR1	1.6	1.8	1.8	<1	<1	4.1	2.6	1.7
MR2	3.7	1.6	1.2	<1	1.0	1.8	1.5	1.5
MR3	5.3	2.3	2.0	<1	<1	1.5	1.7	1.8
MR4	19.8	5.8	4.3	3.3	4.0	4.0	3.7	6.4
R1	7.1	2.0	1.0	1.4	<1	1.3	<1	1.8
R2	21.3	9.4	5.4	5.0	2.8	2.4	1.0	6.7
R3	36.9	24.6	19.6	14.0	10.4	11.7	14.0	18.7
R4	40.6	39.5	28.8	24.8	23.4	16.0	15.4	26.9

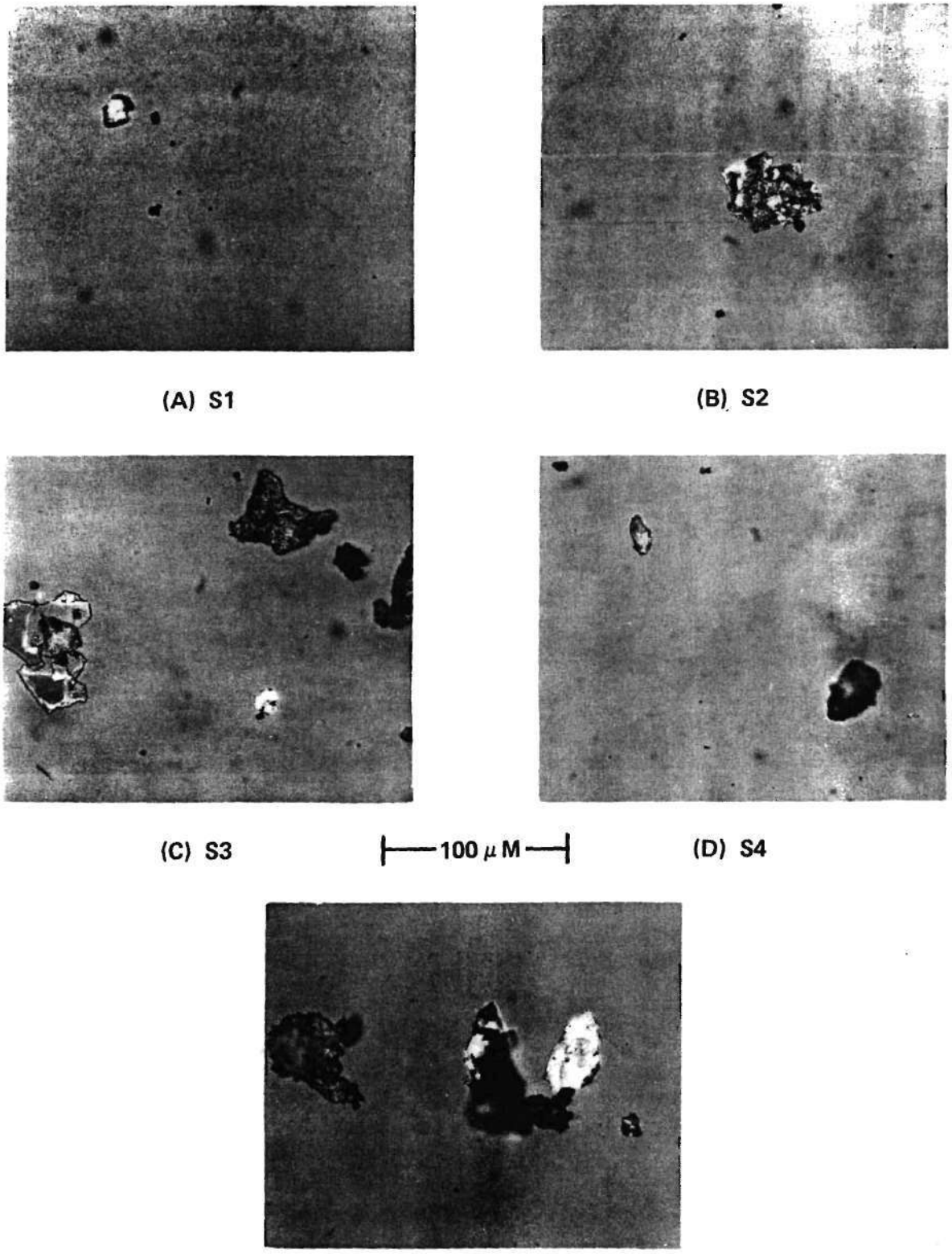

Figure 67. Ferrogram deposit at 54 mm for smooth series.

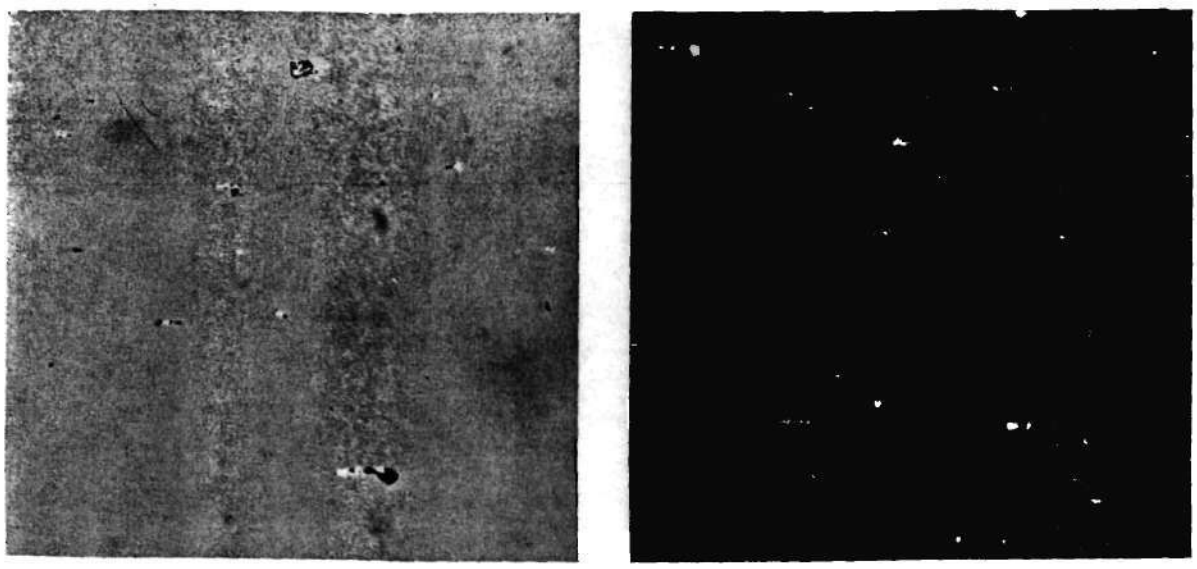

(A) MR1 ⟵100 μM⟶ (B) MR2

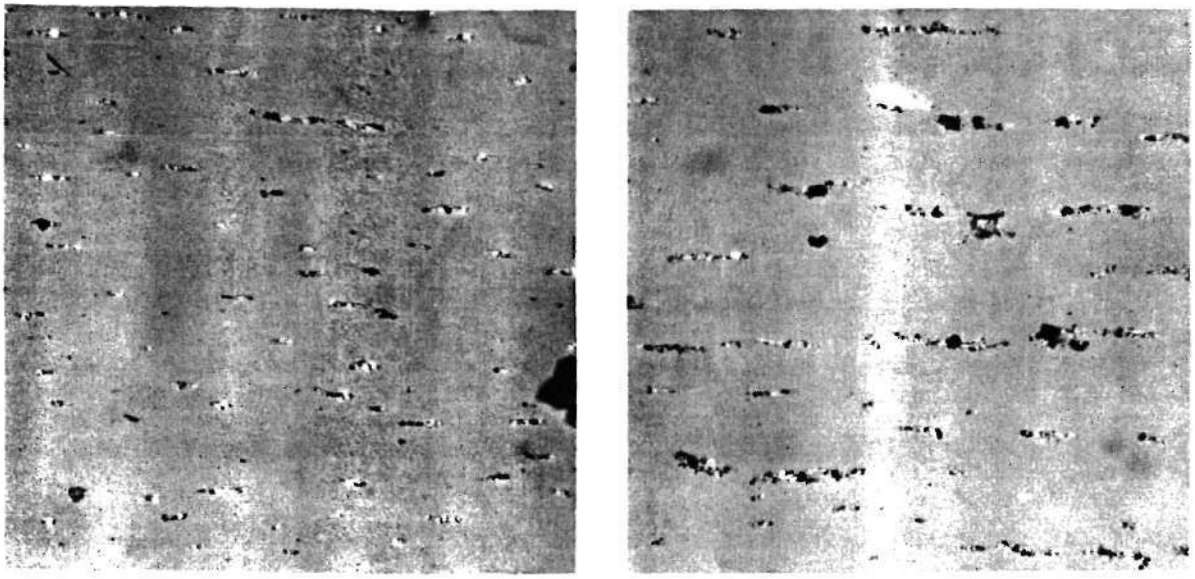

(C) MR3 (D) MR4

Figure 68. Ferrogram deposit at 54 mm for medium rough series.

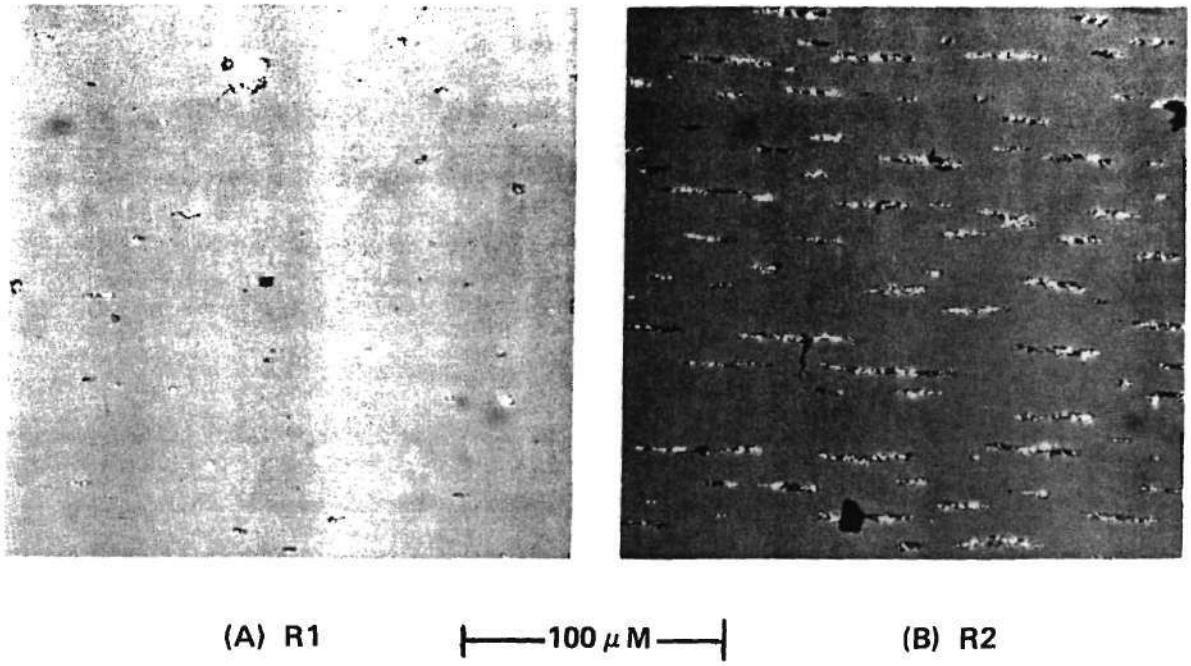

Figure 69. Ferrogram deposit at 54 mm for rough series.

this section and also in the previous section. The wear rate as measured by the amount of debris collected on the Ferrogram appears to be a function of the Λ ratio. Since the oil recirculation system was not used in the wear experiments, the bath temperature increased during the tests as reported in Table 14. In addition, there was a measurable decrease in ball surface roughness for tests MR3 and 4, R2,3 and 4 during running. Taking all these factors, the Λ ratios at test conclusion were lower than initial Λ values. However, it was determined that this change in Λ did not affect the general conclusions reached in the wear experiments.

A plot of composite Ferrogram density for each test as a function of initial Λ ratio appears in Figure 70. The large and very rapid increase in particle density at low Λ values is evident. The transition to the high wear regime occurs as the Λ ratio approaches 1. This is in agreement with the findings of other investigators. Tallian [139] has shown that the onset of surface distress occurs at a Λ value of about 1.5. Czichos [140] reports that the change from a full EHD film to continuous asperity contact occurs as Λ decreases from 2.5 to 0.7. In Figure 70, at Λ values greater than 2, a composite particle density of between 1 and 2 percent is observed. Since a full film should be present at these higher Λ ratios, little wear should take place. Therefore, these density readings represent the background or contaminant particle density for this set of experiments.

As shown in Table 13, there was an overlap of Λ values in each test series. There were four sets of tests that yielded similar initial Λ ratios. These were: S3-MR1, S5-MR2, MR3-R1, and MR4-R2. One would

Table 14. Oil Bath Temperatures (C) at Various Test Times during Oil Samples Tests

Sample No.	Time mins 0	3	6	9	12	15	18	21	24	25
S1	25.5	26	26.3	26.6	26.9	27.2	27.5	27.7	27.8	27.8
S2	25.5	28.5	31.5	32.5	34	35.5	37	38	39.1	39.5
S3	24.5	33.5	38.5	43.7	48.2	52.3	57	58.9	62	63
S4	23.5	30.3	35.7	40	44	47	50.5	54	57.3	58.5
S5	26	32.5	36.9	40.2	43.2	46.1	48.7	51	53.5	54.3
MR1	23.5	23.9	24.4	24.8	25.1	25.4	25.7	25.9	26.1	26.2
MR2	22.3	26.7	29.1	31.1	32.9	36.4	35.9	37.4	38.6	39.0
MR3	23.8	35.8	43.3	50	56.7	61.5	64.6	68.1	72	73.2
MR4	25.2	41.7	55.5	62.8	70.5	76.5	82.3	85.4	*-	-
R1	25	25.6	26.3	26.8	27.2	27.6	28	28.4	28.7	28.8
R2	24.9	30.3	33.7	36.3	38.3	40.1	41.9	43.4	44.8	45.2
R3	25	42.7	52.3	59.3	65.3	71	75.6	80.3	84.2	85.5
R4	22.1	43.2	57.3	65.7	73.3	80	86.4	92.1	*-	-

*Tests terminated at 23 minutes due to failure of adhesive on driving collars.

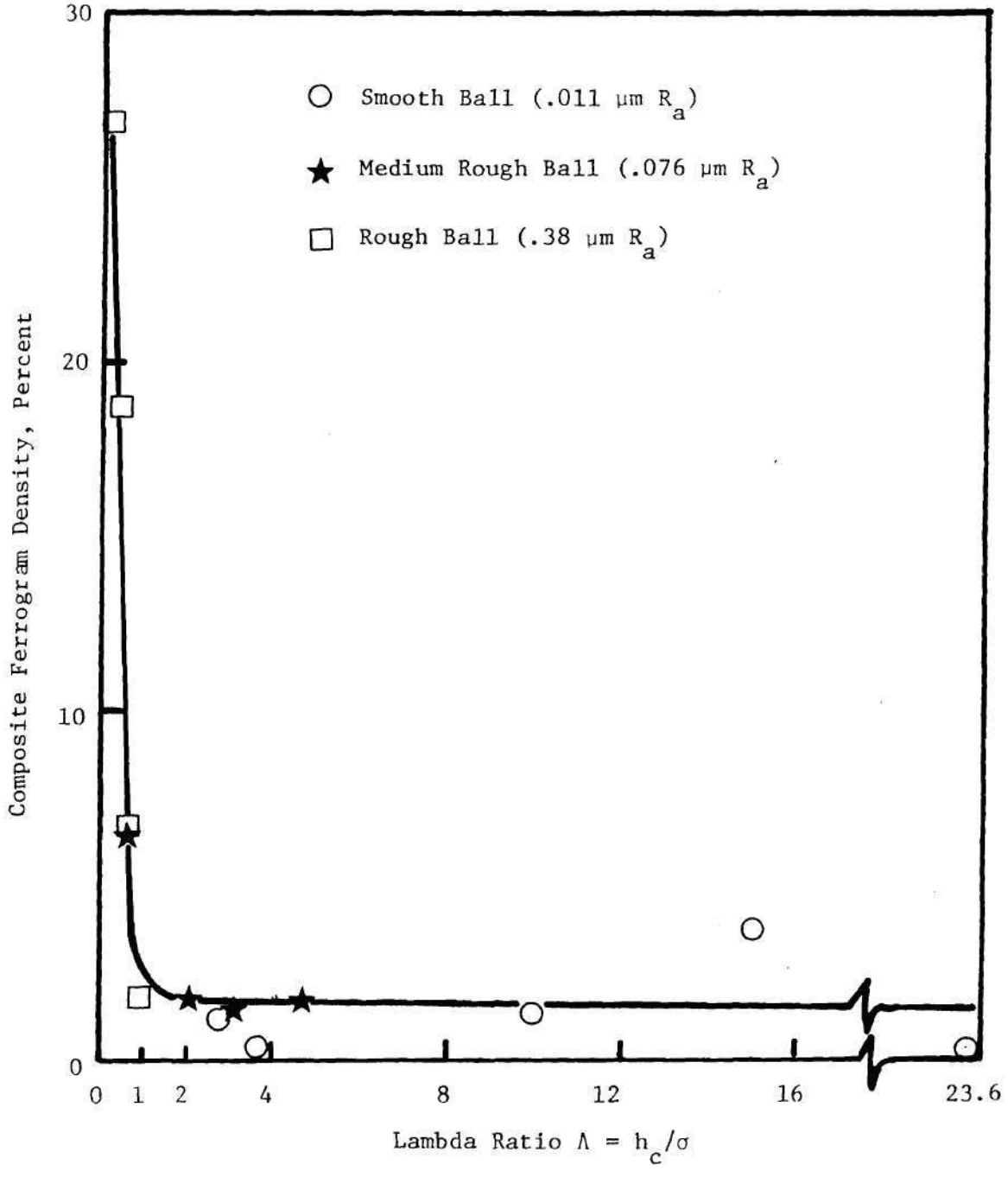

Figure 70. Composite Ferrogram Density versus Lambda Ratio.

expect the generation of a similar amount of debris under these similar test conditions. The composite ferrogram densities for these four sets of experiments appear in Figure 71 and a good correlation is observed, especially at values of Λ less than 1.

Microscopic examination of the wear debris generated during these studies yielded the following information. Essentially, all of the metallic wear particles, regardless of the initial surface roughness, were of the "normal rubbing wear" variety. That is, they were composed of small asymmetric thin (metallic) flakes. These flakes were typically less than 10 μm in major dimension and no more than 1.5 μm thick. On the ferrograms, these particles are typically arranged in strings due to the magnetic field generated by the ferrograph. Some further details of wear particles have been reported in reference [141]. These findings about wear particle morphology are in agreement with the findings of Reda, et al. [158].

Spectrometric Oil Analysis Results. An emission spectrograph was used to analyze each oil sample from this study. An unused oil sample was also tested as a blank. The elemental concentrations from the blank were then subtracted from all other readings and these results appear in Table 15.

It is obvious from Table 15 that most of the samples were barely within the limits of detection for the emission spectrograph. Little iron-containing wear debris was detected until the relatively high wear situation of the rough ball series was reached. However, even at the highest wear condition, R4, which had a composite ferrogram density of 26.9, the spectrograph only detected 4 ppm of iron. This indicates that

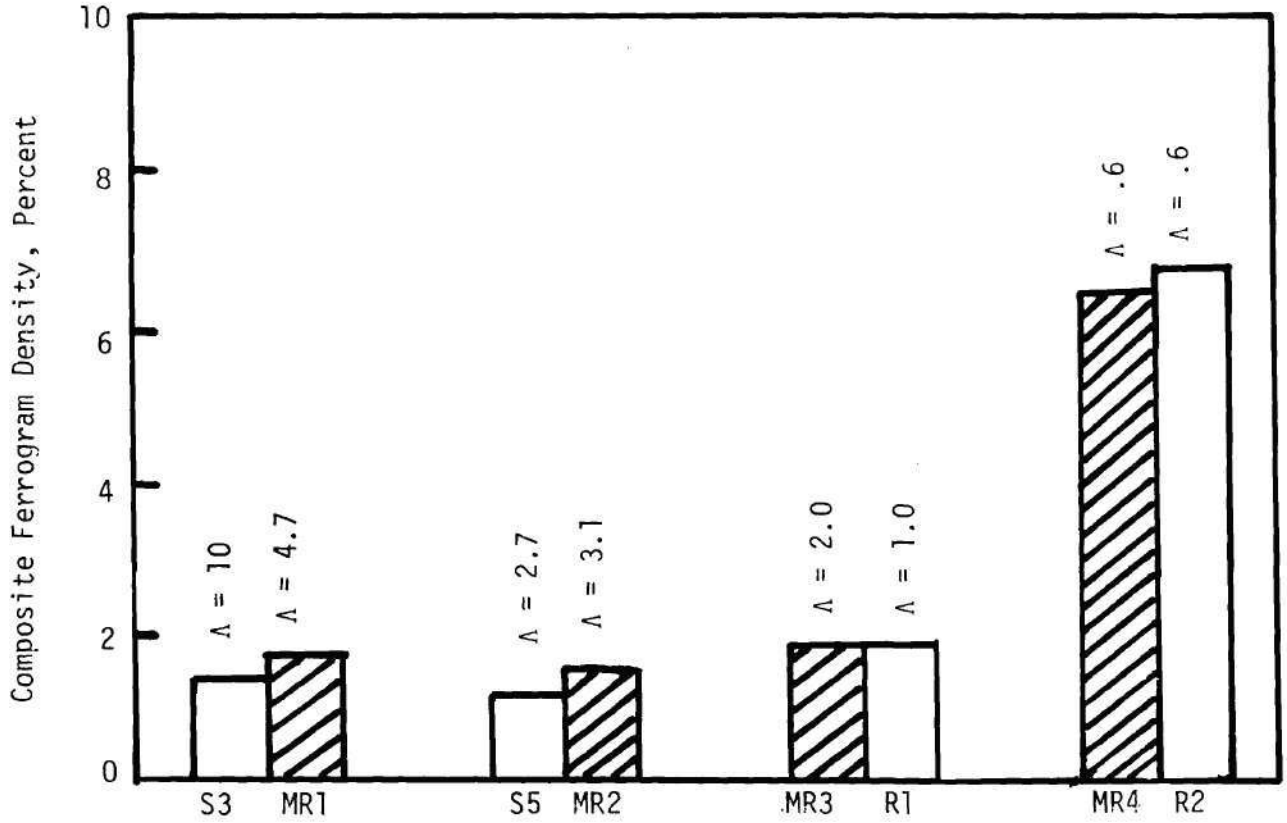

Figure 71. Comparison of Composite Ferrogram Densities at Similar Λ Ratios.

Table 15. Spectrographic Analysis of Oil Samples

	Element Concentration in Parts per Million							
Sample	Fe	Al	Cr	Ni	Pb	V	Mn	Mo
S1	-	-	-	-	-	-	-	-
S2	1	2	1	-	1	-	1	1
S3	1	-	-	-	-	-	-	-
S4	1	-	-	-	1	-	1	-
S5	-	-	1	-	1	-	-	-
MR1	-	-	-	1	-	2	1	-
MR2	1	-	-	-	-	-	-	-
MR3	1	-	-	-	-	-	-	-
MR4	1	-	1	-	1	1	-	-
R1	-	-	-	-	-	-	-	-
R2	2	-	-	-	-	-	-	-
R3	3	-	-	-	-	-	-	-
R4	4	3	-	-	-	-	-	-

for detecting the iron-containing wear debris from these studies, the Ferrograph is more sensitive than the normal SOAP procedures.

The elements, other than iron, present in the oil samples probably reflect the background variation in the blank. Only chromium is present in the 52100 steel (1.5 percent) and it is at too low a concentration to be detected in these experiments. Aluminum in sample R4 is related to the driving collar failure which resulted in rubbing against the aluminum cup.

In order to compare the SOAP and ferrogram the following assumptions were made. The average dimensions of the Ferrogram deposits were assumed to be: 50 mm long x 0.10 mm wide x 1.5 μm thick. Then for complete coverage (100 percent density reading), this corresponds to a particle volume of 7.5×10^{-3} mm^3. With a specific gravity of 8, the total mass of the deposit would be about 60 μg. Since approximately 3 grams of oil are passed over each Ferrogram, 60 μg of wear debris would represent about 20 ppm by weight. Multiplying the fractional optical densities of the rough ball series times 20, one obtains the following results: R1-0.4 ppm, R2-1 ppm, R3-4 ppm, and R4-5 ppm. These results are remarkably close to the SOAP values considering the number of assumptions that were made.

It was also found useful to calculate the wear coefficient K_W corresponding to the above wear experiments. K_W is defined as

$$K_W = \frac{\Omega \cdot H}{W \cdot S} \tag{63}$$

where Ω is the wear volume in mm^3, H is the hardness of steel in MN/m^2,

W is the normal load in N and S is the distance travelled by a point on the ball surface in mm. For a lubricant sample of 3 cm^3, the wear volume is 7.5×10^{-3} mm^3 (from the above calculation). Since a total lubricant charge of 50 cm^3 was used, total wear volume is 125×10^{-3} mm^3. Using the above definition of K_W, and considering that wear occurs in the three support contacts also, a value of $.2 \times 10^{-6}$ was obtained for the sample R4. This value of K_W shows that the operation of the system was still in the low wear regime and therefore no catastrophic failure could be expected.

Average traction coefficients for comparable tests measured at a steady state bath temperature of 40° C appear in Figure 72. As one would expect, fairly constant traction values (0.061 to 0.062) were observed for all tests at Λ ratios greater than 1.5 where a full EHD film existed. As asperity interactions increased as Λ decreased below one, the traction values also increased, as expected. No abrupt traction increases or transitions were observed which would have signaled a boundary film failure or a catastrophic failure mode. This agrees with the wear particle analysis previously discussed.

The following conclusions were reached from the wear study.

(1) The total amount of wear debris correlated well with calculated (film thickness to roughness) ratios. Much debris was observed at $\Lambda < 1$, little debris at Λ's > 1.

(2) The wear particles that were generated were metallic and almost exclusively of the normal rubbing wear type.

(3) Similar amounts of wear debris were observed in the different test series (different ball roughnesses) when compared at similar Λ ratios.

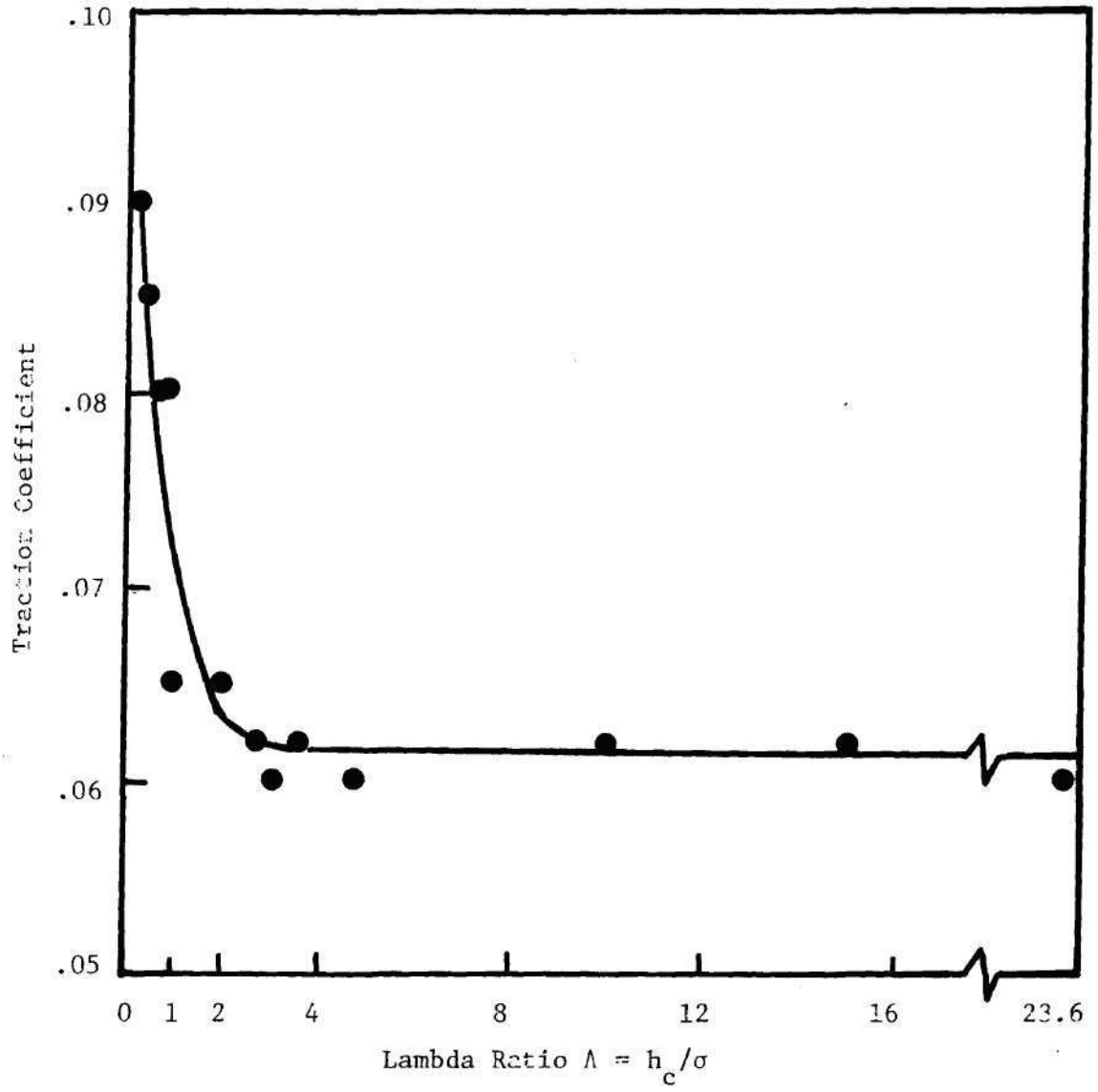

Figure 72. Coefficient of Friction versus Lambda Ratio.

It can be seen that these conclusions clearly support the occurrence of asperity interactions as predicted by the Λ ratio and therefore the onset of temperature fluctuations as postulated earlier in this section.

C. Frequency Analysis of Surface Profiles and Temperature Fluctuations, and their Correlational Study

In the previous sections, surface roughness effects on temperature and wear were described, and the importance of Λ-ratio was investigated. In this section, an extension of the work on the frequency or wavelength aspects of the surface profile signal and its influence on surface temperature, is reported.

In order to study the ball surface profile in the frequency or wavelength domain, the profilometer output was first recorded on magnetic tape. This was done for samples of balls from the three roughness classifications, both before and after running in the EHD simulator. The recording of the profilometer trace was transferred to a Hewlett-Packard Fourier Analyser. The first step in any analysis performed by this instrument is an A/D conversion. After analysis of the digital representation of the input signal, the results were printed, and a D/A conversion made and the results were plotted and displayed on a CRT.

Figure 73a shows the surface profile of the unused ball having an initial surface roughness of 0.38 μm R_a. The trace represents the signal after the A/D and D/A conversions and is an excellent replica of the original signal plotted by the Bendix profilometer. The distance along the ball surface is shown in terms of the Hertzian contact diameter, d. For the conditions of steel on sapphire at 1.24 GPa peak Hertz pressure,

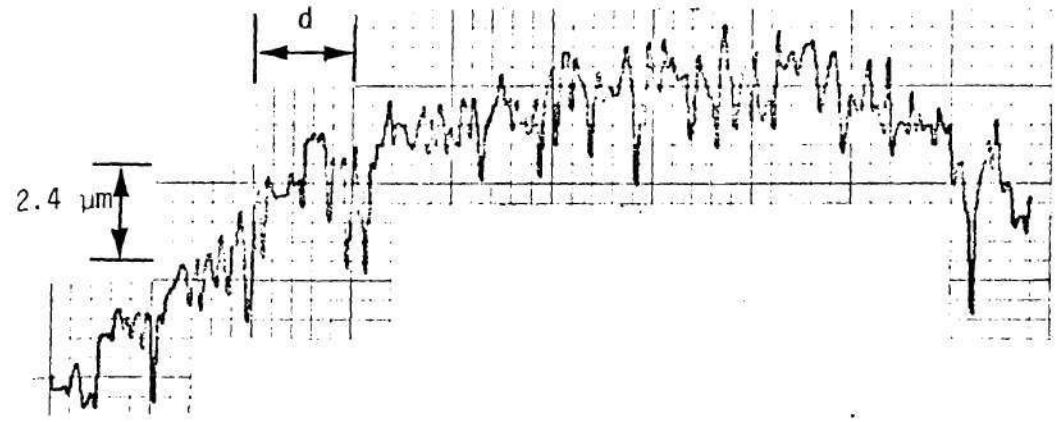

a) Unused ball surface (.38 µm R_a roughness).

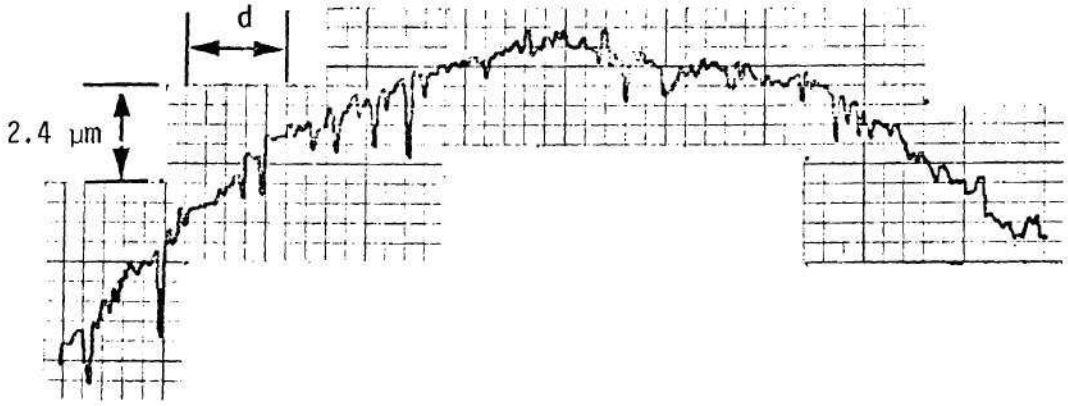

b) Ball surface after running 24 minutes (.25 µm R_a roughness).

Figure 73. Surface Profiles in the Direction of Sliding (P_H = 1.24 GN/m^2, V_s = 1.02 m/s, Hertz Diameter d = 0.43 mm, pure sliding).

the calculated contact diameter is 0.43 mm.

Figure 73b shows the same ball after running for 24 minutes in the simulator. The profile traces shown in Figure 73 were taken in the direction of the sliding motion. No attempt was made to measure the profile at precisely the same location on the ball surface. The traces taken are of sufficient length that they should be representative of any position within the wear track. The conditions of 1.24 GPa and V_s = 1.02 m/s should result in a value of $\Lambda < 1$ based on the unused ball surface roughness. The value $\Lambda < 1$ indicates that asperity interaction should be expected. Comparing the two traces in Figure 73, it is apparent that the 24 minute run-in period has resulted in a smoother surface. The roughness is .25 μm R_a which results in $\Lambda \simeq .4$. The 15.9 mm radius of curvature of the ball surface can also be seen.

The primary function of the Fourier Analyzer is to perform the Fast Fourier Transform (FFT) on the time varying input signal. A convenient way of displaying the amplitudes of the component terms in Fourier series is through the power spectrum. The input to the analyzer is a time varying voltage. After the A/D conversion, the FFT results in a complex amplitude for each of the 127 (plus a constant) terms used in the series. Each of these terms is assigned a pair of channels in the analyzer. The frequency range, and therefore, frequency increment can be selected. The frequency assigned to two adjacent pairs of channels differs by a constant. The resulting plot of the power spectrum is against the independent variable, frequency. The value of the ordinate at each center frequency (channel) is the product of the complex amplitude for that frequency and its conjugate. The units are, therefore, $(\text{volt})^2$

versus Hz. The D/A conversion makes the plotted results appear continuous, but all of the data processing was done digitally in terms of the coefficients of the first 127 terms of the Fourier series.

Although the results are plotted on a linear frequency scale in the analyzer, this is not a convenient representation for this study. This is due to the fact that the frequency is influenced by the profilometer stylus scanning speed and differences between magnetic tape recording and play-back speeds. In order to remove these effects, the abscissa has been changed to read wavelength. The unit of wavelength selected is d, the Hertz contact diameter of 0.43 mm. The power spectra of the profiles shown in Figure 73 are given in Figure 74.

The first four channels (0-3) were cleared prior to plotting. This is because the values are so large compared to the values in higher channels (see insert), that a plot would show only the very low frequency components. The contents of channels 0-3 are however given in the inserts in Figure 74. Therefore, only components having wavelengths <3d have been plotted. In comparing the power spectra for the unused and run-in ball surface profiles, note the factor of two change of scale in Figure 74a versus 74b. The most apparent contrast is the reduction of the components having wavelengths <2d. Comparing the tabular data in Figure 74, it appears that roughness components having wavelengths >2d remain essentially unchanged after the 24 minute run-in period. The nine percent difference in DC level can be attributed to slight differences in signal amplification in obtaining the two surface profiles. The most drastic change occurs for a wavelength of one Hertz diameter. This component has been reduced by more than a factor of eight.

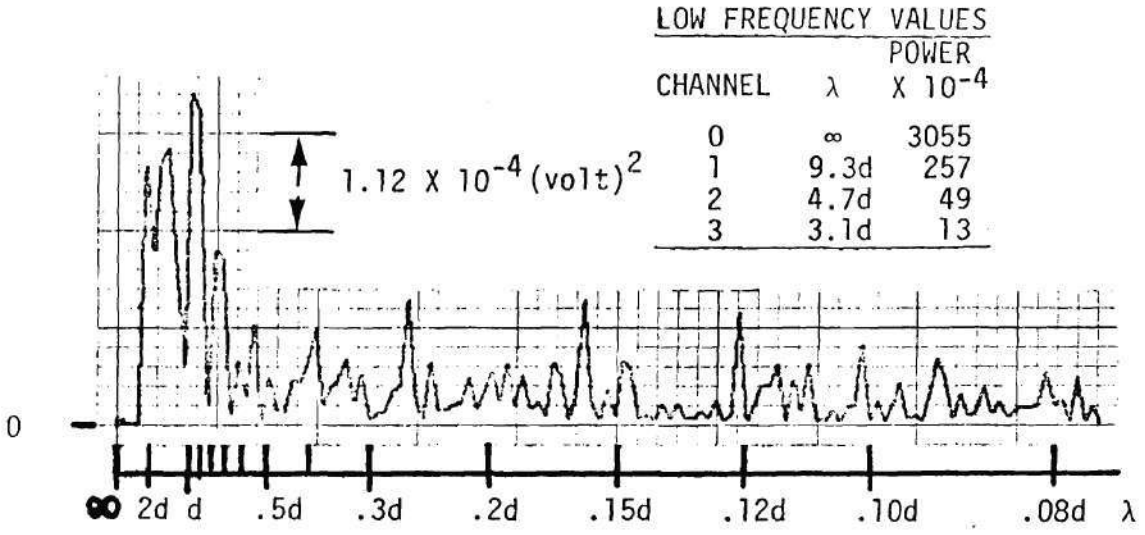

a) Unused ball surface. (.38 μm R_a roughness)

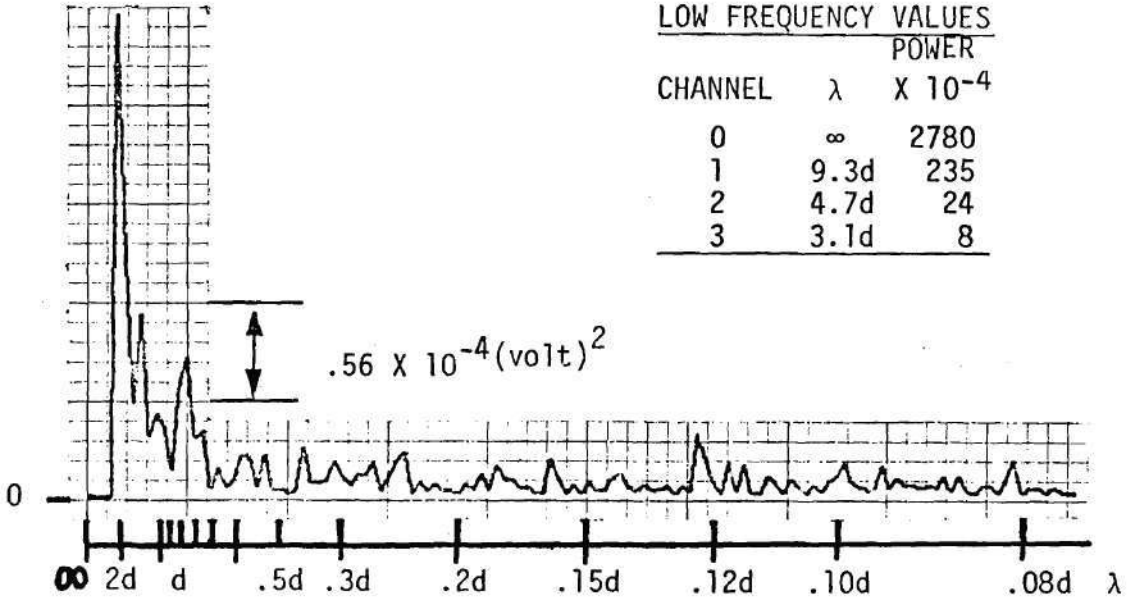

b) Ball surface after running 24 minutes. (.25 μm R_a roughness)

Figure 74. Power Spectra of the Surface Profiles (P_H = 1.24 GN/m², V_s = 1.02 m/s, Hertz diameter d = 0.43 mm, pure sliding.)

In addition to the power spectrum, the autocorrelation function can be useful in describing the surface profile. In fact, Whitehouse and Archard [57] and Peklenik [118] suggest the description of a real surface in terms of only σ, the rms roughness, and β^*, the correlation distance. Briefly, the autocorrelation function is obtained by comparing a time varying signal, in this case the surface profile measurement, with a replica of itself where the replica is shifted some amount of time (or distance at a given velocity). If the shift along the surface profile is β, then the autocorrelation function $C(\beta)$ becomes

$$C(\beta) = \frac{1}{\ell} \int_0^{\ell} a(x)a(x+\beta)dx \tag{64}$$

where $a(x)$ is the amplitude of the surface profile trace at a particular x along the surface. For a truly random signal, $C(\beta)$ will be a maximum at $\beta = 0$. If the signal is periodic, $C(\beta)$ will peak whenever β is a multiple of the wavelength. If a Gaussian distribution of surface roughness amplitudes is considered, equation (64) results in an exponential autocorrelation function. When normalized such that $C(0) = 1.0$,

$$C(\beta) = \exp\ (-\beta/\beta^*) \tag{65}$$

Therefore, when $\beta = 2.3\beta^*$, $C(\beta) = 0.10$. The value 0.10 has been arbitrarily set by Whitehouse and Archard as being sufficiently small that two points on the surface may be regarded as being independent. This follows from the fact that when the autocorrelation function $C(\beta)$ is close to unity, two points on the surface β distance apart are strongly interdependent. However, when $C(\beta)$ attains values close to zero, two

points on the surface β distance apart are weakly correlated and therefore essentially independent. The correlation length $2.3\beta^*$ can also be viewed as roughly being equal to the spacing between equal sized asperities. The power spectrum is the Fourier transform of the autocorrelation function, or

$$P(\omega) = \int_{-\infty}^{\infty} C(t)e^{-i\omega t}dt \tag{66}$$

Substituting equation (65) into (66) results in

$$\begin{aligned} P(\omega) &= 0.5 \qquad \text{for } \lambda_s = 1/\omega = \beta^* \\ P(\omega) &\simeq 0 \qquad \text{for } \lambda_s = 1/\omega < 0.1\beta^* \\ P(\omega) &\simeq k \qquad \text{for } \lambda_s = 1/\omega > 10\beta^* \end{aligned} \tag{67}$$

The wavelength β^* can therefore be thought of as a dividing point between those surface wavelength components having significant amplitudes and the shorter wavelengths which do not. Whitehouse and Archard have shown the model to be in good agreement with a large number of real surface profiles.

Figure 75 shows the autocorrelation function for the unused and run-in ball surfaces shown in Figure 73. The position shift β is shown in terms of the Hertz diameter d. If the Whitehouse-Archard model is applied to the data in Figure 75, the value of β^* can be found from $C(2.3\beta^*) = 0.1\ C(0)$. The correlation distance β^* is .17d (74μm) for the unused ball and .33d (142μm) for the run-in surface. It is apparent that the exponential model of equation (70) can only be used for $\beta \leq 2.3\beta^*$.

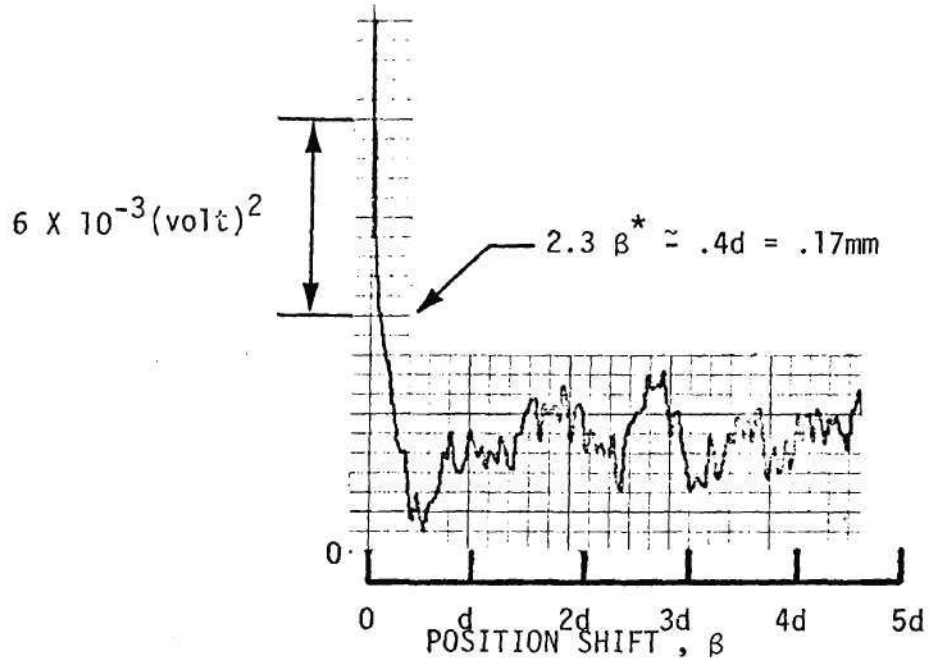

a) Unused ball surface (.38 μm R_a roughness).

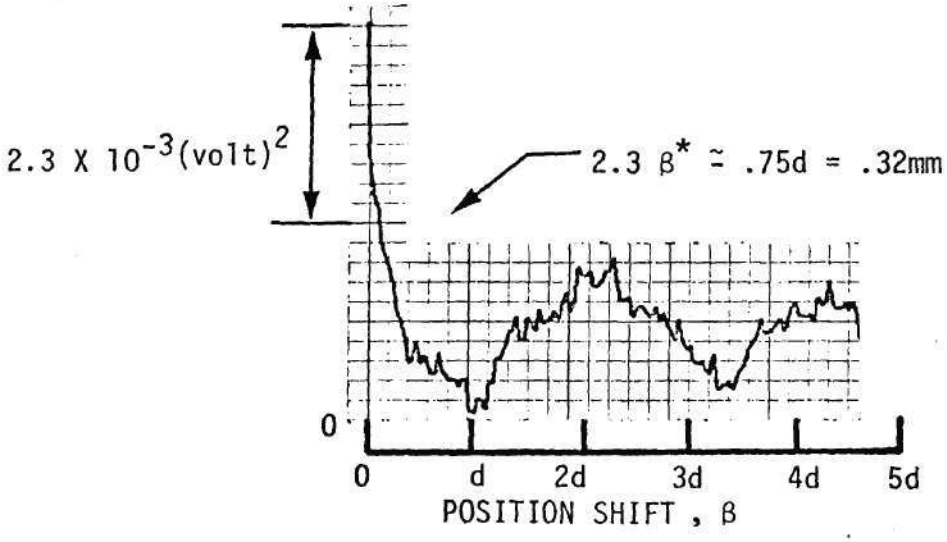

b) Ball surface after running 24 minutes. (.25 μm R_a roughness)

Figure 75. Autocorrelation Functions of the Surface Profiles. ($\lambda > 3d$ not included, P_H = 1.24 GN/m^2, V_s = 1.02 m/s, Hertz diameter d = 0.43 mm, pure sliding)

The further increase in $C(\beta)$ implies that the profile is not truly random, but has strong periodic components with wavelengths > d. This can also be seen from the power spectra shown in Figure 74.

Figure 75 also shows that the correlation distance has doubled as a result of the run-in process. From equation (65), a doubling of β^* implies that two points on the surface must be taken twice as far apart after run-in to be considered independent. Because of the interrelationship between the power spectra and autocorrelation function (equations (66) and (67)), if the surfaces were in fact random, the half power point would be shifted to a wavelength twice the value of that for the unused surface. This is the case when the high frequency components are reduced much more than the low frequency components (see Figure 73). This is also consistent with the notion of independent points. Consider, for example, a surface comprised of only two wavelength components 2d and 0.2d. When the 0.2d wavelength component is present, the autocorrelation function would have a value of 1.0 for $\beta = 2md$ where m is an integer. However, it would also have sizable peaks for $\beta = 0.2md$ (with drops to near zero between). After run-in, however, the 0.2d wavelength component will be substantially reduced. Assuming it to be eliminated, the $C(\beta)$ now peaks only once every $\beta = 2md$ and reaches zero between the peaks. If the correlation distance is defined as the ten percent point, it is apparent that this distance must be increased if high frequency components are reduced or eliminated.

The AC signal from the infrared detector obtained during the run-in process was also recorded and analyzed on the Hewlett-Packard analyzer. However, in order to eliminate noise in the detector signal, a 20 KHz.

3dB filter was used during data acquisition. The noise remaining below 20KHz had a peak power of about 5×10^{-6} $(volt)^2$ whereas the detector signal had a power content on the order of 10^{-4} $(volt)^2$. Furthermore, the sampling technique used by the Fourier analyzer tends to average out the random noise while enhancing the signal. Figure 76 shows the power spectrum of the noise in the detector. 20 KHz frequency in Figure 76 corresponds to a wavelength of .12d.

Figure 77 shows a normalized histogram of the AC signal from the detector obtained at the beginning of the run-in period (Figure 77a) and after running for eight minutes (Figure 77b). The figure shows that the voltage distributions are nearly Gaussian. Secondly, it is apparent that the amount of dispersion is decreased by the run-in process. It is interesting that both the high and low extremes in the radiation signal have been eliminated as the asperity peaks were removed. The symmetry of the fluctuations supports the argument advanced in the previous section that the peak in the temperature fluctuation signal is due to local heating at an asperity; whereas the minimum signal occurs directly after this maximum and is due to the relatively low local pressure in the region following an asperity. The radiation fluctuations of Figure 77 can be turned into temperature fluctuations by adding the time averaged output to the data of Figure 77 and using the IR detector calibration curves.

Figure 78 shows the power spectra for the same IR detector signals as used in Figure 77. The abscissa has been replotted in terms of wavelength in units of d (Hertz diameters). It is apparent from Figure

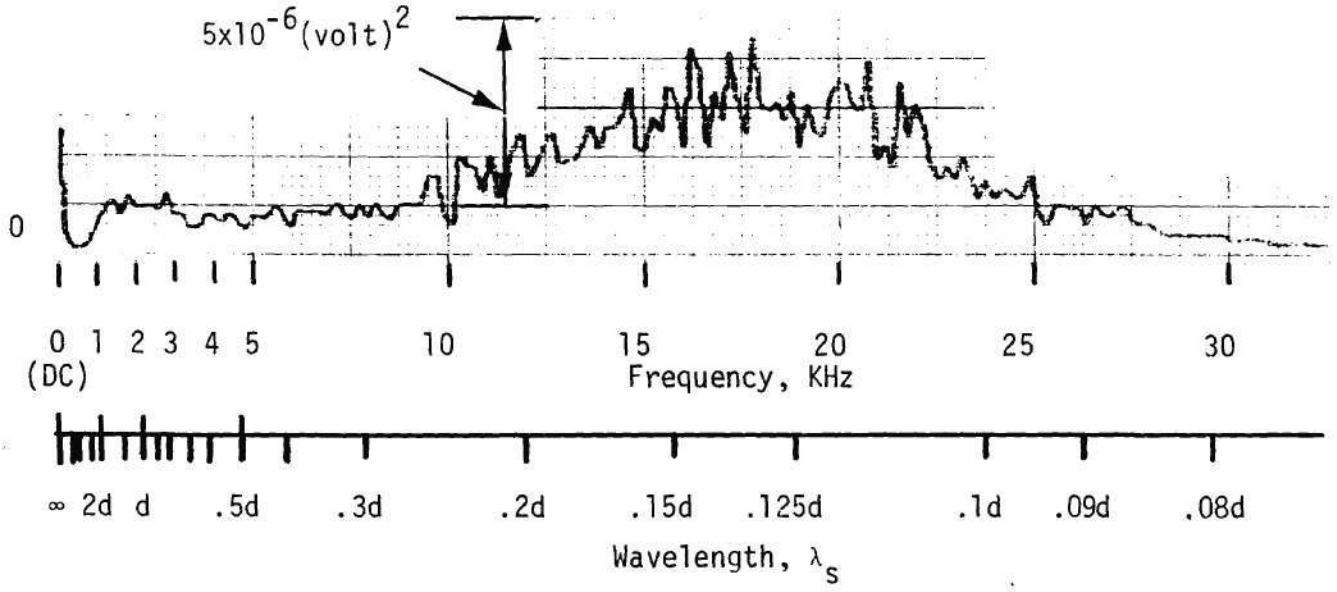

Figure 76. Power Spectrum of Noise in the IR Detector (A Band Pass Filter 1 to 20 KHz is Included).

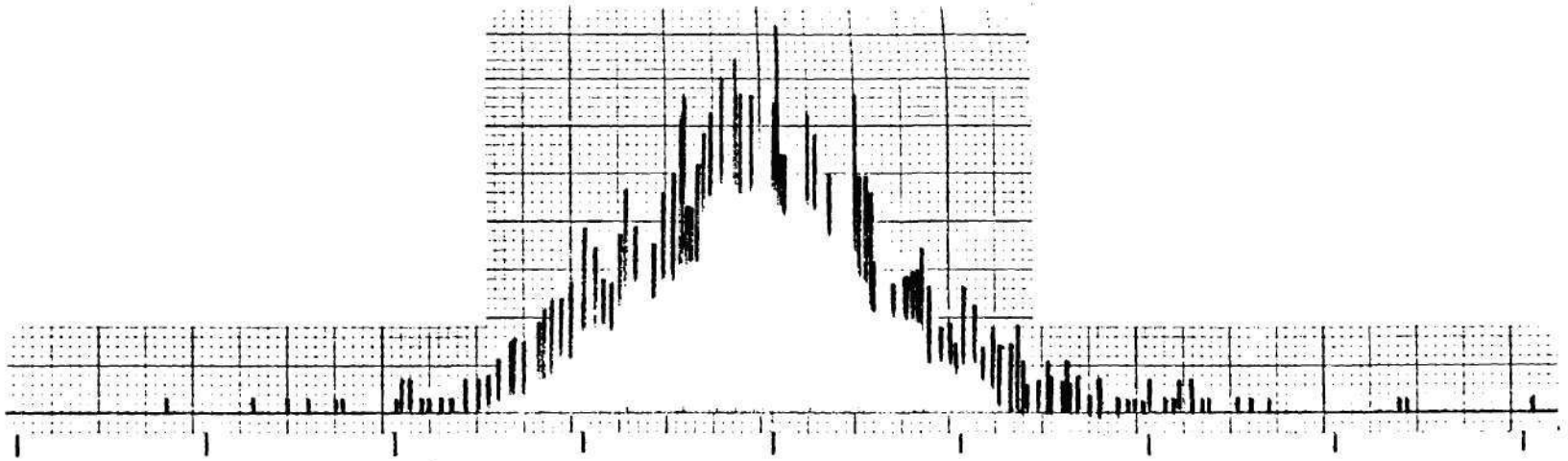

a) Initial Ball Surface Radiation Fluctuations.

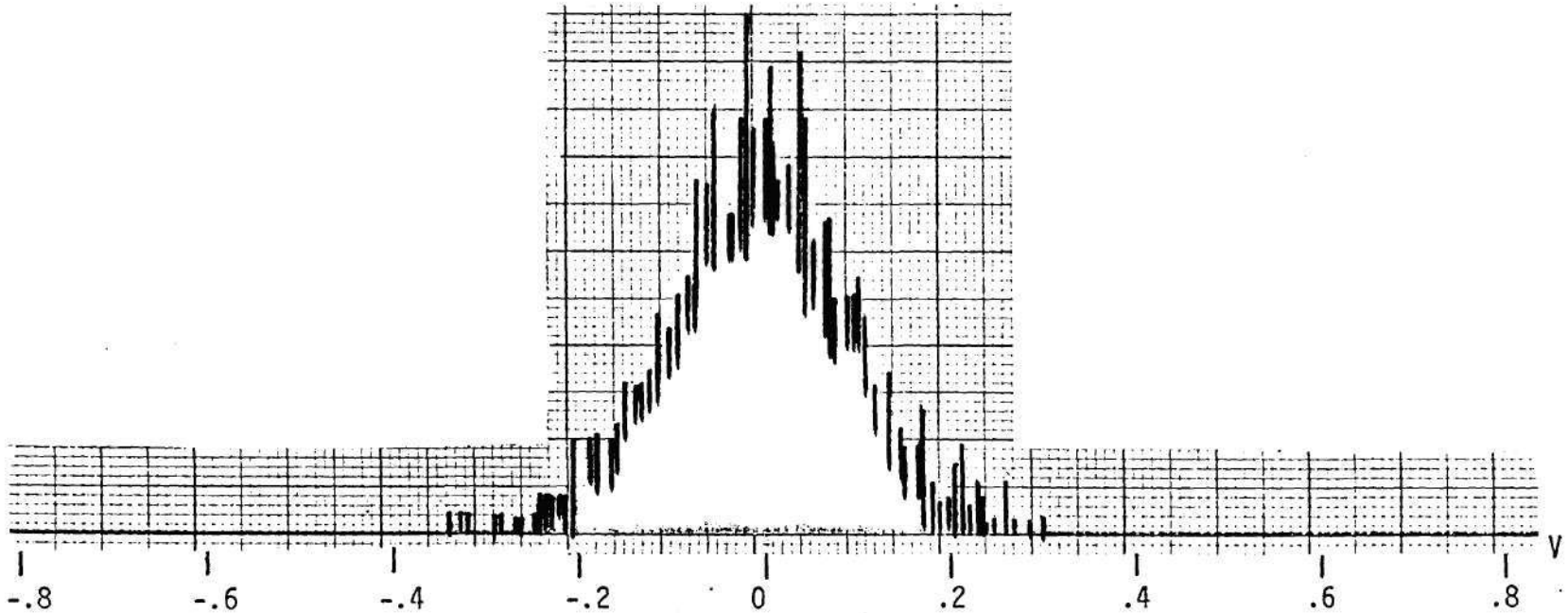

b) Ball Surface Radiation Fluctuations after Running 8 Minutes.

Figure 77. Normalized Histograms of Ball Surface Radiation Fluctuations (.38 μm R_a initial roughness, P_H = 1.24 GN/m^2, V_s = 1.02 m/s, Hertz diameter d = 0.43 mm, pure sliding).

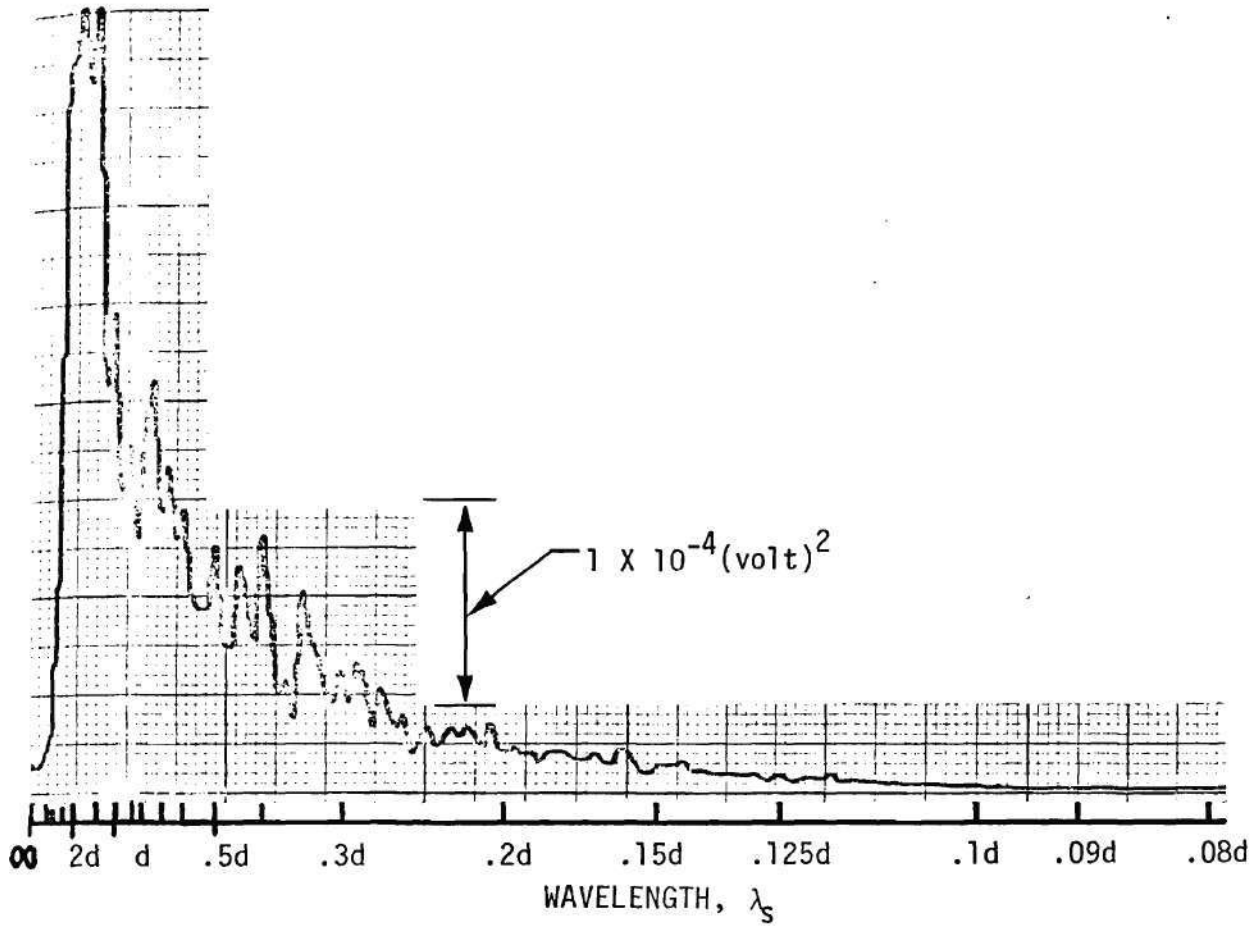

a) Ball Surface Radiation Fluctuations at Start of Run-in.

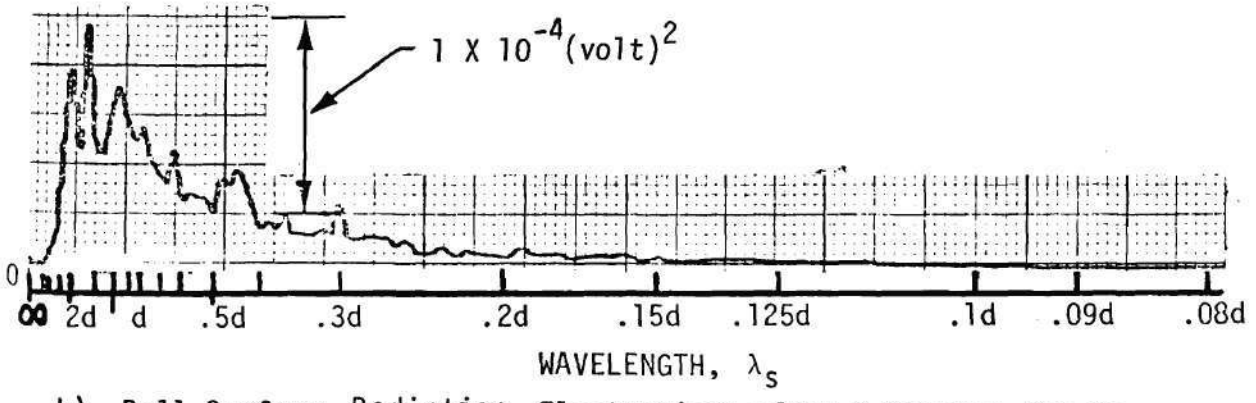

b) Ball Surface Radiation Fluctuations after 8 Minutes Run-in.

Figure 78. Power Spectra of Ball Surface Radiation Fluctuations (.38 μm R_a initial roughness, P_H = 1.24 GN/m^2, V_s = 1.02 m/s, Hertz diameter = 0.43 mm, pure sliding).

78 that the run-in process results in a significant reduction in power at all wavelengths. In both spectra, the peak occurs near $\lambda_s = 2d$, although the run-in process has reduced the peak magnitude by more than a factor of three. It should be noted that the detector signal was also filtered to remove frequency components less than 500 Hz. This corresponds to wavelengths in Figure 78 which are greater than 5d.

Based on the results shown in Figures 75 and 78, the author believes that the methods presently used to determine acceptable levels of the R_a or rms surface roughness may not be the most appropriate. For example, the rms value for the surface shown in Figure 74a (unused rough ball) is equal to the square root of the integral of the power spectrum (Figure 75a). However, the proper limits of integration must be chosen. The Bendix instrument uses an upper limit of .76 mm (through electrical filtering) for averaging purposes and has a lower limit set by the stylus radius of 13 μm. If one assumes that the absence of surface temperature fluctuations is indicative of negligible asperity interaction (as shown in the previous section), then as far as asperity interaction is concerned, one can determine the significant wavelengths of the surface profile. For example, Figure 78a shows that the temperature spectral power content during asperity interaction drops to about ten percent of its peak value for the wavelengths $\lambda_s \leq d/4$. However, Figure 75a shows that there are significant roughness components down to at least $\lambda_s = .08d$ (the power content is essentially the square of the amplitude). The same figures show that the major components for both the roughness profile and the temperature signal are in the range $d \leq \lambda_s \leq 2d$. Therefore,

whereas the roughness wavelength in the range $d \leq \lambda_s \leq 2d$ are obviously important in causing temperature fluctuations, wavelengths shorter than d/4 appear to have no effect. This, of course, is based on the premise that a temperature fluctuation is caused by an asperity interaction. Based on the power reduction to ten percent of its maximum value, the lower bound for rms determination should be $\lambda_s \simeq d/4$. The upper limit is set at $\lambda_s = 2d$ because the temperature signal drops off rapidly for $\lambda_s > 2d$ even though there are roughness components present with wavelengths greater than 2d (see Figure 75).

On the basis of the data taken, it appears that the rms surface roughness to be used in a calculation of $\Lambda(\Lambda = h/\sigma)$ should consider only wavelengths in the range $d/4 \leq \lambda_s \leq 2d$. For this experiment, d = 0.43 mm and the applicable range is then $.11 \leq \lambda_s \leq .86$ mm. A roughness of about .38 μm rms was obtained using the Bendix system with limits of about $.013 \leq \lambda_s \leq .76$ mm, and the standard filter transmission (2CR-type). By integrating the power spectrum of surface profile between the limits of $.11 \leq \lambda_s \leq .86$ mm, and taking the square root, the rms value was .53 μm. This higher rms value is believed to be due to significant power in the range $.76 \leq \lambda_s \leq .86$ mm. The Bendix instrument also has available cut-offs at .25 mm and .067 mm. The use of either of these values would correspond to rms integration limits of $.030d \leq \lambda_s \leq .58d$ and $.030d \leq \lambda_s \leq .18d$ respectively. Since the desired range is $.25d \leq \lambda_s \leq 2d$, the resulting rms values would not be reliable in predicting surface interaction.

In addition to the possibility of getting a value of surface roughness which cannot reliably predict performance, the fact that

wavelengths shorter than 0.25d do not appear to be significant might have an economic impact. For example, under conditions in which the Hertz diameter is relatively large, the final stages in a lapping or polishing process may not be important.

The EHD contact appears to behave like a mechanical filter in which wavelengths outside of a relatively narrow band have a negligible effect on the performance of this system. If relatively thin films are expected during the operation of a highly loaded bearing, an improvement in surface finish should be considered. However, the magnitude of the rms roughness and the processes which might best improve the surface can not be adequately chosen until the Hertz contact diameter is known.

CHAPTER VI

SOME ADDITIONAL OBSERVATIONS

Some additional experiments related to the main discussions presented in Chapters IV and V were conducted. These experiments and subsequent observations are discussed in this chapter.

A. Glass Transition Observations

Recent investigations into the possible role of glass transition and glassy state behavior of lubricants in EHD contacts, by Winer and coworkers [142], has indicated strong possibilities of some lubricants being in the glassy state in EHD contacts during normal operation. The proposition that the mechanical behavior of lubricants in EHD contacts might not be that of a viscous liquid but of an elastic solid under conditions of pressure, temperature and shear rate present in EHD contacts, was first presented by Smith [143] in 1960, and later supported by Johnson and Roberts [144], and Johnson and Cameron [145].

Glass transition temperature has been observed to increase with pressure at a rate ranging from 80 to 350 C/GPa. Thus, it would be expected that some lubricants will be in the glassy state in an EHD contact with average pressures of 0.7 GPa or higher at room temperature. Therefore, it would be expected that many lubricants are in the glassy state for a significant portion of the time they are in the contact.

In the work of Winer and coworkers [142] and Alsaad [146], phase diagrams of pressure versus temperature are available for fluid N1 which

has been used in this study. In their work [142,146] glass transition temperature as a function of pressure based on two different techniques - light scattering and volumetric dilatometry - is reported. The two techniques are complementary because the observation times are similar (about 200 S). If the fluid is in a glassy state according to dilatometry data, it is more likely that the fluid is in glassy state in an EHD contact during normal operation since the rates in an EHD contact are higher than the rates in a dilatometry experiment, and it is known that increased rate increases the glass transition temperature at a constant pressure.

Knowing the temperature and pressure distributions in the EHD contact, the phase diagram will permit determination of whether or not the lubricant is in the glassy state, approximately what operating conditions result in the glassy state behavior, and over what fraction of the contact area the glassy state exists. The measured temperatures of ball surface and fluid film are used and as a first approximation Hertzian pressure profile (modified at inlet) is used.

Figure 79 shows the phase diagram for fluid N1 superposed with temperatures of the ball surface and fluid film at various operating conditions. The two phase lines correspond to the two techniques - light scattering and dilatometry. The liquid and glassy regions have been marked with respect to these lines. The temperatures of the ball surface and fluid film at the inlet boundary, contact center and exit boundary have been marked on the same diagram. For this purpose, Hertzian pressure profile (modified in the inlet region) is assumed and the division

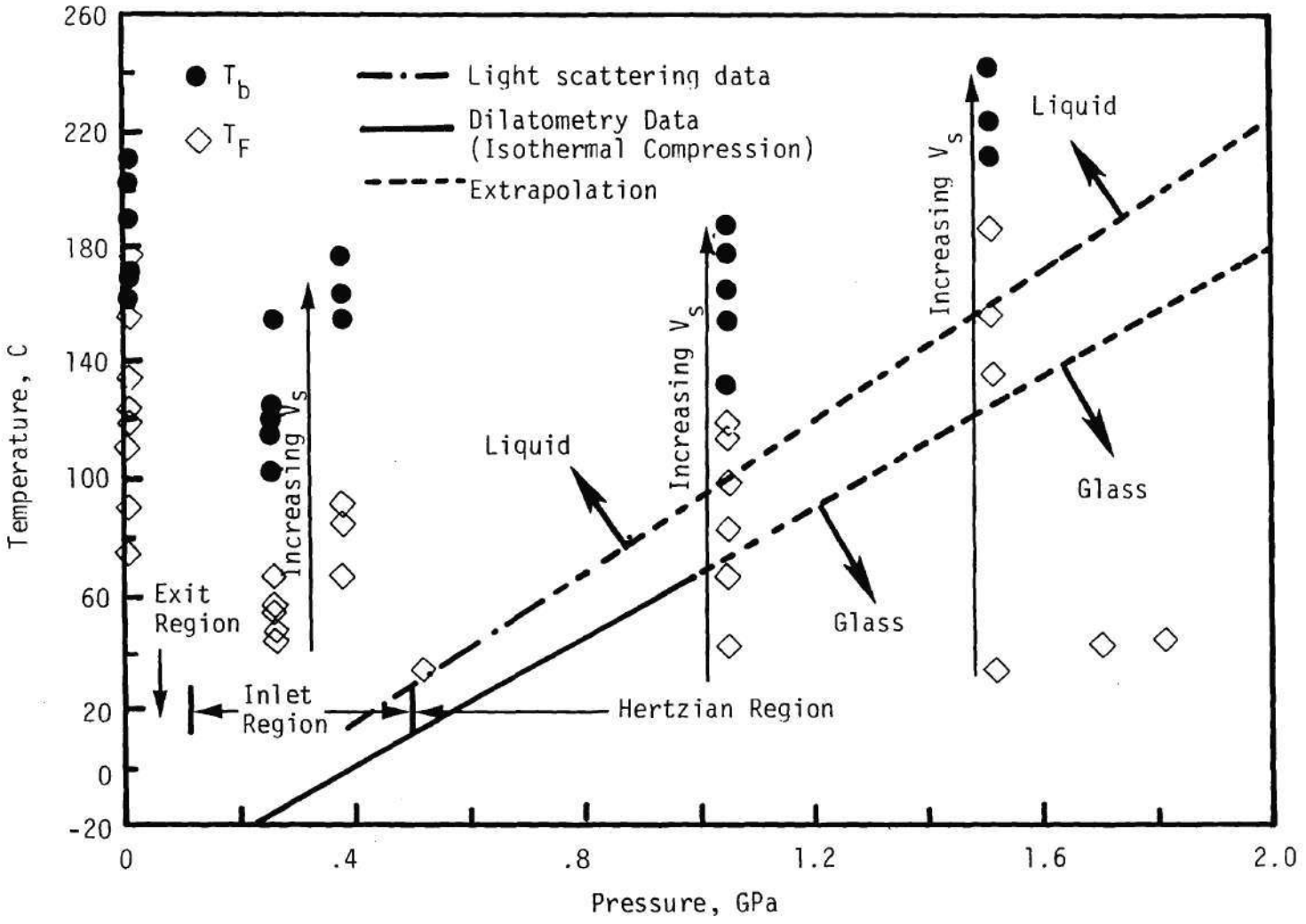

Figure 79. Phase Diagram for Fluid N1 Superposed with Temperatures of the Ball Surface and Fluid Film (for $\Sigma = 2$) at Various Operating Conditions.

between the three regions is made rather arbitrarily. It can be seen from this figure that the glassy state does occur near the ball surface at low sliding speeds and sufficiently high contact pressures.

Figure 80 shows ball surface temperature at the contact center versus sliding speed at various Hertz pressures (same as Figure 37) superposed with the two phase lines. To the left of each line, the fluid is in a glassy state and to the right the fluid is in a liquid state. Same data is shown plotted as a function of peak Hertz pressure in Figure 81 (same as Figure 38) and superposed with the phase lines. Again, to the left of each line, the fluid is in a glassy state and to the right the fluid is in a liquid state. As shown in these figures, the lubricant near the ball surface is in the glassy state at low sliding speeds. At higher sliding speeds, the glassy state exists only at high pressures. This result is to be expected since a sliding contact generates large frictional heat and thus the temperature levels in the contact are relatively high. These results indicate the existence of glassy state in sliding EHD contacts at relatively low speeds or sufficiently high pressures.

Ball surface temperature distributions at different slide-roll ratios and peak Hertz pressure of 1 GPa shown in Figures 47 and 48, are repeated in Figures 82 and 83 but superposed with phase lines for fluid N1. Figure 82 shows temperature distributions for a constant rolling speed of .75 m/s and Figure 83 shows similar data for a slightly higher rolling speed of 1.0 m/s. Based on the measured temperatures, assumed Hertzian pressure distributions, and the glass transition data, it can be estimated what portion of the fluid in contact with the ball surface

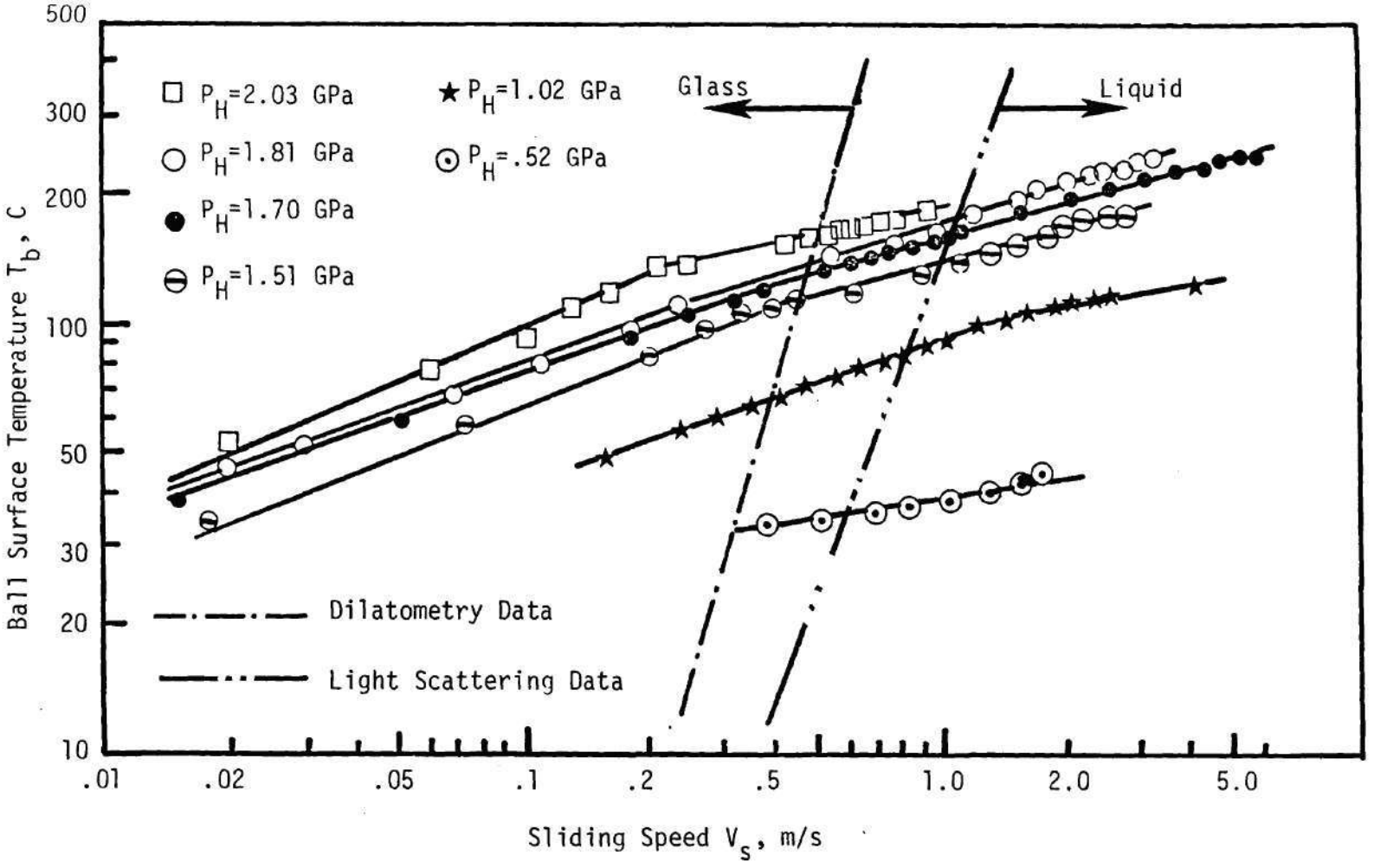

Figure 80. Ball Surface Temperature at Contact Center versus Sliding Speed (See Figure 37) Superposed with Glass Transition Lines for Fluid N1.

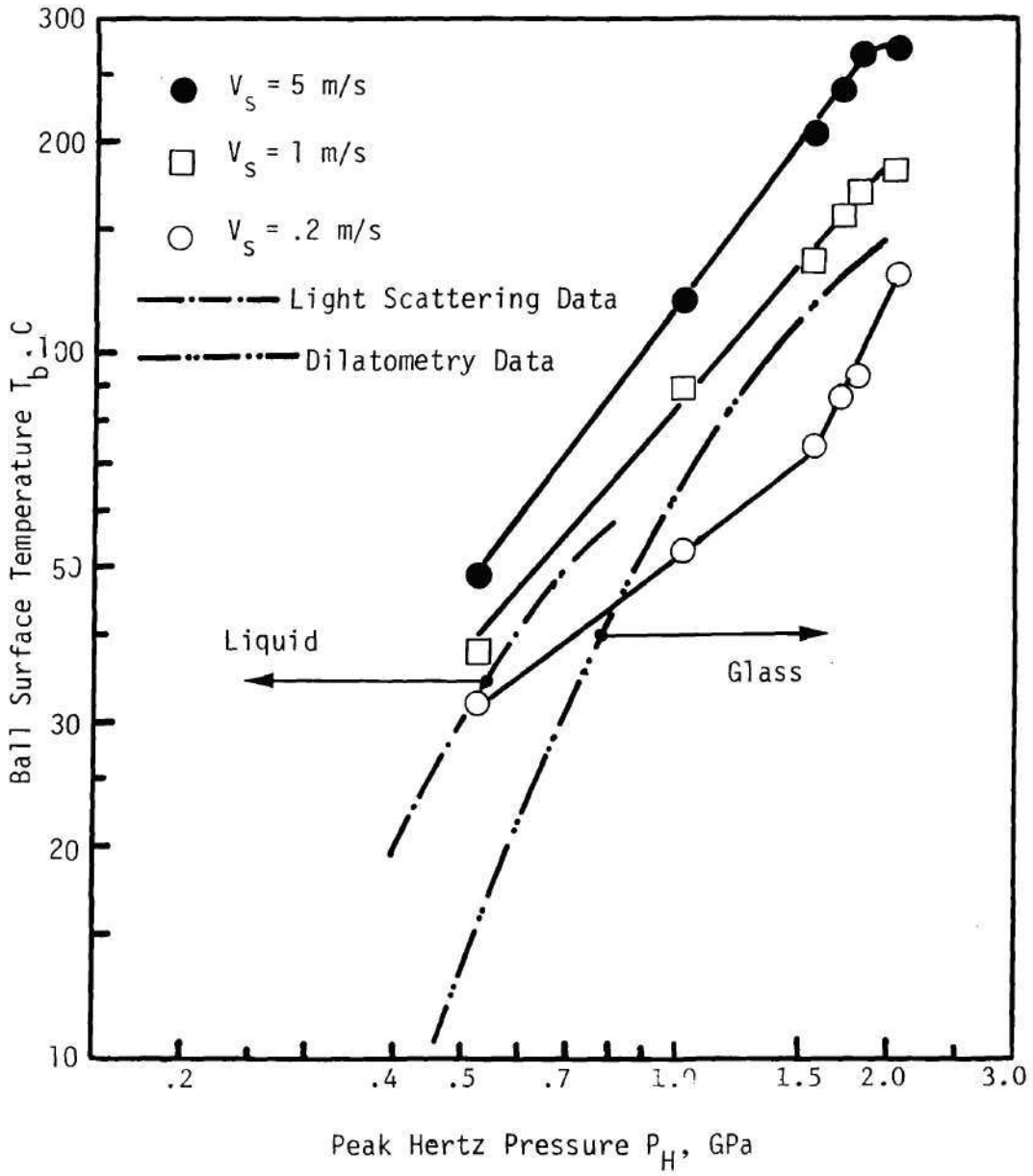

Figure 81. Ball Surface Temperature Rise at Contact Center versus Peak Hertz Pressure (see Figure 38) Superposed with Glass Transition Lines for Fluid N1.

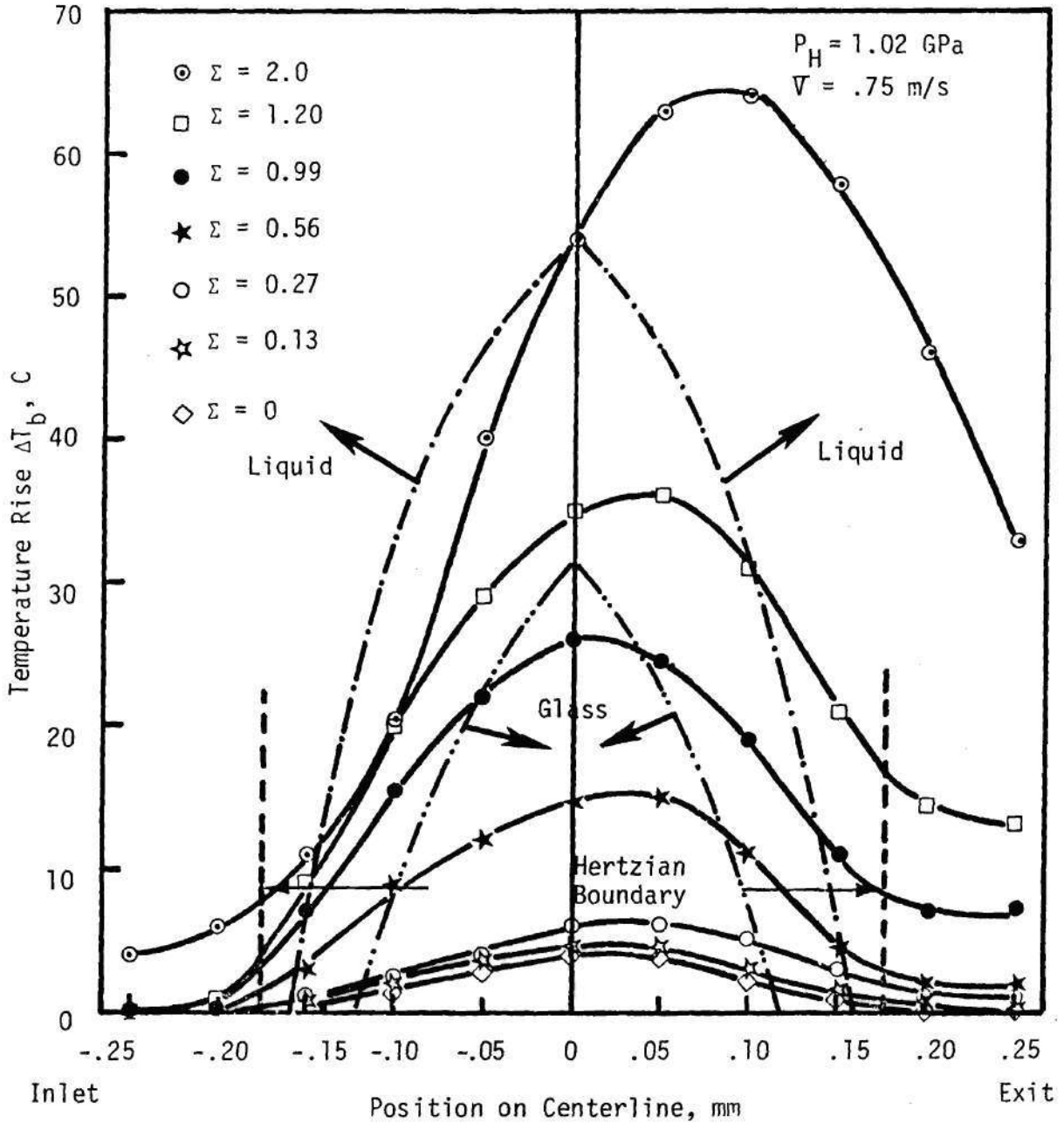

Figure 82. Ball Surface Temperature Rise along the Contact Centerline (see Figure 47) Superposed with Glass Transition Lines (-.- Light Scattering Data, -..- Dilatometry Data).

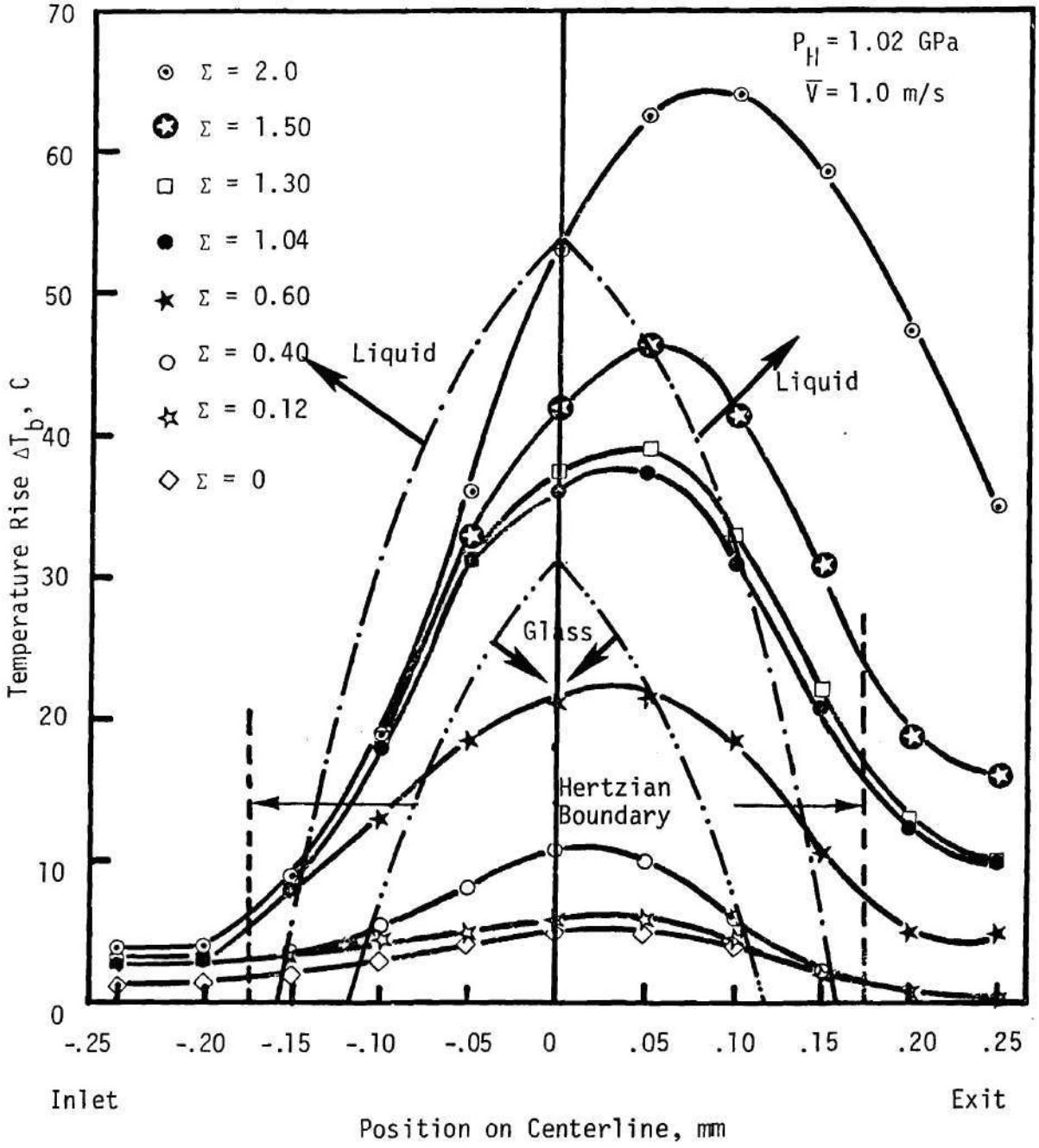

Figure 83. Ball Surface Temperature Rise Along the Contact Centerline (see Figure 48) Superposed with Glass Transition Lines (-.- Light Scattering Data, -..- Dilatometry Data).

will be in the glassy or liquid states. The portions are shown in the bar diagram in Figure 84. The lubricant near the ball surface is definitely in the glassy state for low values of slide-roll ratios (up to ≈ 1.0). At sufficiently low slide-roll ratios, the glassy state occupies all the contact area. These results show that the fluid N1 is in the glassy state in sliding/rolling contacts and glass can occupy all the contact area at low slide-roll ratios.

The existence of the glassy state in an EHD contact has important implications especially on the two most important operating variables of an EHD contact: the film thickness and traction. The presence of a glassy lubricant within the Hertzian pressure zone influences the traction behavior significantly. The significant properties then will be the mechanical properties of the lubricant in the glassy state. Since the relaxation time of a material in the glassy state is long compared to the residence time in the contact [142], it is possible that once the glassy state is reached, the lubricant will remain in the glassy state on the moving surface while the surface moves from one EHD contact to the next. Also, in sliding/rolling contacts, at sufficiently low slide-roll ratios, the lubricant may be in the glassy state in the inlet zone of an EHD contact. These effects may obviously influence the film thickness in the Hertzian region, since the controlling parameters in this case are the lubricant properties in the inlet zone.

As has been demonstrated earlier, temperature measurements can reveal a great deal of information about the state of the lubricant. Many lubricants like five ring polyphenyl ether (5P4E) or MCS 1218 are known to reach a glassy state at lower pressures [142], and these have

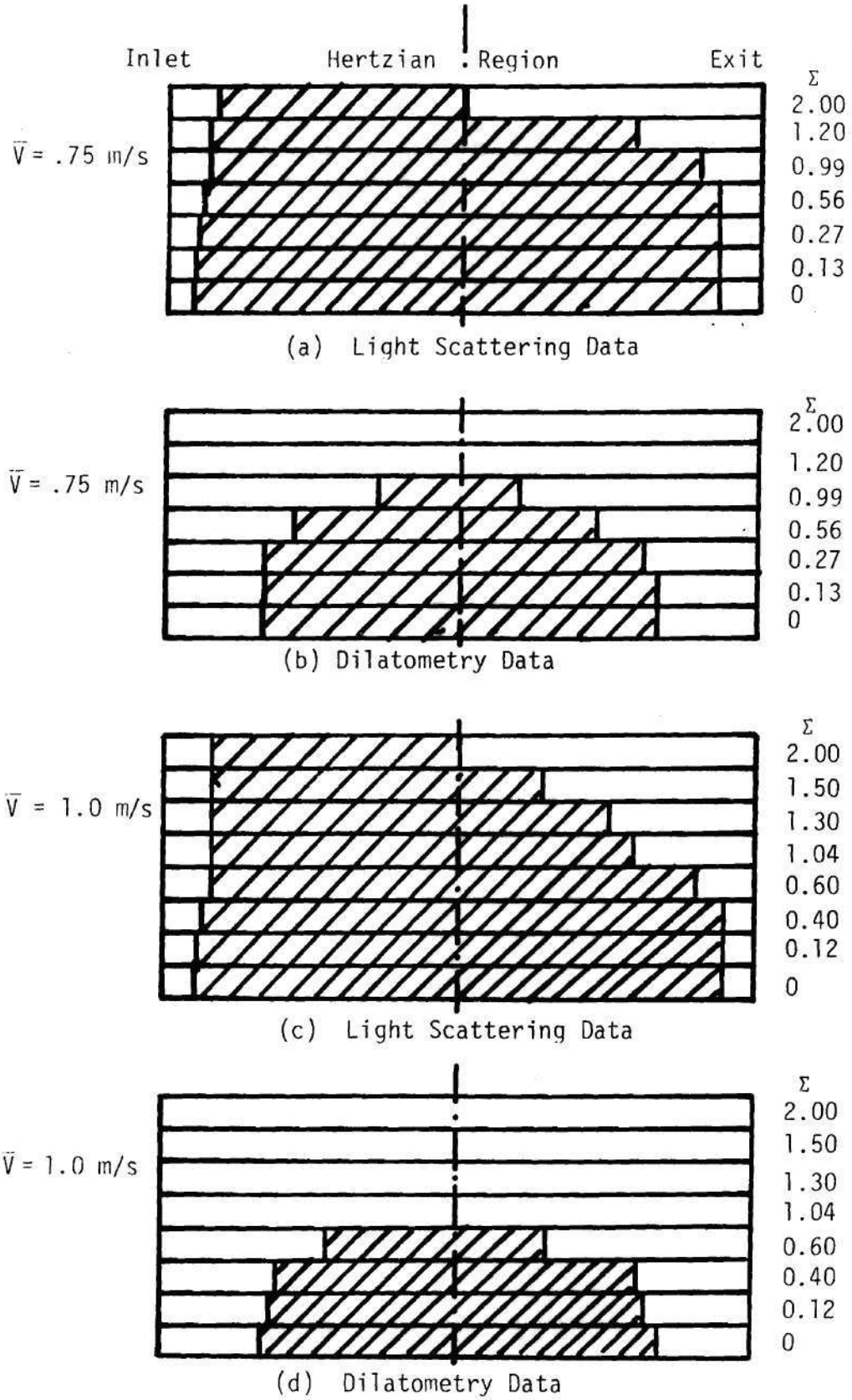

Figure 84. Glassy Regions in Sliding and Rolling EHD Contacts (Smooth ball: .011 μm R_a, Fluid N1, P_H = 1.02 GPa).

been used for EHD lubrication. Therefore, EHD contact temperature measurements with these and similar lubricants, may provide more information on the effect of glassy state on the performance of an EHD contact. It has to be remembered that the state of the lubricant has no influence on the ball surface temperature measurement technique.

B. Starvation Failure Experiments

Failure is characterized by an onset of undesirable performance of a machine element. Depending on the selected performance criterion, various terminologies of the subject [147,148] are used. Scuffing or scoring is 'gross damage characterized by the formation of local welds between the sliding surfaces.' Seizure, which rarely occurs in practice is defined as 'the stopping of a mechanism as the result of interfacial friction.' Smearing and galling occur in high speed rolling bearings and are similar in nature to scuffing or scoring. In this section, only the scoring or scuffing form of failure is considered.

Transition to failure is usually not sudden. On the other hand, a system passes through various regimes before an ultimate failure is encountered. For a typical system, the sequence may be: EHD, partial EHD, boundary, and finally failure [140]. The transition from EHD to partial EHD lubrication regimes has already been considered in detail in Chapter V. The transition from partial EHD to boundary is often accompanied by large increase in friction with the wear rate remaining low. But, ultimate failure in the form of scoring or scuffing is always accompanied by a large increase in wear rate and sudden increases in noise and vibration, and with further operation these are followed by a

progressive increase in operating temperature, which may cause smoke to be given off by the lubricant. Other dramatic effects, such as showers of sparks, may sometimes be seen [147,148].

Rozeanu [149-152] maintains that the final step to failure is always instantaneous and occurs within a few microseconds. Rozeanu sees the seizure process as depending on the gradients of temperature, viscosity and shear strength in the upper layers of the solid surfaces. Low values of these gradients promote scuffing; high values prevent it. This mechanism of scuffing is one among a number of theories that have been put forward. However none of these theories appears to offer much of a clue about what is really happening.

The experiments reported in this section are specifically directed towards determining whether the final step fo failure is really instantaneous. The failure criterion chosen is a local rise in temperature above a certain level. The approach to failure is accelerated by severely starving the EHD contact.

The same experimental apparatus described in Chapter II and shown in Figure 3 is used. The infrared microscope is used in order to measure the ball surface temperature at the contact center but in a fast response mode. The fluid used in this study is the naphthenic base mineral oil N1 (see Appendix A for properties). The balls were made of AISI 52100 (see Appendix B for properties) with 0.011 μm R_a finish. Present investigation is limited to simple sliding with a stationary sapphire and moving ball surface. The following experimental procedure was used;

Experimental Procedure

1. The system is brought into steady state operation (Steady State 1) at any given speed and load conditions. The ball surface temperature at the center of the contact is measured by using the IR temperature measurement technique. The traction coefficient and bath temperature are also measured. This regime is comparable to that used for all previous EHD data given in this research.

2. The microscope is switched to operate in a high frequency response mode (AC mode), keeping it focussed at the center of the contact. The oscilloscope is set to trigger with the signal at a level of 1/2 volt and the oscilloscope camera shutter is kept open for recording the trace.

3. The lubricant circulation and supply is stopped, thereby severely starving the contact. Still, some lubricant appears to adhere to the ball surface. With a clean Q-stab, the ball surface is cleaned as it approaches the contact.

4. This brings the system into the starved state 2. Due to increased traction under these conditions, the ball surface velocity decreases to the values used in Table 16. Operation under these conditions was found to be unsteady.

5. Shortly (approximately 15 to 30 seconds) after the system reaches the unsteady starved state 2, local failure occurs and the temperature level increases. This increase in temperature level triggers the trace on the oscilloscope. The camera shutter is closed after recording the trace. The transient temperature level is estimated by using the

calibration chart for the infrared microscope.

6. Immediately after the local failure the system reaches a state referred to as post failure State 3. This post failure state 3 again appears to be unsteady, in that, local failure may occur any time in the future. In fact, temperature flashes appear corresponding to the spot on the ball where initial failure occurred. Under these conditions the time averaged ball surface temperature and traction coefficient are much higher than their values in steady state 1. Due to further increase in traction, the ball surface velocity decreases even further compared to starved state 2.

The major results from these experiments are shown in Table 16. Five different experiments are reported with sliding speeds ranging from 1.5 to 4.26 m/s and two different loads of 67 and 118.3 N. Load is maintained constant throughout each experiment and the bath temperature is monitored by a thermocouple. Under starved conditions bath temperature is not measured since the lubricant supply is cut off. The ball surface velocity decreased during the test for each experiment and this is perhaps attributable to the significant increase in friction coefficient to 3 or 4 times the starting value. Because of the slow response of velocity readout and traction load cell, the transient values of velocity and friction coefficient could not be measured. Ball surface temperature measured by the IR microscope is also shown in Table 16. Both the transient and the time averaged values of temperature are shown in the table. Since the microscope was set to trigger with the transient temperature rise, the temperature during unsteady Starved State 2 could not be recorded.

Table 16. Experimental Study of Starvation Failure of a Sapphire on Steel Ball Contact

(Smooth ball: .011 μm R_a, Fluid N1, V_{sa} = 0)

Experiment	T_{bath} °C	W/N	V_s m/s	TC (or f)	T_b @ center °C
1. Steady State 1	30	67	1.5	.06	92
Starved State 2 (unsteady)		(P_H = 1.02 GPa)	1.37	-	-
Transient			-	-	650
Post failure State 3 (unsteady)			1.1	.21	135
2. Steady State 1	32	67	2.36	.05	105
Starved State 2 (unsteady)		(P_H = 1.02 GPa)	2.1	-	-
Transient			-	-	690
Post failure State 3 (unsteady)			1.75	.19	150
3. Steady State 1	45	67	4.0	.04	133
Starved State 2 (unsteady)		(P_H = 1.02 GPa)	3.7	-	-
Transient			-	-	700
Post failure State 3 (unsteady)			3.11	.16	185
4. Steady State 1	36	118.3	2.38	.055	130
Starved State 2 (unsteady)		(P_H = 1.24 GPa)	1.95	-	-
Transient			-	-	850
Post failure State 3 (unsteady)			1.89	.2	193
5. Steady State 1	53	118.3	4.26	.045	165
Starved State 2 (unsteady)		(P_H = 1.24 GPa)	3.92	-	-
Transient			-	-	1100
Post failure State 3 (unsteady)			3.87	.19	240

It can be seen in Table 16 that the transient temperature reaches very high values - sometimes up to 1100 C. The temperatures are very high and indeed the material softens under these conditions. The level of transient temperature increases with increasing speed and load, as can be expected.

In addition to noting the values of the transient temperatures, an oscilloscope trace of the fast rise and decay of the transient temperature was recorded. It was found that the initial rise in temperature takes place within a few microseconds (approximately 8 μs). This time span when translated to distance on the surface, corresponds to the width of a single asperity. It can therefore be concluded that failure has occurred first at a single asperity. Furthermore, it was observed that whenever this failed spot again came into the contact, a temperature flash was observed. If the system is allowed to run under these conditions, it appears likely that many asperities begin to fail in just the same manner, finally leading to an inoperable system.

These findings then clearly support Rozeanu's conjecture that the final step to failure is essentially instantaneous and occurs within a few microseconds. These results may have an important implication on the theories for scuffing and scoring.

Further work on the analysis of wear debris generated in these experiments using a scanning electron microscope are under progress in Professor Rozeanu's Laboratory in Israel Institute of Technology; Haifa, Israel. Results are awaited.

C. Scoring with Steel on Steel

The nature of scoring failure has been discussed in the previous section. In this section, the effect of the nature of materials forming a concentrated contact is described.

Scoring was attributed to the formation of local welds under pressure and subsequent tearing. According to this description, the mechanism of welding between the two surfaces has to have an influence on scoring. The formation of local welds is often described by the property of adhesion. Excellent discussion of the nature of the adhesive forces between surfaces is available in the work of Bowden and Tabor [153].

For example, when two clean copper pieces are pressed against each other, the atoms on one asperity approach those on the other until they are as close as the atoms within the copper itself. At this stage the interfacial atoms can no longer distinguish between their own neighbors and those of the other body. Consequently, the interfacial forces are exactly of the same nature as the interatomic forces in the bulk metal. Imperfections at the interface are certain to occur because of mismatching of crystal lattices, which can however be closed either by plastic flow or thermal diffusion. Perfect adhesion results if all imperfections are removed. Therefore strong adhesion is possible with similar materials and such a situation exists with a steel-on-steel contact.

For dissimilar materials a similar argument applies if no alloying is possible such as in sapphire-on-steel contact. The interfacial forces will probably be an average of the interatomic forces, and thus may be greater than the forces in similar materials. However, stronger forces are needed in order to bring the interfacial atoms into a close proximity.

In this respect, the adhesion between dissimilar materials is not as immediate as with similar materials. It should be remembered that contaminant films lower the adhesive forces.

This discussion shows that scoring should be more immediate for steel-on-steel contact than for a sapphire-on-steel contact.

In order to verify this possibility, experiments were run for steel-on-steel system. The EHD apparatus shown in Figure 3 is used in simple sliding configuration. The sapphire disc is replaced with a polished (.006 m R_a) AISI 52100 steel disc. Experiments were run for sliding speeds ranging from .8 to 5.0 m/s at increasing loads until scoring was encountered. For this system, scoring occurred at a sliding speed of 2.7 m/s and at a load corresponding to a peak Hertz pressure of 1.51 GPa. Under these operating conditions, and in fact even at a higher peak Hertz pressure of 1.89 GPa, the sapphire-on-steel system was running without any signs of scoring. Indeed, the system was undergoing a successful running-in process. Figure 85 shows the location of scoring failure witnessed with a steel-on-steel system. Figure 85 also contains information on ball surface temperature rise at the contact center versus sliding speed at various Hertz pressure levels for a sapphire-on-steel system. It can be seen that temperature rise of at least 200 C must have been encountered for the steel-on-steel system.

These results indicate that a system with similar materials is subject to scoring failure more readily than a system with dissimilar materials. They also emphasize the requirement of using a similar material system for studying the scoring phenomenon, which otherwise may lead to erroneous conclusions.

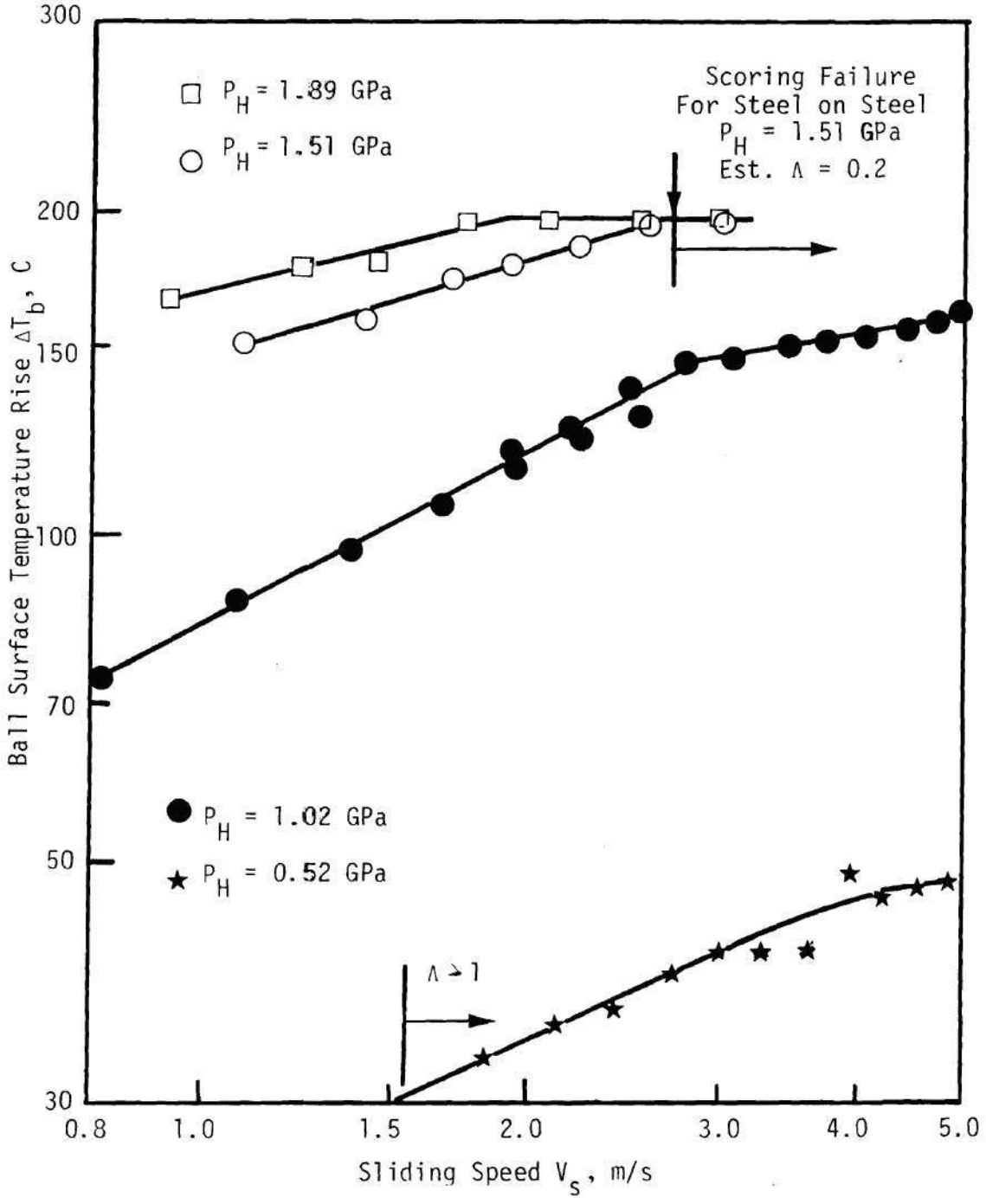

Figure 85. Maximum Ball Surface Temperature Rise versus Sliding Speed (Rough Ball: .38 μm R_a, Fluid N1, Flat Surface Stationary, $\Lambda < 1$ except as Noted).

CHAPTER VII

CONCLUSIONS AND RECOMMENDATIONS

Conclusions

The era of making advances in engineering by improved design resulting from successful investigation of failures in service appears to be past. Prevention of failure is better than any lessons that can be learned from it. A thorough knowledge of failure is then of paramount importance. Machine elements employing concentrated contacts are an important part of most machines, and understanding failure of such concentrated contacts is the key to their better utilization and design. The research reported here, performed under simulated severe conditions can yield good physical insight into several phenomena occurring under such conditions of operation.

The present research was directed toward understanding thermal effects and asperity interactions in elastohydrodynamic lubrication, in order to study the transition from the elastohydrodynamic lubrication regime through the boundary regime leading to failure by scoring of surfaces. Temperatures developed at the contact zone, and changes in surface topography were the main dependent variables in this study.

An infrared technique was developed to measure contact temperatures. A non-contact type of temperature measurement is almost a necessity in order to measure the ball surface and fluid temperatures in an EHD contact, because of the very severe conditions of pressure and shear

stress existing in such a contact. An infrared microdetector (Barnes' mode RM-2A) was used to collect the radiation emitted by the EHD contact from a spot size of .036 mm diameter, which corresponds to one percent of the contact area under moderately heavy loads. Ball surface temperature and fluid film temperature (fourth power average through the thickness) were measured at peak Hertz pressures ranging from .52 GPa (75,500 psi) to 2.03 GPa (294,000 psi) for sliding speeds ranging from .02 m/s to 12.7 m/s. A substantial amount of heating in the inlet zone both of the surface and fluid film was observed. Thermal effects therefore can considerably reduce the film thickness. The temperature measurement results indicate a fluid temperature typically 60 C above the surface temperature which can be as high as 250 C. This may well be the limit of chemical stability of several lubricants. Ball surface temperature at the contact center was measured for a range of loads and sliding speeds. The effect of speed and load on surface temperature is deduced. Comparison of these with flash temperature formulas of Blok, Jaeger, and Archard yield excellent agreement both in trends and actual values.

Surface temperature measurements in combined rolling and sliding EHD contacts were made for a range of rolling speeds and slide-roll ratio varying from -2 to +2. A very small degree of inlet surface heating was observed, even up to an appreciable amount of slip. The stationary ball surface temperature was measured (with sapphire moving and ball stationary). The results indicate that temperature of the stationary surface can be typically 30 to 40 C higher than that of the moving surface. It was also found that a simple flash temperature formula desired for the

case of two moving surfaces, could predict moving surface temperature reasonably well.

A rough surface operating in a regime of low lambda ratio (Λ less than 2) was found to produce higher surface temperatures. Ball surface temperatures were measured for balls of three different roughnesses .011, .076, .38 μm R_a values, at various Hertz pressure levels and a range of sliding speeds. It was found that the percent increase in flash temperature due to roughness correlated very well with predictions from surface roughness factors recommended by AGMA.

During transition from full film elastohydrodynamic lubrication to boundary lubrication, surface asperity interactions are important. This lubrication situation is characterized by the coexistence of an elastohydrodynamic fluid film and interacting asperities, and is usually designated as partial elastohydrodynamic lubrication. Under these conditions of operation high values of local temperatures at the asperity tips were observed. These local temperatures appear as temperature fluctuations about a time averaged value because of the surface movement. An onset of significant asperity interactions was always accompanied by a similar onset of temperature fluctuations. The degree of asperity interactions, often characterized by the lambda ratio (ratio of EHD film thickness to composite surface roughness), is also related to the amount of asperity wear. The surface wear was measured by both relocation profilometry of the surface and lubricant sample analysis (both ferrographic and spectrographic). These results clearly show that surface wear increases rapidly as the lambda ratio decreases below unity while the

magnitude of the temperature fluctuation also increases. Wear coefficients of the order of 10^{-6} were measured. These values indicate a low wear regime operation.

During partial elastohydrodynamic lubrication experiments, a spectral analysis of temperature fluctuations and surface profile was carried out before and after the experiment. It was found that fluctuations in temperature result from specific surface asperities interacting between the two surfaces. Furthermore, it was clear that although the surface consists of features of different wavelengths, only a narrow wavelength range was involved in the asperity interactions which caused the temperature fluctuations. The significant band has wavelengths from about one-quarter to twice the Hertz diameter of the contact. The actual value of wavelength band of interest, therefore depends on the given application. The elastohydrodynamic contact acts as a mechanical filter on the surface profile and is unaffected by surface roughness outside the band of significance defined above. The contact perhaps acts as a cam and flat follower and is unaffected by surface wavelengths beyond twice the Hertzian diameter, and surface features of wavelength less than one quarter of the Hertzian diameter are perhaps plastically deformed or carry on insignificant portion of the load. These results have important implications in the specification, measurement and production of engineering surfaces.

Scuffing or Scoring is gross damage characterized by the formation of local welds between the sliding surfaces, and is indeed a complicated phenomenon to quantify. Transient temperatures were measured during an onset of scoring failure induced by severe lubricant starvation. It was

found that the step to failure is extremely rapid and occurs within a few microseconds (less than 8 μs). It is apparently associated with a single asperity on the surface. This may have an important implication on the theories for scuffing and scoring. It was also determined that scoring occurs more readily in a similar material combination than a dissimilar material combination.

The proposition that the mechanical behavior of lubricants in elastohydrodynamic lubrication might not be that of a viscous liquid but that of an amorphous glassy solid is receiving attention lately. Measured surface temperatures indicate a strong possibility for the existence of a glassy lubricant in elastohydrodynamic contacts. Further temperature measurements with different lubricants may reveal more information in this aspect.

Recommendations

A need for the study of failure of elastohydrodynamic films clearly exists. Because of the complicated nature of this problem area, an extensive amount of research work is needed.

The effect of surface roughness and surface defects continues to be an area of interest.

In the present work, only surfaces with isotropic features were considered. However, in practice, there are many applications where the surfaces have preferred orientation. The effect of surface roughness orientation on film thickness and surface temperature fluctuations needs to be investigated experimentally and analytically. A long range goal in this effort is to understand the effects of orientation of surface pattern on contact scuffing or scoring.

Even though utmost care is exercised during manufacture of surfaces some dents, ridges and surface defects are inevitably present. Furthermore, these defects may be introduced during assembly, handling and transportation. A recent investigation by Wedeven [154] has shown that dents passing through an EHD contact reduce the local film thickness. Associated with these dents, local high temperatures may develop leading to some form of failure. Therefore, the author feels that there is an urgent need for measurement of temperatures during the passage of dents and ridges through an elastohydrodynamic contact.

The purpose of studying starvation initiated failure was to investigate the possibility of measuring the associated temperature changes. More work in this direction is certainly needed. The failure by scoring may also be encountered at high loads. Rigidity of the experimental apparatus was the limiting factor for increasing loads. However, by using a more rigid apparatus, higher loads and speeds could be imposed. In addition to the study of transient temperatures, examination of the wear debris may reveal the mechanism involved during failure.

Another important associated area of research is the investigation of the effect of lubricant rheological properties on failure. Although, the lubricant rheological properties may not be crucial in the final failure stages, they are certainly important during the transition from elastohydrodynamic to boundary lubrication. This area has not been investigated in the present research, but needs some urgent work. The nature of lubricants and additives may have an effect on the degree of asperity interaction. The process of successful running-in may also be affected.

The existence of the glassy state of lubricants in elastohydrodynamic contacts has already been indicated by the temperature measurements reported in this work. Further temperature measurements with lubricants like 5P4E, MCS 1218 which go into the glassy state more readily, are very desirable. The IR technique developed in this work can be used with little or no modification for surface temperature measurements with other fluids.

The infrared technique that has been developed for the simulated EHD conditions of operation appears to have a potential for application in similar and more complex practical situations such as gear teeth contacts. Likewise, the frequency analysis techniques described in this work have potential applications in the three dimensional analysis of surfaces (or microtopography) and their effects on lubrication.

APPENDIX A

DESCRIPTIVE DATA ON NAPHTHENIC BASE FLUID N1

Source:	Sun Oil Company
Supplier's designation:	R 620-15
Symbol used in this study:	N1
Viscosity at 100F, 0 GPa	
m^2/s, Pa.s:	24.06×10^{-6}, 22×10^{-3}
cs, cp, SUS:	24.06, 22, 115.2
Viscosity at 100 F, .138 GPa[1] (20,000 psig)	
m^2/s, Pa.s:	477×10^{-6}, 460×10^{-3}
cs, cp, SUS:	477, 460, 2200
Viscosity at 210 F, OGPa	
m^2/s, Pa.s:	3.728×10^{-6}, 3.228×10^{-3}
cs, cp, SUS:	3.728, 3.228, 38.59
Viscosity-Temperature Coefficient VTC[1]	
@ 100 F [$VTC = 1 - (\mu_{210}/\mu_{100})_p$]	
0 GPa	.873
.138 GPa (20,000 psig)	.950
Viscosity index (ASTM D-2270)	-13
Viscosity-pressure coefficient[1] $\frac{1}{\mu}\frac{\partial \mu}{\partial p}\Big\|_T$, ($Pa^{-1}$, Psi^{-1})	
@ 100 F	
0 GPa	22.19×10^{-9}, 1.53×10^{-4}
.138 GPa (20,000 psig)	22.19×10^{-9}, 1.53×10^{-4}
Density[1] (kg/m^3, g/cm^3) @ 68 F 0 GPa	916, .916
@ 100 F 0 GPa	904, .904
.0724 GPa:	936, .936
.138 GPa	960, .960

@ 210 F	0	GPa:	866, .866
	.0724	GPa:	905, .905
	.138	GPa	933, .933

Refractive Index @ 0 GPa:	1.5085
Flash point (C) @ 0 GPa:	315
Fire point (C) @ 0 GPa	365
Pour point (C) @ 0 GPa	.45
Thermal conductivity (W/mK, Lbf/°F.sec)	.13, .0167
Molecular weight[2]:	305
% C atoms in aromatic rings[3]:	21.5
% C atoms in naphthenic rings[4]:	36.0
% C atoms in paraffinic rings[4]:	42.5
% C atoms in aromatic rings[5]:	20.3
% C atoms in naphthenic rings[5]:	34.5
% C atoms in paraffinic rings[5]:	45.2
Average number of aromatic rings per molecule[5]:	.77
Average number of naphthenic rings per molecule[5]:	1.74
Average number of total rings per molecule[5]:	2.51

---

[1]Novak, J. D., and Winer, W. O., "Some Measurements of High Pressure Lubricant Rheology," Transaction ASME, Journal of Lubrication Technology, July 1968, pp. 580-591.

[2]Calculated from viscosity data using the method of Hirschler, A. E., Journal of the Institute of Petroleum, Vol. 32, 1940, pp. 133-161.

[3]Obtained using the Viscosity-Gravity Constant and the Refractivity Intercept using the method of Kurtz, S. S., Jr., King, R. W. Stout, W. J., and Gilbert, D. J., from a paper, "Relationship between Carbon-type Composition Viscosity-Gravity Constant and Refractivity Intercept," presented before the Petroleum Division, ACS, September 1955.

[4]Same reference as above.

[5]Calculated using the n-d-M method of structural group analysis of mineral oil fractions of Van Nes and Van Westen, "Aspects of the Constitution of Mineral Oils," Elsevier Publishing Company, Inc., 1951.

APPENDIX B

PROPERTIES OF STEEL AND SAPPHIRE

Properties of steel:

Material - AISI 52100 (chromium steel)

(Standard ball bearing steel)

Composition -

Element	C	Mn	P (max)	S (max)	Si	Cr
Percent	.95-1.00	.25-.45	.025	.025	.2-.35	1.3-1.6

Steel balls - Grade 25 (.000025 m/m of diameter)

Finish (.011, .076, and .38 μm R_a)

Diameter = 31.8 mm, mostly

Hardness

Temp. C	40	95	150	205	260	315
Rockwell C.	63	62	59	57	54	52

Thermal Conductivity k

at 23 C, k = 37.0 W/mK (4.62 Lbf/°F sec)

at 100 C, k = 34.7 W/mK (4.34 Lbf/°F sec)

Specific heat C = 429.4 J/kgK (.10 Btu/Lbm °F)

Density γ = 78.33 kg/m^3 (488 lbm/ft^3)

Thermal diffusivity

at 23 C, $\alpha = 11.0 \times 10^{-6}$ m^2/s (1.754×10^{-2} in^2/sec)

at 100 C, $\alpha = 9.56 \times 10^{-6}$ m^2/s (1.49×10^{-2} in^2/sec)

Modulus of Elasticity E = 207 GPa (30×10^6 psi)

Poisson's ratio ν = .3

Properties of Sapphire:

Density γ = 3980 kg/m^3

Hardness - Moh 9, Knoop microindenter 2000

(> 63 Rockwell C)

Modulus of Elasticity E = 365 GPa (53 x 10^6 psi)

Poisson's ratio ν = .25

Compressive strength - 2.07 GPa (300,000 psi)

Tensile Strength (at 20 C) - .4 GPa (58,000 psi)

Modulus of rupture (maximum bending stress depending on orientation)

-.45 - .69 GPa (65 - 100,000 psi)

Modulus of rigidity - 186.2 GPa (27 x 10^6 psi)

Thermal expansion Coefficient (60° orientation)

20 - 50 C: 58 x 10^{-7} m/m·K

20 - 500 C: 77 x 10^{-7} m/m·K

Thermal Conductivity k

at 0 C - 46.1 W/m.K

23 C - 41.9 W/m·K

100 C - 25.1 W/m·K

400 C - 12.6 W/m·K

Specific heat (at 20 C) c = 754 J/kg·K

Thermal diffusivity (at 100 C) α = 13.9 x 10^{-6} m^2/s

Sapphire-steel combination:

Effective modulus E' = 286 GPa (41.4 x 10^6 psi)

where, $$\frac{2}{E'} = \frac{1-\nu_{st}^2}{E_{st}} + \frac{1-\nu_{sa}^2}{E_{sa}}$$

Contact radius a (for ball radius R = 15.9 mm)

$a = .0436\ W^{1/3}$ mm, W in N

$= .00282\ W^{1/3}$ inch, W in Lbf

Peak Hertz Stress P_H (for ball radius R = 15.9 mm)

$P_H = .2515\ W^{1/3}$ GPa, W in N

$= 60{,}000\ W^{1/3}$ psi, W in Lbf

W N	a mm	P_H GPa	W N	a mm	P_H GPa
0	0	0	215	.2612	1.5067
5	.0746	.4301	250	.2747	1.5844
8.9	.0904	.5212	281.4	.2857	1.6481
10	.0939	.5418	300	.2919	1.6836
15	.1075	.6203	307.4	.2943	1.6974
20	.1183	.6827	350	.3073	1.7724
25	.1275	.7354	374.1	.3142	1.8122
50	.1606	.9265	400	.3212	1.8531
67	.1771	1.0215	425.7	.3280	1.8919
75	.1839	1.0606	450	.3341	1.9273
100	.2024	1.1674	500	.3461	1.9962
118.3	.2140	1.2346	522.1	.3511	2.0251
150	.2317	1.3363	550	.3572	2.0625
200	.2550	1.4708	600	.3677	2.1212

APPENDIX C

NUMERICAL VALUES OF FACTORS IN WIDE BAND AND NARROW BAND FILTER CALCULATIONS

Wide band filter:

$\tau_s = .97$

$\rho_1 = .076$

$\rho_2 = .0064$

$\eta_s = \tau_s(1 - \rho_1)(1 - \rho_2) = .8905$

$\rho_s^* = \rho_1 + \tau_s^2 (1 - \rho_1)^2 \rho_2 = .08114$

$N_o = 8.0$ mv or 1.2475 mw/cm^2.sr

$T_b = .1174X^3 + 4.621X^2 + 4.653X + 38.94$

where, $X = \ln(N - N_0) = \ln N_m$

$(N - N_0) = N_m$ in mv

Narrow band filter:

$\tau_s = .95$

$\rho_1 = .076$

$\rho_2 = .0064$

$\eta_s = \tau_s(1 - \rho_1)(1 - \rho_2) = .8722$

$\rho_s^* = \rho_1 + \tau_s^2 (1 - \rho_1)^2 \rho_2 = .08093$

$N_0 = .19$ mv or $.0296$ mW/cm^2·sr

$N_{BB}(T) = \text{Exp}[.000000245\ T^3 - .00015702\ T^2 + .05463T - 2.808]$

where N_{BB} is in mv and T in C.

Emissivity and Transmissivity (Fluid N1):

$$\varepsilon_F(h,T) = 1 - \exp[-.000055h\ e^{.0097T}]$$

$$\tau_F(h,T) = \mathrm{Exp}[-.00000623h\ e^{.01637T}]$$

where T is in K, h is in microinches.

Total radiation through Narrow band filter:

For $\varepsilon_b = .20$,

$$N_T = .1736\ N_{BB}(T_b)\tau_F(h,T_F) + [.1736\ \varepsilon_F(h,T_F) + 65\ \varepsilon_F(2h,T_F)]\ N_{BB}(T_F) + .104\tau_F(2h,T_F) + .0153$$

where, N_{BB}, N_T are in mvs

T_F in K

h in microinches

T_b in C

TEMPERATURE REDUCTION PROGRAMME (P_H = 1,02 GPa, V_b = 1.39 m/s)

```
C END TEMPERATURE PROGRAM
      DIMENSION XJJ(25), XJ(19), XKK(13), XK(10), H(19,10), DATA(2,25,13
     1), X(7), Y(7), CL(2), AA(25), AB(19), T(3,19,10),DAT (19),HA(6,19,
     210),DATB(19)
      EP = 1.E-6
      E = .005
      SIx = 0.
C ARRAY PREPARATION
      XJJ(1) = -9.
      DO 5 JJ = 2,25
    5 XJJ(JJ) = XJJ(JJ-1) + .75
      XJ(1) = -9.
      DO 10 J = 2,19
   10 XJ(J) = XJ(J-1) + 1.
      XKK(1) = 1.
      DO 15 KK = 2,13
   15 XKK(KK) = XKK(KK-1) + 1.
      XK(1) = 0.
      DO 20 K = 2,10
   20 XK(K) = XK(K-1) + 1.
C INPUT
      AMR=8.0
      DO 8006 I=1,5
      DO 1005 K=1,10
 1005 READ (5,1006) (HA(I,J,K),J=1,19)
 1006 FORMAT (19F4.1)
 8002 FORMAT (1H1)
      DO 8000 J=1,19
 8000 WRITE (6,8001) (HA(I,J,K), K=1,10)
 8001 FORMAT (10X,10F6.1)
 8006 CONTINUE
C FILM THICKNESS EXTRAPOLATION FOR 500 IPS
      DO 1161  K=1,10
      DO 1161  J=1,19
      CALL JAGEXT  (HA(1,J,K),HA(2,J,K),HA(3,J,K),HA(4,J,K),HA(5,J,K),H(
     1J,K))
```

```
 1161 CONTINUE
      DO 8010 J=1,19
 8010 WRITE (6,8001) (H(J,K),K=1,10)
      DO 1015 I = 1,2
      DO 1010 KK = 1,13
      READ (5,1007) (DATA(I,JJ,KK), JJ=1,15)
 1007 FORMAT (15F5.2)
      READ (5,1008) (DATA(I,JJ,KK), JJ=16,25)
 1008 FORMAT (10F5.2)
      DO 1010 JJ = 1,25
 1010 DATA(I,JJ,KK) = DATA(I,JJ,KK) + AMB
 1015 AMB =0.19
CENTER LINE CALCULATION
      I = 1
      NLS = 1
      LS = 7
      X(1) = 1.
      DO 1500 KK = 2,7
 1500 X(KK) = X(KK-1) + 1.
 1505 DO 1510 KK = 1,7
      Y(KK) = 0.
      DO 1510 JJ = 1,25
 1510 Y(KK) = Y(KK) + DATA(I,JJ,KK)
      GO TO 3000
 1515 CL(I) = -CLS1/(2.*CLS2)
      I = I + 1
      IF (I.LE.2) GO TO 1505
      CL(1)=-CL(1)
      WRITE (6,1516) (I,CL(I), I=1,2)
 1516 FORMAT (1H1,10X,2HCL,I1,2H =,F5.2///10X,2HCL,I1,2H =,F5.2)
C DATA REDUCTION - Y DIRECTION
      I = 1
      NLS = 2
      LS = 4
 2000 KK = 1
```

```
 2005 DO 2010 JJ = 1,25
      AA(JJ) = DATA(I,JJ,KK)
 2010 DATA (I,JJ,KK) = 0.
      DO 2015 J = 1,19
 2015 AB(J) = 0.
      JJ = 1
 2020 DO 2025 L = 1,4
      X(L) = XJJ(JJ+L-1)
 2025 Y(L) = AA(JJ+L-1)
      GO TO 3000
 2030 DO 2035 J = 1,19
      IF (XJ(J).LT.X(1)-EP.OR.XJ(J).GT.X(4)+EP) GO TO 2035
      DATA(I,J,KK) = DATA(I,J,KK) + (CLS2*XJ(J)+CLS1)*XJ(J) + CLSZ
      AB(J) = AB(J) + 1.
 2035 CONTINUE
      JJ = JJ + 1
      IF (JJ.LE.22) GO TO 2020
      DO 2040 J = 1,19
 2040 DATA (I,J,KK) = DATA(I,J,KK)/AB(J)
      KK = KK + 1
      IF (KK.LE.13) GO TO 2005
      I = I + 1
      IF (I.LE.2) GO TO 2000
      DO 2041 J=1,19
 2041 DAT (J)=DATA(1,J,13)
      DO 2042 J=1,19
 2042 DATB(J)=DATA(2,J,1)
      GO TO 4000
C LEAST SQUARES CALCULATIONS
 3000 XZ = 0.
      X1 = 0.
      X2 = 0.
      X3 = 0.
      X4 = 0.
      Y1 = 0.
      XY = 0.
      X2Y = 0.
```

```
      DO 3005 L = 1,LS
      XZ = XZ + 1.
      X1 = X1 + X(L)
      Y1 = Y1 + Y(L)
      XY = XY + X(L)*Y(L)
      SV = X(L)*X(L)
      X2 = X2 + SV
      X2Y = X2Y + SV*Y(L)
      SV = SV*X(L)
      X3 = X3 + SV
 3005 X4 = X4 + SV*X(L)
      CA = X2 - X3*X3/X4
      CB = X1 - X2*X3/X4
      CC = XY - X2Y*X3/X4
      CD = X3 - X1*X4/X2
      CE = X2 - XZ*X4/X2
      CF = X2Y - Y1*X4/X2
      IF (ABS(CD).LE.EP) GO TO 3010
      IF (ABS(CB*CD-CE*CA).LE.EP) GO TO 7000
      CLS2 = (CC-CF*CA/CD)/(CB-CE*CA/CD)
      CLS1 = (CF-CE*CLS2)/CD
      GO TO 3015
 3010 CLS2 = CF/CE
      CLS1 = (CC-CB*CLS2)/CA
 3015 CLS2 = (X2Y-X2*CLS2-X3*CLS1)/X4
      GO TO (1515,2030,4035), NLS
C DATA REDUCTION - X DIRECTION
 4000 I = 1
      NLS = 3
 4005 J = 1
 4010 DO 4015 KK = 1,13
      AA(KK) = DATA(I,J,KK)
 4015 DATA (I,J,KK) = 0.
      DO 4020 K = 1,10
 4020 AB(K) = 0.
      KK = 1
```

```
4025 IF (CL(I)-XKK(KK).GT.6.0.OR.XKK(KK)-CL(I).GT.9.0) GO TO 4041
     DO 4030 L = 1,4
     X(L) = XKK(KK+L-1) - CL(I)
4030 Y(L) = AA(KK+L-1)
     GO TO 3000
4035 DO 4040 K = 1,10
     IF (XK(K).LT.X(1).OR.XK(K).GT.X(4)) GO TO 4040
     DATA(I,J,K) = DATA(I,J,K) + (CLS2*XK(K)+CLS1)*XK(K) + CLSZ
     AB(K) = AB(K) + 1.
4040 CONTINUE
4041 KK = KK + 1
     IF (KK.LE.13) GO TO 4025
     DO 4045 K = 1,10
4045 DATA(I,J,K) = DATA(I,J,K)/AB(K)
     J = J + 1
     IF (J.LE.19) GO TO 4010
     I = I + 1
     IF (I.LE.2) GO TO 4005
     IF(CL(1).GT.4.) GO TO 4046
4046 DO 4047 J=1,19
4047 DATA(1,J,10)=DAT (J)
     IF(CL(2).LT.1.) GO TO 4048
4048 DO 4049 J=1,19
4049 DATA(2,J,1)=DATB(J)
     WRITE (6,8002)
     DO 8004 I = 1,2
     WRITE (6,8005)
8005 FORMAT (/)
     DO 8004 J = 1,19
8004 WRITE (6,8003) (DATA(I,J,K), K=1,10)
8003 FORMAT (10X,10F8.2)
CALCULATE AND PRINT BALL TEMPERATURE
     WRITE (6,5000) (K, K=1,9)
5000 FORMAT (1H1,26X,28HBALL TEMPERATURE (DEGREES C)///10X,5HINLET,15,8
    1I7//)
     DO 5020 J = 1,19
     JZ = IABS(J-10)
```

```
      DO 5005 K = 1,10
      CA= ALOG(1.4057*(DATA(1,J,K)-8.0))
 5005 T(1,J,K) = ((.11743*CA+4.621)*CA+4.653)*CA + 38.94-1.25-1.50
      IF (J.NE.4.AND.J.NE.7.AND.J.NE.14.AND.J.NE.17) GO TO 5010
      WRITE (6,5006)
 5006 FORMAT ()
 5010 IF (JZ.EQ.0) GO TO 5015
      WRITE (6,5011) (T(1,J,K), K=1,10), JZ
 5011 FORMAT (8X,10F7.2,I4)
      GO TO 5020
 5015 WRITE (6,5016) (T(1,J,K), K=1,10)
 5016 FORMAT (/8X,10F7.2,13H  CENTER LINE/)
 5020 CONTINUE
      WRITE (6,5021)
 5021 FORMAT (//10X,4HEXIT)
CALCULATE AND PRINT FLUID TEMPERATURE
      DO 5070 M = 2,3
      WRITE (6,6000) (K, K=1,9)
 6000 FORMAT (1H1,27X,29HFLUID TEMPERATURE (DEGREES C)///10X,5HINLET,I5,
     1 8I7//)
      DO 6065 J = 1,19
      JZ = IABS(J-10)
      DO 6050 K = 1,10
      CALL NAGTIT (T(1,J,K),T(M,J,K),H(J,K),DATA(2,J,K))
 6050 CONTINUE
      IF (J.NE.4.AND.J.NE.7.AND.J.NE.14.AND.J.NE.17) GO TO 6055
      WRITE (6,5006)
 6055 IF (JZ.EQ.0) GO TO 6060
      WRITE (6,5011) (T(M,J,K), K=1,10), JZ
      GO TO 6065
 6060 WRITE (6,5016) (T(M,J,K), K=1,10)
 6065 CONTINUE
 6070 WRITE (6,5021)
      WRITE (6,8002)
 7000 CALL EXIT
      END
```

```
      SUBROUTINE NAGTIT (T1,T,H,DATA)
      REAL NBBF, NBBF
      NBBF=EXP(((2.45E-7*T1-1.5702E-4)*T1+.05463)*T1-2.808)
      E=0.0001
      N=0
      L=0
      T=45.
 6025 TA=T+273.
      IF(T.GT.600) GO TO 6030
      G=-5.496E-5*H*EXP(.009692*TA)
      EMH = 1. - EXP(G)
      EM2H = 1. - EXP(2.*G)
      G=-6.23E-6*H*EXP(.01637*TA)
      TRH = EXP(G)
      TR2H = EXP(2.*G)
      NBBF=EXP(((2.45E-7*T-1.5702E-4)*T+.05463)*T-2.808)
      FT=.1736*TRH*NBBB+(.1736*EMH+.650*EM2H)*NBBF+.01530+.09760*TR2H-DA
     1TA
      FTP=0.1736*(-0.00000623*H      )*(0.01637)*EXP(0.01637*TA)*TRH*NBBB
     1 +(+0.1736*0.0000549 6*H      *0.009692*EXP(0.009692*TA)*(1-EMH)+0.6
     25*0.00010992*H      *.009692*EXP(.009692*TA)*(1-EM2H))*NBBF+(0.1736
     3*EMH+0.65*EM2H)*NBBF*((0.000000735*T        -0.00031404)*T        +0
     4.05463)-0.0976*0.00001246*H      *0.01637*EXP(0.01637*TA)*TR2H
      CALL NEWTIT(T        ,FT,FTP,E,N,L)
      GO TO (6025,6050,3,4,5,6),I
 6030 T=7.
      GO TO 6050
    3 T        =3
      GO TO 6050
    4 T        = 4.
      GO TO 6050
    5 T        =5.
      GO TO 6050
    6 T        =6.
      GO TO 6050
 6050 CONTINUE
      RETURN
      END
```

APPENDIX E

TYPICAL CALCULATION WITH NARROW BAND FILTER

(Fluid N1, P_H = 1.02 GPa, V_b = 1.39 m/s, V_{sa} = 0, T_{bath} = 40 C)

	At Inlet on ¢_	At Center	At Exit on ¢_	At Side Lobe min. H.
Ball Surface Contribution	30%	50%	57%	30%
Fluid Contribution	50%	40%	36%	50%
Ambient Contribution	20%	10%	7%	20%

APPENDIX F

Table F1. Film Thickness (in units of .025 μm) versus position (in units of .025 mm) (Fluid N1, Load = GTN, P_H = 1.02 GPa, V_b = 0.35 m/s, V_{sa} = 0, T_{bath} = 40 C)

Inlet	1	2	3	4	5	6	7	8	9	
19.1	19.5	20.0	22.6	26.1	31.3	40.9	50.5	60.9	71.4	9
8.7	9.3	10.4	12.4	19.1	22.6	33.1	40.0	50.5	60.9	8
4.4	4.4	4.8	5.2	8.5	15.7	22.6	28.7	40.0	50.5	7
2.6	2.6	2.6	2.6	4.8	8.5	15.7	19.1	29.6	40.9	6
2.6	2.6	2.6	2.6	2.6	4.8	6.1	12.2	22.6	33.1	5
2.5	2.6	2.6	2.6	2.6	2.5	4.8	7.0	15.7	26.1	4
2.6	2.6	2.6	2.6	2.6	2.5	2.5	5.2	12.2	22.6	3
2.6	2.6	2.6	2.6	2.6	2.5	2.0	5.0	8.7	18.3	2
2.6	2.6	2.6	2.6	2.6	2.5	2.0	4.0	7.8	15.7	1
2.6	2.6	2.6	2.6	2.6	2.5	2.0	4.0	7.0	15.7	0
2.6	2.6	2.6	2.6	2.6	2.5	2.0	4.0	7.8	15.7	1
2.6	2.6	2.6	2.6	2.6	2.5	2.0	5.0	8.7	18.3	2
2.6	2.6	2.6	2.6	2.6	2.5	2.0	5.2	12.2	22.6	3
2.6	2.6	2.6	2.6	2.5	2.0	4.0	7.0	15.7	26.1	4
2.5	2.5	2.4	2.0	2.0	2.0	5.0	12.2	22.6	33.1	5
2.0	2.0	2.0	2.6	3.5	4.8	8.7	19.1	29.6	40.9	6
2.6	2.6	4.8	5.2	6.1	11.3	15.7	28.7	40.0	50.5	7
8.7	9.3	10.4	12.4	15.7	19.1	23.5	40.0	50.5	60.9	8
19.1	19.5	20.0	22.6	25.2	29.6	33.1	50.5	60.9	71.4	9
Exit	1	2	3	4	5	6	7	8	9	

Table F2. Film Thickness (in units of .025 μm) versus position (in units of .025 mm) (Fluid N1, Load = 67N, P_H = 1.02 GPa, V_b = 0.7 m/s, V_{sa} = 0, T_{bath} = 40 C)

Inlet	1	2	3	4	5	6	7	8	9	
25.0	26.1	29.6	30.5	33.1	39.2	43.5	57.4	64.5	81.8	9
15.7	16.2	16.5	19.1	22.6	29.6	33.1	47.0	57.4	71.4	8
8.7	8.9	9.2	10.4	15.7	19.1	22.6	36.6	47.0	60.9	7
3.5	3.5	4.4	5.2	8.7	12.2	17.0	26.1	36.6	52.2	6
3.5	3.5	3.5	3.5	5.2	8.7	12.2	19.1	29.6	43.5	5
3.5	3.5	3.5	3.5	3.5	5.0	8.7	12.2	22.6	36.6	4
3.5	3.5	3.5	3.5	3.5	2.6	5.2	8.7	19.1	29.6	3
3.5	3.5	3.5	3.5	3.5	2.6	2.0	4.8	15.7	26.1	2
3.5	3.5	3.5	3.5	3.5	2.6	2.0	4.4	12.2	22.6	1
3.5	3.5	3.5	3.5	3.5	2.6	2.0	4.4	8.7	20.0	0
3.5	3.5	3.5	3.5	3.5	2.6	2.0	4.4	12.2	22.6	1
3.5	3.5	3.5	3.5	3.5	2.6	2.0	4.8	15.7	26.1	2
3.5	3.5	3.5	3.5	3.5	2.6	2.0	5.2	19.1	29.6	3
3.5	3.5	3.5	3.5	3.5	2.6	3.5	8.7	22.6	36.6	4
3.5	3.5	3.5	3.5	3.5	4.4	7.0	13.9	29.6	43.5	5
3.5	3.5	3.5	3.3	5.0	7.0	12.2	18.3	36.6	52.2	6
3.0	3.0	5.2	7.8	8.7	12.2	15.5	26.1	47.0	60.9	7
8.7	9.4	10.4	13.1	15.0	20.0	27.0	33.1	57.4	71.4	8
15.7	17.4	18.3	20.9	26.1	29.6	37.4	43.5	64.0	81.8	9
Exit	1	2	3	4	5	6	7	8	9	

Table F3. Film Thickness (in units of 0.025 μm) versus Position (in units of 0.025 mm) (Fluid N1, Load = 67N, P_H = 1.02 GPa, V_b = 1.39 m/s, V_{sa} = 0, T_{bath} = 40 C)

Inlet	1	2	3	4	5	6	7	8	9	
19.1	22.6	23.0	28.7	32.2	36.6	40.0	54.0	55.7	64.4	9
9.6	14.0	15.7	16.5	21.8	26.1	29.6	43.5	46.1	54.0	8
7.8	8.6	8.7	9.2	12.2	15.7	22.6	33.1	36.6	43.5	7
5.2	5.2	5.2	6.1	7.8	8.7	15.7	22.6	26.1	36.6	6
5.2	5.2	5.2	5.2	5.2	5.2	8.7	15.7	19.1	29.6	5
5.2	5.2	5.2	5.2	5.2	4.4	5.2	8.7	15.7	22.6	4
5.2	5.2	5.2	5.2	5.2	4.4	3.5	5.2	12.2	19.1	3
5.2	5.2	5.2	5.2	5.2	4.4	3.5	2.6	8.7	15.7	2
5.2	5.2	5.2	5.2	5.2	4.4	3.5	2.0	5.2	12.1	1
5.2	5.2	5.2	5.2	5.2	4.4	3.5	2.0	5.2	12.1	0
5.2	5.2	5.2	5.2	5.2	4.4	3.5	2.0	5.2	12.1	1
5.2	5.2	5.2	5.2	5.2	4.4	3.5	5.0	8.7	15.7	2
5.2	5.2	5.2	5.2	5.2	4.4	3.0	7.0	12.2	19.1	3
5.2	5.2	5.2	5.2	5.2	3.5	5.2	8.7	15.7	22.6	4
5.2	5.2	5.2	5.2	4.8	3.5	8.7	15.7	19.1	29.6	5
5.0	5.0	4.2	3.5	5.2	8.7	15.7	22.6	26.1	36.6	6
5.2	6.1	7.8	8.7	11.3	15.7	22.6	33.1	36.6	43.5	7
13.1	13.9	15.5	17.0	20.9	26.1	29.6	43.5	46.1	54.0	8
22.6	22.6	23.5	28.7	33.1	36.6	40.0	54.0	55.7	64.4	9
Exit	1	2	3	4	5	6	7	8	9	

Table F4. Film Thickness (in units of 0.025 μm) versus Position (in units of 0.025 mm) (Fluid N1, Load = 67N, P_H = 1.02 GPa, V_b = 2.54 m/s, V_{sa} = 0, T_{bath} = 40 C)

Inlet	1	2	3	4	5	6	7	8	9	
20.0	21.5	23.0	24.4	31.0	35.0	35.7	46.9	57.4	71.4	9
14.8	14.9	15.7	18.7	22.6	27.2	29.6	40.0	47.0	57.4	8
9.6	8.7	8.7	12.2	14.8	19.1	24.4	29.6	36.6	48.7	7
7.8	7.6	7.5	7.6	8.7	12.2	16.5	26.1	29.6	39.2	6
7.0	7.8	7.5	7.6	7.8	8.7	13.0	15.7	22.6	33.3	5
7.1	7.8	7.2	6.6	6.1	5.2	8.7	10.4	17.4	28.7	4
7.0	7.0	6.8	6.5	6.1	5.2	5.2	8.7	15.7	22.6	3
7.0	7.0	6.8	6.5	6.1	5.2	5.2	4.4	11.3	21.2	2
7.0	7.0	6.8	6.5	6.1	5.2	5.2	3.5	9.6	20.0	1
7.0	7.0	6.8	6.5	6.1	5.2	5.2	3.5	9.6	20.0	0 ℄
7.0	7.0	6.8	6.5	6.1	5.2	5.2	3.8	9.6	20.0	1
7.1	7.1	6.8	6.6	6.1	5.2	2.5	4.8	11.3	21.2	2
7.2	7.3	7.5	7.0	6.3	4.4	2.6	7.8	15.7	22.6	3
7.7	7.9	8.5	8.7	4.4	4.8	6.8	9.6	17.4	28.7	4
8.7	8.7	8.7	4.9	5.2	8.7	10.4	14.8	22.6	33.3	5
5.2	4.8	3.4	6.0	8.7	12.2	15.7	19.1	29.6	39.2	6
7.9	8.5	8.7	14.5	18.3	23.5	20.9	24.4	36.6	48.7	7
14.8	15.7	19.1	20.9	26.1	30.4	31.3	33.1	47.0	57.4	8
23.0	25.0	27.0	31.3	33.1	40.0	43.5	43.5	57.4	71.4	9
Exit	1	2	3	4	5	6	7	8	9	

Table F5. Film Thickness (in units of 0.025 μm) versus Position (in units of 0.025 mm) (Fluid N1, Load - 67 N, P_H = 1.02 GPa, V_b = 5.08 m/s, V_{sa} = 0, T_{bath} = 40 C

Inlet	1	2	3	4	5	6	7	8	9	
26.1	26.1	27.8	30.5	34.8	42.6	51.3	57.4	64.4	74.8	9
17.4	18.3	19.1	22.6	26.1	32.2	40.9	47.0	54.0	64.4	8
12.2	13.9	12.2	15.7	19.1	23.5	30.5	36.6	43.5	57.4	7
8.7	9.6	10.4	12.2	12.2	16.5	22.6	29.6	36.6	50.5	6
8.6	8.7	8.7	8.7	8.7	11.3	17.4	20.9	29.6	46.1	5
8.5	8.5	8.5	8.6	8.7	7.8	12.2	15.7	26.1	40.9	4
9.5	8.5	8.5	8.5	8.6	7.0	8.7	13.9	22.6	36.6	3
8.5	8.5	8.5	8.5	8.5	5.2	7.0	10.4	19.1	32.2	2
8.5	8.5	8.5	8.5	8.5	5.2	5.2	8.7	18.3	29.6	1
8.5	8.5	8.5	8.5	8.5	5.2	5.2	8.7	18.3	29.6	0
8.5	8.5	8.5	8.5	8.6	5.2	5.2	8.7	18.3	29.6	1
8.5	8.5	8.5	8.6	8.7	5.2	5.2	10.4	19.1	32.2	2
8.5	8.5	8.5	8.7	8.7	5.2	8.7	13.9	22.6	36.6	3
8.6	8.5	8.7	8.7	7.0	5.2	12.2	15.7	26.1	40.9	4
8.7	8.7	7.8	5.2	5.2	7.0	17.4	20.9	29.6	46.1	5
7.0	6.8	5.2	5.2	8.7	12.2	22.6	29.6	36.6	50.5	6
5.2	5.2	7.0	8.7	15.7	19.1	30.5	36.6	43.5	57.4	7
10.4	10.4	12.2	15.7	22.6	29.6	40.9	47.0	54.0	64.4	8
19.1	19.1	20.0	22.6	29.6	40.0	51.3	57.4	64.4	74.8	9
Exit	1	2	3	4	5	6	7	8	9	

C_

Table F6. Film Thickness (in Units of 0.025 μm) versus Position (in units of 0.025 mm) (Fluid N1, Load = 67 N, P_H = 1.02 GPa, V_b = 12.7 m/s, V_{sa} = 0, T_{bath} = 40 C)

Inlet	1	2	3	4	5	6	7	8	9	
24.8	26.3	28.1	31.0	37.3	43.6	45.8	54.2	59.9	71.4	9
19.9	21.9	22.6	26.1	27.6	33.8	36.7	45.9	49.7	59.1	8
16.7	18.1	15.5	22.1	23.0	24.1	30.6	36.0	39.4	52.3	7
14.9	16.0	16.5	19.4	15.2	17.6	21.9	32.8	33.7	45.4	6
13.9	14.9	14.6	14.7	14.1	13.0	22.3	22.2	28.6	41.7	5
13.9	14.6	14.0	13.5	13.1	10.2	13.9	17.0	24.6	37.6	4
15.2	13.8	13.5	13.2	12.9	10.2	10.7	15.0	22.5	32.0	3
13.8	13.8	13.6	13.2	12.8	7.8	11.2	7.7	18.3	29.9	2
13.8	13.8	13.6	13.2	12.8	7.8	8.5	6.2	15.8	27.9	1
13.8	13.8	13.6	13.2	12.8	7.8	8.6	6.2	17.4	28.4	0
13.8	13.8	13.6	13.2	12.9	7.8	8.5	6.5	15.8	27.9	1
13.9	13.9	13.6	13.5	13.1	7.8	5.9	9.3	18.3	29.9	2
14.0	14.1	14.3	14.1	13.3	7.2	9.1	16.2	22.5	32.0	3
14.6	14.6	15.6	15.7	9.3	8.0	15.1	17.1	24.6	37.6	4
16.0	16.0	14.9	8.4	8.6	13.1	23.6	22.5	26.6	41.7	5
11.2	10.5	6.7	7.6	13.0	19.2	29.7	29.2	33.7	45.4	6
9.7	10.5	10.0	14.8	27.1	27.9	35.1	34.1	39.4	52.3	7
14.7	14.7	17.9	21.3	29.9	38.0	45.8	43.6	49.7	59.1	8
22.4	22.9	24.5	28.5	35.4	47.2	57.5	54.1	59.9	71.4	9
Exit	1	2	3	4	5	6	7	8	9	

Table F7. Film Thickness (in units of 0.025 μm) versus Position (in units of 0.025 mm) (Fluid N1, Load = 215 N, P_H = 1.51 GPa, V_b = .7 m/s, V_{sa} = 0, T_{bath} = 40 C)

Inlet	1	2	3	4	5	6	7	8	9	10	11	12	
4.4	4.4	5.2	5.5	6.1	8.7	13.9	19.1	24.4	33.1	43.5	50.5	60.9	12
3.5	3.5	3.5	3.5	4.4	5.2	7.0	10.4	15.7	24.4	33.1	40.0	50.5	11
2.6	2.6	2.6	2.6	3.5	4.4	4.4	6.1	8.7	15.7	22.6	29.6	40.0	10
2.6	2.6	2.6	2.6	2.6	2.6	3.5	4.4	6.1	8.7	15.7	22.6	29.6	9
2.6	2.6	2.6	2.6	2.6	2.6	2.6	2.6	4.4	5.2	8.7	15.7	22.6	8
2.6	2.6	2.6	2.6	2.6	2.6	2.6	2.6	2.6	3.5	5.2	8.7	17.4	7
2.6	2.6	2.6	2.6	2.6	2.6	2.6	2.6	2.6	2.6	3.5	6.1	12.2	6
2.6	2.6	2.6	2.6	2.6	2.6	2.6	2.6	2.6	2.6	2.6	5.2	8.7	5
2.6	2.6	2.6	2.6	2.6	2.6	2.6	2.6	2.6	2.6	2.6	3.5	6.1	4
2.6	2.6	2.6	2.6	2.6	2.6	2.6	2.6	2.6	2.6	2.6	2.6	5.2	3
2.6	2.6	2.6	2.6	2.6	2.6	2.6	2.6	2.6	2.6	2.6	2.6	3.5	2
2.6	2.6	2.6	2.6	2.6	2.6	2.6	2.6	2.6	2.6	2.6	2.6	2.6	1
2.6	2.6	2.6	2.6	2.6	2.6	2.6	2.6	2.6	2.6	2.6	2.6	2.6	0
2.6	2.6	2.6	2.6	2.6	2.6	2.6	2.6	2.6	2.6	2.6	2.6	2.6	1
2.6	2.6	2.6	2.6	2.6	2.6	2.6	2.6	2.6	2.6	2.6	2.6	3.5	2
2.6	2.6	2.6	2.6	2.6	2.6	2.6	2.6	2.6	2.6	2.6	2.6	5.2	3
2.6	2.6	2.6	2.6	2.6	2.6	2.6	2.6	2.6	2.6	2.6	3.5	6.1	4
2.6	2.6	2.6	2.6	2.6	2.6	2.6	2.6	2.6	2.6	2.6	5.2	8.7	5
2.6	2.6	2.6	2.6	2.6	2.6	2.6	2.6	2.6	2.6	3.5	6.1	12.2	6
2.6	2.6	2.6	2.6	2.6	2.6	2.6	2.6	2.6	3.5	5.2	8.7	17.4	7
2.6	2.6	2.6	2.6	2.6	2.6	2.6	2.6	4.4	5.2	8.7	15.7	22.6	8
2.6	2.6	2.6	2.6	2.6	2.6	3.5	4.4	6.1	8.7	15.7	22.6	29.6	9
2.6	2.6	2.6	2.6	3.5	4.4	4.4	6.1	8.7	15.7	22.6	29.6	40.0	10
3.5	3.5	3.5	3.5	4.4	5.2	7.0	10.4	15.7	24.4	33.1	40.0	50.5	11
4.4	4.4	5.2	5.5	6.1	8.7	13.9	19.1	24.4	33.1	43.5	50.5	60.9	12
Exit	1	2	3	4	5	6	7	8	9	10	11	12	

Table F8. Film Thickness (in units of 0.025 μm) versus Position (in unots of 0.025 mm) (Fluid N1, Load = 215N, P_H = 1.51 GPa, V_b = 1.39 m/s, V_{sa} = 0, T_{bath} = 40 C)

Inlet	1	2	3	4	5	6	7	8	9	10	11	12	
5.2	5.2	5.2	6.1	8.7	11.3	13.9	19.1	23.5	29.6	36.6	50.5	60.9	12
4.4	4.4	4.4	4.5	5.2	6.1	8.7	10.4	15.7	21.8	24.4	40.0	50.5	11
3.5	3.5	3.5	3.5	4.4	5.2	5.2	6.1	8.7	13.1	17.4	29.6	41.8	10
3.5	3.5	3.5	3.5	3.5	3.5	4.4	4.4	5.2	7.8	12.2	20.9	33.1	9
3.5	3.5	3.5	3.5	3.5	3.5	3.5	3.5	4.4	5.2	8.7	13.9	26.1	8
3.5	3.5	3.5	3.5	3.5	3.5	3.5	3.5	3.5	4.4	5.2	7.8	17.4	7
3.5	3.5	3.5	3.5	3.5	3.5	3.5	3.5	3.5	3.5	4.4	5.2	12.2	6
3.5	3.5	3.5	3.5	3.5	3.5	3.5	3.5	3.5	3.5	3.5	4.4	8.7	5
3.5	3.5	3.5	3.5	3.5	3.5	3.5	3.5	3.5	3.5	3.5	3.5	5.2	4
3.5	3.5	3.5	3.5	3.5	3.5	3.5	3.5	3.5	3.5	3.5	3.5	4.4	3
3.5	3.5	3.5	3.5	3.5	3.5	3.5	3.5	3.5	3.5	3.5	3.5	4.4	2
3.5	3.5	3.5	3.5	3.5	3.5	3.5	3.5	3.5	3.5	3.5	3.5	3.5	1
3.5	3.5	3.5	3.5	3.5	3.5	3.5	3.5	3.5	3.5	3.5	3.5	3.5	0
3.5	3.5	3.5	3.5	3.5	3.5	3.5	3.5	3.5	3.5	3.5	3.5	3.5	1
3.5	3.5	3.5	3.5	3.5	3.5	3.5	3.5	3.5	3.5	3.5	3.5	4.4	2
3.5	3.5	3.5	3.5	3.5	3.5	3.5	3.5	3.5	3.5	3.5	3.5	4.4	3
3.5	3.5	3.5	3.5	3.5	3.5	3.5	3.5	3.5	3.5	3.5	3.5	5.2	4
3.5	3.5	3.5	3.5	3.5	3.5	3.5	3.5	3.5	3.5	3.5	4.4	8.7	5
3.5	3.5	3.5	3.5	3.5	3.5	3.5	3.5	3.5	3.5	4.4	5.2	12.2	6
3.5	3.5	3.5	3.5	3.5	3.5	3.5	3.5	3.5	4.4	5.2	7.8	17.4	7
3.5	3.5	3.5	3.5	3.5	3.5	3.5	3.5	4.4	5.2	8.7	13.9	26.1	8
3.5	3.5	3.5	3.5	3.5	3.5	4.4	4.4	5.2	7.8	12.2	20.9	33.1	9
3.5	3.5	3.5	3.5	4.4	5.2	5.2	6.1	8.7	13.1	17.4	29.6	41.8	10
4.4	4.4	4.4	4.5	5.2	6.1	8.7	10.4	15.7	21.8	24.4	40.0	50.5	11
5.2	5.2	5.2	6.1	8.7	11.3	13.9	19.1	23.5	29.6	36.6	50.5	60.9	12
Exit	1	2	3	4	5	6	7	8	9	10	11	12	

Table F9. Film Thickness (in units of 0.025 μm) versus Position (in units of 0.025 mm) Fluid N1, Load - 215N, P_H = 1.51 GPa, V_b = 2.54 m/s, V_{sa} = 0, T_{bath} = 40 C)

Inlet	1	2	3	4	5	6	7	8	9	10	11	12	
5.2	5.2	5.5	6.1	7.8	9.6	14.8	21.8	27.0	33.1	43.5	50.5	60.9	12
4.4	4.4	4.4	4.5	4.5	5.2	8.7	13.9	19.1	22.6	33.1	43.5	52.2	11
3.5	3.5	3.5	3.5	3.5	3.5	4.4	7.8	10.4	15.7	24.4	36.6	43.5	10
3.5	3.5	3.5	3.5	3.5	3.5	3.5	4.4	6.1	11.3	19.1	29.6	36.6	9
3.5	3.5	3.5	3.5	3.5	3.5	3.5	3.5	3.5	5.2	13.1	20.9	29.6	8
3.5	3.5	3.5	3.5	3.5	3.5	3.5	3.5	3.5	4.4	8.7	10.4	22.6	7
3.5	3.5	3.5	3.5	3.5	3.5	3.5	3.5	3.5	3.5	4.4	6.1	15.7	6
3.5	3.5	3.5	3.5	3.5	3.5	3.5	3.5	3.5	3.5	3.5	4.4	9.6	5
3.5	3.5	3.5	3.5	3.5	3.5	3.5	3.5	3.5	3.5	3.5	4.4	5.2	4
3.5	3.5	3.5	3.5	3.5	3.5	3.5	3.5	3.5	3.5	3.5	3.5	5.2	3
3.5	3.5	3.5	3.5	3.5	3.5	3.5	3.5	3.5	3.5	3.5	3.5	4.4	2
3.5	3.5	3.5	3.5	3.5	3.5	3.5	3.5	3.5	3.5	3.5	3.5	4.4	1
3.5	3.5	3.5	3.5	3.5	3.5	3.5	3.5	3.5	3.5	3.5	3.5	4.4	0
3.5	3.5	3.5	3.5	3.5	3.5	3.5	3.5	3.5	3.5	3.5	3.5	4.4	1
3.5	3.5	3.5	3.5	3.5	3.5	3.5	3.5	3.5	3.5	3.5	3.5	4.4	2
3.5	3.5	3.5	3.5	3.5	3.5	3.5	3.5	3.5	3.5	3.5	3.5	5.2	3
3.5	3.5	3.5	3.5	3.5	3.5	3.5	3.5	3.5	3.5	3.5	4.4	5.2	4
3.5	3.5	3.5	3.5	3.5	3.5	3.5	3.5	3.5	3.5	3.5	4.4	9.6	5
3.5	3.5	3.5	3.5	3.5	3.5	3.5	3.5	3.5	3.5	4.4	6.1	15.7	6
3.5	3.5	3.5	3.5	3.5	3.5	3.5	3.5	3.5	4.4	8.7	10.4	22.6	7
3.5	3.5	3.5	3.5	3.5	3.5	3.5	3.5	3.5	5.2	13.1	20.9	29.6	8
3.5	3.5	3.5	3.5	3.5	3.5	3.5	4.4	6.1	11.3	19.1	29.6	36.6	9
3.5	3.5	3.5	3.5	3.5	3.5	4.4	7.8	10.4	15.7	24.4	36.6	43.5	10
4.4	4.4	4.4	4.4	4.5	5.0	8.7	13.9	19.1	22.6	33.1	43.5	52.2	11
5.2	5.2	5.5	6.1	7.8	209.0	14.8	21.8	27.0	33.1	43.5	50.5	60.9	12
Exit	1	2	3	4	5	6	7	8	9	10	11	12	

APPENDIX G

Table G1. Ball Surface Temperature (C) versus Position (in units of .025 mm) (Fluid N1, Load = 67N, P_H = 1.02 GPa, V_b = .35 m/s, V_{sa} = 0, T_{bath} = 40 C)

INLET	1	2	3	4	5	6	7	8	9	
44.76	42.71	42.51	44.26	44.78	44.49	44.72	44.42	43.72	43.04	9
44.66	42.56	42.13	43.66	44.42	44.33	44.44	44.11	43.36	42.54	8
44.84	43.21	42.81	43.53	43.84	44.13	44.36	43.65	42.58	41.78	7
45.57	44.55	44.65	44.45	43.77	43.34	43.18	42.75	42.15	41.49	6
47.58	47.06	47.71	46.55	44.48	40.78	38.66	40.55	42.34	41.21	5
50.89	50.63	51.73	49.63	45.68	42.94	41.82	41.41	41.01	40.19	4
54.54	54.24	55.73	53.08	47.44	45.24	44.83	42.53	40.34	39.91	3
58.84	58.73	60.15	56.83	49.80	46.63	45.71	42.86	40.21	39.60	2
63.19	63.40	64.51	60.69	53.14	49.21	47.43	43.63	40.11	39.08	1
67.31	67.36	68.25	64.64	56.91	51.99	49.25	44.33	39.85	38.72	CENTER LINE
69.96	69.95	70.44	66.90	59.50	54.38	50.76	44.81	39.56	38.32	1
72.14	71.89	71.98	68.86	62.17	56.54	52.10	45.57	39.81	38.31	2
74.21	73.56	72.81	69.78	64.03	58.42	53.16	46.30	40.36	38.32	3
75.54	74.20	72.20	69.53	65.24	59.57	53.30	46.35	40.67	38.31	4
76.11	75.90	70.49	68.53	65.88	59.78	52.55	46.02	40.98	38.32	5
76.02	75.03	67.85	66.21	65.09	58.55	50.50	44.85	40.94	38.31	6
74.65	71.06	64.46	63.44	63.83	57.24	48.90	43.97	40.88	38.32	7
72.40	68.33	60.72	59.94	61.61	55.38	46.93	42.76	40.60	38.32	8
69.59	65.32	57.28	56.51	59.03	53.06	44.97	41.94	40.58	38.31	9
EXIT										

Table G2. Fluid Temperature (C) versus Position (in units of .025 mm) (Fluid N1, Load = 67N, P_H = 1.02 GPa, V_b = .35 m/s, V_{sa} = 0, T_{bath} = 40 C)

INLET	1	2	3	4	5	6	7	8	9	
124.08	121.56	109.72	96.71	92.92	93.86	87.23	81.06	76.39	72.41	9
145.03	141.21	126.79	110.87	99.24	100.29	91.21	85.45	79.76	75.52	8
165.40	157.98	135.38	130.05	120.17	108.09	98.62	91.78	84.30	79.39	7
181.52	176.55	161.25	151.80	134.81	123.76	107.40	100.87	90.46	83.72	6
181.52	178.02	165.88	154.07	152.52	140.46	133.40	112.42	96.23	88.24	5
181.73	177.20	164.47	154.06	153.33	158.54	138.68	126.34	105.23	93.76	4
182.11	177.64	164.84	154.72	153.89	157.12	155.77	133.94	111.70	97.09	3
183.80	179.14	165.20	155.57	154.94	156.50	162.08	135.44	120.70	102.08	2
186.32	181.01	166.01	156.27	155.24	155.67	161.55	141.51	123.46	105.90	1
188.02	182.62	167.75	157.99	155.72	155.11	161.28	141.43	126.29	106.04	CENTER LINE
189.39	183.93	169.78	160.79	156.87	154.26	160.17	141.51	124.02	106.10	1
190.52	185.06	171.98	162.82	157.59	154.34	160.22	135.42	121.52	103.18	2
190.78	185.48	174.01	164.67	158.13	154.51	160.62	134.72	113.79	100.01	3
190.14	185.58	176.23	166.74	159.46	160.80	140.92	127.34	108.65	98.47	4
191.16	186.97	179.79	176.04	166.79	162.05	136.60	113.86	100.03	93.26	5
197.74	193.89	186.13	169.47	151.86	138.25	123.46	104.11	94.23	88.63	6
189.01	185.71	159.68	149.49	137.35	116.70	109.33	95.48	88.23	84.34	7
152.26	146.92	136.84	125.24	113.18	105.22	101.00	89.09	83.39	79.47	8
129.92	125.73	118.13	109.12	101.58	95.81	94.25	84.91	79.32	74.61	9
EXIT										

Table G3. Ball Surface Temperature (C) versus Position (in units of .025 mm) (Fluid N1, Load = 67N, P_H = 1.02 GPa, V_b = .7 m/s, V_{sa} = 0, T_{bath} = 40 C)

INLET	1	2	3	4	5	6	7	8	9	
46.92	48.64	46.83	45.78	46.20	45.25	44.11	45.24	46.71	46.86	9
46.49	47.42	45.45	45.93	46.35	45.22	43.85	44.89	46.36	46.53	8
45.91	46.07	46.28	45.47	45.05	44.65	43.02	44.08	45.96	46.04	7
47.51	48.08	46.56	45.52	45.98	44.94	42.50	43.44	45.38	45.44	6
50.42	49.15	47.57	46.83	46.57	44.94	42.39	43.43	44.98	43.98	5
54.60	52.00	51.75	51.19	48.67	45.30	42.78	43.90	45.07	43.48	4
62.37	59.24	58.59	57.60	53.47	48.47	44.45	44.29	45.06	43.94	3
69.44	64.99	65.69	64.15	57.83	52.49	47.32	44.76	44.25	43.53	2
75.78	70.72	72.74	70.43	62.76	56.76	50.66	45.58	43.15	43.04	1
82.90	81.97	79.90	75.63	68.71	61.47	53.81	47.11	43.37	43.07	CENTER LINE
88.67	87.91	84.91	81.14	74.28	66.24	57.78	49.82	44.56	43.06	1
92.31	91.76	89.13	85.06	78.73	70.65	61.26	52.07	45.44	43.06	2
94.71	94.67	92.17	87.96	81.48	73.62	63.86	53.45	45.67	43.06	3
95.51	95.43	93.70	89.53	82.68	75.00	65.06	54.56	46.65	43.06	4
94.86	95.37	93.59	88.94	82.40	74.95	64.78	54.84	47.48	43.06	5
93.15	93.83	91.51	86.66	80.00	72.92	63.40	54.13	47.32	43.07	6
89.20	89.72	87.04	83.04	77.48	70.27	60.95	52.92	47.21	43.02	7
83.61	84.58	81.99	78.60	73.82	66.91	57.86	50.93	46.66	43.52	8
78.50	79.00	76.73	73.49	68.53	62.65	54.75	48.89	46.09	44.62	9
EXIT										

Table G4. Fluid Temperature (C) versus Position (in units of .025 mm)
(Fluid N1, Load = 67N, P_H = 1.02 GPa, V_b = .7 m/s, V_{sa} = 0, T_{bath} = 40 C)

INLET	1	2	3	4	5	6	7	8	9	
103.62	105.85	94.69	75.43	83.88	106.97	107.73	87.79	73.43	73.36	9
113.15	115.41	107.28	85.13	89.00	112.48	113.93	91.89	76.54	75.34	8
127.42	131.08	122.82	98.74	94.00	122.29	123.19	97.33	80.30	78.08	7
151.26	157.94	145.01	117.44	104.86	132.91	130.18	104.76	85.02	80.71	6
152.92	158.74	152.19	128.15	117.44	141.33	138.36	111.60	89.09	83.43	5
157.44	160.77	153.11	127.70	128.54	157.54	147.87	122.47	94.19	85.93	4
161.11	162.62	154.27	130.20	131.22	178.65	163.25	130.46	97.15	89.17	3
164.05	164.28	155.05	134.90	137.48	180.24	193.04	146.42	101.83	90.57	2
165.20	167.19	155.88	135.43	143.63	182.00	192.61	147.92	107.90	92.07	1
166.42	167.69	159.05	139.66	147.47	183.78	193.03	147.81	116.34	93.61	CENTER LINE
169.08	171.21	166.19	148.76	151.39	186.15	193.57	148.18	108.40	90.90	1
171.06	173.86	168.98	153.35	154.89	186.47	193.13	145.73	102.56	87.85	2
174.59	175.96	169.88	155.81	156.30	184.86	192.47	143.37	98.13	85.16	3
177.91	178.75	169.47	154.62	155.90	184.94	175.31	129.46	94.19	80.76	4
175.78	177.25	167.63	149.52	152.59	168.86	155.26	117.25	87.48	77.72	5
172.32	173.03	162.35	142.34	138.57	154.86	139.99	110.59	82.57	74.55	6
173.86	174.72	149.39	117.59	121.14	138.53	132.34	103.63	78.30	72.67	7
141.21	139.65	128.71	102.54	101.08	123.71	120.25	100.09	75.52	70.70	8
125.13	143.03	112.85	91.84	87.12	112.04	112.52	96.04	73.76	68.98	9
EXIT										

Table G5. Ball Surface Temperature (C) versus Position (in units of 0.025 mm)
(Fluid N1, Load = 67N, P_H = 1.02 GPa, V_b = 1.39 m/s, V_{sa} = 0, T_{bath} = 40 C)

INLET	1	2	3	4	5	6	7	8	9	
53.61	52.84	52.75	52.81	52.81	52.81	52.85	52.82	52.26	51.72	9
53.62	52.94	52.76	52.80	52.81	52.81	52.85	52.82	52.26	51.72	8
54.53	53.41	52.77	52.74	52.79	52.81	52.85	52.82	52.26	51.72	7
55.91	54.24	53.00	52.71	52.76	52.78	52.83	52.82	52.26	51.72	6
58.74	56.90	54.92	54.11	53.63	53.04	52.90	52.82	52.24	51.72	5
63.26	61.30	59.11	57.59	55.97	54.23	53.29	52.82	52.19	51.72	4
70.49	68.34	65.42	61.95	58.33	55.65	54.05	53.06	52.19	51.65	3
78.91	77.09	73.48	69.14	63.92	59.08	55.98	53.88	52.20	51.43	2
88.61	86.68	83.02	78.20	71.37	64.36	59.34	55.30	52.23	51.06	1
97.38	95.61	92.04	86.25	78.03	69.94	63.24	57.26	52.78	51.03	CENTER LINE
104.52	102.89	98.93	92.92	84.90	75.80	67.23	60.13	54.16	51.16	1
110.53	108.95	104.71	98.44	90.43	81.05	71.51	62.87	55.21	51.17	2
114.87	113.28	109.09	102.61	94.38	84.54	74.38	64.70	55.69	50.92	3
117.12	115.48	111.12	104.65	96.48	86.23	75.37	64.88	55.42	50.69	4
117.29	115.80	111.62	105.12	96.66	86.24	75.13	64.39	55.22	50.83	5
115.45	114.33	110.69	104.10	95.16	84.66	73.82	63.56	54.96	50.88	6
111.33	110.48	107.26	100.98	92.26	81.77	71.17	61.87	54.42	50.95	7
105.84	105.55	102.74	96.91	88.58	78.34	68.23	59.89	53.75	51.05	8
100.14	99.63	97.35	92.34	84.83	74.95	65.42	58.19	53.11	50.99	9
EXIT										

Table G6. Fluid Temperature (C) versus Position (in units of 0.025 mm) (Fluid N1, Load = 67N, P_H = 1.02 GPa, V_b = 1.39 m/s, V_{sa} = 0, T_{bath} = 40 C)

INLET	1	2	3	4	5	6	7	8	9	
105.63	102.44	101.96	94.00	89.77	90.68	91.92	85.87	81.93	75.76	9
122.78	113.87	110.52	106.22	98.26	97.15	97.21	89.62	85.24	78.18	8
127.62	125.42	124.28	121.17	112.59	108.22	102.27	94.66	88.95	80.49	7
137.59	137.62	137.67	131.05	120.04	118.40	108.76	102.90	96.06	82.58	6
135.58	136.46	136.91	133.96	128.54	128.97	121.39	110.81	102.67	85.36	5
131.55	133.65	134.87	132.01	126.64	131.17	132.87	124.34	106.22	89.59	4
130.47	131.95	131.12	128.99	123.70	127.25	140.80	137.10	112.23	93.57	3
139.19	141.70	138.47	129.13	117.46	123.19	139.58	156.93	120.95	97.69	2
147.36	151.17	148.58	136.84	117.75	125.05	145.54	168.42	135.26	103.00	1
155.99	158.80	156.25	147.03	129.53	133.86	152.85	172.35	135.97	102.57	CENTER LINE
160.68	162.52	161.44	153.04	133.97	136.66	156.18	173.08	136.01	102.28	1
164.49	166.48	164.84	156.36	137.83	141.30	156.87	145.78	122.35	96.24	2
168.59	170.47	167.72	159.47	144.01	145.27	161.61	136.01	113.86	92.78	3
170.70	171.89	168.37	161.13	150.95	159.27	148.17	130.87	108.04	89.23	4
170.49	170.97	168.31	162.22	157.65	163.06	133.13	114.91	103.67	84.67	5
169.04	170.54	174.06	174.17	158.61	139.08	115.18	104.58	96.92	82.00	6
162.39	160.30	152.39	143.71	136.58	124.71	106.35	96.56	90.12	79.80	7
132.24	132.93	127.59	119.77	118.53	112.00	100.67	91.68	85.90	76.91	8
115.04	116.98	112.71	104.11	106.52	103.89	94.74	87.24	81.83	74.41	9
EXIT										

Table G7. Ball Surface Temperature (C) versus Position (in units of 0.025 mm)
(Fluid N1, Load = 67N, P_H = 1.02 GPa, V_b = 2.54 m/s, V_{sa} = 0, T_{bath} = 40 C)

INLET	1	2	3	4	5	6	7	8	9	
55.79	55.34	55.26	56.40	56.72	56.49	58.33	60.18	56.48	52.15	9
55.97	55.61	55.72	56.53	56.71	56.60	58.53	59.78	55.13	50.85	8
57.26	56.52	56.37	56.96	57.55	57.68	59.05	59.82	55.07	50.50	7
61.54	59.29	57.73	58.26	59.05	58.67	59.33	60.25	55.24	49.98	6
68.40	64.05	59.10	59.85	61.13	59.54	60.22	61.40	55.47	48.73	5
77.28	71.29	62.57	63.21	65.62	62.91	62.55	63.20	56.07	47.83	4
86.55	79.55	67.48	68.72	72.21	67.61	65.97	66.28	57.86	47.93	3
96.25	88.29	74.28	75.17	78.58	73.48	70.93	69.92	59.97	48.42	2
105.13	97.39	82.52	82.77	86.04	80.05	75.80	73.27	61.71	48.61	1
112.87	105.27	89.94	89.97	93.22	86.06	80.60	76.87	64.00	49.22	CENTER LINE
118.57	112.01	97.65	96.96	98.99	90.85	84.25	79.62	66.09	50.22	1
123.45	117.60	104.48	102.83	103.48	94.92	87.40	81.74	67.45	50.96	2
126.68	121.78	110.61	107.76	106.36	97.19	89.04	82.54	67.87	51.34	3
127.28	124.32	115.79	110.21	105.94	97.50	89.48	82.54	67.70	51.05	4
125.98	125.02	119.10	111.22	104.08	96.49	89.03	82.06	67.16	50.61	5
122.69	123.92	121.42	111.59	100.82	93.74	87.25	80.60	66.27	50.50	6
116.79	120.77	122.62	111.70	96.59	89.01	84.04	78.72	65.41	50.95	7
110.97	117.26	122.25	110.81	92.74	84.51	80.96	76.96	64.73	51.84	8
104.61	113.06	120.86	109.43	89.63	81.19	79.25	76.49	64.67	51.93	9
EXIT										

Table G8. Fluid Temperature (C) versus Position (in units of 0.025 mm)
(Fluid N1, Load = 67N, P_H = 1.02 GPa, V_b = 2.54 m/s, V_{sa} = 0,
T_{bath} = 40 C)

INLET	1	2	3	4	5	6	7	8	9	
102.40	102.08	101.10	98.22	91.61	93.37	97.13	90.60	86.08	78.59	9
110.12	110.79	109.81	104.25	98.58	98.86	101.15	94.55	91.35	83.79	8
121.02	124.03	124.22	114.30	107.89	106.43	105.38	100.98	96.44	86.99	7
123.19	125.68	127.29	125.53	120.05	116.90	114.76	102.83	99.83	90.76	6
117.98	120.66	125.98	124.09	121.51	125.67	120.59	113.77	104.96	93.88	5
107.09	117.56	127.67	125.23	124.81	130.33	130.66	123.15	110.65	97.15	4
107.29	126.21	135.11	122.85	121.99	141.08	145.79	127.16	112.45	102.31	3
115.83	137.14	141.47	121.18	125.11	143.91	147.26	145.74	119.74	103.07	2
124.04	146.69	148.56	120.89	129.27	146.87	148.53	152.01	122.97	103.86	1
131.85	155.44	157.06	125.71	131.99	149.73	149.89	151.67	121.68	102.85	CENTER LINE
144.09	163.18	162.74	129.13	134.49	152.96	153.16	152.07	121.59	101.54	1
151.86	168.38	166.31	133.26	138.93	155.33	176.82	147.71	118.39	99.69	2
157.29	171.11	165.38	138.21	143.50	161.76	176.09	135.36	111.05	98.14	3
161.82	170.69	161.51	141.56	161.12	159.73	147.91	131.10	109.11	92.36	4
164.44	167.98	158.68	154.15	160.47	142.51	136.89	120.52	102.98	89.09	5
184.66	184.35	179.54	160.43	146.48	132.70	127.06	114.52	96.94	86.12	6
175.64	164.23	142.04	136.08	126.33	115.84	120.21	108.14	91.85	81.58	7
157.90	142.09	111.54	126.10	116.83	109.88	110.81	100.48	86.03	77.98	8
144.98	124.83	90.71	115.16	110.08	103.45	103.21	93.77	81.71	74.06	9
EXIT										

Table G9. Ball Surface Temperature (C) versus Position (in units of 0.025 mm) (Fluid N1, Load = 67N, P_H = 1.02 GPa, V_b = 5.08 m/s, V_{sa} = 0, T_{bath} = 40 C)

INLET	1	2	3	4	5	6	7	8	9	
52.61	52.44	53.19	54.69	53.94	52.65	52.88	53.77	54.14	53.26	9
53.79	53.61	53.52	54.54	53.92	52.68	52.86	53.15	53.08	53.73	8
57.59	56.31	55.15	55.09	53.82	52.61	52.67	52.84	53.33	53.89	7
63.12	59.92	56.78	55.47	53.76	52.76	52.95	53.68	54.04	53.30	6
70.52	65.41	59.90	56.66	54.33	54.76	54.51	54.18	53.77	52.88	5
81.18	74.29	65.86	61.36	57.60	57.41	55.68	53.55	53.30	52.86	4
91.96	84.51	75.13	68.73	62.47	60.92	56.97	53.05	53.06	52.86	3
103.02	94.56	84.47	78.09	71.22	68.56	61.01	53.91	53.38	52.87	2
112.48	103.70	93.86	87.72	81.14	76.88	66.24	56.16	53.93	52.87	1
119.73	112.20	103.34	96.53	89.24	84.24	71.44	58.15	54.22	52.30	CENTER LINE
126.37	119.47	111.57	105.22	97.51	90.74	75.57	60.09	54.96	51.77	1
130.73	124.60	117.66	111.94	104.02	95.70	78.87	62.19	55.97	51.73	2
133.28	129.59	123.49	117.34	109.48	99.46	81.82	64.35	55.78	50.64	3
133.97	132.68	128.28	121.89	113.15	101.15	83.10	65.05	54.94	51.60	4
133.00	133.73	131.01	125.38	116.25	100.95	81.68	64.54	54.10	51.76	5
129.16	132.73	132.24	127.12	117.50	99.40	79.12	63.77	53.97	53.32	6
122.10	129.66	131.42	125.66	115.32	96.42	77.08	63.10	53.52	53.43	7
114.42	125.29	128.30	122.04	111.51	92.07	73.96	62.03	52.72	54.16	8
105.88	118.08	122.24	116.90	106.79	86.95	69.13	59.21	52.21	55.42	9

EXIT

Table G10. Fluid Temperature (C) versus Position (in units of 0.025 mm) (Fluid N1, Load = 67N, P_H = 1.02 GPa, V_b = 5.08 m/s, V_{sa} = 0, T_{bath} = 40 C)

INLET	1	2	3	4	5	6	7	8	9	
95.95	95.14	98.71	92.05	87.33	94.20	93.38	86.59	81.09	87.10	9
97.97	97.81	107.41	100.51	96.07	101.72	98.72	91.36	85.40	90.01	8
105.09	102.58	116.58	108.56	104.02	107.78	104.19	96.82	89.89	92.35	7
122.95	118.78	122.15	115.49	116.51	116.16	110.20	101.30	93.76	95.27	6
134.82	133.86	135.20	128.59	128.13	126.46	115.11	108.49	98.65	97.40	5
145.21	147.84	148.60	138.12	132.93	138.73	123.41	114.09	101.21	100.06	4
155.24	150.83	160.35	150.73	141.89	144.65	131.77	115.19	103.86	102.56	3
164.44	170.89	170.67	159.32	146.17	152.64	136.47	121.35	106.99	105.44	2
171.33	177.04	175.91	164.47	151.63	155.40	144.62	124.64	107.19	107.34	1
178.75	180.92	180.04	171.22	161.20	161.37	144.65	123.55	106.37	107.40	CENTER LINE
181.74	183.76	183.53	176.11	165.99	166.14	149.24	124.13	105.01	107.36	1
184.00	185.54	185.23	178.32	168.53	169.53	154.24	120.78	102.00	105.14	2
184.56	184.53	183.87	177.71	168.34	169.82	142.42	115.24	97.44	102.27	3
182.45	180.85	178.71	173.83	170.78	166.55	132.70	113.36	95.04	99.47	4
176.37	171.60	171.65	177.35	168.35	152.33	121.91	106.45	93.13	96.87	5
172.29	161.57	160.19	151.90	136.71	133.09	114.21	97.40	88.99	94.62	6
169.18	147.33	108.89	98.73	109.75	119.92	106.97	92.59	85.68	91.94	7
139.12	99.45	7.00	7.00	88.61	107.76	101.60	88.97	82.24	89.40	8
116.71	7.00	7.00	7.00	88.51	102.13	97.96	87.06	79.63	86.10	9
EXIT										

Table G11. Ball Surface Temperature (C) versus Position (in units of 0.025 mm)
(Fluid N1, Load = 67N, P_H = 1.02 GPa, V_b = 12.7 m/s, V_{sa} = 0, T_{bath} = 40 C)

INLET	1	2	3	4	5	6	7	8	9	
66.79	66.26	67.92	69.70	70.47	71.30	71.00	68.90	68.43	68.69	9
66.75	66.10	67.90	69.70	70.47	71.30	71.00	68.90	68.43	68.69	8
67.13	66.42	67.98	69.66	70.46	71.29	71.01	68.90	68.43	68.69	7
68.35	67.69	68.29	69.60	70.48	71.30	71.00	68.90	68.43	68.69	6
69.91	68.86	68.95	69.85	70.83	71.39	70.97	68.90	68.43	68.69	5
73.27	70.11	69.81	70.78	71.41	71.48	70.93	68.90	68.43	68.69	4
78.06	72.75	72.18	72.82	72.09	71.61	70.95	68.88	68.43	68.69	3
84.84	78.47	76.28	75.02	73.22	72.15	71.07	68.85	68.42	68.69	2
92.72	86.33	82.29	78.39	75.32	73.21	71.40	68.91	68.41	68.69	1
101.46	94.05	89.24	83.28	78.37	75.09	72.24	69.30	68.47	68.69	CENTER LINE
109.49	101.69	95.81	88.94	82.37	77.53	73.61	69.63	68.41	68.69	1
116.35	108.77	101.97	94.05	86.06	79.58	74.53	69.97	68.43	68.69	2
122.03	114.95	107.83	98.93	89.50	81.30	74.93	70.22	68.51	68.69	3
126.24	119.50	111.59	102.13	91.89	82.59	75.29	70.31	68.53	68.69	4
129.15	122.90	114.56	104.30	93.01	82.86	75.09	69.97	68.45	68.69	5
130.12	124.31	116.23	105.95	93.68	82.71	74.60	69.54	68.38	68.69	6
129.60	124.84	116.91	106.03	93.11	82.18	74.22	69.27	68.34	68.69	7
127.83	123.80	115.85	104.85	91.96	81.43	74.10	69.32	68.34	68.69	8
125.79	121.80	113.35	102.08	89.74	80.30	73.82	69.37	68.36	68.69	9
EXIT										

Table G12. Fluid Temperature (C) versus Position (in units of 0.025 mm)
(Fluid N1, Load = 67N, P_H = 1.02 GPa, V_b = 12.7 m/s, V_{sa} = 0, T_{bath} = 40 C)

INLET	1	2	3	4	5	6	7	8	9	
118.67	117.42	112.74	109.05	111.89	110.96	107.10	106.94	111.42	108.00	9
122.38	121.11	116.99	111.40	118.39	116.35	111.67	110.65	115.65	112.25	8
125.57	124.87	125.28	114.18	122.31	124.21	115.57	116.23	121.00	114.94	7
128.06	126.65	122.87	118.26	133.56	132.52	124.03	118.55	124.59	118.05	6
129.73	129.43	127.62	126.25	135.74	140.71	124.80	129.10	130.47	120.67	5
130.20	132.42	131.36	129.37	137.72	147.47	137.92	136.61	132.54	123.60	4
128.56	135.32	133.45	131.82	140.13	149.04	145.88	140.57	135.17	127.54	3
135.98	141.24	140.50	139.02	145.16	158.85	145.16	159.96	141.02	129.36	2
145.26	151.33	151.45	148.65	151.04	162.46	154.04	167.36	145.79	131.11	1
156.74	159.80	160.04	157.50	158.21	167.88	156.91	168.59	143.37	130.45	CENTER LINE
160.98	166.63	167.77	166.55	166.31	174.30	160.21	167.74	145.78	130.73	1
168.22	172.97	174.73	173.32	171.59	178.72	175.23	158.05	141.63	129.46	2
172.28	176.05	176.81	176.03	173.79	182.98	163.00	142.57	136.51	128.42	3
171.38	175.50	175.25	173.69	184.71	179.02	147.56	141.05	134.93	125.29	4
167.74	172.25	176.23	191.38	185.38	162.08	134.32	133.90	134.21	124.28	5
177.04	183.92	199.31	192.56	170.54	149.03	126.74	128.26	129.86	123.09	6
179.18	180.99	183.96	170.68	148.08	137.30	121.62	124.71	126.67	120.11	7
164.03	167.61	163.67	157.09	142.90	128.41	115.41	119.00	121.36	117.43	8
145.91	150.36	150.57	144.22	134.92	121.86	110.54	114.34	117.28	113.33	9

EXIT

Table G13. Ball Surface Temperature (C) versus Position (in units of 0.025 mm)
(Fluid N1, Load = 215N, P_H = 1.51 GPa, V_b = .7 m/s, V_{sa} = 0, T_{bath} = 40 C)

INLET	1	2	3	4	5	6	7	8	9	10	11	12	
[illegible]	64.32	66.89	64.54	65.34	66.19	65.37	64.62	64.26	65.24	66.12	66.06	66.10	12
[illegible]	65.63	[illegible]	64.90	65.15	65.93	65.29	64.54	64.40	66.36	67.84	67.74	66.60	11
[illegible]	68.35	[illegible]	65.75	65.50	66.82	65.79	64.59	64.45	66.92	68.59	68.42	66.73	10
[illegible]	72.70	72.03	68.59	67.22	68.19	66.58	64.47	64.56	67.34	68.98	68.56	67.23	9
[illegible]	79.93	79.35	72.57	69.63	70.50	67.95	65.20	65.18	67.97	69.75	69.42	67.17	8
[illegible]	88.20	86.57	77.[illegible]	74.46	75.22	70.61	66.00	66.06	69.29	70.52	69.60	67.11	7
[illegible]	100.23	96.27	85.96	81.07	81.22	74.85	67.57	66.44	70.00	71.51	70.43	67.30	6
[illegible]	106.37	106.30	95.31	88.96	88.35	79.76	69.60	67.80	72.41	73.20	71.05	68.20	5
[illegible]	116.28	115.47	104.06	97.18	96.07	86.10	74.04	71.32	75.41	75.36	72.42	68.29	4
[illegible]	125.91	122.71	111.77	104.73	103.48	92.78	79.50	75.27	77.96	77.50	73.92	68.19	3
[illegible]	129.[illegible]	129.14	119.01	112.37	110.66	98.68	85.43	79.72	81.29	80.42	75.98	68.68	2
[illegible]	137.50	136.49	126.07	119.37	116.89	105.70	91.42	84.08	83.99	82.47	77.82	69.35	1
[illegible]	145.10	142.20	132.11	125.13	122.26	110.84	96.36	88.45	87.44	84.96	79.71	69.33	CENTER LINE
140.37	140.34	145.53	136.64	129.81	126.23	115.08	101.04	92.67	90.77	87.53	81.27	69.30	1
143.75	149.13	148.24	140.27	133.78	129.55	118.43	104.82	96.25	93.78	89.79	82.91	69.97	2
146.20	150.[illegible]	149.58	142.37	136.91	132.01	121.20	108.42	99.35	95.79	91.25	83.79	70.44	3
147.79	151.59	149.85	144.62	139.12	132.96	122.71	111.06	101.39	96.90	92.31	84.16	70.37	4
148.51	151.83	149.24	145.51	140.26	132.41	122.89	113.01	102.53	96.49	92.05	84.26	70.37	5
148.31	149.52	147.12	144.53	140.03	130.72	121.91	113.71	102.89	95.76	91.52	84.33	70.37	6
147.60	147.[illegible]	144.57	142.39	138.31	127.82	118.93	111.17	100.40	93.86	90.84	84.21	70.37	7
145.75	144.[illegible]	140.76	141.[illegible]	135.27	123.94	115.54	108.86	97.00	90.30	88.94	82.37	70.37	8
144.77	140.30	135.32	137.[illegible]	133.36	119.67	111.17	105.45	94.12	87.61	85.77	78.93	70.37	9
140.75	134.[illegible]	127.49	132.93	129.65	114.12	105.88	101.53	91.37	86.10	84.23	77.39	70.37	10
134.47	126.27	119.74	127.39	125.32	108.26	100.37	97.51	87.98	84.49	83.63	76.80	70.37	11
127.59	118.[illegible]	111.74	121.[illegible]	120.28	103.67	95.78	92.88	83.61	81.98	82.04	75.16	70.37	12

EXIT

Table G14. Fluid Temperature (C) versus Position (in units of 0.025 mm)
(Fluid N1, Load = 215N, P_H = 1.51 GPa, V_b = .7 m/s, V_{sa} = 0, T_{bath} = 40 C)

IN E!	1	2	3	4	5	6	7	8	9	10	11	12	
[illegible]	[illegible]15	142.66	142.[illegible]	142.10	132.51	120.06	111.38	101.80	97.80	94.01	95.08	85.76	12
[illegible]	151.[illegible]	152.35	156.[illegible]	157.02	151.15	138.35	126.79	111.51	100.44	96.36	98.75	89.[illegible]	11
[illegible]	157.35	158.81	164.[illegible]	163.40	155.37	151.09	140.30	125.68	109.67	104.00	105.03	93.07	10
[illegible]	157.44	159.09	160.90	166.18	166.28	156.72	148.75	136.57	133.83	119.42	112.86	100.21	9
[illegible]	160.60	158.97	160.04	163.86	162.79	162.01	161.90	142.14	136.70	126.20	119.56	106.41	8
[illegible]	161.68	167.56	164.47	162.58	160.34	161.21	162.04	155.44	142.22	137.19	134.58	112.66	7
[illegible]	168.68	175.49	169.35	162.95	159.52	164.19	172.43	164.26	149.53	146.48	143.95	121.75	6
[illegible]	181.71	181.05	174.44	164.97	163.56	165.69	162.70	151.76	145.13	153.85	147.93	129.68	5
[illegible]	187.06	179.79	173.42	169.75	170.56	172.07	163.97	146.35	138.43	151.34	158.56	139.63	4
[illegible]	196.36	201.34	190.59	175.37	173.00	177.27	169.48	148.49	135.32	152.02	167.60	143.55	3
[illegible]	206.12	226.73	213.32	183.16	176.93	181.97	172.05	147.17	130.62	151.47	166.98	154.89	2
[illegible]	205.63	182.54	179.16	187.75	185.82	185.41	173.85	148.41	132.92	152.09	166.33	162.[illegible]6	1
[illegible].00	206.86	199.52	194.18	191.46	188.71	188.44	176.03	150.86	134.15	151.31	165.02	162.62	CENTER LINE
[illegible].00	213.02	208.32	201.49	195.33	193.03	191.04	176.96	150.85	131.41	148.55	164.00	166.61	1
[illegible].10	213.65	209.16	201.80	198.01	195.83	192.75	178.92	153.02	129.97	146.64	163.17	160.65	2
[illegible].79	214.06	209.32	203.35	199.99	196.83	192.52	178.61	154.40	130.06	145.19	162.30	151.[illegible]8	3
[illegible].21	213.54	211.00	206.74	201.95	196.13	188.13	175.00	154.01	129.58	145.18	156.08	148.07	4
[illegible].29	209.17	207.94	205.40	202.32	194.51	181.83	169.66	150.45	128.50	148.62	147.85	139.33	5
[illegible].76	203.40	204.79	202.74	201.71	191.80	171.73	159.53	144.96	128.82	143.01	145.40	131.24	6
[illegible].55	201.60	201.36	201.57	199.25	185.31	158.94	151.40	144.04	127.79	135.10	136.50	122.85	7
[illegible].19	193.58	191.14	190.54	192.72	181.78	144.72	139.10	134.15	127.15	122.26	121.68	116.01	8
[illegible].86	174.55	176.69	180.44	183.00	178.05	128.72	120.15	127.15	119.25	109.62	114.20	109.57	9
[illegible].31	151.51	167.28	173.69	176.31	162.72	132.76	120.45	122.60	109.39	102.79	108.91	102.73	10
[illegible].07	129.32	157.09	161.06	166.02	159.23	131.66	115.62	113.82	103.54	94.71	101.96	97.68	11
[illegible].08	131.33	141.93	131.74	146.23	142.19	115.56	103.47	107.24	100.38	90.89	97.62	93.90	12

EXIT

Table G15. Ball Surface Temperature (C) versus Position (in units of 0.025 mm)
(Fluid N1, Load = 215N, P_H = 1.51 GPa, V_b = 1.39 m/s, V_{sa} = 0, T_{bath} = 40 C)

DEPT	1	2	3	4	5	6	7	8	9	10	11	12	
74.04	78.60	77.23	74.64	74.52	75.81	76.01	75.07	75.61	75.88	73.45	72.21	68.26	12
82.10	82.11	80.61	78.29	78.26	76.86	75.69	74.92	75.74	75.90	73.45	72.21	68.26	11
88.04	84.31	82.90	81.65	80.63	77.43	75.74	75.09	76.15	75.82	73.45	72.21	68.26	10
91.38	86.72	85.74	84.52	82.84	78.75	76.59	77.25	76.66	75.65	73.46	72.21	68.26	9
96.22	90.89	89.86	87.51	84.61	80.03	78.42	79.41	77.93	75.71	73.35	72.21	68.26	8
104.30	97.50	94.61	90.95	87.13	82.48	81.00	81.53	79.44	76.67	73.67	72.15	68.26	7
112.25	106.69	103.57	98.40	92.47	86.85	83.98	84.27	81.59	77.38	73.75	72.10	68.26	6
120.36	117.30	113.16	107.25	101.63	95.67	89.80	87.77	84.04	78.26	73.98	72.13	68.26	5
127.81	127.56	123.08	116.56	110.57	104.21	97.50	93.17	86.84	80.17	75.50	72.79	68.26	4
134.63	137.29	132.84	126.74	120.31	112.99	104.99	98.93	91.00	83.24	76.83	73.03	68.26	3
140.58	146.27	141.77	136.12	130.14	122.82	114.42	107.30	97.74	86.91	77.86	73.36	68.26	2
147.51	154.54	150.05	144.79	138.93	131.62	123.41	115.79	104.44	90.98	79.83	74.08	68.21	1
156.17	161.21	157.25	152.70	147.50	140.29	131.81	123.34	110.58	95.82	82.85	75.07	68.10	CENTER LINE
162.65	166.57	162.57	158.57	153.78	146.98	139.19	130.59	117.15	101.16	85.70	75.93	69.27	1
167.85	171.27	167.56	163.49	159.03	152.73	144.64	135.32	122.07	105.69	88.35	76.78	69.35	2
171.56	175.25	171.99	168.29	163.55	156.89	148.94	139.67	126.87	110.27	91.43	78.16	69.33	3
174.12	178.79	175.62	171.71	167.04	160.62	152.63	143.14	130.02	113.23	93.49	79.64	69.33	4
175.35	180.96	177.87	173.85	169.28	163.07	154.75	145.00	132.18	115.61	95.08	80.21	69.33	5
174.89	182.11	178.99	175.41	170.75	164.34	156.07	146.29	133.74	116.94	96.27	80.81	69.33	6
172.19	182.00	179.42	175.68	170.76	164.11	155.50	145.37	132.77	115.44	94.28	80.64	69.33	7
168.52	180.29	177.93	174.21	169.10	162.06	152.84	142.28	129.22	111.81	91.78	79.93	69.33	8
162.96	177.25	174.99	171.39	165.82	158.89	150.33	139.76	125.64	107.92	89.36	78.05	69.33	9
158.16	172.93	170.57	166.86	161.38	154.46	145.95	134.89	120.69	104.00	86.95	76.11	69.33	10
152.22	166.44	164.86	161.08	155.79	148.77	139.81	128.70	114.95	99.93	84.75	74.85	69.33	11
143.45	159.16	158.55	154.77	148.86	141.67	133.22	124.11	111.43	96.77	83.50	74.66	69.33	12

EXIT

Table G16. Fluid Temperature (C) versus Position (in units of 0.025 mm)
(Fluid N1, Load = 215N, P_H = 1.51 GPa, V_b = 1.39 m/s, V_{sa} = 0, T_{bath} = 40 C)

INLET 1	2	3	4	5	6	7	8	9	10	11	12	
163.24	161.40	162.70	157.14	143.91	131.97	124.81	120.49	118.03	113.29	110.20	102.19	91.30	12
162.95	163.71	166.28	161.60	155.17	148.17	136.66	136.44	128.38	120.67	118.93	106.66	95.14	11
163.[illegible]	168.73	168.54	166.90	156.[illegible]	152.26	150.98	150.18	143.50	132.59	124.68	111.94	99.17	10
162.00	167.76	167.34	162.75	161.33	162.56	155.02	158.06	157.28	145.84	132.13	119.45	104.74	9
168.61	168.76	169.87	167.39	161.14	162.42	159.77	162.90	161.45	157.15	140.95	130.47	109.82	8
171.22	171.64	172.61	171.55	168.34	164.27	158.36	161.33	167.67	162.04	155.96	146.99	119.67	7
181.84	178.19	173.08	171.94	170.16	166.05	158.37	158.92	166.57	169.97	162.09	159.08	129.78	6
190.54	184.82	179.66	177.53	174.63	168.78	160.05	157.70	166.30	171.30	169.42	163.82	137.83	5
198.79	188.90	182.24	181.74	180.86	174.38	163.86	158.75	166.33	170.80	168.97	170.50	150.27	4
207.73	193.08	186.74	187.18	185.76	178.68	168.30	161.97	167.15	170.05	166.61	170.40	157.89	3
216.55	197.53	190.08	190.47	188.43	180.32	168.35	161.17	167.16	170.97	170.05	171.31	157.89	2
221.93	202.31	192.52	192.58	192.20	184.66	171.49	163.27	170.29	173.18	170.79	171.68	165.28	1
223.93	208.33	200.19	198.50	194.63	185.75	173.52	169.89	178.20	176.75	176.81	171.09	165.47	CENTER LINE
225.04	208.13	176.17	178.96	197.89	190.60	172.89	170.42	181.70	179.37	172.65	171.69	165.18	1
225.01	210.12	181.71	185.17	201.20	193.21	174.41	173.01	184.79	181.83	174.27	172.45	158.91	2
225.31	214.61	207.98	208.03	205.33	194.1[illegible]	175.83	175.17	185.69	181.52	174.52	173.01	160.01	3
225.48	214.98	205.40	206.41	206.63	195.27	176.84	178.01	184.86	179.65	175.03	174.36	155.98	4
223.69	214.19	205.78	207.67	207.36	194.53	178.25	180.50	181.48	175.16	174.35	169.07	142.10	5
222.02	212.23	204.97	206.95	207.43	194.9[illegible]	178.75	179.86	174.35	167.37	166.55	164.89	132.85	6
220.19	208.65	201.23	205.01	205.26	195.07	179.62	177.60	168.29	155.66	161.27	153.12	123.62	7
217.24	205.08	199.18	203.10	203.74	191.95	177.45	175.66	160.58	151.14	146.76	137.39	113.60	8
214.69	200.87	195.13	196.99	198.58	186.17	157.99	155.19	148.60	139.71	138.25	128.05	108.82	9
207.76	192.60	188.70	191.03	185.18	166.99	144.73	144.61	137.12	128.69	130.13	120.39	102.76	10
193.96	179.52	172.47	174.93	171.36	154.67	132.25	134.70	126.09	119.45	123.17	114.03	98.65	11
185.91	167.06	159.82	160.75	154.90	139.6[illegible]	123.00	118.38	115.97	113.86	114.32	109.03	94.74	12

EXIT

Table G17. Ball Surface Temperature (40C) versus Position (in unots of 0.025 mm)
(Fluid N1, Load = 215N, P_H = 1.51 GPa, V_b = 2.54 m/s, V_{sa} = 0, T_{bath} = 40 C)

FILET	1	2	3	4	5	6	7	8	9	10	11	12	
88.74	97.89	87.39	86.72	87.91	87.27	54.58	83.13	82.75	82.15	82.29	81.89	82.04	12
93.69	96.80	95.59	96.24	95.04	93.62	91.47	88.58	87.45	86.02	83.71	83.68	82.64	11
93.66	102.93	100.79	100.11	99.11	96.73	94.19	91.71	89.47	86.97	84.66	84.24	82.87	10
99.32	110.33	107.51	106.45	104.76	100.69	97.41	94.86	90.87	87.05	85.62	85.54	83.14	9
109.72	120.22	117.40	116.85	114.28	108.29	102.59	98.10	93.06	88.64	86.73	86.43	84.27	8
121.86	130.77	127.12	126.58	124.44	117.46	110.06	103.35	95.98	90.45	88.42	87.65	84.64	7
135.42	141.17	137.92	136.24	135.82	126.83	117.01	108.95	99.59	90.69	87.93	88.38	85.95	6
147.34	151.15	148.12	149.39	147.13	137.76	125.81	114.13	106.69	108.32	102.39	93.17	87.71	5
158.84	160.65	157.63	159.26	157.64	148.54	135.30	121.08	114.42	118.69	110.45	96.64	88.26	4
167.32	169.55	166.11	167.49	166.39	156.07	144.26	129.54	119.78	115.58	106.47	96.90	88.78	3
175.22	177.25	174.38	175.47	174.17	165.85	152.36	137.64	126.36	119.38	108.93	99.17	89.87	2
181.36	184.08	181.54	182.55	180.92	172.35	159.51	145.42	132.60	121.16	109.45	100.96	89.95	1
186.53	189.66	187.05	187.57	185.96	177.77	165.39	151.96	138.56	123.11	110.18	103.65	90.09	CENTER LINE
191.65	193.18	190.79	190.44	188.57	181.32	169.70	156.91	142.96	123.73	109.77	104.37	90.32	1
193.58	196.34	193.95	192.62	190.47	183.61	173.01	161.09	146.78	125.02	110.24	105.87	90.19	2
195.95	198.67	196.59	194.12	191.21	185.05	175.50	164.46	149.66	125.56	110.66	107.57	90.43	3
197.45	200.17	197.34	195.30	189.76	184.02	175.91	166.08	152.56	133.23	118.21	108.87	91.63	4
197.14	199.67	197.55	192.05	186.34	180.98	175.16	166.58	154.58	141.93	127.23	110.82	91.63	5
195.92	198.11	195.72	189.49	183.26	178.40	173.63	165.60	153.14	140.00	126.37	110.62	91.60	6
193.22	196.54	193.64	186.97	178.83	174.06	170.05	163.04	151.03	138.40	124.94	109.28	91.60	7
189.17	194.34	191.23	181.39	171.76	167.72	166.11	160.42	148.86	136.34	122.77	107.79	91.60	8
183.94	191.20	188.17	176.29	164.97	161.18	160.97	156.63	145.46	133.26	119.50	105.07	91.60	9
178.65	186.20	183.75	170.91	157.74	154.09	155.57	152.45	140.96	128.84	116.07	102.30	91.60	10
171.56	179.99	177.91	164.90	150.87	147.45	149.96	147.45	136.61	125.51	114.33	101.49	91.60	11
164.36	173.60	170.63	157.28	144.58	141.85	144.11	142.14	132.25	121.88	111.77	100.13	91.60	12

EXIT

Table G18. Fluid Temperature (C) versus Position (in units of 0.025 mm)
(Fluid N1, Load = 215N, P_H = 1.51 GPa, V_b = 2.54 m/s, V_{sa} = 0, T_{bath} = 40C)

INLET	1	2	3	4	5	6	7	8	9	10	11	12	
147.32	157.31	162.40	154.89	146.62	135.07	122.60	118.83	123.05	119.65	111.06	107.13	106.[illegible]	12
169.56	169.31	173.79	166.96	154.74	144.86	125.57	124.74	129.23	127.20	116.71	109.62	100.[illegible]3	11
183.43	179.97	183.21	175.54	165.49	156.89	145.11	138.28	143.53	135.88	123.61	113.28	113.[illegible]5	10
192.24	185.24	187.66	180.37	171.38	171.08	166.43	155.47	157.49	145.12	124.24	117.52	117.85	9
202.60	192.01	194.89	186.37	178.01	176.37	177.59	172.59	180.39	169.36	137.54	125.01	122.[illegible]0	8
208.86	196.59	199.76	192.73	182.14	182.59	185.15	182.82	186.02	177.03	150.48	143.30	129.[illegible]4	7
215.60	202.68	205.18	194.80	142.41	188.50	194.31	190.89	190.25	168.47	176.24	159.45	137.90	6
221.32	209.33	211.01	199.58	186.14	194.50	202.21	198.53	192.32	180.94	176.97	169.00	150.25	5
226.14	215.07	216.71	204.99	192.44	199.79	208.74	205.74	196.56	177.24	173.67	173.27	167.[illegible]9	4
231.56	219.51	221.70	212.03	197.91	203.24	214.13	211.01	202.65	192.56	185.62	184.21	167.33	3
235.79	223.10	225.37	215.95	203.05	206.09	218.06	215.33	207.79	199.93	193.29	188.73	172.28	2
240.57	227.46	229.19	219.46	206.98	212.69	221.66	219.21	212.70	206.76	199.24	191.86	172.22	1
243.24	230.76	232.59	224.31	212.57	216.33	224.19	221.52	215.59	212.05	204.95	194.48	171.38	CENTER LINE
244.93	234.05	235.72	229.72	219.18	218.32	224.33	222.52	218.36	217.30	210.55	198.00	171.20	1
243.72	230.05	237.83	233.34	225.09	222.14	224.95	223.88	221.27	220.63	213.77	200.94	171.05	2
241.83	236.64	234.46	235.97	229.83	225.86	225.14	223.60	222.90	223.19	216.57	203.60	166.83	3
242.60	236.71	238.67	239.00	235.04	230.33	225.14	222.60	222.93	221.50	215.66	197.94	171.61	4
238.70	235.02	237.78	240.22	237.76	232.42	223.78	221.63	222.43	216.57	211.64	198.40	156.83	5
232.37	234.15	237.49	240.45	238.29	232.03	221.48	219.87	222.80	217.50	204.70	189.23	142.55	6
229.75	232.43	235.72	239.81	239.34	233.44	220.19	218.09	221.99	208.86	185.08	172.41	132.07	7
224.55	230.49	234.36	239.68	240.15	233.39	216.52	214.87	221.22	202.90	170.40	150.56	126.34	8
218.56	225.47	230.43	237.97	239.29	232.69	214.18	203.74	202.44	179.21	158.81	140.37	122.56	9
215.46	223.48	226.84	235.75	238.86	232.78	205.42	182.84	184.54	168.49	150.36	134.19	118.78	10
205.63	215.67	218.26	226.78	230.14	220.95	162.85	164.51	165.79	156.16	139.37	128.13	114.59	11
199.71	207.09	209.97	214.96	209.96	125.90	162.83	147.19	153.51	144.80	131.55	123.40	111.22	12

EXIT

APPENDIX H

ASPERITY LOAD SHARING CALCULATION

Tallian's [135,136] partial EHD theory is used for calculating the ratio $W_{a,E\ell}/W_{EHD}$, where $W_{a,E\ell}$ is equal to the portion of load carried by asperities undergoing elastic deformation. Only elastic deformation of the asperities is considered, because of two reasons: (1) plasticity index calculated using Greenwood and Williamson's [55] theory was around .3, which indicates small amounts of plastic deformation of asperities (2) for low Λ values the assumption of elastic deformation gives lower values for the ratio $W_{a,E\ell}/W_{EHD}$ which then means a higher estimate on W_{EHD}.

$$\frac{W_{a,E\ell}}{W_{EHD}} = \frac{E'\sigma_\theta \; I(\frac{h}{\sigma}, \alpha)}{4\pi^2 \; P_H \; \psi_2(\frac{h}{\sigma})}$$

and, $W_{EHD} = W/(1 + (W_{a,E\ell}/W_{EHD}))$.

where, $\alpha = 10$, assuming a reasonable spread in power spectrum of the surface

I & ψ_2, given by Tables VI and VII pages 257 and 258 of Ref. 136. (Intermediate values were estimated)

$\Lambda = \frac{h}{\sigma}$, Computed from measured values of h and (estimates where h was not known)

σ_θ = .0349 and .122 corresponding to $\theta = 2°$ and $7°$ - a practical range of values for θ

θ = inclination of the asperity flank with the mean surface, rad

σ_θ = tangent θ

α = Number indicating the spread of power spectrum

(α = 1 for spectrum of single frequency

$\alpha = \infty$ for spectrum extending over all frequencies)

W_{EHD} portion of load carried by EHD film, N

P_{EHD} EHD load divided by contact area, GPa

$P_{avg.}$ Average Hertz pressure; GPa

APPENDIX I

FERROGRAPHIC AND SPECTROGRAPHIC OIL ANALYSIS TECHNIQUES

1. Ferrographic Oil Analysis Technique

Ferrography is a technique developed to separate wear debris from the lubricant and arrange the particles according to size on a transparent substrate for examination in an optical or scanning electron microscope. The scientific principles underlying this technique have been well described in references [155-159].

The Ferrograph analyzer used in this technique consists of a pump to deliver an oil sample at a low rate (.2 cm^3/mm), a magnet to provide a high gradient magnetic field near its poles and a treated transparent substrate on which the particles are deposited. The magnetic particles adhere to the substrate and are distributed approximately according to their size. Ferrogram which is the substrate with deposited particles, is approximately 50 mm long. The largest particles (up to a few hundred microns) appear at entry (55-56 mm position). As the oil flows down the ferrogram, the size of the particles reduces continuously until only submicron particles are deposited near the exit and (10 mm position). The deposit in addition to containing magnetic particles of metals such as iron, nickel, cobalt, also consists of various paramagnetic alloys nonferrous metals and oxides.

The optical densities of the deposit at various places along the ferrogram may be observed with a ferrogram reader (a densitometer) to give the amount and size distribution of the particles. Optical density expressed as percent area covered is used for preliminary analysis.

A unique instrument called the Ferroscope which is essentially a bichromatic microscope can be used to identify the nature of particles on the ferrogram. Red light is employed for reflected light and green light is employed for transmitted light. This technique provides a good color contrast and a color distinction between metals and compounds.

A scanning electron microscope can also be used to study the particles deposited on the Ferrogram.

2. Spectrographic Oil Analysis Technique

Emission spectrographic oil analysis technique has been used quite extensively for detection of abnormal wear. This method commonly called SOAP analysis yields the wear debris concentration in ppm. Light projected through the vaporized sample is dispersed by a diffraction grating. Photomultipliers tubes, each sensitive only to the light wavelengths characteristic of a particular element, generate a signal proportional to the light received.

3. Oil Sampling for Wear Debris Analysis

All oil contacting parts in the EHD apparatus were washed with acetone, dried, and rinsed with distilled water. Then all parts were washed with a dilute acid solution. This solution was prepared by adding 10 drops of concentrated nitric acid and 10 drops of concentrated hydrochloric acid to 50 cm^3 of distilled water. This solution dissolved any metallic debris left from the previous test. The parts were then rinsed with distilled water, a dilute sodium bicarbonate solution, distilled water again, and finally with 95 percent ethanol.

Care was taken not to introduce any extraneous particles while taking out oil samples. Settling of wear debris to the bottom of the reservoir, was not a serious problem since several minutes of settling time [160] are required for particles 5 μm or less in size.

REFERENCES

1. Fuller, Dudley D., "Theory and Practice of Lubrication for Engineers," John Wiley and Sons, New York, 1956.

2. Department of Education and Science, "Lubrication (Tribology) - A Report on the Present Position and Industry's Needs," H. M. Stationery Office, London, 1966.

3. Jost, Peter H., "Economic Impact of Tribology," Mechanical Engineering, August 1975, pp. 26-33.

4. Ling, F. F., "Socio-Economic Impacts of Tribology," Proc. Tribology Workshop, National Science Foundation, April 1974, pp. 32-64.

5. Tallian, T. E., "Elastohydrodynamic Hertzian Contacts," Mechanical Engineering; Part 1, Nov. 1971, pp. 14-18; part 2, Dec. 1971, pp. 17-22.

6. Wedeven, Lavern D., "What is EHD," Lubrication Engineering, Vol. 31, No. 6, June 1975, pp. 291-296.

7. Reynolds, O., "On the Theory of Lubrication and its Application to Mr. Beauchamp Tower's Experiments Including an Experimental Determination of the Viscosity of Olive Oil," Phil. Trans. Roy. Soc., Lond., Vol. 177, pt. 1, 1886, pp. 157-234.

8. Dowson, D. and Higginson, G. R., "Elastohydrodynamic Lubrication," Pergamon Press, Lond., 1965.

9. Dowson, D., "Elastohydrodynamic Lubrication: An Introduction and a Review of Theoretical Studies," Proc. Inst. Mech. Engrs., 1965-66, Vol. 180, Pt. 3B, pp. 7-16.

10. Archard, J. F., "Experimental Studies of Elastohydrodynamic Lubrication," Proc. Inst. Mech. Engrs., 1965-66, Vol. 180, Pt. 3B, pp. 17-30.

11. Dowson, D., "Elastohydrodynamics," Proc. Inst. Mech. Engrs., 1967-68, Vol. 182, Pt. 3A, pp. 151-167.

12. Winer, W. O., "A Review of Experimental Elastohydrodynamic Lubrication (EHD) Research," Proc. Tribology Workshop, National Science Foundation, April 1974, pp. 207-228.

13. Cheng, H. S., "A Review of Theoretical Elastohydrodynamic Lubrication (EHD) Research," Proc. Tribology Workshop, National Science Foundation, April 1974, pp. 183-206.

14. Martin, H. M., "Lubrication of Gear Teeth," Engineering, Lond., 1916, Vol. 102, p. 199.

15. Beeck, O., Givens, W. J., and Smith, A. E. (1940), "The Mechanism of Boundary Lubrication," Proc. Roy. Soc. Lond., Series A, Vol. 177, p. 9.

16. Grubin, A. N., Central Scientific Research Institute for Technology and Mechanical Engineering, Book No. 30 (Moscow) 1949; D.S.I.R. Trans. No. 337.

17. Blok, H., Communications, Proc. Inst. Mech. Engrs. 1965-66, Vol. 180, Pt. 3B, p. 237.

18. Dowson, D., and Higginson, G. R., "New Roller-bearing Lubrication Formula," Engineering, Lond., 1961, Vol. 192, p. 158.

19. Cheng, H. S., and Sternlicht, B., "A Numerical Solution for the Pressure, Temperature, and Film Thickness between Two Infinitely Long, Lubricated Rolling and Sliding Cylinders, under Heavy Loads," Trans. ASME, J. Basic Eng., Sept. 1965, pp. 695-707.

20. Cheng, H. S., "A Refined Solution to the Thermal Elastohydrodynamic Lubrication of Rolling and Sliding Cylinders," ASLE Trans., Vol. 8, pp. 397-410, 1965.

21. Cheng, H. S., "Calculation of Elastohydrodynamic Film Thickness in High Speed Rolling and Sliding Contacts," MTI Report 67TR24, May 1967.

22. Archard, J. F., and Cowking, E. W., "Elastohydrodynamic Lubrication at Point Contacts," Proc. Inst. Mech. Engrs., 1965-66, Vol. 180, Pt. 3B, pp. 47-56.

23. Hamrock, B. J., and Dowson, D., "Isothermal Elastohydrodynamic Lubrication of Point Contacts: Part I - Theoretical Formulation," Trans. ASME, Jour. of Lub. Tech., Vol. 98, Ser. F, No. 2, April 1976, pp. 223-229.

24. Hamrock B. J., and Dowson, D., "Isothermal Elastohydrodynamic Lubrication of Point Contacts: Part II - Ellipticity Parameter Results," Trans. ASME, Jour. of Lub. Tech., ASME Paper No. 75-LUB-12, presented at the Joint ASME-ASLE Lubrication Conf., Miami, Florida, Oct. 1975.

25. Hamrock, B. J., and Dowson, D., "Isothermal Elastohydrodynamic Lubrication of Point Contacts: Part III - Fully Flooded Results," Trans. ASME, Jour. of Lub. Tech., ASME Paper No. 76-LUB-30, presented at the Joint ASME-ASLE Lubrication Conference, Boston, Massachusetts, October 1976.

26. Hamrock, B. J., and Dowson, D., "Isothermal Elastohydrodynamic Lubrication of Point Contacts: Part IV - Starvation Results," Trans. ASME, Jour. of Lub. Tech., Paper No. 76-LUB-31, presented at the Joint ASME-ASLE Lubrication Conference, Boston, Massachusetts, October 1976.

27. Lee, D., Sanborn, D. M., and Winer, W. O., "Some Observations of the Relationship between Film Thickness and Load in High Hertz Pressure Sliding Elastohydrodynamic Contacts," Trans. ASME, J. Lub. Tech., Vol. 95, 1973, pp. 386-390.

28. Sanborn, D. M., Winer, W. O., "Fluid Rheological Effects in Sliding Elastohydrodynamic Point Contacts with Transient Loading: I - Film Thickness," Trans. ASME, J. Lub. Tech., Vol. 93, pp. 262-271, 1971.

29. Hamilton, G. M., and Robertson, W. G., "Lubrication of Rollers with Oils Containing Polymers," Proc. Inst. Mech. Engrs., Vol. 181, Pt. 3, No. 3, 1966-67.

30. Kannel, J. W., and Walowit, J. A., "Simplified Analysis for Tractions Between Rolling-Sliding EHD Contacts," Trans. ASME, Jour. of Lub. Tech. Vol. 93, Ser. F, No. 1, Jan. 71, pp. 39-46.

31. Archard, J. F., and Baglin, K. P., "Nondimensional Presentation of Frictional Tractions in Elastohydrodynamic Lubrication - Part I: Fully Flooded Conditions," Trans. ASME, Jour. of Lub. Tech., Vol. 97, Ser. F., No. 3, July 1975, pp. 398-411.

32. Archard, J. F., and Baglin, K. P., "Nondimensional Presentation of Frictional Tractions in Elastohydrodynamic Lubrication - Part II: Starved Conditions," Trans. ASME, Jour. of Lub. Tech., Vol. 97, Ser. F, No. 3, July 1975, pp. 412-423.

33. Jakobsen, J., and Winer, W. O., "Traction of Elastohydrodynamic Contacts with Thermal Shearing Flow," Trans. ASME, Jour. of Lub. Tech., Vol. 97, Ser. F, No. 3, July 1975, pp. 424-429.

34. Kunz, R., and Winer, W. O., "Prediction of Traction in Sliding EHD Contacts," Trans. ASME, Jour. of Lub. Tech., Vol. 98, Ser. F, No. 3, July 1976, pp. 362-366.

35. Allen, C. W., "A Simplified Model for the Elastohydrodynamic Traction Between Rollers," Trans. ASME, Jour. of Lub. Tech., Vol. 98, Ser. F, No. 3, July 1976, pp. 357-361.

36. Trachman, E. G., "A Simplified Technique for Predicting Traction in Elastohydrodynamic Contacts," ASLE Trans., Paper No. 76-LC-1A-1, presented at the Joint ASME-ASLE Lubrication Conf., Boston, Massachusetts, October 1976.

37. Blok, H., "The Postulate About the Constancy of Scoring Temperature," Interdisciplinary Approach to the Lubrication of Concentrated Contacts (Ed. P. M. Ku), NASA SP-237 (1970).

38. Cheng, H. S., and Orcutt, F. K., "A Correlation between the Theoretical and Experimental Results on the Elastohydrodynamic Lubrication of Rolling and Sliding Contacts," Proc. Inst. Mech. Eng., Vol., 180 Pt. 3B, 1965-66, pp. 158-168.

39. Hamilton, G. M., and Moore, S. L., "Deformation and Pressure in an Elastohydrodynamic Contact," Proc. Roy. Soc., Lond., 322A, 1971, pp. 313-330.

40. Bartz, W. J., and Ehlert, J., "Influence of Pressure Viscosity of Lubricating Oils on Pressure Temperature, and Film Thickness in Elastohydrodynamic Rolling Contacts," presented at the ASME Lubrication Symposium on Concentrated Contacts, Atlanta, May 1976.

41. Turchina, V., Sanborn, D. M., and Winer, W. O., "Temperature Measurements in Sliding Elastohydrodynamic Point Contacts," J. Lub. Tech., Trans. ASME, Series F, Vol. 96, No. 3, July 1974, pp. 464-471.

42. Blok, H., "Surface Temperatures under Extreme Pressure Lubricating Conditions," 2nd World Petroleum Congress, Paris, June 1937, Vol. 3, Section 4.

43. Blok, H., "Theoretical Study of Temperature Rise at Surface of Actual Contact Under Oiliness Lubricating Conditions," General discussions on Lubrication, London, 1937, Vol. 2, Institution of Mechanical Engineers, p. 222.

44. Jaeger, J. C., "Moving Sources of Heat and the Temperature at Sliding Contacts," Proc. Roy. Soc. N.S.W., Vol. 56, (1942), p. 203.

45. Archard, J. F., "The Temperature of Rubbing Surfaces," Wear, Vol. 2, No. 6, Oct. 1959, p. 438.

46. Holm, Ragnar, "Calculation of the Temperature Development in a Contact Heated in the Contact Surface, and Application to the Problem of the Temperature Rise in a Sliding Contact," J. Appl. Phys., Vol. 19, April 1948, pp. 361-366.

47. Holm, Ragnar, "Electric Contacts Handbook," Springer-Verlag, 1958.

48. Bowden, F. P., and Ridler, K. E. W., "A Note on the Surface Temperature of Sliding Metals," Proc. Cambridge Phil. Soc., Vol. XXXI, Pt. III, pp. 431-432, 1935.

49. Bowden, F. P., and Ridler, R. E. W., "Physical Properties of Surfaces III - The Surface Temperature of Sliding Metals, the Temperature of Lubricated Surfaces," Proc. Roy. Soc., Lond., Ser. A., No. 883, Vol. 155, pp. 640-656, May 1936.

50. Bowden, F. P. and Hughes, T. P., "Surface Temperature of Rubbing Solids and the Formation of the Beilby Layer," Nature, Vol. 139, pp. 152-153, Jan. 23, 1937.

51. American Gear Manufacturers Association (AGMA), "Gear Scoring Design Guide for Aerospace Spur and Helical Power Gears," AGMA Information Sheet 217.01 (Prepared by Lemanski, A. J.), Oct. 1965.

52. Dudley, Darle W., "Practical Gear Design," McGraw-Hill Book Company, Inc., New York, 1954.

53. Kelley, B. W., "A New Look at the Scoring Phenomena of Gears," Trans. Soc. Automot. Engrs., 1953, Vol. 61, pp. 175-188.

54. Kelley, B. W., and Lemanski, A. J., "Lubrication of Involute Gearing," Proc. Inst. Mech. Engrs., 1967-68, Vol. 182, Pt. 3A, pp. 173-184.

55. Greenwood, J. A., and Williamson, J. B. P., "Contact of Nominally Flat Surfaces," Proc. Roy. Soc. Lond., Vol. 295, Ser. A., pp. 300-319, 1966.

56. Greenwood, J. A., and Tripp, J. H., "The Elastic Contact of Rough Spheres," Trans. ASME, J. Appl. Mech., Vol. 89, Ser. E, pp. 153-159, 1967.

57. Whitehouse, D. J., and Archard, J. F., "The Properties of Random Surfaces of Significance in their ontact," Proc. Roy. Soc. Lond., Vol. 316, Ser. A, pp. 97-121, 1970.

58. Archard, J. F., "Elastohydrodynamic Lubrication of Real Surfaces," Tribology, Feb. 1973, pp. 8-14.

59. Nayak, P. R., "Random Process Model of Rough Surfaces," Trans. ASME, J. Lub. Tech., Vol. 93, No. 3, pp. 398-407, July 1971.

60. Nayak, P. R., "Some Aspects of Surface Roughness Measurement," Wear, Vol. 26, pp. 165-174, 1973.

61. Nayak, P. R., "Random Process Model of Rough Surfaces in Plastic Contact," Wear, Vol. 26, pp. 305-333, 1973.

62. Archard, J. F., "Surface Topography and Tribology," Tribology International, Oct. 1974, pp. 213-220.

63. Whitehouse, D. J., "The Measurement and Analysis of Surfaces," Tribology International, Dec. 1974, pp. 249-259.

64. Christensen, H., "Stochastic Models for Hydrodynamic Lubrication of Rough Surfaces," Proc. Inst. Mech. Engrs., Vol. 184, Pt. 1, 1969-70, p. 1013.

65. Jackson, A., and Cameron, A., "An Interferometric Study of the EHD Lubrication of Rough Surfaces," ASLE Paper No. 74-LC-2A-2, presented at the Joint ASME/ASLE Lubrication Conf., Montreal, Oct. 74 (to be published in Trans. ASLE).

66. Chow, L. S., and Cheng, H. S., "Pressure Perturbations in EHD Contacts due to an Ellipsoidal Asperity," Trans. ASME, Jour. of Lub. Tech., Vol. 98, Ser. F, No. 1, January 1976, pp. 8-15.

67. Chow, L. S., and Cheng, H. S., "The Effect of Surface Roughness on the Average Film Thickness between Lubricated Rollers," Trans. ASME, Jour. of Lub. Tech., Vol. 98, Ser. F, No. 1, Jan. 1976, pp. 117-124.

68. Fein, R. S., and Kruez, K. L., "Discussion on Boundary Lubrication," Interdisciplinary Approach to Friction and Wear (Ed. P. M. Ku), NASA SP-181, 1968, p. 358.

69. Fowles, P. E., "The Statistical Application of a Thermal Ehl Theory for Individual Asperity-Asperity Collisions to the Sliding Contact of Rough Surfaces," Trans. ASME, J. Lub. Tech., Vol. 97, Ser. F, No. 2, April 1975, pp. 311-320.

70. Dawson, P. H., "Effect of Metallic Contact on the Pitting of Lubricated Rough Surfaces," J. Mech. Engr. Sci., Vol. 4, No. 2, p. 16, 1962.

71. Johnson, K. L., Greenwood, J. A., and Poon, S. Y., "A Simple Theory of Asperity Contact in Elastohydrodynamic Lubrication," Wear, Vol. 19, p. 81, 1972.

72. Bamberger, E. N., et al., "Life Adjustment Factors for Ball and Roller bearings - An Engineering Design Guide," ASME, 1971.

73. Kirk, M. T., "Hydrodynamic Lubrication of Perspex," Nature, Vol. 194, June 9, 1962, pp. 965-966.

74. Archard, J. F., and Kirk, M. T., "Lubrication at Point Contacts," Proc. Roy. Soc., Ser. A, London, Vol. 253, 1961, p. 52.

75. Archard, J. F., and Kirk, M. T., "Influence of Elastic Modulus on the Lubrication of Point Contacts," I. Mech. E., Lond., Lubrication and Wear Convention, 1963, Paper No. 15, p. 181.

76. Archard, J. F., and Kirk, M. T., "Film Thickness for a Range of Lubricants under Severe Stress," J. Mech. Eng. Sci., Vol. 6, 1964, p. 101.

77. Foord, C. A., Wedeven, L. D., Westlake, F. J., and Cameron, A., "Optical Elastohydrodynamics," Proc. I, Mech. Engrs., London, Vol. 184, Part 1, Paper No. 28/70, 1969-70.

78. Wedeven, L. D., "Traction and Film Thickness Measurements under Starved Elastohydrodynamic Conditions," Trans. ASME, Jour. of Lub. Tech., Vol. 97, Ser. F, No. 2, April 1975, pp. 321-329.

79. Sanborn, D. M., "An Experimental Investigation of the Elastohydrodynamic Lubrication of Point Contacts in Pure Sliding," Ph.D Thesis, University of Michigan, Ann Arbor, Michigan, and University microfilms, Ann Arbor, Michigan, 1969.

80. Gentle, C. R., and Cameron, A., "An Investigation of Traction in Elastohydrodynamic Point Contacts using Optical Interferometry," ASLE Trans., Vol. 18, No. 3, pp. 222-228.

81. Stejskal, E. O., and Cameron, A., "Optical Interferometry Study of Film Formation in Lubrication of Sliding and/or Rolling Contacts," NASA CR-120842, April 1972.

82. Gohar, R., and Cameron, A., "The Mapping of Elastohydrodynamic Contacts," ASLE Trans., Vol. 10, 1967, pp. 215-225.

83. Tolansky, S., "An Introduction to Interferometry," John Wiley and Sons, New York, 1973.

84. Hottel, H. C., and Sarofim, A. F., "Radiative Transfer," McGraw-Hill, New York, 1977.

85. Wiebelt, J. A., "Engineering Radiation Heat Transfer," Holt, Rinehart and Winston, New York, 1966.

86. Wolfe, William L., ed. "Handbook of Military Infrared Technology," U. S. Government Printing Office, Washington, D. C., 1965.

87. Holden, J., "Multiple-beam Interferometry; Intensity Distribution in the Reflected System," Proc. Phys. Soc., Vol. 62, 1949, p. 405.

88. Kebler, R. W.,"Optical Properties of Synthetic Sapphire," booklet, Linde Company - A division of Union Carbide, New York.

89. Lauer, James L., and Peterkin, M. E., "Analysis of Infrared Spectra of Fluid Films in Simulated EHD Contacts," Trans. ASME, Jour. of Lub. Tech., Vol. 97, Ser. F, No. 2, April 1975, pp. 145-150.

90. Lauer, James L., and Peterkin, M. E., "Infrared Emission Spectra of Elastohydrodynamic Contacts," Trans. ASME, Jour. of Lub. Tech., Vol. 98, Ser. F, No. 2, April 1976, pp. 230-235.

91. Wedeven, L. D., "Preliminary Study of the Use of Infrared Radiation to Reveal Lubrication Behavior," NASA TM X-67883, July 1971.

92. Barnes Engineering Company, "Instruction Manual - Infrared Radiometric Microscope - Model RM-2A, Stamford, Connecticut.

93. Bivans, Ernest W., "Measuring Infrared Detector Noise," Electronic Design, Aug. 2, 1962.

94. Carlson, S. F., Jakobsen, J., Nagaraj, H. S., Molina-Combita, M. A., Sanborn, D. M. and Winer, W. O., "Investigations of Lubricant Rheology as Applied to Elastohydrodynamic Lubrication," NASA CR-134730, Georgia Institute of Technology, Atlanta, Georgia, Sept. 1974.

95. Ausherman, V. K., Nagaraj, H. S., Sanborn, D. M., and Winer, W. O., "Infrared Temperature Mapping in Elastohydrodynamic Lubrication," Trans. ASME, Jour. of Lub. hech., Vol. 98, Ser. F, No. 2, April 1976, pp. 236-243.

96. Kane, P. F., and Larrabee, G. B., Ed., "Characterization of Solid Surfaces," Plenum Press, New York, 1976.

97. Whitehouse, D. J., "Stylus Techniques," Ch. 3, pp. 49-74, in "Characterization of Solid Surfaces," Ed. Kane, P. F., and Larrabee, G. B., Plenum Press, New York, 1974.

98. British Standards Institution, "Centre-Line-Average Height Method for the Assessment of Surface Texture," B. S. 1134: 1961.

99. American Standard, "Surface Texture - Surface Roughness, Wariness and Lay," ANSI B46.1, April 1976 (Preliminary draft).

100. Whitehouse, D. J., "Improved Type of Wave-Filter for Use in Surface-finish Measurement," Proc. I. Mech. E., London, Vol. 182, Pt. 3K, 1967-68, pp. 306-318.

101. Whitehouse, D. J. and Reason, R. E., "The Equation of the Mean Line of Surface Texture Found by an Electric Wave Filter," Rank-Taylor Hobson, Leicester, U. K., 1965.

102. Whitehouse, D. J., and Van Herck, P., "Survey of Reference Lines in the Assessment of Surface Texture," Annals of the CIRP, Vol. 21/2, 1972, pp. 267-273.

103. Shunmugam, M. S., and Radhakrishnan, V., "Two and Three-dimensional Analyses of Surfaces Accoraing to the E-System," Proc. I. Mech. E., Vol. 188, 1975, pp. 691-699.

104. Radhakrishnan, V., "On an Appropriate Radius for the Enveloping Circle for Roughness Measurement in the E-System," Annals of the CIRP, Vol. 20/1, 1971, pp. 109-110.

105. Higginson, G. R., and Leaver, R. H., "Fluid Lubrication of Tapered Roller Bearings," Proc. I. Mech. E., Vol. 184, pt. 3L, 1969-70, pp. 18-25.

106. Leaver, R. H., Sayles, R. S., and Thomas, T. R., "Mixed Lubrication and Surface Topography of Rolling Contacts," Proc. I. Mech. E., Vol. 188, 1974, pp. 461-469.

107. Williamson, J. B. P., "The Shape of Solid Surfaces," in "Surface Mechanics," by ASME, 1968, p. 24.

108. Spragg, R. C., and Whitehouse, D. J., "A New Unified Approach to Surface Metrology," Proc. I. Mech. E., Vol. 185, 1970-71, pp. 697-707.

109. Whitehouse, D. J., "Review of Topography of Machined Surfaces," Presented at the SME Meeting, Pittsburgh, 1973.

110. Whitehouse, D. J., Vanherck, P., deBruin, W., and van Luttenvelt, C. A., "Assessment of Surface Typology Analysis Techniques in Turning," Annals of the CIRP, Vol. 23/2, 1974, pp. 265-282.

111. Whitehouse, D. J., "Typology of Manufactured Surfaces," Annals of the C.I.R.P., Vol. XVIV, 1971, pp. 417-431.

112. Tabor, D., "A Simplified Account of Surface Topography and the Contact Between Solids," Wear, Vol. 32, 1975, pp. 269-271.

113. Thomas, T. R., "Recent Advances in the Measurement and Analysis of Surface Microgeometry," Wear, Vol. 33, 1975, pp. 205-233.

114. Williamson, J. B. P., and Hunt, R. T., "Asperity Persistence and the Real Area of Contact Between Rough Surfaces," Proc. Roy. Soc., Lond., Ser. A, Vol. 327, 1972, pp. 147-157.

115. Pullen, J., and Williamson, J. B. P., "On the Plastic Contact of Rough Surfaces," Proc. Roy. Soc., Lond., Ser. A, Vol. 327, 1972, pp. 159-173.

116. Williamson, J. B. P., "Topography of Solid Surfaces," NASA SP-181, 1968 (ed. Ku, P. M.).

117. Williamson, J. B. P., "Topography of Solid Surfaces," NASA SP-181, 1968 (ed. Ku, P. M.).

118. Peklenik, J., "New Developments in Surface Characterization and Measurements by Means of Random Process Analysis," Proc. I. Mech. E., Vol. 182, Pt. 3K, 1967-68, pp. 108-126.

119. Sayles, R. S., and Thomas, T. R., "Microtopometry of Engineering Surfaces," Presented at the 3rd Intn. Tribology Conf., Paisley, Scotland, 1975.

120. Carlson, John, "Fourier Analyser Training Manual," AN 140-0, Hewlett-Packard, April 1970.

121. Hewlett-Packard, "System Operating Manual - Fourier Analyzer System, HP 5451 A."

122. Bendat, Julius S., and Piersol, Allan G., "Measurement and Analysis of Random Data," John Wiley and Sons Inc., New York, 1966.

123. Jenkins, Gwilym M., and Watts, Donald G., "Spectral Analysis and its Applications," Holden-day, San-Francisco, 1968.

124. Otnes, R. K., and Enochsen, L. D., "Digital Time Series Analysis," John Wiley and Sons Inc., New York, 1972.

125. Chamberlain, Leo J., "A Simple Discussion of Time-Series Analysis," Sound and Vibration, April 1971, pp, 18-25.

126. Doebelin, E. D., "Measurement Systems: Application and Design," McGraw-Hill Book Company, New York, 1966.

127. Greenwood, J. A., and Kauzlarich, J. J., "Inlet Shear Heating in Elastohydrodynamic Lubrication," Trans. ASME, J. Lub. Tech., Oct. 1973, pp. 417-426.

128. Crook, A. W., "The Lubrication of Rollers - III," Phil. Trans. Roy. Soc., Lond., Ser. A, Vol. 254, 1961, pp. 237-258.

129. Woolveridge, P. E., and Archard, J. F., "Temperature Distributions in Elastohydrodynamic Films: A New Analytical Solution," I. Mech. E., Paper No. CA/72, pp. 48-54.

130. Jakobsen, J., "Lubricant Rheology at High Shear Stress," Doctoral dissertation, Georgia Institute of Technology, Atlanta, Georgia, and University Microfilms, Ann Arbor, Michigan, 1973.

131. Sanborn, D. M., and Winer, W. O., "Fluid Rheological Effects in Sliding Elastohydrodynamic Point Contacts with Transient Loading: 2-Traction," Trans. ASME, Jour. of Lub. Tech., Vol. 93, Ser. F, No. 3, 1971, pp. 342-348.

132. Kunz, R. K., Nagaraj, H. S., Sanborn, D. M., and Winer, W. O., "Investigations of Lubricant Rheology as Applied to Elastohydrodynamic Lubrication," NASA CR-134882, Georgia Institute of Technology, Atlanta, Georgia, August 1975.

133. Nagaraj, H. S., Sanborn, D. M., and Winer, W. O., "Effect of Load, Speed and Surface Roughness on Sliding EHD Contact Temperatures," Trans. ASME, Jour. of Lub. Tech., Paper No. 76-Lub - 23, presented at the Joint ASME-ASLE Lubrication Conference, Boston, Massachusetts, Oct. 1976.

134. Williamson, J. B. P., and Hunt, R. T., "Relocation Profilometry," Journal of Scientific Instruments (Journal of Physics E), 1968, Series 2, Volume 1, pp. 749-752.

135. Tallian, T. E., "The Theory of Partial Elastohydrodynamic Contacts," Wear, Vol. 21, 1972, pp. 49-101.

136. Tallian, T. E., "Author's Comments on "The Theory of Partial Elastohydrodynamic Contacts," Wear, Vol. 24, 1973, pp. 255-258.

137. Bell, J. C., and Dyson, A., "Mixed Friction in an Elastohydrodynamic System," I. Mech. E., Elastohydrodynamic Lubrication, 1972 Symposium, 1972, pp. 68-76.

138. Thompson, R. A., and Bocchi, W., "A Model for Asperity Load Sharing in Lubricated Contacts," Trans. ASLE, Vol. 15, No. 1, pp. 67-79.

139. Tallian, T. E., "On Competing Failure Modes in Rolling Contact," ASLE Trans., Vol. 10, 1967, pp. 418-439.

140. Czichos, H., "Influence of Asperity Contact Conditions on Failure of Sliding Elastohydrodynamic Contacts," to be published in Wear Magazine, 1976.

141. Jones, W. R., Nagaraj, H. S., and Winer, W. O., "Ferrographic Analysis of Wear Debris Generated in a Sliding Elastohydrodynamic Contact," to be presented at the 32nd ASLE Annual Meeting, Montreal, April 1977, and to be published in Trans. ASLE.

142. Alsaad, M., Kunz, R. K., Nagaraj, H. S., Bair, S. S., Rentzepis, G. M. Sanborn, D. M., and Winer, W. O., "Investigations of Lubricant Rheology as Applied to Elastohydrodynamic Lubrication," NASA Contractor Report (to be published), Georgia Institute of Technology, Atlanta, Ga., Aug. 1976.

143. Smith, R. W., "Lubricant Behavior in Concentrated Contact - Some Rheological Problems," ASLE Trans., Vol. 18, No. 3, 1960.

144. Johnson, K. L., and Roberts, A. D., "Observation of Viscoelastic Behavior of an EHD Lubricant Film," Proc. Roy. Soc. Lond., Ser. A, Vol. 337, 1974, p. 217.

145. Johnson, K. L., and Cameron, R., "Shear Behavior of Elastohydrodynamic Oil Films at High Rolling Contact Pressures," Proc. I. Mech. E., Vol. 182, Pt. 1, 1967/68, p. 307.

146. Alsaad, M., "Light Scattering Study of the Glass Transition and the Glassy State in Lubricating Oils," Ph.D. Thesis, Georgia Institute of Technology, Atlanta, Ga., and University Microfilms, Ann Arbor, Michigan, Aug. 1976.

147. Dyson, A., "Scuffing - A Review," Tribology International, April 1975, pp. 77-87.

148. Dyson, A., "Scuffing - A Review; Part 2: The Mechanism of Scuffing," Tribology International, June 1975, pp. 117-122.

149. Rozeanu, L., "A Model for Seizure," ASLE Trans., Vol. 16, No. 2, 1973, pp. 115-120.

150. Rozeanu, L., and Godet, M., "The Phenomenology of Friction Thermal Failure," Presented at the Production Engineering Conference, Tokyo, 1974.

151. Rozeanu, L., "Friction Transients - their Role in Friction Failures," Presented at the Joint ASLE - JSLE International Lubrication Conf., Tokyo, 1975, to be published in Trans. ASLE, Oct. 1976.

152. Rozeanu, L., "Friction Interaction of Metallic Materials," to be offered for Limits of Lubrication Conf., London, July 1977.

153. Bowden, F. P., and Tabor, D., "Friction and Lubrication of Solids - Vol. II," Oxford Univ. Press, London, 1964.

154. Wedeven, L. D., "Influence of Debris Dent on EHD Lubrication," Trans. ASLE, ASLE Paper No. 76-LC-1A-3, Presented at the Joint ASME - ASLE Lubrication Conference, Boston, Massachusetts, Oct. 1976.

155. Seifert, W. W., and Westcott, V. C., "A Method for the Study of Wear Particles in Lubricating Oil," Wear, Vol. 21, 1972, pp. 27-42.

156. Scott, D., Seifert, W. W., and Westcott, V. C., "The Particles of Wear," Scientific American, Vol. 230, No. 5, May 1974, pp. 88-97.

157. Foxboro/Trans-Sonics, "Ferrograph Fluid Analyzer System," Information Bulletin, Burlington, Mass., 1976.

158. Reda, A. A., Bowen, R., and Westcott, V. C., "Characteristics of Particles Generated at the Interface Between Sliding Steel Surfaces," Wear, Vol. 34, 1975, pp. 261-273.

159. Scott, D. , Seifert, W. W., and Westcott, V. C., "Ferrography - an Advanced Design Aid for the 80's," Wear, Vol. 34, 1975, pp. 251-260.

160. Foxboro/Trans-Sonics, "Oil Sampling Technique," Ferrograph Technical Bulletin - 1.

VITA

Holavanahally Seshachar Nagaraj was born in Markonahally, Karnataka State, India, on September 14, 1949. After starting the elementary school education in 1953, he graduated from High School in 1964. With the completion of Preuniversity course in 1965, he joined the Bangalore University, Bangalore, India, in 1965. He obtained his Bachelor's degree (B.E.) in Mechanical Engineering in 1970 from the Bangalore University. He also obtained his Master's degree (M.E.) in Mechanical Engineering in 1972 from the Indian Institute of Science, Bangalore, India. After completing the fall semester of 1972 at the State University of New York, Stony Brook, N.Y., he enrolled in the Georgia Institute of Technology, Atlanta, Georgia for the doctoral program in the School of Mechanical Engineering in January 1973. His background and interest have been in the areas of Lubrication, Tribology and Mechanical design. He has published in the areas of Numerical Control of machine tools and Elastohydrodynamic Lubrication.